Model Mismatch Paradigm for Probe based Nanoscale Imaging

A DISSERTATION
SUBMITTED TO THE FACULTY OF THE GRADUATE SCHOOL
OF THE UNIVERSITY OF MINNESOTA
BY

Pranav Agarwal

IN PARTIAL FULFILLMENT OF THE REQUIREMENTS
FOR THE DEGREE OF
Doctor Of Philosophy

Advisor: Dr. Murti V. Salapaka

October, 2010

© Pranav Agarwal 2010
ALL RIGHTS RESERVED

Acknowledgements

Doctoral studies have been the finest years of my life. When I look back at myself six year back, I see an unsure person who did not know what to expect in doctoral studies, whether I would be able to adjust to American culture and whether I would be able to contribute worthwhile to a field I barely knew to start with. Traces of anxiety and lots of excitement still remains as I am stepping out of doctoral studies looking forward to working on completely new technologies. But a lot has changed too. I have much more faith in myself and that I would be able to carve out new areas of research and nurture them with patience, hardwork and good collaborations. I could go on and on to list out the number of ways in which I have been forced to explore different aspects of myself in past years but I'll just like to mention that I thoroughly enjoyed the journey.

My mentor and advisor, Dr. Murti Salapaka, has influenced me in unimaginable ways over past years. He has and will always be my role model for everything I do in life. I cannot thank him enough for providing me with an independent environment to innovate and look after my interest at each step of the Ph.D. program. There were a number of instances where he asked me to do things which I would not even understand at that time. But just having faith in him and executing the tasks patiently helped me realize much later that he actually shaped me consciously throughout these years. He was always around me whether I required personal or professional counseling. Complementing him in a number of ways, Durga embraces every member of NanoDynamics Systems Lab (NDSL) family. She took such good care of me that I could finally get over my nostalgia. We could all share things with her which we would not even dare to talk to Dr. Murti. Thanks a lot Durga for endless fun parties, fantastic food and being my family during Ph.D.. I was fortunate to be around when they had two energetic kids, Siddhartha and Pranav. Seeing them grow, so closely, made me realize that having a

family is probably not such a bad idea after all. I do not know if you both will remember me later but I'll miss you both kiddos a lot and I will love you forever.

NDSL has had a constant inflow and outflow of splendid students over years. I got a chance to interact with Abu, Anil, Deepak, Tatha, Vikas, Hullas, Tanuj, Govind, Subhrajit and Sayan. Yes, I have been in this program long enough now. I got an opportunity to work with Abu on a collaborative project with IBM Research Lab, Zurich. His sincerity, intellect and a million dollar smile reassures me that research is always fun. Anil's dedication and passion for perfection is truely amazing. At one point in time, we had five students from the same batch (Batch of 2000). I had a lot of fun times with them, whether it was being invited for a pot-luck party or watching world cup soccer match or just plain sitting and chatting aimlessly. I have known Hullas for past fifteen years now. But I only got to know him clearly enough during Ph.D.. He has constantly been painfully funny throughout my PhD, be it from hiding my shaving equipment because he did not approve of my shaving daily or writing obnoxious status messages on my social networking accounts. Nothing is impossible for Hullas. At least so he believed while he laid aimlessly and dirty in his cubicle chair voraciously consuming random information from wikipedia, youtube and news websites. I firmly believe that if Hullas is smiling with a strange twist of his tongue, then you better prepare yourself for being the subject of some unknown crazy prank in near future. But he actually made me do things that I always thought were impossible. I started running (my best distance being 8.6 miles, my wardrobe changed from fifty dollar shirts to two dollar t-shirts and my mind started firing random prank ideas in his presence. My wife, Sabarni, was subjected to some such ideas. Yes, I got married to my childhood crush during Ph.D.. No wonder it took me so long to finish my studies. She has been the driver of my emotional state of mind (well I guess that is how it is going to be for the rest of my life now). She always planned things for me two steps ahead in time. My parents and my sister have been very supportive throughout these years. I very recently decided to google my Dad and I found out that he had seven journal publications. Some of his publications are being cited till date. Papa, you make me so proud and I hope I too make you proud now. I can only consider myself lucky to have got such nice and caring in-laws and sister-in-law.

I have also had a chance to collaborate with a number of excellent research groups

during my Ph.D.. I got to work in a world class research facility at IBM research lab, Zurich as a part of "Millipede" technology. I would especially like to thank Evangelos, Haris, Abu, Angeliki, Deepak, Dorothea, Peter and Walter for their support and intense technical discussions during the project. At IBM, I got a first hand glimpse into the development of cutting edge technologies and the challenges and volatility involved in the process. I also grateful to Aditya and Naveen from Iowa State University with whom I worked on modeling of the dynamic mode operation as a communication channel. I got to learn a lot from them. I would also like to thank Dr. Greg Haugstad with whom I collaborated on the project for characterization of polymers. It was fun to do those long experiments together and I learned a lot from him about the correct interpretation of AFM data.

I would also like to thank my committee members, Dr. Gary Balas, Dr. Tryphon Georgiou, Dr. Joey Talghader, Dr. Evangelos Eleftheriou and Dr. Greg Haugstad for agreeing to be on my committee. Last but not the least, I would like to thank my friends, Rajat Mittal, Pushkar Modi, Manoj Paul and Shourya Otta, whom I got close to over years. Thanks a lot for being there for me.

Dedication

To my parents, Dr. Dhirendra Swarup Gupta and Dr. Mridubala Gupta, my sister, Swati Agarwal and my wife, Sabarni Palit, whose unshakable faith in my decision to pursue a Ph.D. degree made this possible.

To my mentor, Dr. Murti Salapaka, who has influenced me and shaped my thought process in so many ways.

ABSTRACT

Scanning Probe Microscopes (SPMs) are widely used for investigation of material properties and manipulation of matter at the nanoscale. These instruments are considered critical enablers of nanotechnology by providing the only technique for direct observation of dynamics at the nanoscale and affecting it with sub Angstrom resolution. Current SPMs are limited by low throughput and lack of quantitative measurements of material properties. Various applications like the high density data storage, sub-20 nm lithography, fault detection and functional probing of semiconductor circuits, direct observation of dynamical processes involved in biological samples viz. motor proteins and transport phenomena in various materials demand high throughput operation. Researchers involved in material characterization at nanoscale are interested in getting quantitative measurements of stiffness and dissipative properties of various materials in a least invasive manner.

In this thesis, system theoretic concepts are used to address these limitations. The central tenet of the thesis is to model, the known information about the system and then focus on perturbations of these known dynamics or model, to sense the effects due to changes in the environment such as changes in material properties or surface topography. Thus a model mismatch paradigm for probe based nanoscale imaging is developed.

The topic is developed by presenting physics based modeling of a particular mode of operation of SPMs called the dynamic mode operation. This mode is modeled as a forced Lure system where a linear time invariant system is in feedback with an unknown static memoryless nonlinearity. Tools from averaging theory are used to tame this complex nonlinear system by approximating it as a linear system with time varying parameters. Material properties are thus transformed from being parameters of unknown nonlinear functions to being unknown coefficients of a linear plant.

The first contribution of this thesis deals with real time detection and reduction of spurious areas in the image which are also known as probe-loss areas. These areas become severely detrimental during high speed operations. The detection strategy is based on thresholding of a distance measure, which captures the difference between

sensor models in absence and presence of probe-loss. A switching gain control strategy based on the output of a Kalman Filter is used to reduce probe-loss areas in real time. The efficacy of this technique is demonstrated through experimental results showing increased image fidelity at scan rates that are 10 times faster than conventional scan rates.

The second contribution of this thesis deals with developing multi-frequency input excitation strategy and deriving a bias compensated adaptive parameter estimation strategy to determine the instantaneous equivalent cantilever model. This is used to address the challenge of quantitative imaging at high bandwidth operation by relating the estimated plant coefficients to conservative and dissipative components of tip-sample interaction. The efficacy of the technique is demonstrated for quantitative material characterization of a polymer sample, resulting in material information not previously obtainable during dynamic mode operation. This information is obtained at speeds which are two orders faster than existing techniques. Quantitative verification strategies for the accuracy of estimated parameters are presented.

The third contribution of this thesis deals with developing real time tractable models and characterization methodology for an electrostatically actuated MEMS cantilever with an integrated solid state thermal sensor. Appropriate modeling assumptions are made to delineate various nonlinear forces on the cantilever viz. electrostatic force, tip-sample interaction force and capacitive coupling. Experimental strategy is presented to measure the thermal sensing transfer function from DC-100kHz. A quantitative match between experimental and simulated data is obtained for the large range nonlinearities and small signal dynamics.

Contents

List of Figures

Chapter 1

INTRODUCTION

Ever since the invention of atomic force microscope by Binnig et. al. in 1986 [1], cantilever-beam shaped probes with a sharp tip at one end are used to interrogate material properties such as topography ([2]), and mechanical ([2]), electrical ([3]), thermal ([4]) and optical ([5]) properties. The field of probe based sensors is fueled by developments in three critical fields.

- MEM Fabrication Technology:

  Cantilever probes or arrays of cantilever probes with a sharp tip at one end can be manufactured using semiconductor fabrication technology. By varying the size and the material of cantilever beam (typical sizes are 100μm $\times 30\mu$m $\times 1\mu$m), one can achieve probes with stiffness varying from 0.001 N/m to 140 N/m and resonant frequency till 1.5 MHz ([6]). Tips can be grown on the cantilever beams with tip radius $\approx$ 10 nm or less and from different materials for varying hardness or conductive properties. As a result, various kinds of probe-based sensors are available in market today that can sense topography, and electrical, magnetic, thermal, optical and piezoelectric properties of the sample ([7, 6]).

- Sensing Technology:

  Optical detection techniques like the beam-bounce method and interferometry are used to sense cantilever deflection with a resolution of $< 1A^o$. In the beam-bounce method, a laser beam is focused at the back of the cantilever tip, which reflects it into a split photodiode. The ratio of the intensity of light in the two

halves indicates the motion of the cantilever tip. Integrated sensing methods like capacitive sensing ([8]), thermal sensing ([9]) and piezoresistive sensing ([10]) are also commonly used.

- Application of Control Theory:

  Control or feedback principles formed an integral part of the first design of the scanning tunneling microscope (STM) and atomic force microscope (AFM) ([1]), and still play a pivotal role in the development of probe-based sensing and imaging schemes. Typically, the idea is to maintain the sensor (i.e. the tip) under a constant influence of the sample for prolonged periods of time. For instance, in contact mode AFM, a constant force is maintained on the tip by regulating the cantilever deflection to a set value. In tapping mode AFM, the amplitude of the oscillating cantilever is regulated. In frequency modulated AFM (FMAFM), the resonant frequency of the cantilever is regulated. A control systems viewpoint also plays a pivotal role in the positioning of the sample with respect to the tip of a probe-based sensor with a positioning resolution of $< 1A^o$ and high bandwidth.

The idea of using a probe based sensor with a sharp tip in contact mode operation is similar to the operation of a gramophone stylus. The tip is in constant contact with the sample and moves over the sample in a raster fashion. If there is a hill in the surface topography then the cantilever is pushed up by the sample. Likewise if there is valley then the cantilever is pushed down by its spring force. Corresponding deflections of the cantilever are recorded through an optical detection method as a proportional measure of sample topography. The cantilever is modeled as a spring with a spring constant k. Thus $F = kp$, where F is the spring force on the cantilever, k is the spring constant and p is the measured cantilever deflection, is used to infer the force from the measured deflection. This equation also indicates that for higher signal to noise ratio (SNR) of measured deflection with respect to the measurement noise, one would require softer cantilevers. A problem arises from the fact that the intermolecular forces between tip atoms and sample atoms are not monotonic in nature ([11]). These intermolecular forces are modeled as the Lennard Jones force where the long range Van Der-Waals forces act in addition to the short range chemical forces to result in a force profile as shown in Figure 1.1. This results in a "snap-in" condition when the tip approaches the sample

wherein the tip suddenly snaps into the sample and no longer interrogates the entire force profile. To measure this force profile, typically, large stiffness cantilevers are used in contact mode. Also the information in this mode of sensing is located in the low frequency range, which is heavily affected by $\frac{1}{f}$ measurement noise, thereby reducing the SNR of the measured signal. Thus to obtain a decent SNR, it is required to engage the tip harder with the sample. This implies large tip-sample forces and consequent tip-sample wear and tear in contact mode.

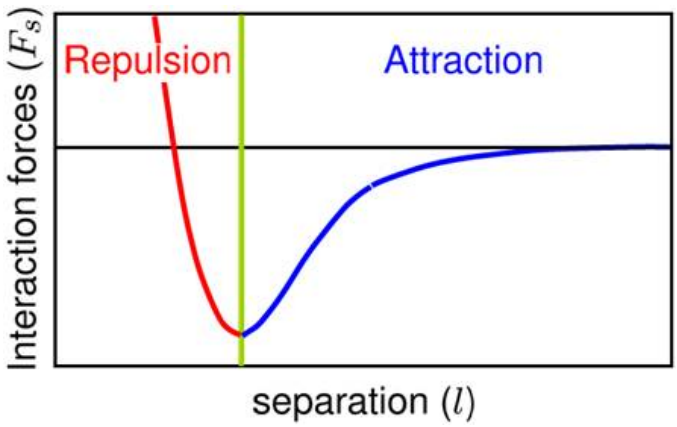

Figure 1.1: Nonlinear Tip-Sample interaction force modeled as Lennard Jones force. This has contributions from long range Van Der-Waals forces and short range chemical forces.

The second mode of sensing that was developed for probe-based sensors had the following rationale. The cantilever beam in fixed-free configuration is modeled as a superposition of infinite modes. Each mode is a second order spring-mass-damper system. Typically, a first mode approximation of the cantilever beam suffices to predict the deflection trajectories. If we oscillate the cantilever with small amplitudes near the sample at its first resonance then the following force balance equation results.

$$m\ddot{p} + c\dot{p} + kp \quad = \quad kg(t) + \phi(p) \tag{1.1}$$

where $\phi(p)$ is the nonlinear static memoryless tip-sample interaction force which is only dependent on the tip-sample separation. Since the amplitude of cantilever oscillation is

small, we can linearize $\phi(p)$ about a nominal operating point and get

$$\begin{aligned} m\ddot{\tilde{p}} + c\dot{\tilde{p}} + k\tilde{p} &= kg(t) + \tfrac{d\phi(p)}{dp}|_{p_0}\tilde{p} \\ m\ddot{\tilde{p}} + c\dot{\tilde{p}} + (k - \tfrac{d\phi(p)}{dp}|_{p_0})\tilde{p} &= kg(t) \end{aligned} \tag{1.2}$$

where $\tilde{p}$ captures small changes in tip deflection about a nominal operating point. Thus the equivalent stiffness of the cantilever changes in the presence of the external force. Since $\frac{d\phi(p)}{dp}|_{p_0} > 0$ for an attractive force (see Figure 1.1), $k_{\text{eff}} = (k - \frac{d\phi(p)}{dp}|_{p_0}) < k$ and since $\frac{d\phi(p)}{dp}|_{p_0} < 0$ for a repulsive force, $k_{\text{eff}} = (k - \frac{d\phi(p)}{dp}|_{p_0}) > k$. Also since the resonant frequency of the cantilever, $\omega_0^2 = \frac{k}{m}$, the resonant frequency of the first mode of the cantilever will increase for a repulsive force and decrease for an attractive force. From a feedback perspective, the idea is to regulate the resonant frequency of the cantilever to a set value. Since the direction of the change of resonant frequency flips signs depending on the nature of the force, we can only stabilize the tip in the attractive part of the tip-sample force. Therefore this mode requires the samples to be extremely flat in topography. Moreover, since the amplitudes of the operation are small, this mode of operation requires high stiffness cantilevers to avoid "snap-in" condition. This is because kA, where A is the amplitude of oscillation, should be large to overcome the snap-in force. In this operation

$$\begin{aligned} \omega_{\text{eff}}^2 &= \tfrac{k_{\text{eff}}}{m} = \tfrac{(k - \frac{d\phi(p)}{dp}|_{p_0})}{m} \\ \tfrac{d\phi(p)}{dp}|_{p_0} &= k - m\omega_{\text{eff}}^2. \end{aligned} \tag{1.3}$$

This mode measures the gradient of the tip-sample interaction force ([12]).

If there are dissipative as well as conservative parts to the tip-sample interaction force then $\phi = \phi(p, \dot{p})$ depends on tip velocity in addition to the tip position. Linearization results in

$$\begin{aligned} \Delta\phi(p, \dot{p}) &= \tfrac{d\phi(p,\dot{p})}{dp}|_{p_0}\tilde{p} + \tfrac{d\phi(p,\dot{p})}{d\dot{p}}|_{\dot{p}_0}\dot{\tilde{p}} \\ m\ddot{\tilde{p}} + c\dot{\tilde{p}} + k\tilde{p} &= kg(t) + \tfrac{d\phi(p)}{dp}|_{p_0}\tilde{p} + \tfrac{d\phi(p,\dot{p})}{d\dot{p}}|_{\dot{p}_0}\dot{\tilde{p}} \\ m\ddot{\tilde{p}} + (c - \tfrac{d\phi(p,\dot{p})}{d\dot{p}}|_{\dot{p}_0})\dot{\tilde{p}} + (k - \tfrac{d\phi(p)}{dp}|_{p_0})\tilde{p} &= kg(t) \end{aligned} \tag{1.4}$$

Thus ω_{eff}^2 captures the conservative part of the force and $Q_{\text{eff}} = \frac{c_{\text{eff}}}{m}$ captures the dissipative part of the force.

Good SNR in this operation comes from the fact that the operation is away from DC and centralized around the resonance of the first mode of the cantilever. At that

frequency, $1/f$ measurement noise is negligible and the operation is thermal noise limited ([13]). Moreover, high Q of the cantilever provides higher gain to the signal as compared to the measurement noise and thus improves SNR. Thus to achieve a resolution of $< 1A^o$, in this mode, we require very high Q cantilever operation (typically 10000-15000) ([12]). Also to stabilize the tip in the attractive regime of the tip-sample force, one requires to control the environment and the temperature carefully. This mode is thus used in low temperature and ultra high vacuum conditions. Low temperatures reduce the thermal vibrations of the cantilever and increase the SNR, and ultra high vacuum increases the quality factor of the cantilever and stabilizes the tip-sample forces by avoiding any further growth on the sample. Since there is a large spectrum of samples that require to be imaged in their native conditions viz. biological species in their native buffers, this mode is rendered less useful for such applications.

The third more commonly used mode of operation, which also forms the main focus of this thesis, is the tapping mode ([14]) or intermittent contact mode operation. In this mode, the cantilever is oscillated near its resonance at large amplitudes such that the tip traverses a substantial part of the force profile in every oscillation cycle. Typical operational amplitudes are in the range of $25 - 40$ nm. Since the tip-sample forces are localized typically within $1 - 4$ nm from the sample surface, it means that the tip experiences tip-sample interaction forces for a small amount of time in the entire oscillation period. In this operation

$$m\ddot{p} + c\dot{p} + kp \quad = \quad kg(t) + \phi(p, \dot{p}) \tag{1.5}$$

where $\phi(p, \dot{p})$ cannot be linearized. The amplitude and sine of the phase of the cantilever oscillations change linearly with sample height ([15]) and are measured and used for feedback and imaging purposes.

The desired sensitivity for this operation relies on the high quality factor of the cantilever. Since this mode is used in ambient conditions and at room temperature, typical values of Q in this operation are between $100 - 250$. This gets much worse under liquid since the quality factors drop to $10 - 20$ and so does the sensitivity of operation. Also, inferring sample properties from the measured observables is not a straightforward task since the only measureables are the amplitude and the phase at the excitation frequency. It can be shown that deriving basic sample properties like elasticity and

stiffness of the sample from amplitude and phase measurements can be quite challenging ([16, 17]). Moreover these signals are dependent on cantilever dynamics since these are the outputs of the cantilever beam model. Thus the desire for obtaining high sensitivity by opting for high quality factor of the beam sets off a trade off with respect to the imaging bandwidth. Imaging is usually done by mapping steady state measureables of the cantilever trajectory with the sample properties. Cantilever transients decay inversely with respect to the quality factor of the system. Thus one has to image slowly thereby effecting the throughput of the device. Thus there is a clear need to define signals which are of high bandwidth as compared to the amplitude and phase signals and can be used for high throughput operation. There is also a need for developing real time observable quantities that are a direct measure of sample properties when the probe based sensor is operating in intermittent contact mode.

Besides these basic AFM operation modes, a slew of other modes have been developed independently for imaging various material properties viz. optical, electrical, magnetic, thermal etc. Most of these modes of operations utilize the fact that a cantilever beam is a very sensitive force sensor with localized sensing property. Hence it can be used to nanoscale imaging. Moreover operating in dynamic mode and utilizing the gain of the cantilever beam at its mode resonances helps to increase the signal to noise ratio (SNR) with respect to the measurement noise.

Another important application where the knowledge of probe models in real time play a pivotal role is in bio sensing. The application setup involves observing a cellular process in its native environment from a distance using a probe based sensor without a tip. Depending on the rate and type of cellular process and the diffusivity of the surrounding media, the cell releases different proteins. Probes are biologically modified to be specific to a particular protein. If that specific protein is released from the cell, then it attaches to the cantilever modifying its effective mass. This results in a change of the equivalent cantilever model. Knowledge of the equivalent cantilever model in real time can help detect the presence of certain pathogens in the atmosphere and help study the rates of various cellular processes.

One major drawback of probe-based sensors is the low throughput and slow rates at which imaging can be done. Typical tapping mode operations require $6 - 7$ min/frame. A number of biomolecular dynamics like motion of kinesin motor on a microtubule and

DNA transcription, take place at μsec time scales. To observe these processes in real time, imaging rates of $30 - 40$ frames/sec are required. Another promising application that requires high throughput from probe based sensors is that of high density data storage. Owing to the capabilities of manipulating and sensing material at nanoscale, probe based sensors offer the possibility of data storage with aerial densities exceeding 1 Tb/in^2 ([18]). But to compete with current available techniques like flash technology, the read/write rates must be compatible.

The challenges faced by probe-based sensors can thus be categorized as follows:

- Challenge of Spatial Scales

  Probe based sensors provide excellent spatial resolutions ($< 1A^o$) and are able to sense a large variety of material properties at nanoscale. But mapping material properties for macro scale sized samples ($\approx$ mm) requires considerable time and in some cases it is not practical. Some key applications that require solutions to this challenge are nanolithography for technologies beyond 20 nm sized features, fault detection which includes electrical faults in fabricated chips or detection of cracks in sheets, nanopatterning of media and high density data storage. A basic difficulty arises from the fact that a single probe with a tip with nanometer dimensions has to interact with each sample point, a process that takes time. Secondly, positioning the sample with resolution ($< 1A^o$) with $\approx$ mm scale scan sizes is an issue.

- Challenge of Temporal Scales

  A number of processes occur at nanometer to micrometer scales which have time scales $\approx \mu$sec. Monitoring these processes at these time scales can help in understanding the dynamics involved in nanoscale physics, for eg. chemical reactions, motion of kinesis motor on a microtubule, DNA transcription and charge dissociation process in solar cell materials ([19]). Even though current probe sensor based instruments can monitor samples at the required spatial scales, they do not have enough temporal resolution. The basic problem lies in the lack of algorithms that can place the probe in proximity of the desired event at fast rates, and algorithms that can decipher these events from the observed variables of the probe.

- Challenge of Quantitative Imaging

Typically, the desired sample properties are deciphered from the output of the probe based sensor without any knowledge about the reliability of that output or the fidelity with which it represents the properties that need to be monitored. At very slow operational speeds, the probe is in quasi-static operation where the probe interacts with the sample in steady state. This, however, is not the case at high speeds of operation, where the probe can be in prolonged transients due to sample interaction, it might interact with the sample at different interaction levels or it might not interact with the sample at all. Sample properties are still inferred from the probe output in a manner similar to the quasi-static operation without a handle on image fidelity. Thus, there is a need for algorithms that provide real time handles for quantitative imaging.

There are currently two approaches for increasing the sensing rates of probe-based sensors. The first approach focuses on increasing the rates for a single probe by developing what is called a "video rate AFM" ([20, 21]). The idea is to increase the X-Y scan rates such that values of $30-40$ frames/sec are achieved. This is achieved by decreasing the size of the scanners, which increases their mechanical resonant frequency, designing new flexure stage designs with higher mechanical resonances or by exploiting mechanical resonances of certain devices like tuning forks. Several techniques are developed to ensure continuous interaction of the tip with the sample at such high tip velocities and then mapping the acquired data to sample properties. The second approach is to employ several probe-based sensors in parallel to increase the throughput ([9]). In this approach, an array of cantilevers is used to simultaneously probe different areas of the sample. Even though this technique cannot be used for observing fast processes occurring at a single point, they are well disposed for data storage applications where the data bits from multiple areas on the sample can be read at the same time for high read/write rates.

A general notable trend in the development of SPM field is the following. Researchers are trying to discern more information from the sample by increasing the degrees of freedom in the sensor model and defining multiple signals that can be measured to gain more knowledge about the sample. For instance, in contact mode, the cantilever is not actuated and is modeled as a spring. Thus, deflection is the only measureable. In dynamic

mode, the cantilever is being excited by a single sinusoid. In this, the cantilever is modeled as a second order spring mass damper system with certain resonant frequency and a quality factor. Additional measureable quantities are amplitude, phase and resonant frequency of the beam which can then be related to the sample properties. After this, the researchers developed schemes where two mode approximation of the cantilever was used such that the cantilever would amplify two harmonics in the cantilever trajectory due to nonlinear tip-sample interaction forces ([22]). Here we have amplitude, phase and resonant frequency of two modes of cantilever for deciphering sample information. Very recently, researchers suggested multi-frequency excitation techniques to estimate the quality factor of the cantilever which made simultaneous mapping of conservative and dissipative properties of the sample possible ([23]). There is thus a clear need to define new imaging signals by either redefining cantilever excitation signals or by shaping the cantilever transfer function such that more information about the tip sample nonlinearity can be accessed.

Another widely prevalent field in signal processing, control systems and communication is based on the idea of extracting information from changes in the models or deviations from nominal behavior. For instance, in robust control, the idea is to design a linear controller such that the required performance objectives are met for a certain class of uncertain models. Thus the change in models is treated as an uncertainty and a controller is designed with sufficient margins such that performance specifications are achieved across the entire set of plants. If the uncertainty magnitude is very large or if the operating conditions of the plant change during the operation then techniques like switching gain control, linear parameter varying control and multi linear plant designs are used to transit between optimal controllers for each operating point. In detection algorithms, any deviation from the nominal behavior is used for fault detection or for identifying outliers. Concepts of “model mismatch” or “distance between models” or “deviation from nominal model” is not present in MEMS sensors including probe based sensors. In this thesis, the paradigm of model mismatch is developed for probe based sensors and for imaging and mapping of material properties.

1.1 Organization of the Thesis

This thesis emphasizes on developing a model mismatch paradigm for probe-based sensors for nanoscale imaging in dynamic mode operation. Such a development requires

- Development of modeling and characterization techniques that provide real time information of the instantaneous probe model. This shall set the platform to map model based algorithms to probe based sensing.
- Developing a measure to capture the distance of an instantaneous probe model when it is under the influence of the sample from a nominal model. This requires the comparison of sensitivity of such a measure with conventional imaging parameters, and development of algorithms that amplify this sensitivity for sensing purposes.
- Using this measure to address some of the challenges that plague probe based sensing applications, viz. detection of events based on the deviations from the expected behavior or developing improved controllers that, apart from maintaining stable operation and constant tip-sample force, also amplify the sensitivity of this measure and achieve high bandwidth at higher resolutions.

The thesis is organized as follows:

- In video rate imaging, a critical problem that arises is that of "probe-loss". During probe-loss, the tip loses contact with the sample for some time and hence is no longer a reliable source of sample information. Such areas become more pronounced during high speed imaging. For quantitative imaging, a real time handle is required along with the image that tells which area of the image is reliable and which is not. Also such areas of probe-loss need to be minimized in real time to ensure continuous interaction of the tip with the sample. Chapter 2 exploits the knowledge of models to address this situation.
  - The problem is formulated as a two state model mismatch situation.
  - RMS of innovation error is used to achieve high bandwidth operation as opposed to currently used amplitude signal which is dependent on cantilever dynamics.

  - Switching gain PI controllers are used to reduce probe-loss areas in real time.
  - Lost DNA strands (typical height 1.4 nm) are recovered at speeds 30 times faster than conventional speeds.

- Chapter 3 deals with the development of a real time recursive technique for estimating an equivalent probe model in dynamic mode operation.

  - Sufficient cantilever excitation is chosen in a manner that is least disruptive to normal dynamic mode operation and is sufficient to estimate the model parameters.
  - The bandwidth of estimating these parameters is $< 400\mu$sec, which is two orders better than existing techniques and shall enable monitoring various processes at native time scales.
  - The resolution of the technique for detecting topographic changes is better than 1 nm.
  - A biased compensated exponentially weighted recursive least squares (BCEWRLS) algorithm is developed to estimate these parameters.
  - Detailed verification of the estimates provided by the REEP algorithm is done for both off-sample and on-sample situations.

Chapter 4 and 5 present two independent measures based on model mismatch principle, that can be used to enhance imaging performance in dynamic mode operation. These chapters utilize the development presented in chapter 3 in their analysis.

- In Chapter 4, use of resonant frequency estimate of the cantilever as an imaging signal is proposed during low Q tapping mode operation.

  - Analytical expression for sensitivity of resonant frequency estimate, damping coefficient estimate and amplitude with respect to changes in sample topography is derived
  - Experimental and analytical demonstration of increasing sensitivity of the resonant frequency estimates with reducing quality factors of the cantilever. This trend is opposite to the amplitude sensitivity which reduces with reducing quality factor and is upper bounded.

- In Chapter 5, observer based imaging technique for tapping mode AFM is proposed.
  - Sensitivity expression for RMS of the observer error signal with respect to the changes in the plant model is derived.
  - It is shown that by choosing an appropriate observer model that is different from the nominal plant model, one can obtain enhanced steady state sensitivity and signal to noise ratio and good imaging bandwidth.

Chapter 6 and 7 develop model mismatch paradigm for electrostatically actuated cantilevers. One particular realization of probe based high density data storage application is the "Millipede" project being executed by researchers at IBM Research Labs, Zurich. The probes in this application are electrostatically actuated and have integrated thermal sensing. The bits are stored by thermally making indentations on a polymer media. Presence of an indentation implies bit 1 and absence implies bit 0. In the initial phases of the project, these bits were sensed in contact mode operation. This led to huge wear and tear of the tip and the media over a large number of read operations and consequent reduction in device durability. If the tip gets blunt over time, bit widths increase and areal density of the device reduce. Also, scratching of the polymer media could lead to degradation of the media over time. So the idea was to move towards dynamic mode operation to lower tip-sample forces and consequent wear and tear. In dynamic mode, the read out rates are typically lower than contact mode and hence an algorithm for fast bit detection is required. This requires development of tractable models that can be characterized easily from thermal sensor data alone and are able to predict cantilever trajectories accurately. Such a model can then be used to develop abstract algorithms for high speed bit detection using a model mismatch based paradigm.

- Chapter 6 deals with developing tractable modeling and characterization methodology for electrostatically actuated cantilever with integrated thermal sensor.
  - Development of tractable models that can predict cantilever trajectories quantitatively and can be simulated in MATLAB environment to test advanced algorithms as compared to resource intensive FEM simulations or analytical models for simplified cantilever geometries.

  - Identification of model parameters using only the thermal sensor data. This is critical in an integrated environment where optical sensing is not available.
  - Identification of thermal sensing transfer function till a bandwidth of 100 kHz. This matches well with the currently available results from FEM simulations.

- Chapter 7 uses the modeling and characterization technique developed in chapter 6 and model mismatch concept to demonstrate high bandwidth image reconstruction in electrostatically actuated cantilevers.

  - Techniques for precise characterization of electrostatic force models is presented.
  - Extended Kalman filter is designed to predict the nominal behavior of the cantilever.
  - Experimental and simulation demonstration of high bandwidth sample reconstruction which can be both in topography disturbance and voltage disturbance.

Chapter 2

Real Time Reduction of Probe-loss using Switching Gain Controller for High Speed Atomic Force Microscopy

2.1 Introduction

Ever since the invention of scanning tunneling microscope by Binnig et al. [1] in 1986, scanning probe microscopes (SPMs) have found widespread use for probing materials and their related properties with spatial resolution at atomic scale and measurement of forces in the range of 1 pN-100 pN. Despite their versatility and usefulness, SPMs are plagued by slow imaging rates typically in the range of $3-6$ min/frame and consequently low throughput. A large number of applications viz. fault detection [24], nanolithography [25] and visualization of the dynamics of molecular proteins [20] demand a higher imaging rate (greater than $30-40$ frames/sec is needed).

Tapping mode operation is desirable in most applications since it reduces the lateral forces exerted by the tip on the sample thereby reducing tip-sample wear. In tapping mode, the cantilever is actuated near its first mode resonant frequency and interacts with the sample intermittently. These intermittent contacts with the sample as the cantilever

oscillates, transduce sample topography and its properties onto steady state amplitude and phase of the cantilever which are then interpreted to infer sample properties. Given the need for high speed imaging and the advantages of tapping mode operation, the need for tapping mode high speed AFM is evident.

There are many factors that need to be carefully accounted for while developing a high speed atomic force microscope (HSAFM) employing tapping mode operation [26, 27]. One of the primary challenges for HSAFM is that of probe-loss. Consider the scenario during imaging where the tip encounters a valley-like feature on the sample topography. Suppose also that prior to the arrival of such a feature, the tip is interacting with the sample as it oscillates, with the amplitude being maintained close to the set point amplitude, A_s. On encountering the valley, the tip loses contact with the sample and it is no longer interacting with the sample. Such a scenario leads to probe-loss [28] or parachuting [29].

In this thesis, we report significant reduction of probe-loss effected areas by implementing a switching gain PID controller which is based on the thresholding of the reliability index. It is shown that reliability index provides a faster thresholding signal as compared to amplitude signal. Real time reduction of probe-loss areas is shown on imaging of calibration sample at tip velocity of 240 μm/sec. It is shown that features that are lost during a high imaging rate with constant low gain controller are recovered by the use of switching gain controller even for a high aspect ratio sample. Finally a plasmid DNA on mica, with a height of 1.4 nm, is imaged at 30 Hz scan rate and reconstruction of a lost strand is shown to reveal that the resolution of the technique is better than 2 nm.

2.2 Problem Formulation

Note that as the cantilever is not interacting with the sample during probe-loss, the amplitude dynamics is decoupled from the sample topography and the positioning dynamics in z-direction. Indeed the amplitude increases as

$$\Delta a(t) \quad = \quad (A_0 - A_s)(1 - e^{-\omega_0 t/2Q}), \tag{2.1}$$

which is completely determined by operating parameters Q, ω_0, A_0 and A_s where Q, ω_0, A_0 and A_s are the quality factor, resonant frequency, free air amplitude and set

point amplitude of the cantilever respectively. The positioning dynamics in z-direction is governed by the difference, Δe, from the setpoint amplitude A_s of the current amplitude, $a(t)$, given by

$$a(t) \quad = \quad A_s + (A_0 - A_s)(1 - e^{-\omega_0 t/2Q}), \tag{2.2}$$

which makes $\Delta e(t) = \Delta a(t) = (A_0 - A_s)(1 - e^{-\omega_0 t/2Q})$. If a PI controller is employed, the sample position, $u(t)$, in z-direction, is given by

$$u(t) \quad = \quad g_{piezo}(t) * \{K_I \int_0^t \Delta a(\tau) d\tau + K_p \Delta a(t)\} \tag{2.3}$$

where $g_{piezo}(t)$ is the impulse response of the z-piezo actuator and $*$ denotes the convolution operator. In typical cases, it follows from (2.3) that if $\Delta a(t)$ is large, the sample is pushed towards the cantilever faster. If Δh is the separation between the tip and the sample at the onset of probe-loss then the minimum time, t_d, needed to recover from probe-loss is given by

$$(A_0 - A_s)(1 - e^{-\omega_0 t_d/2Q}) + \Big[g_{piezo}(t) * \{K_I \int_0^t \Delta a(\tau) d\tau + K_p \Delta a(t)\}\Big]_{t=t_d} \quad = \quad \Delta h, \tag{2.4}$$

which is obtained by adding (2.1) and (2.3) since the tip is not interacting with the sample.

A strategy employed by Sulcheck et. al. [26] for reducing probe-loss is to actively reduce the quality factor Q of the cantilever that lets the amplitude increase and reach its maximum value $(A_0 - A_s)$ faster that leads to a larger $\Delta a(t)$. However, the drawback of this methodology is that the quality factor remains reduced when there is no probe-loss and thus the on-sample behavior can suffer due to low Q operation. Another strategy for reducing t_d is to increase controller gains, on the positioning piezo, K_I and K_p beyond values that might be optimal for the particular sample. This strategy will lessen probe-loss affected area, however, it will lead to worsened on-sample behavior due to large tip-sample forces and can also induce instabilities due to the uncertain on-sample behavior. The trade off arises due to conflicting requirements of imaging parameters viz. Q, K_I and K_P when the tip is on-sample versus when it is off-sample. Choice of optimal controller gains for imaging a sample depend on g_{piezo} dynamics and sample features. Typically controller gains are chosen as high as possible to enable better tracking of sample topography and maintaining required set point amplitude.

However controller gains cannot be chosen arbitrarily high since that leads to unstable behavior of the tip over the sample. This results in large tip-sample forces leading to wear and tear of the tip and the sample. However, controller gains can be significantly higher when the cantilever is not interacting with the sample when compared to on sample scenario, without the adverse effect of instabilities on imaging.

A better alternative is to have separate strategies when the cantilever is on-sample and when it is off-sample. However, such a strategy is possible only if there is a means to infer when the cantilever is interacting with the sample and when it is not, in real time. Ando et. al. [29] employ the cantilever amplitude as a means of indicating a loss of interaction with the sample. Probe-loss is inferred if $a(t)$ is larger than a threshold amplitude A_{upper}. For this strategy, it is better that $a(t)$ reaches A_{upper} faster and thus from (2.1) it follows that this can be achieved by increasing $(A_0 - A_s)$ and/or by lowering Q. Large $(A_0 - A_s)$ values imply large forces on the sample when the cantilever regains its interaction with the sample. Such an alternative is not desirable for soft samples and thus large $\Delta a(t)$ is primarily obtained by relying on low Q operation [29]. In general, $(A_0 - A_s)$ is also governed by the imaging application and it is desirable to keep this parameter for the user to decide.

It needs to be noted that probe-loss can occur even when the amplitude $a(t)$ is reasonably close to the setpoint A_s and below a given threshold value A_{upper}. This is evident when the cantilever interacts with a sample feature that leads to a complex and prolonged transient phase, where the sample topography is reasonably benign but the cantilever trajectory does not allow interaction with the sample.

Thus, it is desirable to employ a signal that provides an independent measure of probe-loss that is effective for real time applications without overly constraining operation parameters viz. $(A_0 - A_s)$, Q and ω_0. Such a probe-loss detection technique called the "reliability index" signal was reported previously[28]. Such an independent measure can be employed to (a) actively alter the cantilever dynamics by, for example, lowering quality factor when off-sample and increasing quality factors on-sample thereby reducing the time required by the cantilever to reach its free air amplitude during probe-loss without worsening on-sample resolution (b) actively change controller gains of the positioning system with higher than optimal controller gains when the cantilever is off-sample and thereby increasing the rate at which cantilever and sample separation

reduces while switching back to smaller controller gains on-sample thereby reducing instabilities and thus being gentle on-sample. An independent measure of probe-loss in real-time facilitates the use of K_I, K_p and effective Q that are different when on-sample compared to off-sample without constraining A_0, A_s or Δh.

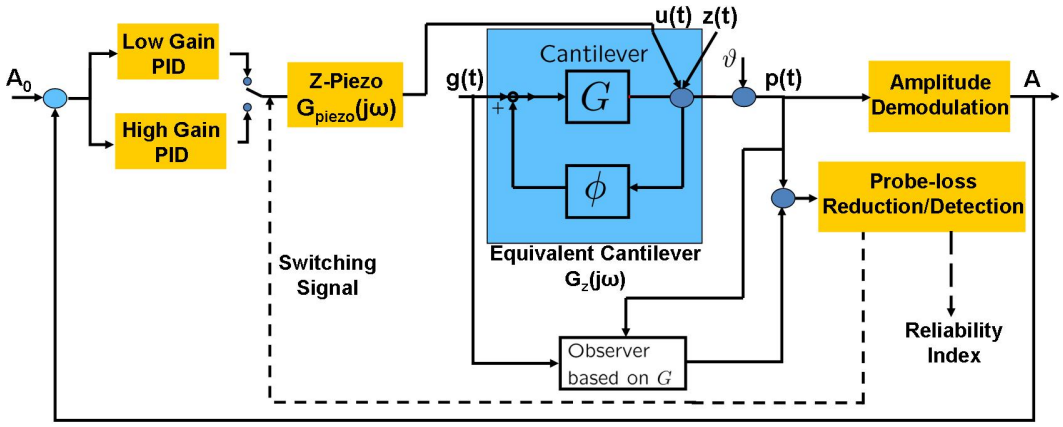

Figure 2.1: Modeling cantilever-sample interaction in tapping mode operation as a $G - \Phi$ interconnection where $G(j\omega)$ is the second order cantilever beam model, Φ is the nonlinear tip-sample force, $g(t)$ is the dither forcing, $z(t)$ is the sample height profile, ϑ is the measurement noise and $p(t)$ is the measured cantilever deflection. This interconnection can also be viewed as an equivalent second order system, $G_z(j\omega)$, which is dependent on sample height. Observer is built on the free air cantilever model $G(j\omega)$ and takes $g(t)$ and $p(t)$ as inputs and provides $\hat{p}$ as an estimate of $p(t)$. Two PID controllers, one with low gain and the other with high gain are switched depending on the magnitude of the reliability index signal.

2.3 Two-Level Model Mismatch Based Strategy for Probe-loss Reduction

Cantilever dynamics in tapping mode can be modeled as a $G - \Phi$ interconnection [30] (see Figure 2.1) where $G(j\omega)$ is a second order approximation of the first mode of the cantilever beam and Φ models the nonlinear force exerted by the sample on the tip. It is through Φ that different sample properties like elasticity, height and charge get modulated onto interacting cantilever trajectories. $G - \Phi$ interconnection, with a one

mode approximation of the cantilever dynamics, can be written as

$$\ddot{p} + \tfrac{\omega_0}{Q}\dot{p} + \omega_0^2 p \;\; = \;\; \omega_0^2 \left[g(t) + \tfrac{1}{k}\Phi(p, \dot{p}) \right]. \tag{2.5}$$

In the absence of the sample interaction, $\Phi(p, \dot{p})$, we have

$$\ddot{p} + \tfrac{\omega_0}{Q}\dot{p} + \omega_0^2 p \;\; = \;\; \omega_0^2 g(t) \tag{2.6}$$

where $p(t)$ is the instantaneous cantilever position, ω_0 is the resonant frequency of the first mode, Q is the quality factor, k is the spring constant of the cantilever, $g(t)$ is the dither excitation and $\Phi(p, \dot{p})$ is the nonlinear static memoryless tip-sample force. The model (2.6) will be termed as "free air" model of the cantilever where the cantilever is away from the sample and experiences no forces from the sample. This model can be identified accurately through thermal [31] or frequency sweep methods. As the cantilever comes close to the sample, damping and tip-sample forces (Φ) effect the cantilever dynamics. The related models are unknown but using averaging theory [32] it can be shown that the cantilever-sample interconnected system can be modeled as an equivalent cantilever with the dynamics

$$\ddot{p} + \tfrac{\omega_0'}{Q'}\dot{p} + (\omega_0')^2 p \;\; = \;\; (\omega_0')^2 g(t) \tag{2.7}$$

where ω_0' is the equivalent resonant frequency and Q' is the equivalent quality factor. Thus in the presence of tip-sample interaction, $G-\Phi$ interconnection can be represented by an equivalent second order model $G_z(j\omega)$ (see Figure 2.1) that is determined by the parameters ω_0' and Q'.

Accurate identification of the model of the cantilever when it is not experiencing any tip sample interaction enables creation of a reference circuit called an "observer" which takes in as input, cantilever excitation $g(t)$ and cantilever output $p(t)$ and estimates the cantilever output as closely as possible taking into account the known dynamics of the cantilever $G(j\omega)$ in free air. A particular implementation of the observer can be represented as

$$\underbrace{\ddot{\hat{p}} + \frac{\omega_0^2}{Q}\dot{\hat{p}} + \omega_0^2 \hat{p} = \omega_0^2 g(t)}_{\text{nominal dynamics}} + \underbrace{L(p(t) - \hat{p})}_{\text{correction term}} \tag{2.8}$$

where $\hat{p}$ is the estimated cantilever trajectory by the observer and L is the observer gain. The nominal dynamics captures the cantilever response to applied excitation $g(t)$

and the correction term tries to correct for the differences in p and $\hat{p}$ due to tip-sample interaction forces or initial condition mismatch, as fast as possible depending on the gain L. Higher the gain L, faster the correction. For $\hat{p}$ to accurately track p, the parameters ω_0 and Q used to build the observer (2.8) need to match the effective resonant frequency and quality factor. Indeed the equivalent cantilever parameters ω_0' and Q' are equal to ω_0 and Q when the cantilever is off-sample and thus the error $p - \hat{p}$ when off-sample is small leading to a low value of the reliability index signal. In this case the observer gain L can be chosen such that $\hat{p}$ tracks p in only a couple of cycles. However, when on-sample, the equivalent cantilever parameters ω_0' and Q' differ from ω_0 and Q and thus the observer dynamics propagates away from the equivalent cantilever dynamics causing a larger error $p - \hat{p}$ and the reliability index is larger. The above strategy thus provides a signal (the reliability index signal) for the detection of the loss of tip-sample interaction within a couple of cycles.

This can also be explained by viewing the plant and the observer dynamics in state space. In state space the off-sample cantilever dynamics is given by

$$\begin{aligned} \dot{x} &= Ax + Bg + B_1\eta \\ y &= Cx + \nu \end{aligned} \tag{2.9}$$

where $A = \begin{bmatrix} 0 & 1 \\ -\omega_0^2 & \frac{\omega_0}{Q_0} \end{bmatrix}$, $B = \begin{bmatrix} 0 \\ 1 \end{bmatrix}$, $C = \begin{bmatrix} \omega_0^2 & 0 \end{bmatrix}$.

The observer dynamics is given by

$$\begin{aligned} \dot{\hat{x}} &= A\hat{x} + Bg + L(y - \hat{y}) \\ \hat{y} &= C\hat{x} \end{aligned} \tag{2.10}$$

If we define $e = x - \hat{x}$ then the off-sample error dynamics is given by

$$\dot{e} = (A - LC)e + B_1\eta - L\nu \tag{2.11}$$

Thus any non zero initial condition or transients in the error dynamics will decay to a low value depending on the eigen values of $(A - LC)$ matrix.
On-sample cantilever model is given by

$$\begin{aligned} \dot{x} &= A_z x + B_z g + B_1\eta \\ y &= C_z x + \nu \end{aligned} \tag{2.12}$$

where $A_z = \begin{bmatrix} 0 & 1 \\ -\omega_e^2 & \frac{\omega_e}{Q_e} \end{bmatrix}$, $B_z = \begin{bmatrix} 0 \\ 1 \end{bmatrix}$, $C_z = \begin{bmatrix} \omega_e^2 & 0 \end{bmatrix}$

Thus on-sample error dynamics is given by

$$\dot{e} = (A - LC)e + B\eta - L\nu + \underbrace{(A - A_z - L(C - C_z))x}_{\text{Forcing Term}} \tag{2.13}$$

This forcing term will not allow the error signal to decay in steady state. Thus on-sample error rms will be higher than the off-sample error rms. This fact will be utilized in detecting the presence and absence of probe-loss by thresholding of this signal.

2.4 Switching Gain PID Controller Architecture

Since a real time indication of when the tip is interacting with the sample and when it is not (probe-loss) is available, a controller gain can be chosen when the tip is interacting with the sample that avoids imaging instabilities and large interaction forces and a high controller gain can be chosen when the tip is not interacting with the sample pushing the piezo faster towards the cantilever while its amplitude is growing and eventually engage with the tip. It must be noted that if such a high gain is chosen throughout the imaging then it will damage the sample or the tip and lead to on-sample ringing. Furthermore, choosing low gain throughout will lead to lost features at high scan rates or large probe-loss areas. However, intelligently switching between the two gains provides the best of both scenarios.

The architecture shown in Figure 2.1 is implemented on field programmable gate array (FPGA-Xilinx Virtex 2-pro) where the amplitude based feedback, as in normal tapping mode operation, is implemented but instead of one controller, two PID controllers are implemented whose gains are chosen for optimal on-sample imaging and probe-loss scenario. Which controller is being used at any instance depends on a switching signal which is calculated in real time based on thresholding on the reliability index signal.

2.5 Experimental Results

To study the efficiency of the method, experiments were performed on Multimode AFM (Veeco Inc.) with AC240 cantilever (Asylum Research Inc., $f_0 = 70720$ Hz, $Q = 210$,

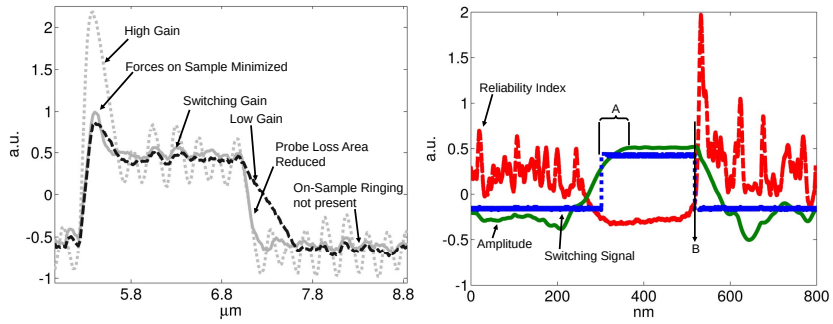

(a) (b)

Figure 2.2: Experimental data (a) shows line traces of controller effort while imaging calibration sample at 4 Hz (with a tip velocity of 80μsec). Dotted line shows high gain controller effort; Dash line shows low gain controller effort; Solid line shows switching gain controller effort. (b) Line trace of amplitude (green-solid), reliability index (red-dash) and switching signal (green-dot) while imaging calibration sample at 4 Hz (with a tip velocity of 80μsec) in closed loop operation. Label A in the figure indicates that the switching signal based on the reliability index switches from a low to high state with the amplitude signal trailing the switching signal by $\approx$ 68 nm in the lateral direction before it reaches its free air amplitude. Therefore, thresholding based on the reliability index signal provides a higher bandwidth probe-loss correction method as compared to thresholding based on the cantilever amplitude. Label B indicates that once the tip re-engages with the sample, the reliability index signal rises faster than the rate at which the cantilever amplitude reduces. The switching signal switches before the cantilever amplitude registers any noticeable change.

k = 2 N/m). Free air model was identified using frequency sweep method wherein excitation frequency ω of $g(t) = A_0 \sin \omega t$ was varied from $0 - 100$ kHz and $p(t)$ was recorded. Magnitude and phase information about $G(j\omega)$ was obtained by evaluating the ratios between steady state amplitude and phase of output vs input excitation respectively. Experiments were performed with this setup where a calibration grating, with 20 nm deep pits and a 3.5μm pitch, is imaged at 4 Hz, 8 Hz and 12 Hz with a scan size of 10μm. Figure 2.2(a) shows that if low gain is used throughout then there is good on-sample performance but a significant probe loss area. If high gain is used throughout then there is negligible probe-loss area but there is considerable on sample ringing and consequently large tip-sample forces. By employing a switching gain controller, the probe-loss regions are limited and comparable to the probe-loss regions when using a

high gain controller with the benefit that on-sample behavior matches the on-sample behavior when low gains are employed with ringing effects minimized.

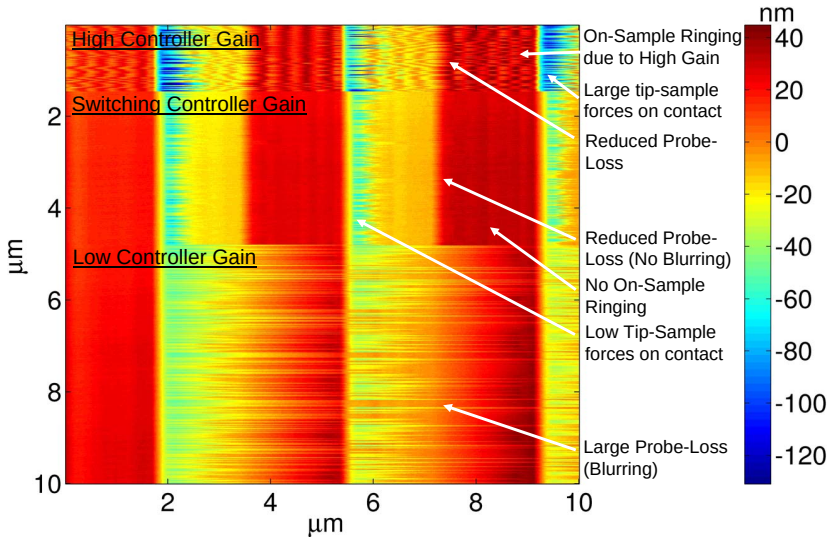

Figure 2.3: Calibration sample imaged at 8 Hz (with a tip velocity of 160μsec) in tapping mode.

Similar characteristics are revealed through an image of a calibration sample at 8 Hz (see Figure 2.3) where the use of low gain controller leads to large probe loss areas (blurring) leading to image artifacts, high gain controller leads to on-sample ringing while switching gain controller gives a better image. At 12 Hz (see Figure 2.4) using low gain controller leads to loss of features but using switching gain controller recovers the square profile. In Figure 2.2(b), the line traces of reliability index, amplitude and switching signal are shown while imaging a calibration sample at 4 Hz scan speed in closed-loop operation. Region A (see Figure 2.2(b)) indicates that switching signal goes from a low to high state with the amplitude signal trailing the switching signal by roughly 68 nm in lateral direction before it reaches the free air amplitude value thereby indicating that thresholding based on reliability index can provide a higher bandwidth operation. Region B indicates that when the tip re-engages with the sample, reliability index signal rises faster than the amplitude signal and the switching signal goes low before the amplitude signal shows any change thereby controlling the force with which

the tip re-engages with the sample. As the tip approaches the sample during probe-loss, the model of the cantilever changes due to damping effects before the cantilever tip regains interaction with the sample and is different from the free air model $G(j\omega)$ on which the observer is based. Thus the thresholding can be set such that the controller gain is switched to a low value slightly before the tip actually makes contact with the sample thereby reducing the piezo velocity and making a soft contact with the sample.

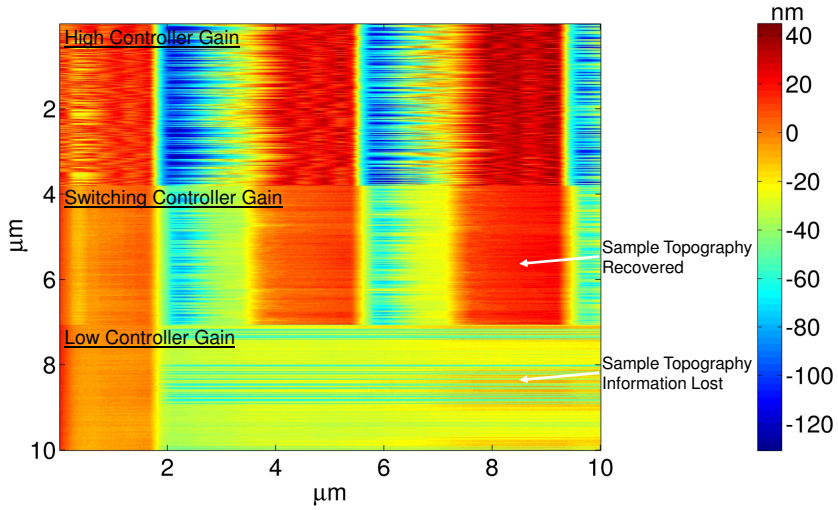

Figure 2.4: Calibration sample imaged at 12 Hz (with a tip velocity of 240μsec) in tapping mode.

Plasmid DNA was imaged on mica in air at 12 Hz and 30 Hz. Figure 2.5 reveals clear reduction of probe-loss areas on the use of switching gain controller. Indeed at 30 Hz (see Figure 2.6) (with a tip velocity of 60μsec) using switching gain controller leads to recovery of a lost DNA strand, which is close to 1.4 nm in height, compared to a low gain controller operation where the DNA strand is lost. This provides evidence that the proposed technique can be used for improved imaging of biological samples at high scan rates and that it has resolution better than 2 nm.

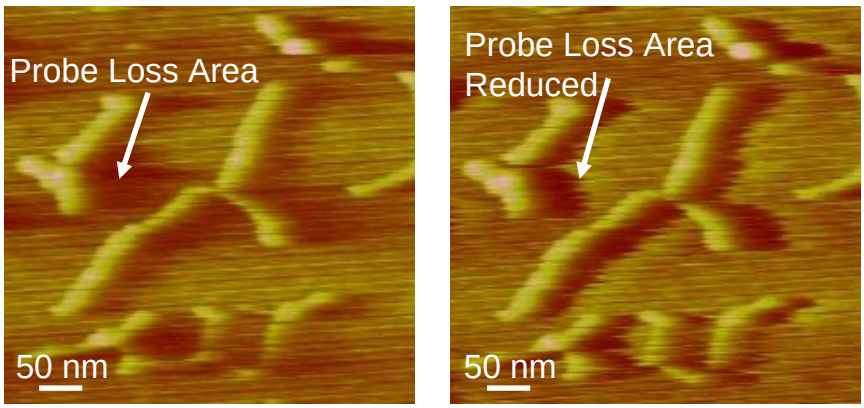

Figure 2.5: Plasmid DNA on mica imaged in air at a tip velocity of 24μsec (12 Hz) in tapping mode. Left image indicates presence of probe loss areas (dark areas) due to use of low gain controller. Right image indicates reduction of probe loss areas in real time (reduction of dark areas) by using switching gain controller thereby emphasizing that the resolution of the proposed technique is $\approx$ 2 nm.

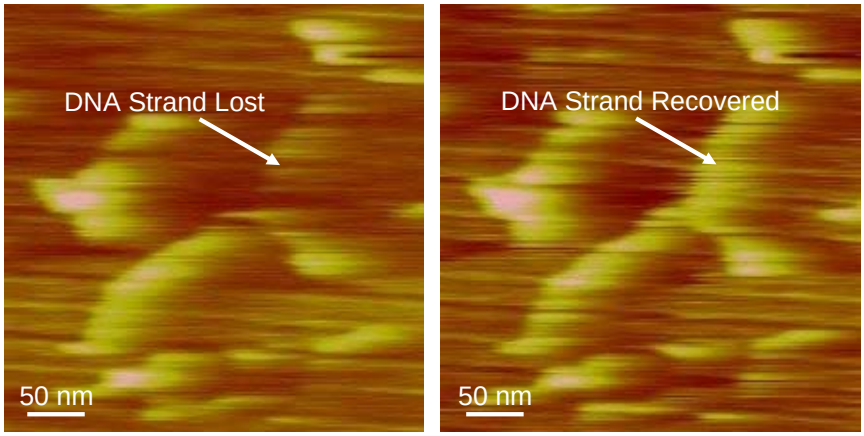

Figure 2.6: Plasmid DNA on mica imaged in air at a tip velocity of 60μsec (30 Hz) in tapping mode. Left image indicates loss of a DNA strand since it is present in the probe loss area during high speed imaging with low controller gain. Right image indicates recovery of same DNA strand by using switching gain controller at same scanning speed.

2.6 Conclusion

This chapter presents a scheme for real time reduction of probe-loss affected areas during high speed tapping mode imaging based on thresholding of reliability index signal. This technique is implemented on hardware and its efficacy shown on imaging of calibration sample and plasmid DNA at high tip velocities. The method not only helps in reduction of probe-loss areas but also in recovering features that were lost at high imaging speeds with a resolution of better than 2nm. Reliability index signal can be used for modifying the cantilever dynamics in real time helping to choose different quality factor for different on-sample and off-sample behavior and will form a part of future work.

Chapter 3

Real Time Estimation of Equivalent Cantilever Parameters in Tapping Mode Atomic Force Microscopy

3.1 Introduction

In the recent past, several ways of exciting the cantilever in an atomic force microscope (AFM) were developed with the aim of determining equivalent cantilever parameters [23, 33]. All of these techniques rely on the fact that the cantilever interacting with the sample can be modeled as a spring-mass-damper system whose parameters, equivalent resonant frequency, ω_0', and quality factor, Q', vary depending on sample properties. There is an open question on the simplest excitation of the cantilever that can lead to a real time estimation of the equivalent cantilever parameters.

In the recently developed, band excitation (BE) method [23] and fast chirp methods [33], the cantilever is excited with a continuous or discrete band of frequencies near the resonance. The cantilever input and output are recorded simultaneously and a second order model is fitted to the measured response. This gives the information about the equivalent resonant frequency and quality factor at each sample point with the image

resolution limited by the image size, $(M \times N)$ pixels, where same procedure has to be carried out at each pixel. In the BE and fast chirp methods, the cantilever response to the input excitation has large amplitude variation which makes it difficult to obtain equivalent cantilever model parameters at one particular interaction level. Also these techniques provide the information at discretized levels in the vertical z direction in force spectroscopy experiments.

In this chapter, a technique is presented to estimate equivalent cantilever resonant frequency and quality factor during normal tapping mode operation. Further it is shown that an excitation by sum of three sinusoids is sufficient to extract equivalent cantilever parameters.

3.2 Modeling Cantilever Dynamics in Tapping Mode as Linear Time Varying Plant

Cantilever dynamics in tapping mode can be modelled as a $G - \Phi$ interconnection [28] (see Figure 3.1(a)) where $G(i\omega)$ is a second order approximation of the first mode of the cantilever beam and Φ models the nonlinear force exerted by the sample on the tip. It is through Φ that different sample properties like elasticity, height and charge get modulated onto interacting cantilever trajectories. The $G - \Phi$ interconnection, with a one mode approximation of the cantilever dynamics, can be written as

$$\ddot{p} + \tfrac{\omega_0}{Q}\dot{p} + \omega_0^2 p \;=\; \omega_0^2 \left[g(t) + \tfrac{1}{k}\Phi(p, \dot{p}) \right] \tag{3.1}$$

where $p(t)$ is the instantaneous cantilever position, ω_0 is the resonant frequency of the first mode, Q is the quality factor, k is the spring constant of the cantilever, $g(t)$ is the dither excitation and $\Phi(p, \dot{p})$ is the nonlinear static memoryless tip-sample force.

The model (3.1) with $\Phi = 0$ will be termed as "sample-free" model of the cantilever where the cantilever experiences no forces from the sample. As the cantilever comes close to the sample, damping and tip-sample forces (Φ) effect the cantilever dynamics. The related models are unknown but using averaging theory [34] it can be shown that the cantilever-sample interconnected system (3.1) can be modeled as an equivalent cantilever with the dynamics

$$\ddot{p} + \tfrac{\omega_0'}{Q'}\dot{p} + (\omega_0')^2 p \;=\; (\omega_0')^2 g(t) \tag{3.2}$$

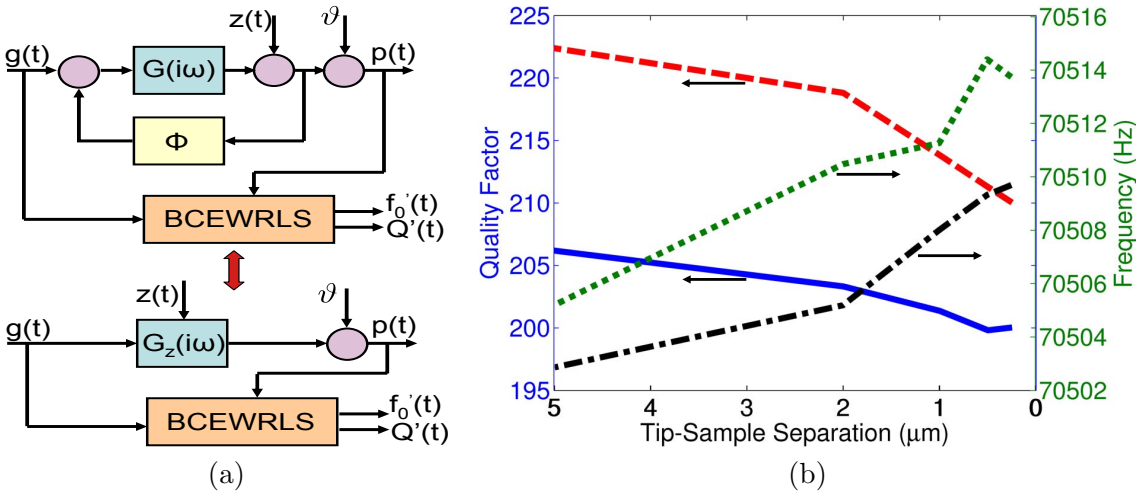

(a) (b)

Figure 3.1: (a) Modeling cantilever-sample interaction in tapping mode operation as a $G-\Phi$ interconnection where $G(i\omega)$ is the second order cantilever beam model and Φ is the nonlinear tip-sample force. $g(t)$, $z(t)$, ϑ and $p(t)$ are the dither forcing, the sample height profile, the measurement noise and measured cantilever deflection respectively. This interconnection can also be viewed as an equivalent second order system, $G_z(i\omega)$, which is dependent on sample height. BCEWRLS algorithm takes $g(t)$ and $p(t)$ as input and gives equivalent resonant frequency, f_0', and quality factor, Q', of the cantilever in real time. (b) Experimentally obtained equivalent resonant frequency f_0' and quality factor, Q', of the cantilever at different nominal tip-sample separations. Tip is not interacting with the sample. Blue-solid and Black-dash-dot curves are obtained by a second order fit to the cantilever response to frequency sweep. Red-dash and Green-dot curves are obtained by BCEWRLS scheme. This indicates that in most cases estimates of f0 are accurate within +5 Hz and quality factor estimates are accurate to within +15 of actual values.

where ω_0' is the equivalent resonant frequency and Q' is the equivalent quality factor. Thus in the presence of tip-sample interaction, $G-\Phi$ interconnection can be represented by an equivalent second order model $G_z(i\omega)$ (see Figure 3.1(a)) that is determined by the parameters ω_0' and Q'.

3.3 Adaptive Parameter Estimation Strategy to Estimate Equivalent Cantilever Model

In this section, a recursive parameter estimation algorithm is derived for a general plant whose dynamics can be captured by a rational transfer function. The parameters of the plant can change with time. Rate of convergence of the estimates provided by the algorithm can be tweaked through an exponential forgetting factor depending on the application. Later we will adapt this algorithm for a cantilever-sample system and present experimental results.

3.3.1 Derivation of Bias Compensated Exponentially Weighted Recursive Least Squares (BCEWRLS) Technique

Consider a plant whose dynamics is represented as:
Plant Dynamics :

$$\begin{aligned} x(t+1) &= Ax(t) + Bu(t) \\ y(t) &= Cx(t) + Du(t) + v(t) \end{aligned} \tag{3.3}$$

where $u(t)$ is the input to the plant, $v(t)$ is the measurement noise, $y(t)$ is the output of the system.
This gives

$$\begin{aligned} y(t) &= \left[C(zI - A)^{-1}B + D\right] u(t) + v(t) \\ &= \frac{\beta(z^{-1})}{\alpha(z^{-1})} u(t) + v(t) \end{aligned} \tag{3.4}$$

where
$\beta(z^{-1}) = \beta_0 + \beta_1 z^{-1} + ... + \beta_n z^{-n}$ and $\alpha(z^{-1}) = 1 + \alpha_1 z^{-1} + ... + \alpha_n z^{-n}$.

Define $e(t) := \alpha(z^{-1})v(t)$ then

$$\begin{aligned} y(t) &= \phi^T(t)\theta + \psi^T(t)\theta + v(t) \\ &= \phi^T(t)\theta + e(t) \end{aligned} \tag{3.5}$$

where
$\theta = \left[\begin{array}{cccccccc} \alpha_1 & \alpha_2 & . & . & \alpha_n & \beta_0 & \beta_1 & . \; . \; \beta_n \end{array} \right]^T$,
$\phi(t) = \left[\begin{array}{cccccccc} -y(t-1) & -y(t-2) & . & . & -y(t-n) & u(t) & u(t-1) & . \; . \; u(t-n) \end{array} \right]^T$ and

$\psi(t) = \left[\ v(t-1)\ v(t-2)\ .\ .\ v(t-n)\ 0\ 0\ .\ .\ 0\ \right]^T$.
$e(t)$ is a correlated noise process and hence it leads to a biased estimate of least squares estimate of vector θ.

For exponentially weighted recursive least squares estimates, define the cost function as

$$J(t) \ := \ \Sigma_{i=1}^{t} \lambda^{t-i}(y(i) - \phi^T(i)\hat{\theta}(t))^2. \tag{3.6}$$

Consider the problem

$$\min_{\hat{\theta}(t)} J(t) \ = \ \min_{\hat{\theta}(t)} \Sigma_{i=1}^{t} \lambda^{t-i}(y(i) - \phi^T(i)\hat{\theta}(t))^2. \tag{3.7}$$

Let $Y(t) = \left[\ y(1)\ y(2)\ .\ .\ y(t)\ \right]^T$, $\Phi(t) = \left[\ \phi^T(1)\ \phi^T(2)\ .\ .\ \phi^T(t)\ \right]^T$,

$$W = \begin{bmatrix} \lambda^{t-1} & . & . & 0 \\ 0 & \lambda^{t-2} & . & 0 \\ 0 & 0 & . & 0 \\ 0 & 0 & . & \lambda^0 \end{bmatrix}.$$

Thus (3.7) can be written as

$$\min_{\hat{\theta}(t)} J(t) \ = \ \min_{\hat{\theta}(t)} \left[Y(t) - \Phi(t)\hat{\theta}(t)\right]^T W \left[Y(t) - \Phi(t)\hat{\theta}(t)\right] \tag{3.8}$$

Solution to equation (3.8) is given by

$$\begin{aligned} \hat{\theta}_{LS}(t) &= \left[\Phi^T(t) W \Phi(t)\right]^{-1} \left[\Phi^T(t) W Y(t)\right] \\ &= \left[\Sigma_{i=1}^{t} \lambda^{t-i}\phi(i)\phi^T(i)\right]^{-1} \left[\Sigma_{i=1}^{t} \lambda^{t-i}\phi(i) y(i)\right] \\ &= \left[\Sigma_{i=1}^{t} \lambda^{t-i}\phi(i)\phi^T(i)\right]^{-1} \left[\Sigma_{i=1}^{t} \lambda^{t-i}\phi(i) \left[\phi^T(i)\theta + \psi^T(i)\theta + v(i)\right]\right] \\ &= \theta + \left[\Sigma_{i=1}^{t} \lambda^{t-i}\phi(i)\phi^T(i)\right]^{-1} \left[\Sigma_{i=1}^{t} \lambda^{t-i}\phi(i)\psi^T(i)\theta + \Sigma_{i=1}^{t} \lambda^{t-i}\phi(i)v(i)\right]. \end{aligned} \tag{3.9}$$

Equation (3.9) can be written as

$$\left[\Sigma_{i=1}^{t} \lambda^{t-i}\phi(i)\phi^T(i)\right] \left(\hat{\theta}_{LS}(t) - \theta\right) \ = \ \left[\Sigma_{i=1}^{t} \lambda^{t-i}\phi(i)\psi^T(i)\theta + \Sigma_{i=1}^{t} \lambda^{t-i}\phi(i)v(i)\right] \tag{3.10}$$

A stochastic process $x(t)$ is ergodic in second moment if $\lim_{t\to\infty} \frac{1}{t}\Sigma_{i=1}^{t} x^2(i) = E\left[x^2(i)\right]$ ([35]). If $v(t)$ is assumed to be a zero mean white noise and is uncorrelated to inputs and has variance σ^2 then

$E\left[v(i)\right] = 0$; $E\left[v(t)v(t+j)\right] = 0 \ \forall \ j \neq 0$; $E\left[v^2(i)\right] = \sigma^2$ and $E\left[v(t)u(j)\right] = 0$.

Assuming v is ergodic in the second moment, we have

$$\begin{array}{rcccl} \lim_{t\to\infty} \frac{1}{t}\Sigma_{i=1}^{t} v(i) & = & E\left[v(i)\right] & = & 0 \\ \lim_{t\to\infty} \frac{1}{t}\Sigma_{i=1}^{t} v(i)v(i+j) & = & E\left[v(i)v(i+j)\right] & = & 0 \ \forall \ j \neq 0 \\ \lim_{t\to\infty} \frac{1}{t}\Sigma_{i=1}^{t} v^2(i) & = & E\left[v^2(i)\right] & = & \sigma^2 \\ \lim_{t\to\infty} \frac{1}{t}\Sigma_{i=1}^{t} v(i)u(i+j) & = & E\left[v(i)u(i+j)\right] & = & 0 \ \forall \ j \geq 0. \end{array} \tag{3.11}$$

The above four equations tell us that if we average all the related measurements equally by $1/t$ then as $t \to \infty$, the pdf of the left hand side will converge to a dirac delta pdf with mean as the ensemble mean and variance zero. But in this θ is assumed to be constant. In a time varying plant, θ has some dynamics which needs to be tracked. If θ is constant then it can be conceived that the LHS of eqn (3.11) will converge to RHS asymptotically. Since they are converging series $\exists \ t_o$ st $\forall \ t > t_o \ |RHS - LHS| < \epsilon$ in eqn (3.11). It can then be hypothesized that if the rate of change of θ is slower than the window over which the process mean and variance converge to within ϵ of the limit then instead of weighting all the samples equally as is done in the definition of ergodicity, one can introduce an exponentially weighting term in the definition and obtain a time varying ergodicity. So we introduce a definition of modified ergodicity as

A stochastic process $x(t)$ is modified ergodic if $\lim_{t\to\infty} \frac{1-\lambda}{1-\lambda^t}\Sigma_{i=1}^{t} \lambda^{t-i} x(i) = E\left[x(i)\right]$ for $\lambda \approx 1$. Assuming $v(t)$ to be a modified ergodic process, one gets

$$\begin{array}{rcccl} \lim_{t\to\infty} \frac{1-\lambda}{1-\lambda^t}\Sigma_{i=1}^{t} \lambda^{t-i} v(i) & = & E\left[v(i)\right] & = & 0 \\ \lim_{t\to\infty} \frac{1-\lambda}{1-\lambda^t}\Sigma_{i=1}^{t} \lambda^{t-i} v(i)v(i+j) & = & E\left[v(i)v(i+j)\right] & = & 0 \ \forall \ j \neq 0 \\ \lim_{t\to\infty} \frac{1-\lambda}{1-\lambda^t}\Sigma_{i=1}^{t} \lambda^{t-i} v^2(i) & = & E\left[v(^2i)\right] & = & \sigma^2 \\ \lim_{t\to\infty} \frac{1-\lambda}{1-\lambda^t}\Sigma_{i=1}^{t} \lambda^{t-i} v(i)u(i+j) & = & E\left[v(i)u(i+j)\right] & = & 0 \ \forall \ j \geq 0 \end{array} \tag{3.12}$$

Thus LHS of eqn(3.12) will converge to RHS fast and then track it in case it changes. This can be controlled depending on the process by choosing the appropriate λ. Clearly if $\lambda = 1$ then eqn (3.12) is the same as eqn(3.11).
Multiplying (3.10) with $\frac{1-\lambda}{1-\lambda^t}$ and taking $\lim_{t\to\infty}$ on both sides results in

$$\begin{aligned} \lim_{t\to\infty} \tfrac{1-\lambda}{1-\lambda^t} \left[\Sigma_{i=1}^{t} \lambda^{t-i}\phi(i)\phi^T(i)\right](\hat{\theta}_{LS}(t) - \theta) &= \lim_{t\to\infty} \tfrac{1-\lambda}{1-\lambda^t}\Sigma_{i=1}^{t}\lambda^{t-i}\phi(i)\psi^T(i)\theta \\ &\quad + \lim_{t\to\infty} \tfrac{1-\lambda}{1-\lambda^t}\Sigma_{i=1}^{t}\lambda^{t-i}\phi(i)v(i) \end{aligned} \tag{3.13}$$

The next step is to evaluate right hand side of equation(3.13). Using the definition of modified ergodicity one can solve

$$\begin{aligned} \lim_{t\to\infty} \tfrac{1-\lambda}{1-\lambda^t}\Sigma_{i=1}^{t}\lambda^{t-i}\phi(i)v(i) &= \lim_{t\to\infty} \tfrac{1-\lambda}{1-\lambda^t}\Sigma_{i=1}^{t}\lambda^{t-i} \begin{bmatrix} -y(i-1)v(i) \\ -y(i-2)v(i) \\ . \\ . \\ -y(i-n)v(i) \\ u(i)v(i) \\ . \\ . \\ u(i-n)v(i) \end{bmatrix} \\ &= 0 \end{aligned} \tag{3.14}$$

$$\begin{aligned}\lim_{t\to\infty}\frac{1-\lambda}{1-\lambda^t}\Sigma_{i=1}^{t}\lambda^{t-i}\phi(i)\psi^T(i)\theta &= \lim_{t\to\infty}\frac{1-\lambda}{1-\lambda^t}\Sigma_{i=1}^{t}\lambda^{t-i}\begin{bmatrix}-y(i-1)\\-y(i-2)\\.\\.\\-y(i-n)\\u(i)\\.\\.\\u(i-n)\end{bmatrix}\begin{bmatrix}v(i-1)\\v(i-2)\\.\\v(i-n)\\0\\.\\0\end{bmatrix}^T\theta \\ &= -\sigma^2\Lambda\theta \end{aligned} \tag{3.15}$$

Thus (3.13) becomes

$$\lim_{t\to\infty}\frac{1-\lambda}{1-\lambda^t}\left[\Sigma_{i=1}^{t}\lambda^{t-i}\phi(i)\phi^T(i)\right](\hat{\theta}_{LS}(t)-\theta) = -\sigma^2\Lambda\theta \tag{3.16}$$

Assuming that the input is stationary and modified ergodic it can be shown that

$$\lim_{t\to\infty}\frac{1-\lambda}{1-\lambda^t}\Sigma_{i=1}^{t}\lambda^{t-i}\phi(i)\phi^T(i) = R_\phi = E\left[\phi(i)\phi^T(i)\right] \tag{3.17}$$

From (3.13) one can then obtain

$$\lim_{t\to\infty}\hat{\theta}_{LS}(t) = \theta - \sigma^2 R_\phi^{-1}\Lambda\theta. \tag{3.18}$$

(3.18) shows that vector $\hat{\theta}_{LS}$ is a biased estimator and thus there is a need to estimate the bias term recursively and compensate for it in real time, to obtain an unbiased estimate of vector θ

Define an unbiased estimator of θ as

$$\hat{\theta}_C(t) = \hat{\theta}_{LS}(t) + \hat{\sigma}^2(t)(\tfrac{1-\lambda^t}{1-\lambda})\left[\Sigma_{i=1}^{t}\lambda^{t-i}\phi(i)\phi^T(i)\right]^{-1}\Lambda\hat{\theta}_C(t-1) \tag{3.19}$$

Define $P(t) = \left[\Sigma_{i=1}^{t} \lambda^{t-i}\phi(i)\phi^T(i)\right]^{-1}$ then eqn (3.19) can be written as

$$\hat{\theta}_C(t) \;=\; \hat{\theta}_{LS}(t) + \hat{\sigma}^2(t)(\tfrac{1-\lambda^t}{1-\lambda})P(t)\Lambda\hat{\theta}_C(t-1). \tag{3.20}$$

This is an unbiased estimator of θ since assuming $\lim_{t\to\infty}\hat{\sigma}^2(t) = \sigma^2$ one can show that

$$\lim_{t\to\infty}\hat{\theta}_C(t) \;=\; \lim_{t\to\infty}\hat{\theta}_{LS}(t) + \lim_{t\to\infty}\hat{\sigma}^2(t)\tfrac{1-\lambda^t}{1-\lambda}P(t)\Lambda\hat{\theta}_C(t-1). \tag{3.21}$$

Thus

$$\lim_{t\to\infty}\hat{\theta}_C(t) \;=\; \tfrac{(1-\sigma^2 R_\phi^{-1}\Lambda)\theta}{1-\sigma^2 R_\phi^{-1}\Lambda} = \theta. \tag{3.22}$$

Next we need to find an unbiased estimator of $\sigma^2(t)$.

Let $E_{LS}(i) := y(i) - \phi^T(i)\hat{\theta}_{LS}(t)$
Since $\hat{\theta}_{LS}(t)$ is chosen at any instance t to minimize least square error $\sum_{i=1}^{t}\lambda^{t-i}E_{LS}^2(i)$, the orthogonality condition gives :

$$\begin{aligned}
\left[W^{1/2}Y(t) - W^{1/2}\Phi(t)\hat{\theta}_{LS}\right]^T\left[W^{1/2}\Phi(t)\right] &= 0\\
\left[Y(t) - \Phi(t)\hat{\theta}_{LS}(t)\right]^T W\Phi(t) &= 0\\
\Sigma_{i=1}^{t}\left[y(i) - \phi^T(i)\hat{\theta}_{LS}(t)\right]\phi^T(i)\lambda^{t-i} &= 0\\
\Sigma_{i=1}^{t}\lambda^{t-i}E_{LS}(i)\phi^T(i) &= 0
\end{aligned} \tag{3.23}$$

Next we evaluate using equation (3.23),

$$\begin{aligned}
\Sigma_{i=1}^{t}\lambda^{t-i}E_{LS}^2(i) &= \Sigma_{i=1}^{t}\lambda^{t-i}E_{LS}(i)\left[y(i) - \phi^T(i)\hat{\theta}_{LS}(t)\right]\\
&= \Sigma_{i=1}^{t}\lambda^{t-i}E_{LS}(i)\left[\phi^T(i)\theta + \psi^T(i)\theta + v(i)\right]\\
&= \Sigma_{i=1}^{t}\lambda^{t-i}E_{LS}(i)\left[\psi^T(i)\theta + v(i)\right]\\
&= \Sigma_{i=1}^{t}\lambda^{t-i}\left[y(i) - \phi^T(i)\hat{\theta}_{LS}(t)\right]\left[\psi^T(i)\theta + v(i)\right]\\
&= \Sigma_{i=1}^{t}\lambda^{t-i}\left[\phi^T(i)\theta + \psi^T(i)\theta + v(i) - \phi^T(i)\hat{\theta}_{LS}(t)\right]\left[\psi^T(i)\theta + v(i)\right]
\end{aligned} \tag{3.24}$$

$$\Sigma_{i=1}^{t}\lambda^{t-i}E_{LS}^{2}(i) \;=\; \Sigma_{i=1}^{t}\lambda^{t-i}\phi^{T}(i)\left[\theta-\hat{\theta}_{LS}(t)\right]\left[\psi^{T}(i)\theta+v(i)\right]+\Sigma_{i=1}^{t}\lambda^{t-i}\left[\psi^{T}(i)\theta+v(i)\right]^{2} \tag{3.25}$$

Multiplying (3.25) by $\frac{1-\lambda}{1-\lambda^{t}}$ and taking $\lim_{t\to\infty}$ results in

$$\begin{aligned}\lim_{t\to\infty}\tfrac{1-\lambda}{1-\lambda^{t}}\Sigma_{i=1}^{t}\lambda^{t-i}E_{LS}^{2}(i) \;=\;& \lim_{t\to\infty}\tfrac{1-\lambda}{1-\lambda^{t}}\Sigma_{i=1}^{t}\lambda^{t-i}\phi^{T}(i)\left[\theta-\hat{\theta}_{LS}(t)\right]\left[\psi^{T}(i)\theta+v(i)\right]\\ &+\lim_{t\to\infty}\tfrac{1-\lambda}{1-\lambda^{t}}\Sigma_{i=1}^{t}\lambda^{t-i}\left[\psi^{T}(i)\theta+v(i)\right]^{2}\end{aligned} \tag{3.26}$$

$$\begin{aligned}&\lim_{t\to\infty}\tfrac{1-\lambda}{1-\lambda^{t}}\Sigma_{i=1}^{t}\lambda^{t-i}\left[\psi^{T}(i)\theta+v(i)\right]^{2}=\\ &\qquad\lim_{t\to\infty}\tfrac{1-\lambda}{1-\lambda^{t}}\Sigma_{i=1}^{t}\lambda^{t-i}\left[\theta^{T}\psi(i)\psi^{T}(i)\theta+2\theta^{T}\psi(i)v(i)+v(i)^{2}\right]\end{aligned} \tag{3.27}$$

By definition of modified ergodicity
$\lim_{t\to\infty}\frac{1-\lambda}{1-\lambda^{t}}\Sigma_{i=1}^{t}\lambda^{t-i}v^{2}(i)=\sigma^{2}$.

$$\lim_{t\to\infty}\tfrac{1-\lambda}{1-\lambda^{t}}\Sigma_{i=1}^{t}\lambda^{t-i}2\theta^{T}\begin{bmatrix} v(i-1)\\ v(i-2)\\ .\\ .\\ v(i-n)\\ 0\\ .\\ 0\end{bmatrix}v(i)=2\theta^{T}.0=0$$

$$\lim_{t\to\infty} \frac{1-\lambda}{1-\lambda^t}\Sigma_{i=1}^{t}\lambda^{t-i}\theta^T \begin{bmatrix} v(i-1) \\ v(i-2) \\ . \\ . \\ v(i-n) \\ 0 \\ . \\ 0 \end{bmatrix} \begin{bmatrix} v(i-n) \\ v(i-2) \\ . \\ v(i-n) \\ 0 \\ . \\ 0 \end{bmatrix}^T \theta = \theta^T\sigma^2\Lambda\theta$$

Thus equation (3.27) becomes

$$\lim_{t\to\infty} \frac{1-\lambda}{1-\lambda^t}\Sigma_{i=1}^{t}\lambda^{t-i}\left[\psi^T(i)\theta + v(i)\right]^2 = \theta^T\sigma^2\Lambda\theta + \sigma^2 \tag{3.28}$$

Moreover using equation (3.14) results in

$$\lim_{t\to\infty} \frac{1-\lambda}{1-\lambda^t}\Sigma_{i=1}^{t}\lambda^{t-i}\phi^T(i)v(i)\left[\theta - \hat{\theta}_{LS}(t)\right] = 0 \tag{3.29}$$

and using equation (3.15) results in

$$\lim_{t\to\infty} \frac{1-\lambda}{1-\lambda^t}\Sigma_{i=1}^{t}\lambda^{t-i}\phi^T(i)\left[\theta - \hat{\theta}_{LS}(t)\right]\psi^T(i)\theta = -\theta^T\sigma^2\Lambda\left[\theta - \hat{\theta}_{LS}(t)\right] \tag{3.30}$$

Thus using equations 3.26 - 3.30 results in

$$\lim_{t\to\infty} \frac{1-\lambda}{1-\lambda^t}\Sigma_{i=1}^{t}\lambda^{t-i}E_{LS}^2(i) = \sigma^2\left[1 + \theta^T\Lambda\hat{\theta}_{LS}(t)\right] \tag{3.31}$$

This implies

$$\sigma^2 = \frac{\lim_{t\to\infty} \frac{1-\lambda}{1-\lambda^t}\Sigma_{i=1}^{t}\lambda^{t-i}E_{LS}^2(i)}{1+\theta^T\Lambda\hat{\theta}_{LS}(t)} \tag{3.32}$$

Let $J(t) := \Sigma_{i=1}^{t}\lambda^{t-i}E_{LS}^2(i)$. If we define an estimator of σ^2 as

$$\hat{\sigma}^2(t) = \frac{\frac{1-\lambda}{1-\lambda^t}J(t)}{1+\hat{\theta}_C^T(t-1)\Lambda\hat{\theta}_{LS}(t)} \tag{3.33}$$

then $\lim_{t\to\infty}\hat{\sigma}^2(t) = \sigma^2$ is an unbiased estimator of σ^2.

The last step of the algorithm involves finding a recursive way to evaluate $J(t)$. Exponentially Weighted Recursive Least Squares equations for $\hat{\theta}_{LS}(t)$ that will be used to evaluate J(t) are

$$\begin{array}{rcl} \hat{\theta}_{LS}(t) & = & \hat{\theta}_{LS}(t-1) + P(t)\phi(t)\left[y(t) - \phi^T(t)\hat{\theta}_{LS}(t-1)\right] \\ P(t) & = & \frac{1}{\lambda}\left[P(t-1) - \frac{P(t-1)\phi(t)\phi^T(t)P(t-1)}{\lambda+\phi^T(t)P(t-1)\phi(t)}\right] \end{array} \tag{3.34}$$

$$\begin{array}{rcl} J(t) & = & \Sigma_{i=1}^{t}\lambda^{t-i}E_{LS}^2(i) \\ & = & \Sigma_{i=1}^{t}\lambda^{t-i}\left[y(i) - \phi^T(i)\hat{\theta}_{LS}(t)\right]^2 \\ & = & \Sigma_{i=1}^{t}\lambda^{t-i}\left[y(i) - \phi^T(i)\left[\hat{\theta}_{LS}(t-1) + P(t)\phi(t)\left[y(t) - \phi^T(t)\hat{\theta}_{LS}(t-1)\right]\right]\right]^2 \end{array} \tag{3.35}$$

Then equation (3.35) can be written as

$$\begin{array}{rcl} J(t) & = & \Sigma_{i=1}^{t}\lambda^{t-i}\left[(y(i) - \phi^T(i)\hat{\theta}_{LS}(t-1)) - \phi^T(i)P(t)\phi(t)\left[y(t) - \phi^T(t)\hat{\theta}_{LS}(t-1)\right]\right]^2 \\ & = & \Sigma_{i=1}^{t}\lambda^{t-i}(y(i) - \phi^T(i)\hat{\theta}_{LS}(t-1))^2 \\ & - & 2\Sigma_{i=1}^{t}\lambda^{t-i}(y(i) - \phi^T(i)\hat{\theta}_{LS}(t-1))\phi^T(i)P(t)\phi(t)\left[y(t) - \phi^T(t)\hat{\theta}_{LS}(t-1)\right] \\ & + & \Sigma_{i=1}^{t}\lambda^{t-i}\left[y(t) - \phi^T(t)\hat{\theta}_{LS}(t-1)\right]^2\phi^T(t)P(t)\phi(i)\phi^T(i)P(t)\phi(t) \\ & = & \lambda\Sigma_{i=1}^{t-1}\lambda^{t-i-1}(y(i) - \phi^T(i)\hat{\theta}_{LS}(t-1))^2 + (y(t) - \phi^T(t)\hat{\theta}_{LS}(t-1))^2 \\ & - & 2\lambda\left[\Sigma_{i=1}^{t-1}\lambda^{t-i-1}(y(i) - \phi^T(i)\hat{\theta}_{LS}(t-1))\phi^T(i)\right]P(t)\phi(t)\left[y(t) - \phi^T(t)\hat{\theta}_{LS}(t-1)\right] \\ & - & 2(y(t) - \phi^T(t)\hat{\theta}_{LS}(t-1))^2\phi^T(t)P(t)\phi(t) \\ & + & \left[y(t) - \phi^T(t)\hat{\theta}_{LS}(t-1)\right]^2\phi^T(t)P(t)\underbrace{\left[\Sigma_{i=1}^{t}\lambda^{t-1}\phi(i)\phi^T(i)\right]}_{P(t)^{-1}}P(t)\phi(t) \\ & = & \lambda J(t-1) + \left[y(t) - \phi^T(t)\hat{\theta}_{LS}(t-1)\right]^2 - \left[y(t) - \phi^T(t)\hat{\theta}_{LS}(t-1)\right]^2\phi^T(t)P(t)\phi(t) \\ & = & \lambda J(t-1) + \left[y(t) - \phi^T(t)\hat{\theta}_{LS}(t-1)\right]^2\left[1 - \phi^T(t)P(t)\phi(t)\right] \end{array} \tag{3.36}$$

Then by using the relationship

$$\begin{aligned} 1-\phi^T(t)P(t)\phi(t) &= 1-\frac{\phi^T(t)}{\lambda}\left[P(t-1)-\frac{P(t-1)\phi(t)\phi^T(t)P(t-1)}{\lambda+\phi^T(t)P(t-1)\phi(t)}\right]\phi(t) \\ &= \frac{1}{\lambda}\left[\lambda-\phi^T(t)P(t-1)\phi(t)+\frac{\phi^T(t)P(t-1)\phi(t)\phi^T(t)P(t-1)\phi(t)}{\lambda+\phi^T(t)P(t-1)\phi(t)}\right] \\ &= \frac{\lambda}{\lambda+\phi^T(t)P(t-1)\phi(t)} \end{aligned} \tag{3.37}$$

one can obtain

$$J(t) = \lambda\left[J(t-1)+\frac{\left[y(t)-\phi^T(t)\hat{\theta}_{LS}(t-1)\right]^2}{\lambda+\phi^T(t)P(t-1)\phi(t)}\right] \tag{3.38}$$

Thus the final equations for Bias Compensated Exponentially Weighted Recursive Least Squares technique are the following :

$$\begin{aligned} \hat{\theta}_{LS}(t) &= \hat{\theta}_{LS}(t-1)+P(t)\phi(t)\left[y(t)-\phi^T(t)\hat{\theta}_{LS}(t-1)\right] && \hat{\theta}_{LS}(0)=[\mathbf{0}] \\ P(t) &= \frac{1}{\lambda}\left[P(t-1)-\frac{P(t-1)\phi(t)\phi^T(t)P(t-1)}{\lambda+\phi^T(t)P(t-1)\phi(t)}\right] && P(0)=P_0 I \\ J(t) &= \lambda\left[J(t-1)+\frac{\left[y(t)-\phi^T(t)\hat{\theta}_{LS}(t-1)\right]^2}{\lambda+\phi^T(t)P(t-1)\phi(t)}\right] && J(0)=0 \\ \hat{\sigma}^2(t) &= \frac{\frac{1-\lambda}{1-\lambda^t}J(t)}{1+\hat{\theta}_C(t-1)\Lambda\hat{\theta}_{LS}(t)} && \\ \hat{\theta}_C(t) &= \hat{\theta}_{LS}(t)+\hat{\sigma}^2(t)(\tfrac{1-\lambda^t}{1-\lambda})P(t)\Lambda\hat{\theta}_C(t-1) && \hat{\theta}_C(0)=[\mathbf{0}] \end{aligned} \tag{3.39}$$

3.3.2 Persistently Excited Cantilever Excitation (Sum of Three Sinusoids)

The question of the sufficiency of the input excitation in determining the equivalent cantilever parameters is discussed next. A general discretized second order dynamics that represents the first mode approximated model of the cantilever is given as,

$$\begin{aligned} e(n) &= \vartheta(n)+b_1\vartheta(n-1)+b_0\vartheta(n-2) \\ u(n) &= a_2 g(n)+a_1 g(n-1)+a_0 g(n-2) \\ p(n)+b_1 p(n-1)+b_0 p(n-2) &= u(n)+e(n), \end{aligned} \tag{3.40}$$

where $p(n)$ and $g(n)$ denote the cantilever deflection and dither forcing at sampled time $t=nT_s$ where T_s is the sampling interval and $\vartheta(n)$ is zero mean white measurement noise with variance σ_ϑ^2. Thus to identify the dynamics in (3.40), five parameters, (b_1,

$b_0,\ a_2,\ a_1,\ a_0$), need to be identified. It is well known [36] that to identify $n = 5$ parameters in real time $\lceil n/2 \rceil = 3$ sinusoids at the input are needed for identifying the second order model in (3.40). Any less richness of the input will lead to divergence in parameter estimates. The three sinusoids are chosen such that one sinusoid is at or near the resonance as is the case in normal tapping mode operation. This will lead to a nominal periodic cantilever oscillations which ensures that the cantilever is interacting with the sample under operating condition found in conventional tapping mode operation. Other two sinusoids are chosen at $f_0 \pm 6$ kHz (with $f_0 = \frac{\omega_0}{2\pi}$) because $G(i\omega)$ is a high Q system for operation in air and the forcing away from resonance of the cantilever will be heavily attenuated at the cantilever output. Indeed, if the cantilever forcing is $g(t) = A\sin\omega_0 t + B\sin(\omega_0 + \Delta\omega_0)t + B\sin(\omega_0 - \Delta\omega_0)t$ then the deflection of the sample-free cantilever is $p(t) = |G(i\omega_0)|\sin(\omega_0 t + \angle G(i\omega_0))\{A + C\}$ where $C = 2B\frac{|G(i\omega_0+\Delta\omega_0)|}{|G(i\omega_0)|}\cos(\Delta\omega_0 t + \frac{\angle G(i\omega_0+\Delta\omega_0)-\angle G(i\omega_0-\Delta\omega_0)}{2})$ characterizes the change in the output amplitude due to the added excitation at frequencies $f_0 + \Delta f_0$ and $f_0 - \Delta f_0$ and $\angle G(i\omega)$ represents the phase between $g(t)$ and $p(t)$ at input frequency ω. Thus, we have $-2B\frac{|G(i\omega_0+\Delta\omega_0)|}{|G(i\omega_0)|} \leq C \leq 2B\frac{|G(i\omega_0+\Delta\omega_0)|}{|G(i\omega_0)|}$. Choosing amplitudes $B = A/2$ with $A \approx 25$ nm, quality factor, $Q \approx 225$ as representative tapping mode parameters and $\Delta f_0 \approx 6$ kHz, results in a total variation of 1 nm in the amplitude of output trajectory from the nominal tapping mode trajectory.

3.3.3 Recursive Estimation of Equivalent Parameters (REEP) Technique for Atomic Force Microscopy

In this section, the algorithm in section (3.3.1) is adapted for atomic force microscopy. On identification of plant at several points on the force curve, it was observed that the coefficients a_2, a_1 and a_0, which capture the delays in the system, do not change much and contribute to the response of system at frequencies considerably away from the cantilever resonance. These coefficients are attributed to the dither piezo dynamics or beam dynamics which is not effected by sample properties. Subsequently the values of a_2, a_1 and a_0 are fixed to the sample-free model values. It must be noted that even though $\vartheta(n)$ is uncorrelated noise process, $e(n)$ is not uncorrelated noise process.

Equation (3.40) can be written as

$$z(n) = \underbrace{[b_1 \; b_0]}_{\theta} \underbrace{\begin{bmatrix} -p(n-1) \\ -p(n-2) \end{bmatrix}}_{\phi(n)} + e(n) \tag{3.41}$$

where θ represents the vector of unknown parameters and $z(n) = p(n) - a_2 g(n) - a_1 g(n-1) - a_0 g(n-2)$. At any time instant $t = nT_s$, past data $z(k)$ and ϕ_k for $k = 0, 1, ...n$ are available. An estimate $\hat{\theta}_{LS}(n)$ can be computed by solving the standard exponentially weighted least squares problem

$$\min_{\hat{\theta}_{LS}(n)} \Sigma_{k=0}^{n} \lambda^{n-k} (z(k) - \hat{\theta}_{LS}(n)\phi(k))^2. \tag{3.42}$$

It is well known [36] that (3.42) can be solved recursively in an update manner with $\hat{\theta}_{LS}(n)$ computable from $\hat{\theta}_{LS}(n-1)$ alone using exponentially weighted recursive least squares (EWRLS) method. When $e(n)$ is uncorrelated, it can be shown [36] that $\hat{\theta}_{LS}(n) \rightarrow \theta$, the true parameter, with the multiple sine excitation. However, $e(n)$ is correlated as $e(n)$ given in (3.40) is dependent on $\vartheta(n)$, $\vartheta(n-1)$ and $\vartheta(n-2)$. This leads to the estimate $\hat{\theta}_{LS}(n)$ converging to θ within a bias. Recently [37], a bias compensated recursive least squares is reported that provides an unbiased estimate when the noise is correlated. Bias compensated exponentially weighted recursive least squares (BCEWRLS) method is developed instead as presented in previous section since a handle on convergence rate of the parameter estimates is required. At time instant $t = nT_s$, assuming $z(n)$, $\phi(n)$, $\hat{\theta}_{LS}(n-1)$, $P(n-1)$, $J(n-1)$ and $\hat{\theta}_C(n-1)$ are available, the corresponding updated values can be found as

$$\begin{aligned}
&\hat{\theta}_{LS}(n) = \hat{\theta}_{LS}(n-1) + P(n)\phi(n)l(n) \\
&l(n) = \left[z(n) - \phi'(n)\hat{\theta}_{LS}(n-1) \right] \\
&P(n) = \tfrac{1}{\lambda} \left[P(n-1) - \tfrac{P(n-1)\phi(n)\phi'(n)P(n-1)}{\lambda + \phi'(n)P(n-1)\phi(n)} \right] \\
&J(n) = \lambda \left[J(n-1) + \tfrac{\left[z(n) - \phi'(n)\hat{\theta}_{LS}(n-1) \right]^2}{\lambda + \phi'(n)P(n-1)\phi(n)} \right] \\
&\hat{\theta}_C(n) = \tfrac{\hat{\sigma}^2(n)}{1-\lambda} n P(n) \hat{\theta}_C(n-1) \\
&\hat{\sigma}^2(n) = \tfrac{((1-\lambda)/n)J(n)}{1 + \hat{\theta}'_C(n-1)\hat{\theta}_{LS}(n)}
\end{aligned} \tag{3.43}$$

where $\lambda = 0.995$ is the exponential forgetting factor, $\hat{\theta}_{LS}(n)$ is the parameter estimate of θ at time instant $t = nT_s$ using EWRLS and $\hat{\theta}_C(n)$ is the bias compensated $\hat{\theta}_{LS}(n)$.

Note that in (3.43), the estimate $\hat{\theta}_{LS}(n)$ at time $t = nT_s$ can be obtained from past estimate $\hat{\theta}_{LS}(n-1)$ and an update term that depends on certain gain $P(n)\phi(n)$ and the instantaneous error term $(z(n) - \phi'(n)\hat{\theta}_{LS}(n-1))$. $P(n)$ represents the variance of the error in the parameter estimates $(\theta - \hat{\theta}_{LS}(n))$ and $J(n)$ represents the least square error in (3.42) that is being minimized at any given instance. $\hat{\sigma}^2(n)$ is an estimate of the variance of noise $e(n)$ at any instance. The algorithm is initialized with $\hat{\theta}_{LS}(0) = \begin{bmatrix} 0 \\ 0 \end{bmatrix}$, $P(0) = \begin{bmatrix} 1 & 0 \\ 0 & 1 \end{bmatrix} \times 10^6$, $J(0) = 0$ and $\hat{\theta}_C(0) = \begin{bmatrix} 0 \\ 0 \end{bmatrix}$. The advantage of (3.43) is that it requires a small amount of memory since only current estimated values need to be stored and can be implemented on hardware for real time operation with ease. f_0' and Q' can be calculated from estimated b_1 and b_0 values in closed form.

3.3.4 Deriving f_0 and Q from REEP Output

Triangular transformation method is used to convert a continuous transfer function to discrete transfer function. If $H(s)$ is the continuous transfer function then it's discrete equivalent is given by

$$H_{tri}(z) = \frac{(z-1)^2}{Tz} Z\left(\frac{H(s)}{s^2}\right) \tag{3.44}$$

If the cantilever model is represented as a second order transfer function with one zero then its tranfer function will be

$$H(s) = \frac{a_1 s + a_0}{s^2 + b_1 s + b_0} \tag{3.45}$$

One can then derive the discrete transfer function of $H(s)$ using triangular transformation using following steps:

$$\begin{aligned} \frac{H(s)}{s^2} &= \frac{a_1 s + a_0}{s^2(s^2 + b_1 s + b_0)} \\ &= \frac{A}{s} + \frac{B}{s^2} + \frac{C}{s^2 + b_1 s + b_0} + \frac{Ds}{s^2 + b_1 s + b_0} \\ &= \frac{\overbrace{(a_1/b_0 - b_1 a_0/b_0^2)}^{A}}{s} + \frac{\overbrace{(a_0/b_0)}^{B}}{s^2} + \frac{\overbrace{-a_0/b_0 - b_1 a_1/2b_0 + b_1^2 a_0/b_0^2}^{C_1}}{s^2 + b_1 s + b_0} \\ &\quad + \frac{\overbrace{-a_1/b_0 + b_1 a_0/b_0^2}^{D_1}(s + b_1/2)}{s^2 + b_1 s + b_0} \end{aligned} \tag{3.46}$$

If the two complex roots of characteristic polynomial are $s_1, s_2 = -p \pm iq$, then $s^2 + b_1 s + b_0 = (s+p)^2 + q^2$ where $b_1 = 2p$ and $b_0 = p^2 + q^2$. Then we have

$$\begin{aligned} \frac{(z-1)^2}{Tz} Z\left(\frac{a_1 s + a_0}{s^2(s^2 + b_1 s + b_0)}\right) &= \frac{A}{T}(z-1) + B + \frac{C_1}{qT} \frac{(z-1)^2 e^{-pT} \sin qT}{z^2 - 2e^{-pT} \cos qT z + e^{-2pT}} \\ &\quad + \frac{D(z-1)^2}{T} \frac{(z - e^{-pT} \cos qT)}{z^2 - 2e^{-pT} \cos qT z + e^{-2pT}} \\ &= \frac{1}{T} \frac{z^2 P + zQ + R}{z^2 - 2e^{-pT} \cos qT z + e^{-2pT}} \end{aligned} \tag{3.47}$$

where

$P = (-Ae^{-pT} \cos qT + A + BT + (C_1/q)e^{-pT} \sin qT)$

$Q = (Ae^{-2pT} - 2BTe^{-pT} \cos qT - (2C_1/q)e^{-pT} \sin qT - A)$

$R = (-Ae^{-2pT} + BTe^{-2pT} + (C_1/q)e^{-pT} \sin qT + Ae^{-pT} \cos qT)$

Thus we have

$$\begin{aligned} p &= \frac{-1}{2T} \log(b_0) \\ q &= \frac{1}{T} acos\left(\frac{b_1}{-2e^{-pT}}\right) \\ f_0 &= \frac{1}{2\pi} \sqrt{p^2 + q^2} \\ Q &= \frac{\pi f_0}{p} \end{aligned} \tag{3.48}$$

3.4 Verification of REEP Estimates

In this section, we will develop techniques to verify the accuracy of the estimates obtained from REEP algorithm. The verification is done in three different ways.

3.4.1 Validation of Off-Sample Estimates

When the cantilever is not interacting with the sample i.e. it is not subjected to any nonlinear forcing in feedback, then the system is linear. Sample-free model was identified using frequency sweep method wherein excitation frequency ω of $g(t) = A_0 \sin \omega t$ was varied from $0 - 100$ kHz and $p(t)$ was recorded. Magnitude and phase information about $G(i\omega)$ was obtained by evaluating ratios between steady state amplitude and phase of output vs input excitation respectively. f_0 and Q were extracted by a second order fit around resonance. The same sample-free model parameters were extracted in real time with BCEWRLS scheme using (3.43). These two sets of independent estimates are compared in (Figure 3.1(b)). Comparison between the two independent estimates

for equivalent cantilever parameters when the cantilever is not interacting with the sample, indicates that in most cases estimates of f_0 are accurate within +5 Hz and quality factor estimates are accurate to within +15 of actual values identified using the frequency sweep method. As the cantilever is brought close to the sample it experiences squeeze film damping effect. This increases the damping coefficients of the cantilever as the tip sample distance decreases even though the cantilever is not interacting with the sample. Thus multiple points for verification can be obtained in off-sample situation by predicting the cantilever response subjected to varying amount of squeeze film damping.

3.4.2 Minimum Error RMS Based Validation of On-Sample Estimates

When the cantilever is interacting with the sample i.e. when it is subjected to a non-linear forcing in feedback then obtaining input output frequency sweep based transfer function is not possible. This is because when we apply a frequency chirp at the input of the cantilever then the output cantilever deflection varies in amplitude depending on the cantilever transfer function at that particular tip-sample separation. Thus the interaction level of the cantilever with the sample changes during the experiment. Since cantilever model is a function of how the cantilever is interacting with the sample, one would obtain false estimates of cantilever response using frequency sweep based methods.

REEP estimates obtained while the cantilever is interacting with the sample can be verified using minimum innovation rms concept. Let's assume that the cantilever model can vary in a set $\Omega : \{(\omega_e, Q_e) | \omega_0 - \Delta_1 \leq \omega_e \leq \omega_0 + \Delta_1; Q_0 - \Delta_2 \leq Q_e \leq Q_0 + \Delta_2\}$ where ω_0 is the off-sample cantilever resonant frequency, Q_0 is off-sample quality factor, Δ_1 is the expected variation in the equivalent resonant frequency and Δ_2 is the expected variation in the equivalent quality factor of the cantilever. If we pick a point $(\omega_k, Q_k) \in \Omega$ and build a Kalman filter based on this plant dynamics where dynamics is given by

$$\begin{aligned} \dot{\hat{x}} &= A_k \hat{x} + Bg + L(y - \hat{y}) \\ \hat{y} &= C\hat{x} \end{aligned} \tag{3.49}$$

where the plant dynamics is given by

$$\begin{aligned} \dot{x} &= A_e x + Bg + B\eta \\ y &= Cx + \nu \end{aligned} \tag{3.50}$$

Then it can be proved that

$$E\{e^T e\} \quad = \quad \lim_{T\to\infty} \frac{1}{T} \int_0^T e^T(t)e(t)dt \tag{3.51}$$

where e is the innovation error output of the Kalman filter, is minimum iff $A_k = A_e$ (ref).

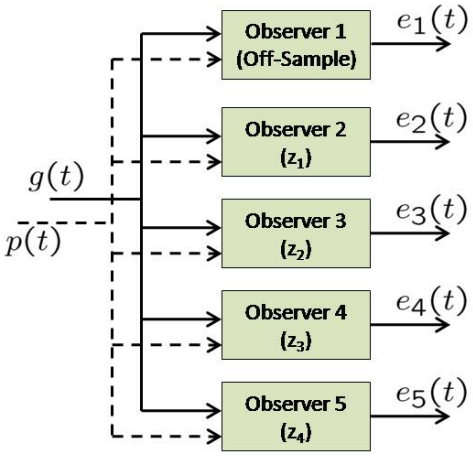

Figure 3.2: Schematic for a bank of Kalman Filters where each filter is based on a distinct equivalent cantilever model corresponding to a distinct tip-sample separation, z_i. This scheme is used for verification of on-sample REEP estimates.

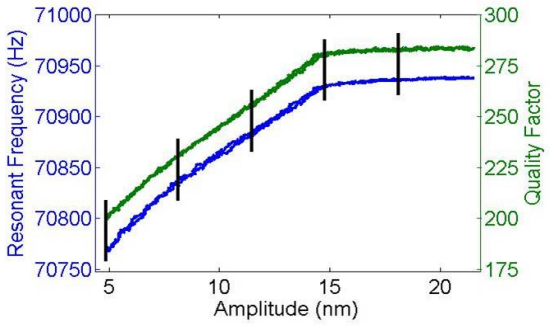

Figure 3.3: Five discrete points in Ω space are picked. Five Kalman filters based on these points are build and the innovation signals are matched to verify the REEP estimates. The figure shows the estimated equivalent resonant frequency (blue curve) and the quality factor (green curve) of the cantilever during a force curve experiment.

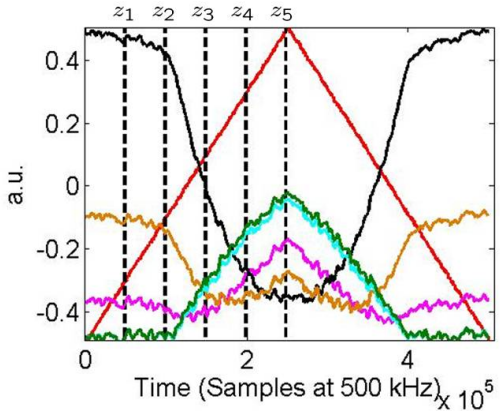

Figure 3.4: RMS of innovation signals from the bank of five Kalman filters are plotted. Red curve shows the voltage applied to the z-piezo during the force curve. Dashed black lines indicate five different z-piezo positions and correspondingly five equivalent cantilever models at which the bank of Kalman filters are constructed. Dark green, cyan, magenta, orange and black represent the rms of innovation signals of Kalman filters corresponding to z_1, z_2, z_3, z_4 and z_5 points respectively. The minima of each curve is reached precisely at the point when the z-piezo voltage corresponds to the corresponding equivalent plant model. Each rms signal remains minimum in the vicinity of its chosen plant model indicating that there is some continuous equivalent plant model space where that particular observer model is the "closest" as compared to other chosen discrete points.

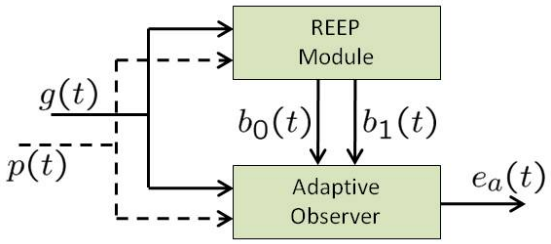

Figure 3.5: Schematic of an adaptive observer. The instantaneous plant model to the observer is provided by the REEP algorithm. RMS of the innovation signal of the adaptive observer is monitored.

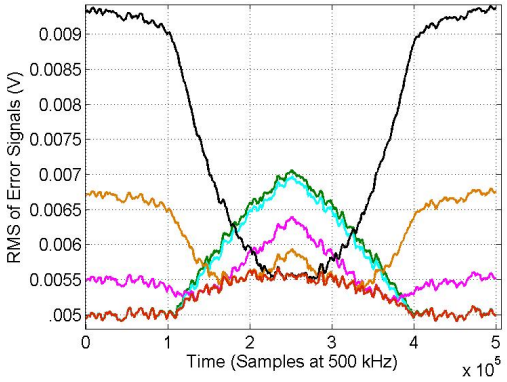

Figure 3.6: Dark green, cyan, magenta, orange and black represent the rms of innovation signals of Kalman filters corresponding to z_1, z_2, z_3, z_4 and z_5 points respectively. Red curve is the rms of the innovation signal of the adaptive observer. The instantaneous equivalent cantilever model is provided to this observer through the REEP algorithm. The fact that the red curve remains the minimum at all instances indicates that the adaptive observer is able to track the plant output at each instance. Thus the estimates provided to us by the REEP algorithm provide the closest equivalent plant model at each instance.

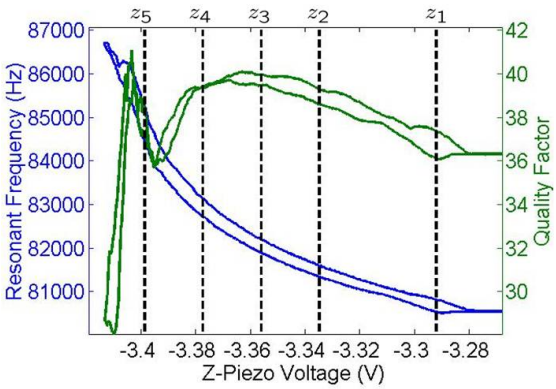

Figure 3.7: Five discrete points in Ω space are picked. Five Kalman filters based on these points are build and the innovation signals are matched to verify the REEP estimates. The figure shows the estimated equivalent resonant frequency (blue curve) and the quality factor (green curve) of the cantilever during a force curve experiment.

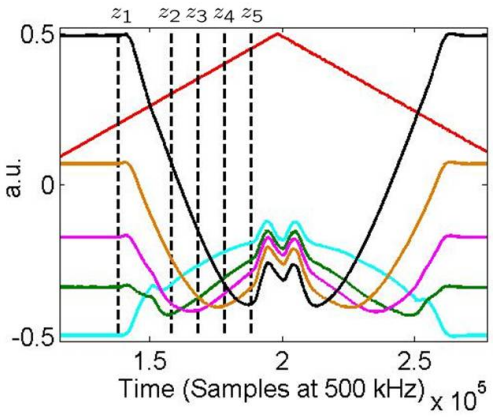

Figure 3.8: RMS of innovation signals from the bank of five Kalman filters are plotted. Red curve shows the voltage applied to the z-piezo during the force curve. Dashed black lines indicate five different z-piezo positions and correspondingly five equivalent cantilever models at which the bank of Kalman filters are constructed. Dark green, cyan, magenta, orange and black represent the rms of innovation signals of Kalman filters corresponding to z_1, z_2, z_3, z_4 and z_5 points respectively. The minima of each curve is reached precisely at the point when the z-piezo voltage corresponds to the corresponding equivalent plant model. Each rms signal remains minimum in the vicinity of its chosen plant model indicating that there is some continuous equivalent plant model space where that particular observer model is the "closest" as compared to other chosen discrete points.

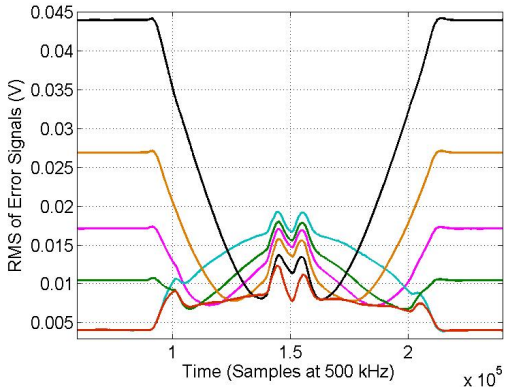

Figure 3.9: Dark green, cyan, magenta, orange and black represent the rms of innovation signals of Kalman filters corresponding to z_1, z_2, z_3, z_4 and z_5 points respectively. Red curve is the rms of the innovation signal of the adaptive observer. The instantaneous equivalent cantilever model is provided to this observer through the REEP algorithm. The fact that the red curve remains the minimum at all instances indicates that the adaptive observer is able to track the plant output at each instance. Thus the estimates provided to us by the REEP algorithm provide the closest equivalent plant model at each instance.

The set Ω can be identified for the cantilever-sample system by performing a force curve where the tip-sample separation is reduced and then increased linearly. Cantilever amplitude varies from its free air value to near zero value during this experiment. Cantilever excitation and deflection are monitored simultaneously and provided to the REEP algorithm. REEP algorithm provides the estimates of (ω_e, Q_e) for each value of z-piezo position, z_s. Five points from this space are chosen arbitrarily corresponding to five z-piezo positions $(z_1, z_2, z_3, z_4, z_5)$ and five Kalman filters are designed, one for each plant model in this set. Thus we have bank of five Kalman filters whose models should match the cantilever model when the z-piezo position is in the set $(z_1, z_2, z_3, z_4, z_5)$ (see Figure 3.2). Another set of experiments are performed where z-piezo position is again varied linearly and cantilever input and output are captured simultaneously. This data is provided to the bank of Kalman filters and five innovation rms signals are plotted against z-piezo position. Figure 3.3 shows the equivalent resonant frequency and the equivalent quality factor estimates for the cantilever obtained via REEP method for

an amplitude force curve. The cantilever used for this experiment is AC-240TS cantilever from Asylum Research. It has an off-sample resonant frequency of 70938.44 Hz and a quality factor of 271.39. Five discrete points in this space corresponding to $(z_1, z_2, z_3, z_4, z_5)$ tip-sample separation are picked for constructing the bank of Kalman filters. Figure (3.4) shows that the minimum of each signal is achieved at its corresponding $(z_1, z_2, z_3, z_4, z_5)$ position as expected by theory. This indicates that the plant model obtained from REEP for the discrete set of points are indeed the closest models at that z-piezo positions. These discrete sets of points in Ω space can be randomly chosen and across experiments where the z-piezo position is varying across these points it can be verified that minimum innovation rms is achieved at the corresponding z-piezo position.

To verify if the REEP method does provide closest plant model estimates in continuous domain Ω, an adaptive observer is designed whose model parameters (ω_k, Q_k) are provided by REEP estimates at any particular instance (see Figure 3.5). Thus the observer model is expected be the closest to the plant model throughout the experiment irrespective of the z-piezo position. Thus rms of the innovation signal should always be minimum. Figure (3.6) shows that the rms of innovation error of adaptive observer is minimum throughout the experiment thus validating the experimental accuracy of the REEP estimates.

Similar experiments were also done for a low quality factor cantilever. The cantilever used in this experiment was AC-240TS cantilever from Asylum Research. Off-sample resonant frequency of this cantilever was 80327.99 Hz and a quality factor of 188.5. Quality factor of this cantilever was then artificially lowered by active Q-control to a value of 36. Amplitude force curve with three sinusoids, for REEP algorithm, as the the cantilever input was performed (see Figure 3.7). Five discrete points were chosen along these curves for building the bank of Kalman filters. Figure 3.8 shows the rms of the innovation signals from each of the five kalman filters. Again the minimum of these signals is reached in the vicinity of their corresponding equivalent plant model. This indicates that even for low quality factor cantilevers, REEP algorithm is able to provide the "closest" equivalent cantilever model. Figure 3.9 shows the rms of innovation signal of the adaptive observer. This signal which is represented in red is minimum throughout the experiment indicating that one can obtain continuous equivalent cantilever model estimates for low Q conditions as well.

3.4.3 Direct Validation of Estimates using Averaging Theory

Cantilever equivalent model parameters obtained using REEP method can also be verified analytically using averaging theory. This verification is a simulation based verification wherein the tip-sample interaction force is assumed to be a piecewise linear nonlinearity as presented in eqn (4.1). With this assumed nonlinearity, simulations can be done of the cantilever interacting with the nonlinearity at different interaction levels and with different nonlinear model parameters.

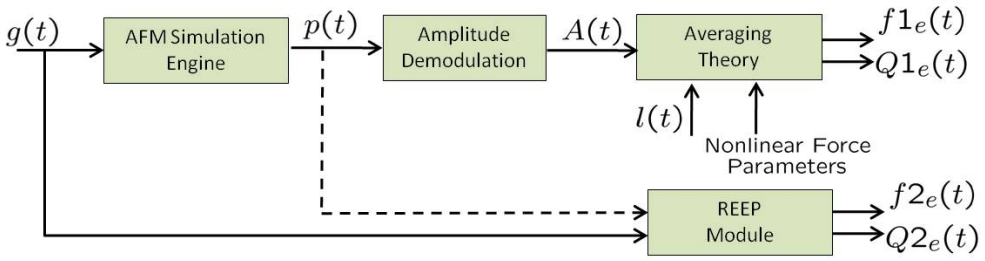

Figure 3.10: Schematic representing the simulation setup for verification of REEP algorithm and averaging theory. Simulations are performed for different values of nonlinear tip-sample force parameters and the two independent estimates are then compared.

Averaging theory requires instantaneous amplitude $A(t)$, tip-sample separation $\ell(t)$ and nonlinear model parameters for computation. It then provides us with analytical estimates of ω_e and Q_e as presented in (4.6, 4.7, 4.8) (see Figure 3.10). Instantaneous amplitude is obtained by demodulating the cantilever deflection signal. Instantaneous tip-sample separation and nonlinear force model parameters are known a-priori in a simulated environment. In experiments, instantaneous tip-sample separation can be estimated from the z-piezo voltage and its sensitivity. Nonlinear force parameters can be estimated using techniques outlined in [38]. If the cantilever can be approximated as a lightly damped oscillator where the nonlinear forces it experiences are small then it can be shown theoretically that the averaged dynamics are a close approximation of the actual trajectories ([39]). This approximation is valid when the quality factor of the cantilever is high. When the quality factor of the cantilever is low, then the estimates provided by averaging theory might be incorrect.

REEP algorithm requires cantilever excitation and cantilever deflection as its inputs. It then estimates the equivalent cantilever model recursively. Since averaging theory and REEP algorithm are two independent sources of obtaining the equivalent cantilever model, the comparison of their corresponding estimates can be used in essence to validate both or either of the theories. Although there are theoretical justifications of the estimates obtained from averaging theory, to be correct at high quality factor operations of the cantilever ([39]).

Simulations were done for three different sets of nonlinear force parameters. The off-sample cantilever model was assumed to have a resonant frequency of 80318 Hz and a quality factor of 168. The three sets of nonlinear tip-sample force parameters used were

- For predominant attractive interaction: $d = 4$; $\omega_a = (0.31 \times 1e6)^2$; $\omega_b = (3.03 \times 1e6)^2$; $c_a = 0.042 \times 1e6$; $c_b = 0 \times 1e6$;
- For attractive/repulsive interaction : $d = 4$; $\omega_a = (0.1 \times 1e6)^2$; $\omega_b = (0.303 \times 1e6)^2$; $c_a = 0.0092 \times 1e6$; $c_b = 0 \times 1e6$;
- For predominant repulsive interaction: $d = 5$; $\omega_a = (0.11 \times 1e6)^2$; $\omega_b = (0.63 \times 1e6)^2$; $c_a = 0.0042 \times 1e6$; $c_b = 0 \times 1e6$;

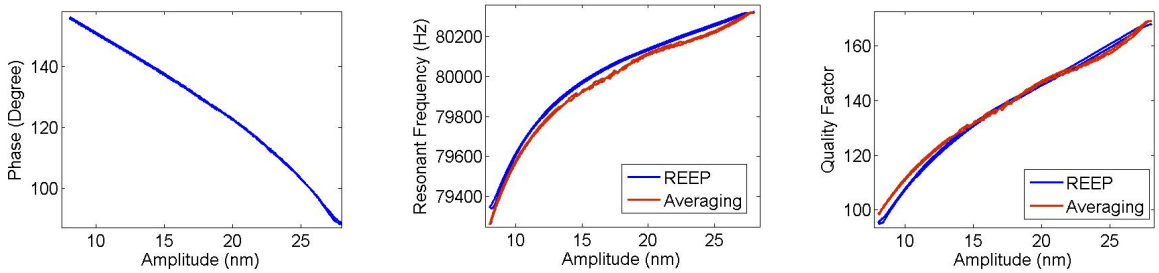

(a) (b) (c)

Figure 3.11: Figure shows a) phase b) equivalent resonant frequency and c) equivalent quality factor of the cantilever when an amplitude force curve is being done. The off-sample quality factor of the cantilever is low (168). The phase plot indicates that the tip-sample interaction is net attractive throughout the force curve. Thus the phase is increasing from its off-sample value and the equivalent resonant frequency and quality factor are decreasing. Red plots are obtained from averaging theory while the blue plots are obtained from the REEP algorithm.

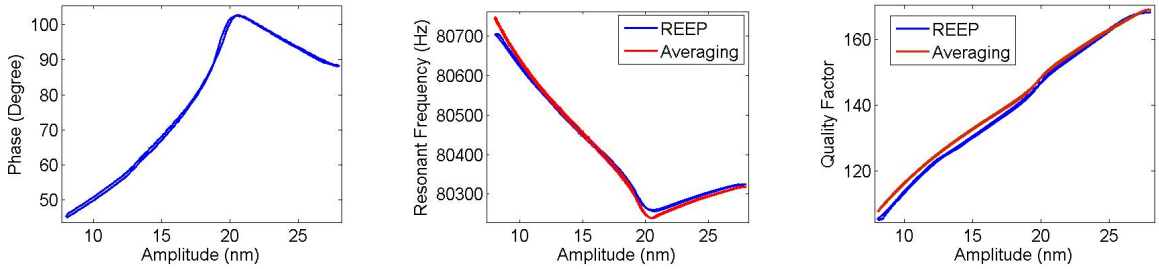

(a) (b) (c)

Figure 3.12: Figure shows a) phase b) equivalent resonant frequency and c) equivalent quality factor of the cantilever when an amplitude force curve is being done. The phase plot indicates that the tip-sample interaction is attractive at low interaction levels while it is net repulsive at higher interaction levels during the force curve. This behavior is consistent in all the three figures. Red plots are obtained from averaging theory while the blue plots are obtained from the REEP algorithm.

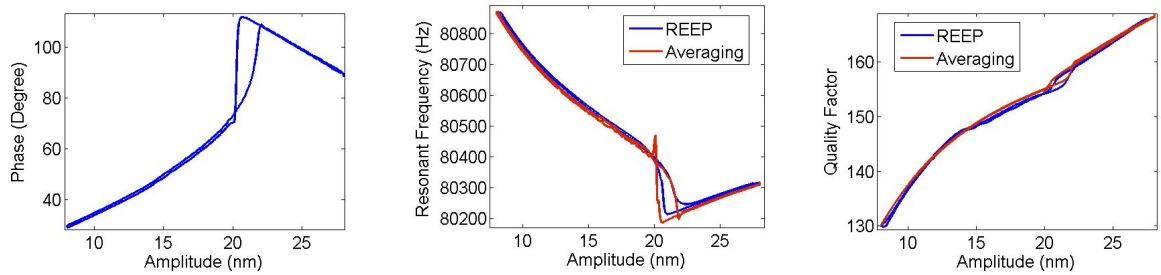

(a) (b) (c)

Figure 3.13: Figure shows a) phase b) equivalent resonant frequency and c) equivalent quality factor of the cantilever when an amplitude force curve is being done. The phase plot indicates that the tip-sample interaction is attractive at low interaction levels while it is net repulsive at higher interaction levels during the force curve. The cantilever amplitude also jumps from the stable attractive branch to the stable repulsive branch and vice-versa during the force curve. This behavior is consistent in all the three figures. The jump locations and magnitudes are also captured in both the algorithms. Red plots are obtained from averaging theory while the blue plots are obtained from the REEP algorithm.

Figure (3.11) shows the phase, estimated resonant frequency and estimated quality factor for the first case where the tip-sample interaction is predominantly attractive. The blue curve estimates are obtained using the REEP algorithm and the red curve estimates are obtained analytically using the equations of averaging theory. Figure (3.12) shows the phase, estimated resonant frequency and estimated quality factor for the second case where the tip-sample interaction is attractive as well is repulsive. Figure (3.13) shows the phase, estimated resonant frequency and estimated quality factor for the third case where the tip-sample interaction is predominantly repulsive which leads to a sudden jump in the cantilever model between stable branches of the net attractive and repulsive tip-sample interaction forces. It can be seen from these plots that the two independent equivalent resonant frequency and quality factor estimates match quantitatively. The slight deviation between the two estimates at very low set point of amplitude might be because the averaging theory might provide us with incorrect estimates when the cantilever is interacting with the sample harshly.

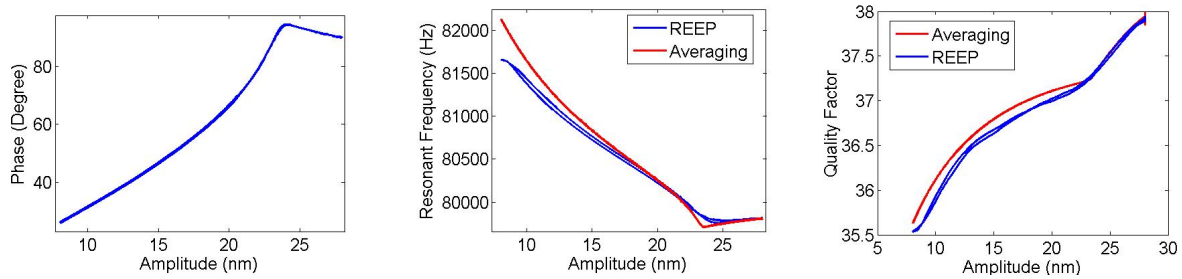

(a) (b) (c)

Figure 3.14: Figure shows a) phase b) equivalent resonant frequency and c) equivalent quality factor of the cantilever when an amplitude force curve is being done. The off-sample quality factor of the cantilever is low (38). The phase plot indicates that the tip-sample interaction is net attractive throughout the force curve. Thus the phase is increasing from its off-sample value and the equivalent resonant frequency and quality factor are decreasing. Red plots are obtained from averaging theory while the blue plots are obtained from the REEP algorithm.

Simulations were also done for the case when the cantilever has low quality factor to verify the extent of validity of the estimates provided by the averaging theory. It must be noted that the estimates provided by the REEP algorithm have been verified independently using a minimum rms approach for both low and high quality factors of the cantilever in the previous section. Figure (3.14) shows the phase, equivalent resonant frequency and equivalent quality factor for the case when the off-sample quality factor of the cantilever is 38. The nonlinear model parameters for this simulation were $d = 5$; $\omega_a = (0.11 \times 1e6)^2$; $\omega_b = (1.83 \times 1e6)^2$; $c_a = 0.0012 \times 1e6$; $c_b = 0 \times 1e6$. Again we obtain a reasonable match between the two estimates at this quality factor. The two independent estimates differed at quality factors below this value.

3.5 Experimental Results

To study the efficiency of the method, experiments were performed on Multimode AFM (Veeco Inc.) with AC240 cantilever (Asylum Research Inc., $f_0 = 71500$ Hz, $Q = 206$, $k = 2$ N/m). Dither and deflection signals were sampled simultaneously at 500 kHz.

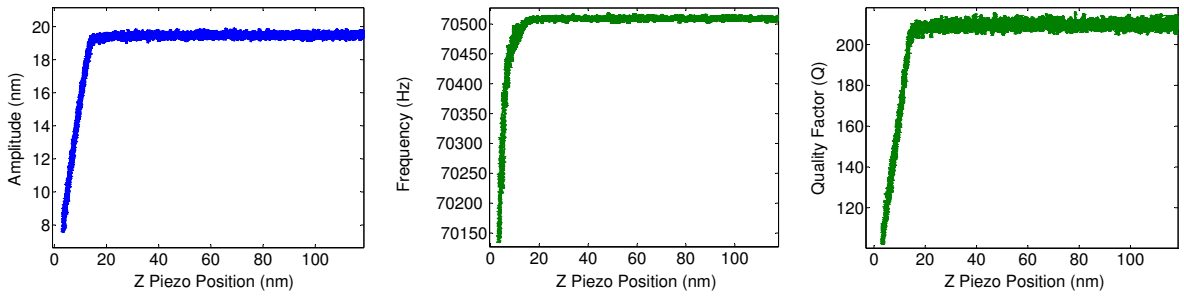

(a) (b) (c)

Figure 3.15: Experimentally obtained a) Amplitude b) Estimated f_0' c) Estimated Q' response during z-force curve experiment. Δ Amplitude = 12 nm; $\Delta f_0 = 350$ Hz; $\Delta Q = 110$. There are two different slopes in f_0' estimate curve. Both f_0' and Q' decrease with decrease in tip-sample separation.

(3.43) was then computed offline to get estimates of f_0' and Q'. Rate of convergence of parameters is lesser than 400μsec. This means the sample can have a spatial frequency upto 2.5kHz. These convergence rates are faster than conventional imaging signals like amplitude and phase of the cantilever deflection. This property, together with the recursive least squares algorithm (3.43), makes it possible to estimate equivalent cantilever model in real-time in the sense that they can be computed in a time scale smaller than the time-scales of amplitude and phase of the cantilever oscillations. The rate of convergence can be tuned by the exponential forgetting factor λ at the expense of increased variance in the error in estimating parameters. It is seen that the rate of convergence will be faster with smaller height changes in sample profile.

Equivalent cantilever parameters were identified during force curves done at 1 Hz to observe how $G_z(i\omega)$ modifies with sample height. Equivalent resonant frequency f_0' and quality factor Q' are experimentally estimated together with amplitude and phase (see Figure 3.15). Modified plant parameters were estimated when the deflection amplitude varied from sample-free amplitude ($\approx$ 25 nm) till 8 nm. A reduction in equivalent resonant frequency and quality factor was observed as expected with an increase in tip sample interaction. A sample with periodic features, which are less than 1 nm in height (see Figure 3.16), was imaged in tapping mode at 10 Hz and 100 Hz frequency. Controller gains were kept sufficiently small so that the controller just canceled the sample slope and the Z-piezo drifts. It is evident that the algorithm presented in the paper can

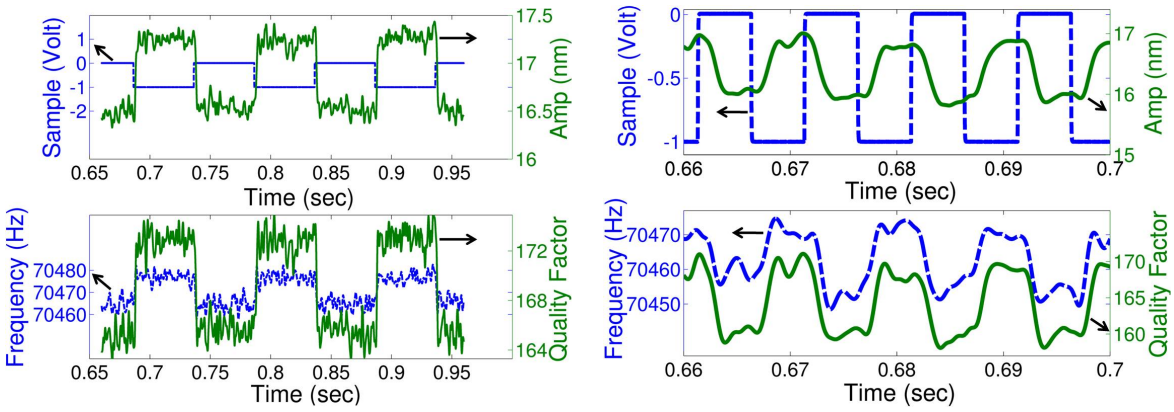

Figure 3.16: Experimentally obtained Sample Profile (top-blue-dash curve), Amplitude (top-green-solid curve), f_0' estimate (bottom-blue-dash curve), Q' estimate (bottom-green-solid curve) while imaging ≤ 1 nm square profile at (a) 10 Hz (b) 100 Hz. ≤ 1 nm steps are clearly visible in f_0' and Q' estimates.

generate f_0' and Q' estimates in real time providing simultaneous images of amplitude, phase, f_0' and Q'. Experimental results (see Figures 3.16(a) and Figure 3.16(b)) indicate that the method has an estimation resolution of better than 1 nm and can be used during normal tapping mode operation without any dependence on the image pixel size. Force spectroscopy experiments were done on a freshly cleaved mica sheet, and then subsequently after 45 min, 2 hour and 16 hours. It was observed that due to the presence of negative charges on a freshly cleaved mica sheet, the resonant frequency and quality factor started decreasing at a distance of $\approx 1\mu$m from the sample indicating the presence of long distance forces in addition to the van de waal forces. It took roughly 16 hours for this charge to neutralize. Changes in resonant frequency and quality factor after 16 hours were localized to within 20 nm from the sample surface indicating the presence of only short range forces (see Figure 3.17).

3.6 Conclusion

This chapter presents a scheme for estimating equivalent resonant frequency and quality factor Q with resolution better than 1 nm and speed of ≤ 400 μsec which is at least two orders of magnitude better than current available techniques. It has also been

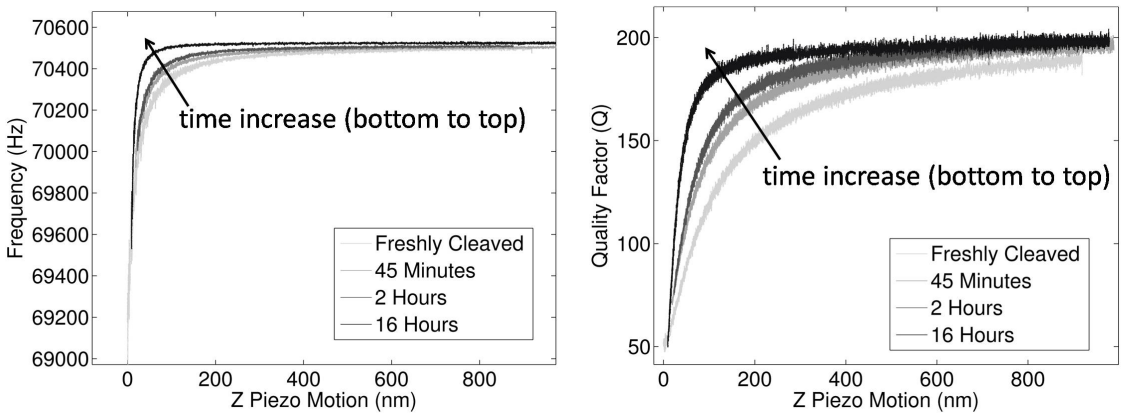

Figure 3.17: Experimentally obtained a) f_0' estimate b) Q' estimate during force spectroscopy experiment done on a freshly cleaved mica surface and then subsequently at 45 min, 2 hrs and 16 hrs. Localization of surface forces within 20 nm of the sample surface occurs after 16 hrs of cleaving a mica surface.

established that sum of three sinusoids is sufficient to provide such estimates. Detailed verification of the accuracy of these estimates is also provided.

Chapter 4

Resonant Frequency Based Sensing for Low Q Operations of Dynamic Mode Atomic Force Microscopy

4.1 Introduction

Intermittent contact dynamic mode AFM operation, also known as tapping mode, is the most prevalent form of operation to image soft samples and biological samples. When compared to contact mode operation, tapping mode operation is gentle on the sample due to reduced lateral and frictional forces on the sample. In tapping mode operation, the cantilever is typically oscillated by a single sinusoid which is at or near the resonant frequency of first mechanical mode of the cantilever. Amplitude or phase of the oscillating cantilever, which interacts with the sample intermittently, are used to maintain a constant tip-sample interaction and image the sample topography.

Some studies show that by increasing the quality factor of the cantilever, one can increase the amplitude based sensitivity and decrease the forces on the sample ([40, 41, 42, 43, 44]). There is an upper bound of '1' on amplitude sensitivity ([45]). This sensitivity might drop below '1' for non compliant surfaces and low quality factor

cantilevers [46, 47]).

Several biological samples need to be imaged in buffers which are their native environment. Under fluid, tapping mode results in low quality factor operation on soft samples ([40]). Reduced quality factor is due to additional viscous damping of the surrounding liquid. Similarly in integrated sensor application where the actuator and the sensor are integrated on the cantilever, it makes the cantilever bulky. This leads to reduced quality factor as well ([48]).

This chapter explores resonant frequency based topography imaging during tapping mode operation. We present analytical expressions to study f_0 sensitivity with respect to topography for variations in the off sample quality factor of the cantilever. It is shown that this sensitivity increases with reducing quality factor which is an opposite trend as compared to the amplitude sensitivity. Experimental results are shown to demonstrate the assertions of the work. In this chapter, expressions for equivalent resonant frequency and equivalent damping of the cantilever with respect to changes in the tip-sample interaction levels and nonlinear force parameters are derived assuming a piecewise linear tip-sample interaction model. These expressions are then used to derive the sensitivity expressions of equivalent resonant frequency and equivalent damping and amplitude with respect to changes in sample topography. Then the behavior of these sensitivities is analyzed with respect to changes in the off sample cantilever's quality factor. Finally it is shown analytically as well as experimentally that while the amplitude and the quality factor sensitivities reduce with reducing quality factor, the sensitivity of equivalent resonant frequency increases with reducing quality factor.

4.2 Piecewise Linear Tip-Sample Interaction Force

Van De Waal's interaction forces are modeled in a variety of ways ([]Garcia2002). A piecewise linear tip-sample separation model which has the possibility to incorporate dissipative forces as well as the conservative force interactions was presented in ([32]). This model is shown to accurately predict the bistable behavior in amplitude during tapping mode operation ([32]). Analytical derivations in this work are done assuming a piecewise linear tip-sample interaction force.

$$F_{ts}(p,\dot{p}) = \begin{cases} 0 & \text{if } p \geq -l+d \\ -\omega_a^2(p+l-d)+c_a\dot{p} & \text{if } -l \leq p \leq -l+d \\ \omega_b^2(p+l)-\omega_a^2(p+l-d)+c_a\dot{p}+c_b\dot{p} & \text{if } p < -l \end{cases} \quad (4.1)$$

where l is the initial tip-sample separation, d is the spatial difference between the onset of attractive and repulsive forces, ω_a^2 is the attractive spring constant per unit mass, ω_b^2 is the repulsive spring constant per unit mass, c_a is the attractive damping coefficient per unit mass and c_b is the repulsive damping coefficient per unit mass (see Figure 4.1). In this work these parameters are chosen to be $d = 1.65$ nm; $\omega_a^2 = (0.18 \times 1e6)^2$; $\omega_b^2 = (4.03 \times 1e6)^2$; $c_a = 0.042 \times 1e6$ and $c_b = 1.45 \times 1e6$ for simulations.

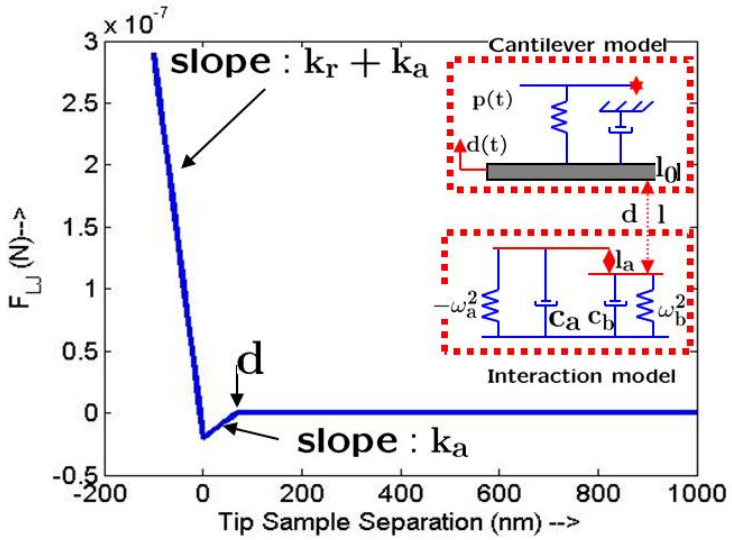

Figure 4.1: Piecewise nonlinear tip-sample interaction force model.

4.3 Deriving Expressions for Equivalent Cantilever Parameters using Averaging Theory

When the cantilever is interacting with the sample during tapping mode operation, its dynamics can be expressed as

$$m\ddot{p} + c\dot{p} + kp = mg(t) + \Phi(p,\dot{p}) \quad (4.2)$$

where m is the mass of the cantilever, c is the off sample damping, k is the off sample stiffness, p is the cantilever deflection, $\dot{p}$ is the cantilever velocity, $\Phi(p,\dot{p}) = F_{ts}(p,\dot{p})m$, ω is the excitation frequency, A is the amplitude of the excitation, $g(t) = \gamma\cos(\omega t)$ and $\gamma = \frac{kA}{m}$. This dynamics can be rewritten as

$$m\ddot{p} + kp = \epsilon f(p,\dot{p}) + \epsilon E\cos(\omega t) \tag{4.3}$$

where $E = \frac{m\gamma}{\epsilon}$ and $f(p,\dot{p}) = \frac{-c\dot{p}+\Phi(p,\dot{p})}{\epsilon}$.

The cantilever deflection can be assumed to be a sinusoidal trajectory in the steady state for a high quality factor operation. Thus

$$\begin{aligned} p(t) &= a\cos(\omega t + \phi) \\ \dot{p}(t) &= -a\omega\sin(\omega t + \phi) \end{aligned} \tag{4.4}$$

where $\dot{p}(t)$ is the cantilever velocity, a is the amplitue of the cantilever and ϕ is the phase of cantilever deflection w.r.t cantilever driver signal. On applying the above transformation to equation 4.3 the cantilever dynamics cn be represented in amplitude and phase coordinates as

$$\begin{aligned} \dot{a} &= \frac{-1}{\omega}\left[a(\omega^2-\omega_0^2)\cos(\omega t+\phi) + \frac{\epsilon f(p,\dot{p})}{m} + \frac{\epsilon E\cos(\omega t)}{m}\right]\sin(\omega t+\phi) \\ \dot{\phi} &= \frac{-1}{a\omega}\left[a(\omega^2-\omega_0^2)\cos(\omega t+\phi) + \frac{\epsilon f(p,\dot{p})}{m} + \frac{\epsilon E\cos(\omega t)}{m}\right]\cos(\omega t+\phi) \end{aligned} \tag{4.5}$$

Using averaging theory it can be proved ([32]) that the resultant cantilever trajectories of eqn (4.5) can be approximated by an averaged amplitude and phase dynamics where the averaging is done over one period of cantilever trajectory.

Averaged amplitude dynamics is given by

$$\begin{aligned} \dot{\bar{a}} &= -\delta_e(a)a - \epsilon\frac{E\sin(\phi)}{m(\omega_0+\omega)} \\ \delta_e(a) &= \frac{c}{2m} + \frac{1}{a\omega}\Phi_d \\ \Phi_d &= \frac{1}{2\pi}\int_0^{2\pi}\frac{\Phi(a\cos(\theta),-a\omega\sin(\theta))}{m}\sin(\theta)d\theta \end{aligned} \tag{4.6}$$

where $\delta_e(a)$ is the equivalent damping coefficient of the cantilever at any instance and Φ_d is the average dissipative force per oscillation cycle.

Averaged phase dynamics is given by

$$\begin{aligned} \dot{\bar{\phi}} &= \omega_e(a) - \omega - \frac{\epsilon E\cos(\phi)}{ma(\omega_0+\omega)} \\ \omega_e^2(a) &= \omega_0^2 - \frac{2}{a}\Phi_c \\ \Phi_c &= \frac{1}{2\pi}\int_0^{2\pi}\frac{\Phi(a\cos(\theta),-a\omega\sin(\theta))}{m}\cos(\theta)d\theta \end{aligned} \tag{4.7}$$

where $\omega_e(a)$ is the equivalent resonant frequency of the cantilever at any instance and Φ_c is the average conservative force per unit cycle.

Using a piecewise linear tip-sample interaction force model as mentioned in eqn (4.1) the integrals of Φ_d and Φ_c in eqns (4.6) and (4.7) can be evaluated analytically as

$$\Phi_d = \begin{cases} 0 & \text{if } a < (l-d) \\ \frac{-1}{2\pi} c_a a\omega(\pi - S_1 + \sin(2S_1)/2) & \text{if } l-d \le a < l \\ \frac{-1}{2\pi}\left[c_a a\omega(\pi - S_1 + \sin(2S_1)/2) + c_b a\omega(\pi - S_2 + \sin(2S_2)/2)\right] & \text{if } a \ge l \end{cases}$$

$$\Phi_c = \begin{cases} 0 & \text{if } a < (l-d) \\ \frac{-1}{2\pi}\left[-\omega_a^2 a(\pi - S_1 - \sin(2S_1)/2) + 2\omega_a^2(l-d)\sin(S_1)\right] & \text{if } l-d \le a < l \\ \frac{-1}{2\pi}[-\omega_a^2 a(\pi - S_1 - \sin(2S_1)/2) + 2\omega_a^2(l-d)\sin(S_1) & \\ \quad + \omega_b^2 a(\pi - S_2 - \sin(2S_2)/2) - 2\omega_b^2 l\sin(S_2)] & \text{if } a \ge l \end{cases} \tag{4.8}$$

where $S_1 = \cos^{-1}(\frac{-l+d}{a})$ and $S_2 = \cos^{-1}(\frac{-l}{a})$. The nonlinear model parameters can be obtained either by design during the simulation or estimated via experiment by using the technique presented in ([38]). ℓ and a can be obtained by performing a force curve experiment and assuming the snap-in point a $\ell = 0$. Thus relationships of ω_e Vs z and δ_e Vs z can be plotted using equations (4.6, 4.7, 4.8). These relationships are presented in Chapter 3 for various force parameter models in Figs. 3.11, 3.12, 3.13 and 3.14.

4.4 Deriving Resonant Frequency Sensitivity to changes in Sample Topography

In this section the derivation for the sensitivity of resonant frequency with respect to the sample topography in tapping mode operation is presented. The following equations are used to derive this relationship.

$$\omega_e^2(a) = \omega_0^2 - \frac{2}{a}\Phi_c$$

$$\Phi_c = \begin{cases} 0 & \text{if } a < (l-d) \\ \frac{-1}{2\pi}\left[-\omega_a^2 a(\pi - S_1 - \sin(2S_1)/2) + 2\omega_a^2(l-d)\sin(S_1)\right] & \text{if } l-d \le a < l \\ \frac{-1}{2\pi}\{-\omega_a^2 a(\pi - S_1 - \sin(2S_1)/2) + 2\omega_a^2(l-d)\sin(S_1) \\ \quad + \omega_b^2 a(\pi - S_2 - \sin(2S_2)/2) - 2\omega_b^2 l\sin(S_2)\} & \text{if } a \ge l \end{cases} \tag{4.9}$$

where $S_1 = \cos^{-1}(\frac{-l+d}{a})$, $S_2 = \cos^{-1}(\frac{-l}{a})$, $\sin(S_1) = \frac{\sqrt{(a^2-(-l+d)^2)}}{a}$ and $\sin(S_2) = \frac{\sqrt{(a^2-(-l)^2)}}{a}$. $\sin(S_1)$ and $\sin(S_2)$ will be positive by design since S_1 and S_2 should lie in the third quadrant.

Sensitivity of equivalent resonant frequency with respect to changes in sample topography can be written as

$$\frac{d\omega_e}{dl} = \frac{1}{2\omega_e}\frac{d\omega_e^2}{dl} \tag{4.10}$$

The sensitivity of equivalent resonant frequency with respect to the sample topography will be different in the attractive and repulsive regions of tip-sample interactions. If the cantilever is interacting in the attractive regime then we have

$$\frac{d\omega_e^2(l)}{dl} = \frac{-\omega_a^2}{\pi}\frac{d}{dl}(\cos^{-1}(\frac{-l+d}{a})) + \frac{\omega_a^2}{\pi}\frac{d}{dl}(\frac{(-l+d)\sqrt{a^2-(-l+d)^2}}{a^2}) \tag{4.11}$$

Let $x = \frac{-l+d}{a}$. Then

$$\begin{aligned} \frac{dx}{dl} &= \frac{\partial x}{\partial l} + \frac{\partial x}{\partial a}\frac{\partial a}{\partial l} \\ &= \frac{-1}{a} - \frac{-l+d}{a^2}\frac{\partial a}{\partial l} \end{aligned} \tag{4.12}$$

$$\frac{\partial\omega_e^2(l)}{\partial l} = \frac{\omega_a^2}{\pi}\left[\frac{\partial}{\partial l}(-\cos^{-1}(x) + x\sqrt{1-x^2})\right] \tag{4.13}$$

$$\frac{\partial\omega_e^2(l)}{\partial l} = \frac{-\omega_a^2}{\pi a}(2\sqrt{1-x^2})(1 + x\frac{\partial a}{\partial l}) \quad \sin(S_1) > 0 \tag{4.14}$$

If the cantilever is interacting with the sample in repulsive regime then the sensitivity of

equivalent resonant frequency of the cantilever with respect to the sample topography is given by

$$\begin{aligned}\frac{\partial\omega_e^2(l)}{\partial l} &= \frac{-\omega_a^2}{\pi}\frac{\partial}{\partial l}(\cos^{-1}(\frac{-l+d}{a})) - \frac{\omega_a^2}{\pi}\frac{\partial}{\partial l}(\frac{(-l+d)\sqrt{a^2-(-l+d)^2}}{a^2}) + \frac{2\omega_a^2}{\pi}\frac{\partial}{\partial l}(\frac{(-l+d)\sqrt{a^2-(-l+d)^2}}{a^2}) \\ &\quad + \frac{\omega_b^2}{\pi}\frac{\partial}{\partial l}(\cos^{-1}(\frac{-l}{a})) + \frac{\omega_b^2}{\pi}\frac{\partial}{\partial l}(\frac{(-l)\sqrt{a^2-(-l)^2}}{a^2}) - \frac{2\omega_b^2}{\pi}\frac{\partial}{\partial l}(\frac{(-l)\sqrt{a^2-(-l)^2}}{a^2})\end{aligned} \tag{4.15}$$

Let $y = \frac{-l}{a}$. Then

$$\frac{dy}{dl} = \frac{-1}{a} + \frac{l}{a^2}\frac{\partial a}{\partial l} \tag{4.16}$$

Then using eqn (4.12) and eqn (4.16) we have

$$\begin{aligned}\frac{\partial\omega_e^2(l)}{\partial l} &= \frac{\omega_a^2}{\pi}\left[\frac{\partial}{\partial l}(-\cos^{-1}(x) + x\sqrt{1-x^2})\right] - \frac{\omega_b^2}{\pi}\left[\frac{\partial}{\partial l}(-\cos^{-1}(y) + y\sqrt{1-y^2})\right] \\ &= \frac{-\omega_a^2}{\pi a}(2\sqrt{1-x^2})(1 + x\frac{\partial a}{\partial l}) + \frac{\omega_b^2}{\pi a}(2\sqrt{1-y^2})(1 + y\frac{\partial a}{\partial l}) \\ &\qquad \sin(S_1) > 0; \sin(S_2) > 0\end{aligned} \tag{4.17}$$

The nonlinear model parameters can be obtained either by design during the simulation or estimated via experiment by using the technique presented in ([38]). ℓ and a can be obtained by performing a force curve experiment. Thus relationships of $\frac{\partial\omega_e^2}{\partial l}$ Vs z can be plotted using equation (4.17). Figure 4.2(a) shows the simulation results for the equivalent resonant frequency force curves with changing quality factor of the cantilever. Figure 4.2(b) shows the simulation results for the sensitivity of the equivalent resonant frequency with respect to changing quality factor of the cantilever. It can be seen that as the quality factor of the cantilever decreases, the sensitivity as well as the total change in the cantilever's equivalent resonant frequency during the force curve increases.

4.5 Deriving Equivalent Damping Coefficient Sensitivity to changes in Sample Topography

In this section we will present the derivation for the sensitivity of equivalent damping coefficient with respect to the sample topography in tapping mode operation. This is

done by using the following equations.

$$\begin{aligned}
\delta_e &= \tfrac{c}{2m} + \tfrac{1}{a\omega}\Phi_d \\
&= \begin{cases} 0 & \text{if } a < (l-d) \\ \tfrac{-1}{2\pi} c_a a\omega(\pi - S_1 + \sin(2S_1)/2) & \text{if } l-d \le a < l \\ \tfrac{-1}{2\pi}\left[c_a a\omega(\pi - S_1 + \sin(2S_1)/2) + c_b a\omega(\pi - S_2 + \sin(2S_2)/2)\right] & \text{if } a \ge l \end{cases}
\end{aligned} \tag{4.18}$$

If the cantilever is interacting in the attractive regime then we have

$$\begin{aligned}
\tfrac{\partial \delta_e}{\partial l} &= \tfrac{-1}{2\pi}\tfrac{\partial}{\partial l}(c_a\pi - c_a S_1 + c_a \sin(2S_1)/2) \\
&= -\tfrac{c_a}{2\pi}\left[\tfrac{\partial}{\partial l}(-\cos^{-1}(x) + x\sqrt{1-x^2})\right] \\
&= \tfrac{c_a}{2\pi a}(2\sqrt{1-x^2})(1 + x\tfrac{\partial a}{\partial l}) \quad \sin(S_1) > 0
\end{aligned} \tag{4.19}$$

If the cantilever is interacting with the sample in repulsive regime then we have

$$\begin{aligned}
\tfrac{\partial \delta_e}{\partial l} &= -\tfrac{c_a}{2\pi}\left[\tfrac{\partial}{\partial l}(-\cos^{-1}(x) + x\sqrt{1-x^2})\right] - \tfrac{c_b}{2\pi}\left[\tfrac{\partial}{\partial l}(-\cos^{-1}(y) + y\sqrt{1-y^2})\right] \\
&= \tfrac{c_a}{2\pi a}(2\sqrt{1-x^2})(1 + x\tfrac{\partial a}{\partial l}) + \tfrac{c_b}{2\pi a}(2\sqrt{1-y^2})(1 + y\tfrac{\partial a}{\partial l}) \quad \sin(S_1) > 0; \sin(S_2) > 0
\end{aligned} \tag{4.20}$$

The nonlinear model parameters can be obtained either by design during the simulation or estimated via experiment by using the technique presented in ([38]). ℓ and a can be obtained by performing a force curve experiment. Thus relationships of $\frac{\partial \delta_e}{\partial l}$ Vs z can be plotted using equation (4.20). Figure 4.3(a) shows the simulation results for the equivalent quality factor force curves with changing off-sample quality factor of the cantilever. Figure 4.3(b) shows the simulation results for the sensitivity of the equivalent damping with respect to changing quality factor of the cantilever. It can be seen that as the off-sample quality factor of the cantilever decreases, the sensitivity in the cantilever's equivalent damping during the force curve also increases. This trend is similar to the one we observed in the sensitivity of the equivalent resonant frequency. The sensitivity of the equivalent quality factor decreases with decrease in the off-sample cantilever's quality factor.

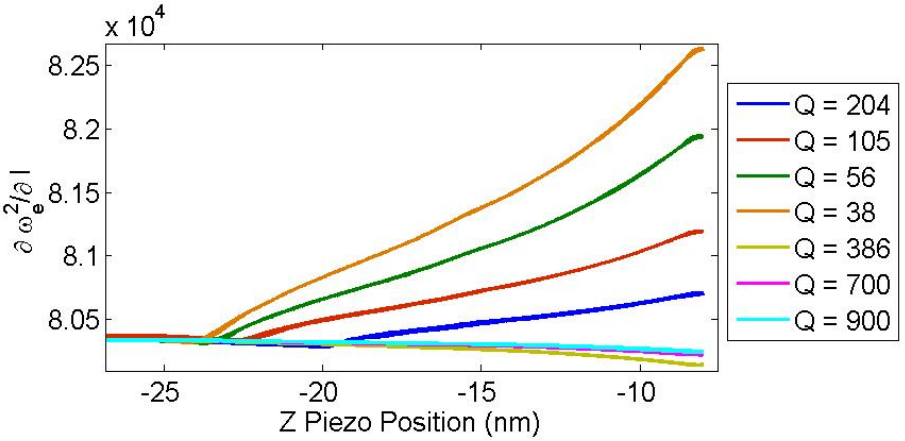

(a)

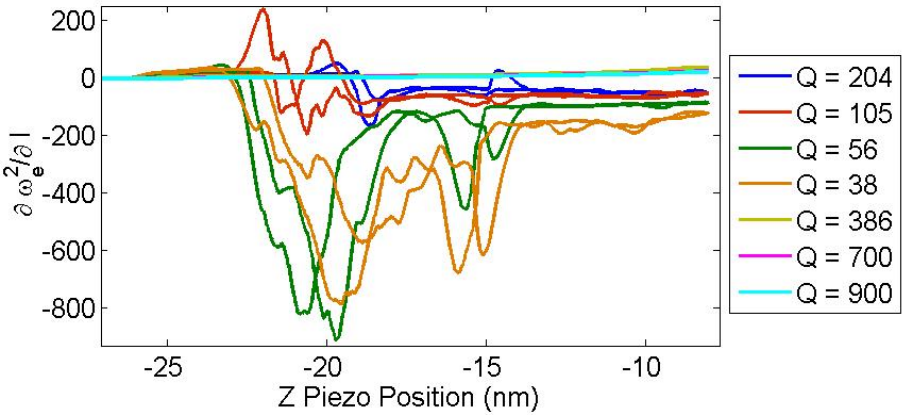

(b)

Figure 4.2: Figure shows simulations results of (a) equivalent resonant frequency force curves obtained from the REEP algorithm (b) Sensitivity of the equivalent resonant frequency during these force curves. Each curve is obtained for a particular off-sample quality factor of the cantilever. Seven such plots are obtained for varying off-sample cantilever quality factor as detailed in the legend. It is shown through these plots that the net change in the equivalent resonant frequency during a force curve increases with decrease in the off-sample cantilever quality factor. The sensitivity of equivalent resonant frequency with respect to the sample topography increases as well.

4.6 Deriving Amplitude Sensitivity to changes in Sample Topography

As explained in the modeling section, the equivalent cantilever model in steady state at any instance can be represented by $G(j\omega) = \frac{\omega_0^2}{s^2+2\delta_e s+\omega_e^2}$. If the cantilever excitation is $g(t) = A_0 \cos(\omega t)$ then the cantilever amplitude in steady state is given by
$a = \frac{\omega_0^2 A_0}{\sqrt{(\omega_e^2-\omega^2)^2+4\delta_e^2\omega^2}}$.

Let $D = (\omega_e^2 - \omega^2)^2 + 4\delta_e^2\omega^2$. Then one can obtain

$$\begin{aligned} \frac{\partial a}{\partial l} &= -\frac{\omega_0^2 A_0}{2D^{3/2}}\left[\frac{\partial D}{\partial \omega_e}.\frac{\partial \omega_e}{\partial l} + \frac{\partial D}{\partial \delta_e}.\frac{\partial \delta_e}{\partial l}\right] \\ &= -\frac{A_0\omega_0^2}{2D^{3/2}}.\left[4(\omega_e^2-\omega^2)\omega_e\frac{\partial \omega_e}{\partial l} + 8\delta_e\omega^2.\frac{\partial \delta_e}{\partial l}\right] \end{aligned} \tag{4.21}$$

If the cantilever is interacting in the repulsive regime then the amplitude sensitivity can be calculated using eqn 4.17 and eqn 4.20. Assume that $\sin(S_1) > 0$ and $\sin(S_2) > 0$. Then

$$\frac{\partial a}{\partial l} = \frac{A_1+A_2}{1-A_1x-A_2y} \tag{4.22}$$

where $A_1 = -\frac{A_0\omega_0^2}{2D^{3/2}}(2\sqrt{1-x^2})(\frac{-2\omega_a^2(\omega_e^2-\omega^2)}{a\pi} + \frac{8\delta_e\omega^2 c_a}{2\pi a})$ and
$A_2 = -\frac{A_0\omega_0^2}{2D^{3/2}}(2\sqrt{1-y^2})(\frac{2\omega_b^2(\omega_e^2-\omega^2)}{a\pi} + \frac{8\delta_e\omega^2 c_b}{2\pi a})$.
Similarly if the cantilever is interacting with the sample in attractive regime then the amplitude sensitivity to changes in sample topography is given by

$$\frac{\partial a}{\partial l} = \frac{A_1}{1-A_1x} \tag{4.23}$$

The nonlinear model parameters can be obtained either by design during the simulation or estimated via experiment by using the technique presented in (). ℓ and a can be obtained by performing a force curve experiment. Thus relationships of $\frac{\partial a}{\partial l}$ Vs z can be plotted using equation (4.22). Figure 4.4(a) shows the simulation results for the amplitude force curves with changing off-sample quality factor of the cantilever. Figure 4.4(b) shows the simulation results for the sensitivity of the amplitude with respect to changing off-sample quality factor of the cantilever. The amplitude sensitivity of the cantilever remains constant at 1 even with changes in off-sample quality factor. This

is in agreement with the work reported in [45]. Amplitude sensitivity is expected to reduce for non-compliant and soft surfaces with reduced off-sample quality factors of the sample. But for large range of samples it remains constant at 1. For completeness sake, Figures (4.5) presents the phase force curves with changes in the off-sample cantilever quality factor. As quality factor decreases, the net repulsive part of tip-sample interaction grows and net attractive part reduces as expected from literature.

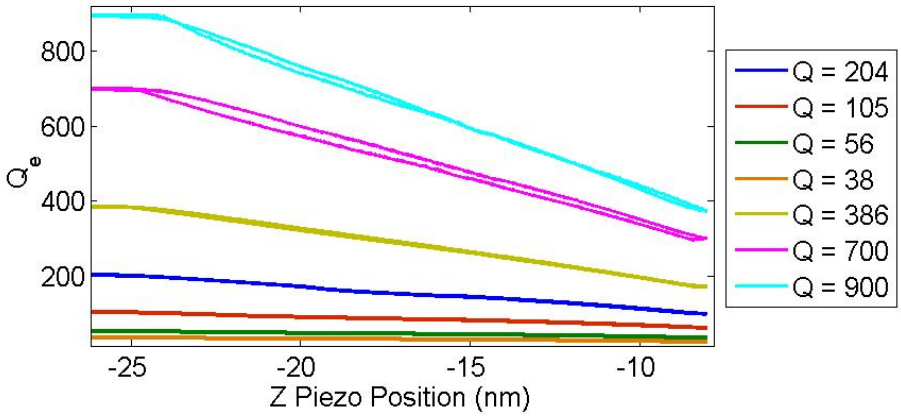

(a)

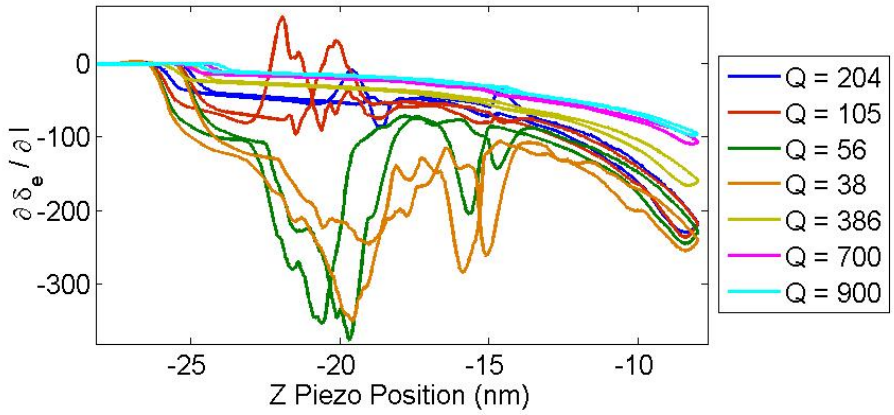

(b)

Figure 4.3: Figure shows simulations results of (a) equivalent quality factor force curves obtained from the REEP algorithm (b) Sensitivity of the equivalent damping during these force curves. Each curve is obtained for a particular off-sample quality factor of the cantilever. Seven such plots are obtained for varying off-sample cantilever quality factor as detailed in the legend. The net change in the quality factor during a force curve decreases with a decrease in the off-sample cantilever quality factor even though the sensitivity of the equivalent cantilever damping has an increasing trend.

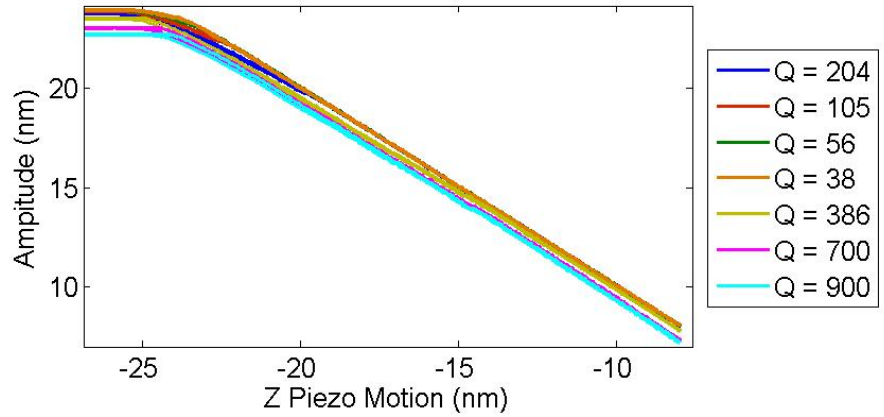

(a)

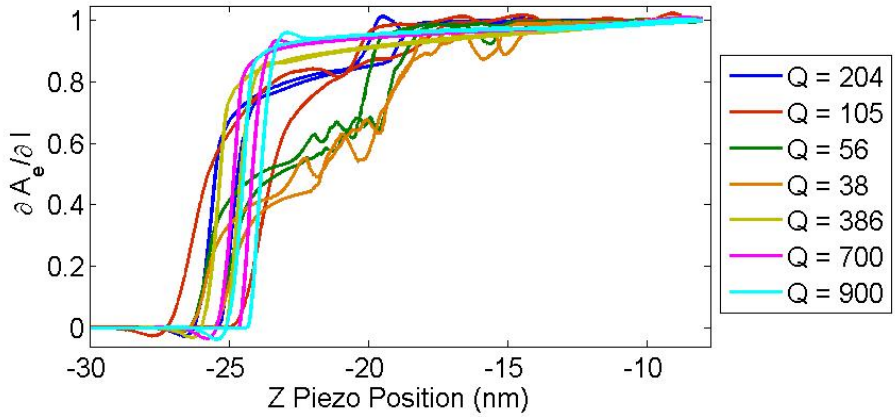

(b)

Figure 4.4: Figure shows simulations results of (a) amplitude force curves (b) Sensitivity of the amplitude during these force curves. Each curve is obtained for a particular off-sample quality factor of the cantilever. Seven such plots are obtained for varying off-sample cantilever quality factor as detailed in the legend. Amplitude sensitivity remains fixed at one as expected from the reporting in the literature. The amplitude sensitivity is reported to reduce with decreasing off-sample cantilever quality factor for non-compliant surfaces.

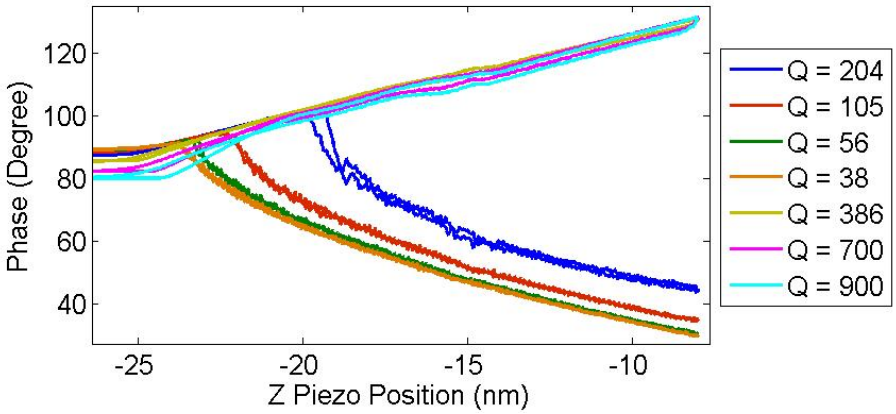

Figure 4.5: Figure shows simulations results of phase force curves. Each curve is obtained for a particular off-sample quality factor of the cantilever. Seven such plots are obtained for varying off-sample cantilever quality factor as detailed in the legend. The net attractive regime decreases and net repulsive regime increases with reducing off-sample cantilever quality factor.

4.7 Experimental Results

In this section, the theory developed in the previous sections is validated through experiments. The cantilever used for these experiments was an AC-240TS cantilever from Asylum Research. It has an off-sample resonant frequency of 80328 Hz and a quality factor of 189.32. The force curves were done on a mica sheet. The quality factor of the off-sample cantilever is varied by active Q-control circuit. Amplitude and phase force curves were obtained by demodulating the cantilever deflection signal. Corresponding amplitude and phase sensitivites were obtained by applying the difference method on the amplitude and phase force curve. Equivalent resonant frequency and quality factor force curves were obtained by providing the cantilever excitation and cantilever deflection to the REEP algorithm. Corresponding sensitivites were obtained by applying difference method on these estimated force curves.

Figures (4.6 (a) and (b)) show the experimentally obtained amplitude force curves and its sensitivity with respect to the sample topography. As expected, the amplitude sensitivity remains constant at 1 with changes in the off-sample quality factor of the

cantilever since these force curves are done on a mica sheet.

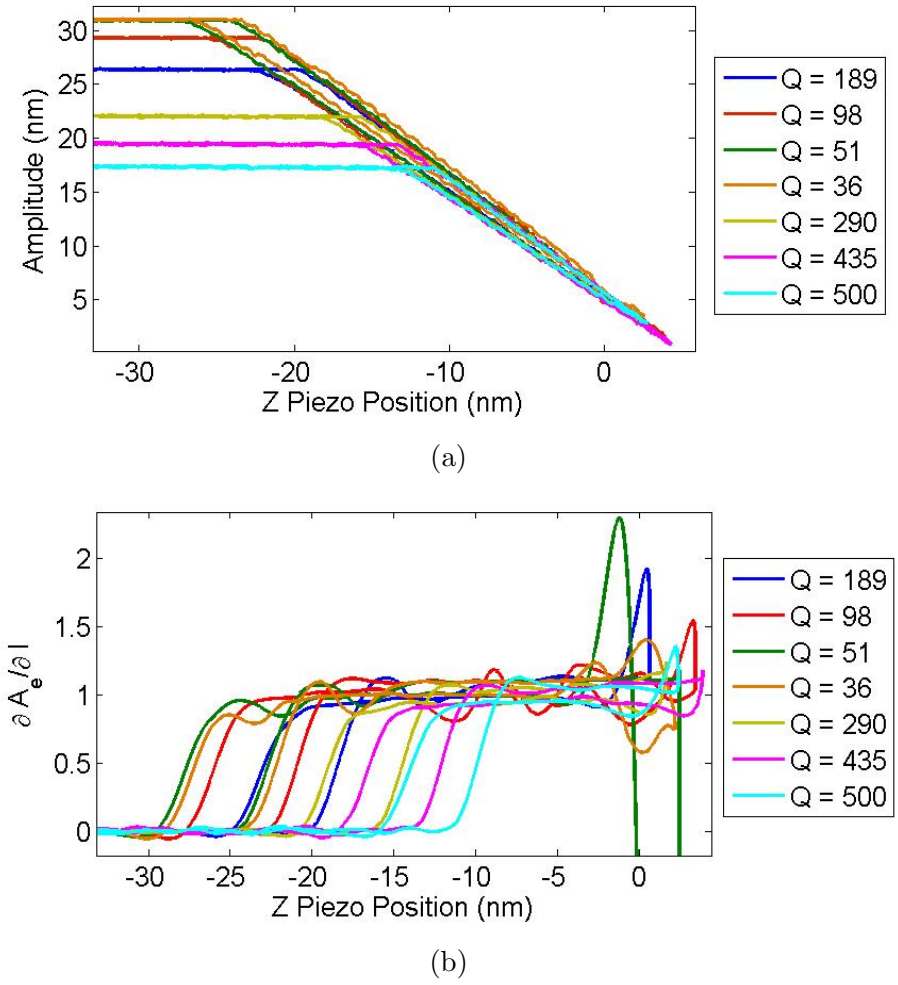

Figure 4.6: Figure shows experimental results of (a) amplitude force curves (b) Sensitivity of the amplitude during these force curves. Each curve is obtained for a particular off-sample quality factor of the cantilever. Seven such plots are obtained for varying off-sample cantilever quality factor as detailed in the legend. Amplitude sensitivity remains fixed at one as expected from the reporting in the literature. The amplitude sensitivity is reported to reduce with decreasing off-sample cantilever quality factor for non-compliant surfaces.

Figure (4.7 (a) and (b)) show the experimentally obtained equivalent resonant frequency and its sensitivity with respect to changes in sample topography. It can be seen that the net change in the equivalent resonant frequency during force curves increases with decrease in off-sample cantilever quality factor. Moreover, its sensitivity also increases with decrease in the quality factor as expected from the analytical plots.
Figure (4.8 (a) and (b)) show the experimentally obtained equivalent quality factor and its sensitivity with respect to the sample topography. It can be seen that the net change in the equivalent quality factor reduces with reducing off-sample cantilever quality factor. Also its sensitvity decreases with reducing off-sample cantilever quality factor as expected from analytical results.
For competeness sake, we are also including the phase force curves for these experiments. Figure (4.9 (a) and (b)) shows the phase force curves and its sensitivity with respect to the sample topography for changing off-sample cantilever quality factor. It can be seen the the net attractive regime decreases and net repulsive regime increases with decrease in the off-sample cantilever quality factor as reported in literature previously.

4.8 Conclusion

Thus in this chapter, we derived the expressions for the equivalent resonant frequency and the equivalent damping of the cantilever assuming a piecewise linear tip-sample force interaction model. These expressions were used to obtain the expressions for the sensitivity of the equivalent resonant frequency and quality factor and amplitude with respect to changes in sample topography. The behavior of these equations were studied with changing off-sample cantilever quality factor. It was shown that trends in the sensitivity of equivalent resonant frequency and equivalent damping of the cantilever are opposite to that of the amplitude sensitivity that is usually used for sensing at nanoscale. These sensitivities increase with reducing off-sample cantilever quality factor. Hence these signals can potentially be used for imaging under liquid and in integrated applications with low Q sensors. These trends were confirmed through exhaustive experiments on a mica sheet.

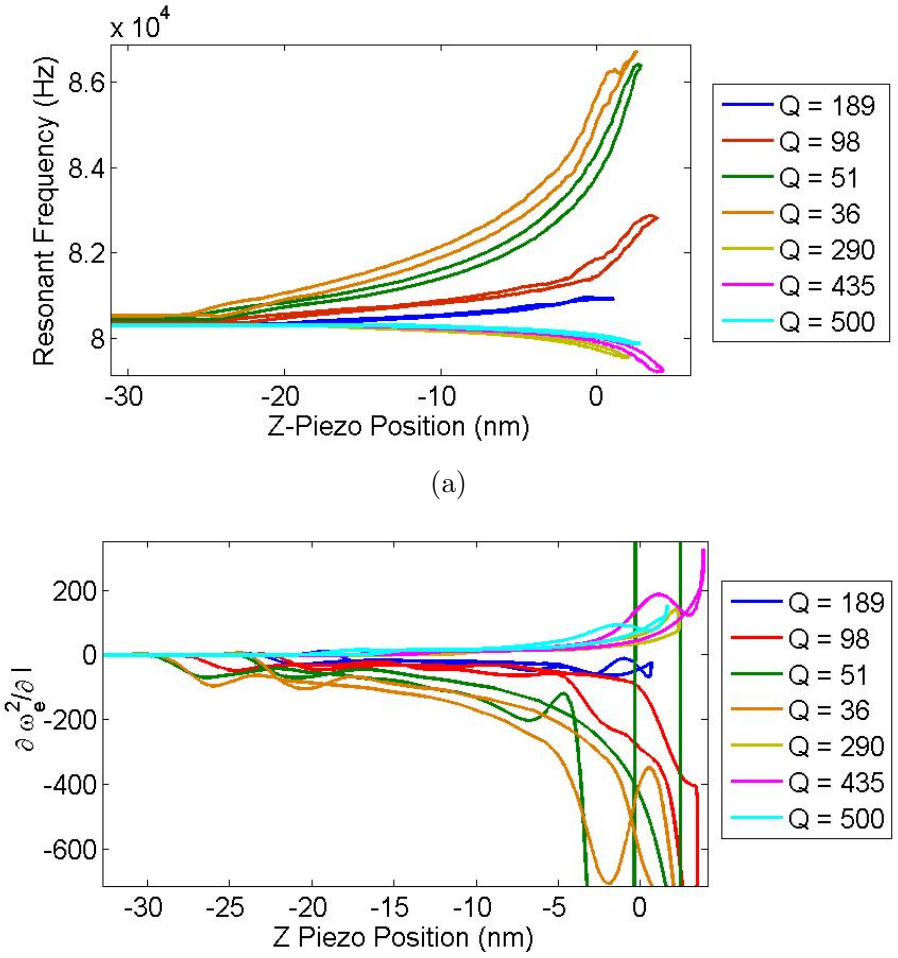

Figure 4.7: Figure shows experimental results of (a) equivalent resonant frequency force curves obtained from the REEP algorithm (b) Sensitivity of the equivalent resonant frequency during these force curves. Each curve is obtained for a particular off-sample quality factor of the cantilever. Seven such plots are obtained for varying off-sample cantilever quality factor as detailed in the legend. It is shown through these plots that the net change in the equivalent resonant frequency during a force curve increases with decrease in the off-sample cantilever quality factor. The sensitivity of equivalent resonant frequency with respect to the sample topography increases.

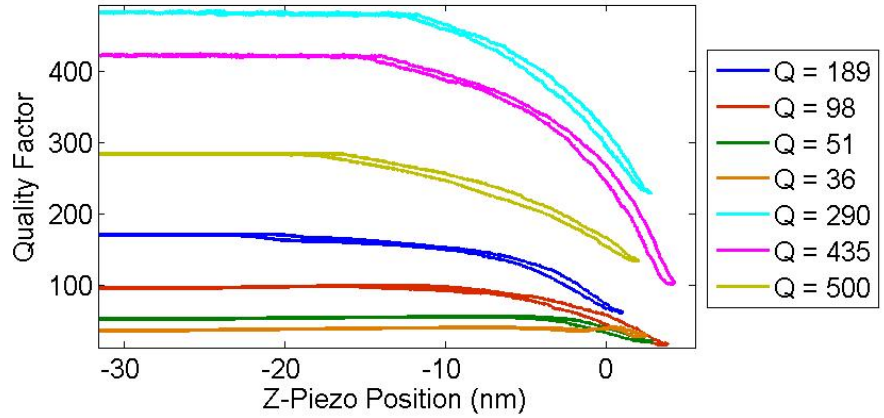

(a)

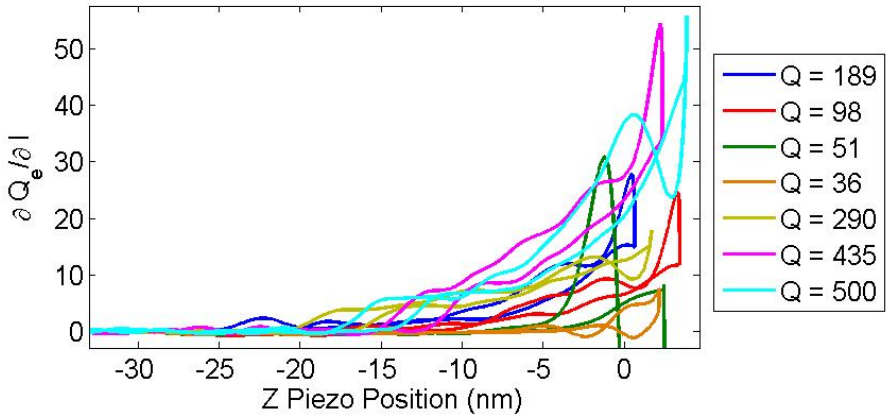

(b)

Figure 4.8: Figure shows experimental results of (a) equivalent quality factor force curves obtained from the REEP algorithm (b) Sensitivity of the equivalent quality factor during these force curves. Each curve is obtained for a particular off-sample quality factor of the cantilever. Seven such plots are obtained for varying off-sample cantilever quality factor as detailed in the legend. The net change in the quality factor during a force curve and its sensitivity with respect to sample topography decreases with a decrease in the off-sample cantilever quality factor.

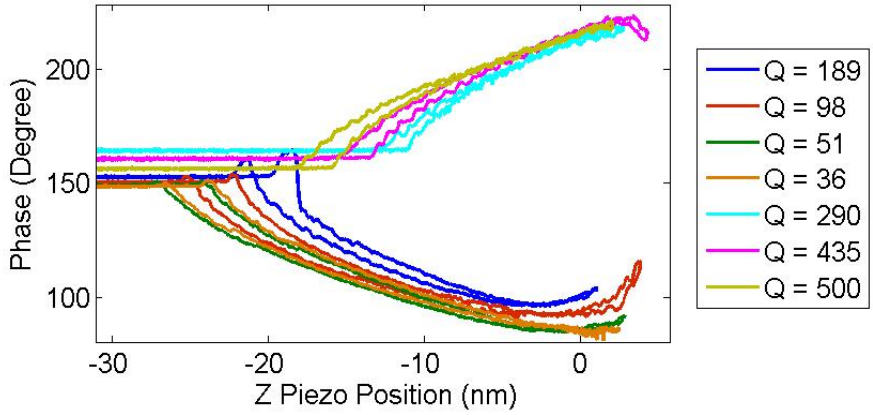

(a)

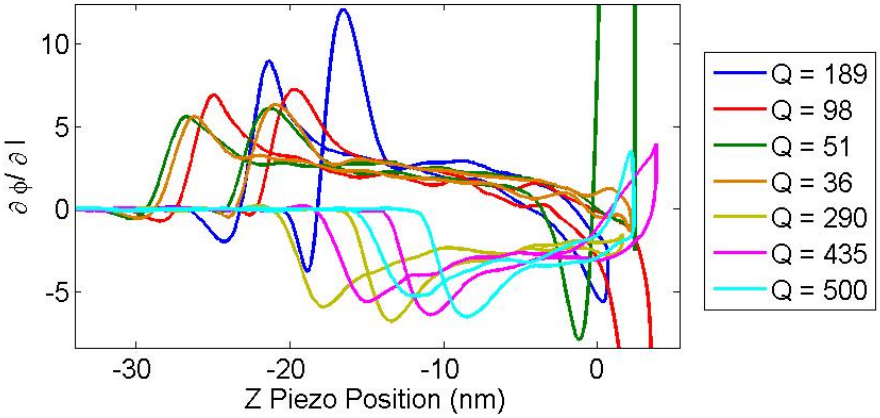

(b)

Figure 4.9: Figure shows experimental results of (a) phase force curves (b) Phase sensitivity with respect to sample topography. Each curve is obtained for a particular off-sample quality factor of the cantilever. Seven such plots are obtained for varying off-sample cantilever quality factor as detailed in the legend. The net attractive regime decreases and net repulsive regime increases with reducing off-sample cantilever quality factor.

Chapter 5

Observer Based Tapping Mode AFM

5.1 Introduction

Tapping mode or intermittent contact mode atomic force microscopy is one of the most prevalent mode for imaging topography of samples at nanoscale. It is specially preferred for under fluid imaging or imaging of soft samples because it exerts lower forces on the sample due to reduced lateral and frictional forces.

In tapping mode operation, the cantilever is typically excited by a single sinusoid whose frequency is chosen to be at or near the resonance of first mechanical mode of the cantilever. Amplitude or phase of the excitation frequency is typically used as the feedback signals to maintain a constant tip-sample interaction. Amplitude of the cantilever deflection is dependent on the cantilever beam dynamics. If the quality factor of the cantilever is high, which is preferred to obtain higher sensitivity and lower forces on the sample, then any transients in the cantilever amplitude takes a long time to decay. This reduces imaging speeds considerably. Moreover image interpretation is very difficult while the cantilever is in transients.

To detect a sudden increase in the topographic profile, observer based methods were suggested in ([49]), where it was experimentally demonstrated that detection bandwidths could be increased by three orders of magnitude by observing the innovation signal of the output. Observer error rms based methods to detect and reduce sudden

reduction in topographic profile, which leads to condition of probe-loss, were presented in ([50, 51]). Thus it is demonstrated in the earlier works that the rms of innovation error is a higher bandwidth imaging signal as compared to the amplitude signal where sudden topographic transitions, either increasing or decreasing, can be detected or imaged even while the cantilever is in transients. The observer that was used in these studies was based on the off-sample cantilever dynamics.

This chapter discusses that by appropriate choice of the observer model or the reference model, which could be different from the off-sample cantilever dynamics, one can obtain a handle on the trade off between the bandwidth and sensitivity of the rms error signal to changes in the equivalent cantilever model, for imaging purposes. It will be shown analytically that as the observer model moves "farther" from the nominal plant model, there is an increase in the sensitivity of the rms error signal with respect to the changes in the plant model. Signal to noise ratio also improves with similar trends. The transients of the observer error are dependent on the observer dynamics only as long as the observer and the plant model are same. In case they are different, then the transients of the error signal will be dominated by the plant dynamics itself. Transients have a better SNR when the observer model is close to the plant model. Their contributions in the error signal can be controlled by an appropriate choice of the observer model. Thus by appropriate choice of the observer model and the observer gains one can find a sweet spot where the sensitivity of the rms of error signal to changes in the equivalent plant model is high and the transients are still detectable in the signal. It must be noted that such handles are not available for amplitude and phase signals based imaging.

5.2 Analyzing Innovation Error Sensitivity to changes in Plant Model

In this section, we assume that there is a second order linear plant with time varying parameters whose dynamics is given by $G(s) = \frac{c_1 s + c_0}{s^2 + b_1 s + b_0}$. In state space this can be

represented as

$$\begin{aligned} \dot{x} &= Ax + Bg + B_1\eta \\ y &= Cx + \nu \\ x(0) &= x_0 \end{aligned} \tag{5.1}$$

where $A = \begin{bmatrix} 0 & -b_0 \\ 1 & -b_1 \end{bmatrix}$, $B = \begin{bmatrix} c_0 \\ c_1 \end{bmatrix}$, $C = \begin{bmatrix} 0 & 1 \end{bmatrix}$, $D = 0$ and $B_1 = \begin{bmatrix} f_0 \\ f_1 \end{bmatrix}$. The coefficients c_1, c_0, b_1 and b_0 of the plant are varying with time. Such a variation might be due to a change in the sensor model due to changes in external environment for which it is sensitive. For instance, if a cantilever beam shaped sensor is being used for mass sensing application, then as external agents deposit on the beam, the mass of the cantilever will change. Thus the sensor model will change with time.

We then build an observer to estimate the states of the plant. Since the plant has time varying coefficients, the observer model cannot be same as the plant dynamics as is usually the case. Moreover, the idea here is not to estimate plant states accurately. The idea is to synthesize a signal which selectively amplifies the changes in the plant model for sensing purposes.

Let the observer dynamics in state space be represented as

$$\begin{aligned} \dot{\hat{x}} &= A_k\hat{x} + B_k g + L(y - \hat{y}) \\ \hat{y} &= C\hat{x} \\ \hat{x}(0) &= \hat{x}_0 \end{aligned} \tag{5.2}$$

where $A_k = \begin{bmatrix} 0 & -b_0^k \\ 1 & -b_1^k \end{bmatrix}$, $B_k = \begin{bmatrix} c_0^k \\ c_1^k \end{bmatrix}$ and $L = \begin{bmatrix} L_1 \\ L_2 \end{bmatrix}$.

The error signal is defined as $e = (x - \hat{x})$. The error dynamics can be written as

$$\begin{aligned} \dot{e} &= (A_k - LC)e + (A - A_k)x + (B - B_k)g + B_1\eta - L\nu \\ e_1 &= Ce \\ e(0) &= x_0 - \hat{x}(0) \end{aligned} \tag{5.3}$$

If plant and observer model are same then

$$\dot{e} = (A - LC)e + B_1\eta - L\nu \tag{5.4}$$

which is the standard observer error equation.

5.2.1 Steady Steady Analysis of Error Signal when Plant and Observer Models are Different

In steady state, the initial condition response of eqn 5.3 is zero since we assume that the matrix $(A_k - LC)$ is Hurwitz and it has four inputs x, g, η and ν. Thus resultant error output will have contributions from four transfer functions.

- $T.F.1_{x\to e_1}$: Transfer function from x to e
- $T.F.2_{g\to e_1}$: Transfer function from g to e
- $T.F.3_{\eta\to e_1}$: Transfer function from η to e
- $T.F.4_{\nu\to e_1}$: Transfer function from ν to e

These transfer functions can be evaluated from eqn 5.3. These transfer functions are

$$\begin{aligned} T.F.1_{x\to e_1} &= C(sI-(A_k-LC))^{-1}(A-A_k) \\ &= \frac{\begin{bmatrix} 0 & (-b_0+b_0^k)+s(-b_1+b_1^k) \end{bmatrix}}{s^2+(b_1^k+L_2)s+(b_0^k+L_1)} \end{aligned} \tag{5.5}$$

$$\begin{aligned} T.F.2_{g\to e_1} &= C(sI-(A_k-LC))^{-1}(B-B_k) \\ &= \frac{(c_0-c_0^k)+s(c_1-c_1^k)}{s^2+(b_1^k+L_2)s+(b_0^k+L_1)} \end{aligned} \tag{5.6}$$

$$\begin{aligned} T.F.3_{\eta\to e_1} &= C(sI-(A_k-LC))^{-1}B_1 \\ &= \frac{f_0+f_1 s}{s^2+(b_1^k+L_2)s+(b_0^k+L_1)} \end{aligned} \tag{5.7}$$

$$\begin{aligned} T.F.4_{\nu\to e_1} &= -C(sI-(A_k-LC))^{-1}L \\ &= \frac{-L_1-sL_2}{s^2+(b_1^k+L_2)s+(b_0^k+L_1)} \end{aligned} \tag{5.8}$$

From input-output point of view (see Figure 5.1), there are three inputs to the system g, η and ν. Therefore, we need to evaluate two more transfer functions.

- $T.F.5_{g\to x}$: Transfer function from g to x
- $T.F.6_{\eta\to x}$: Transfer function from η to x

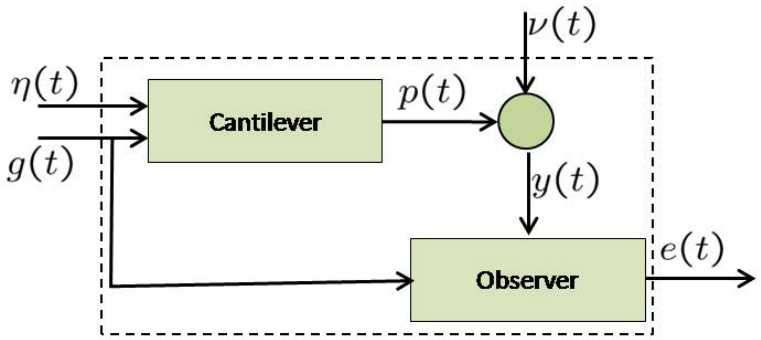

Figure 5.1: Input Output Model of a plant-observer system. Cantilever excitation ($g(t)$), thermal noise ($\eta(t)$) and measurement noise ($\nu(t)$) are three independent inputs to the system and output is the innovation signal ($e(t)$).

$$\begin{aligned} T.F.5_{g\to x} &= (sI-A)^{-1}B \\ &= \frac{1}{s^2+b_1s+b_0}\begin{bmatrix} c_0(s+b_1)-b_0c_1 \\ c_0+sc_1 \end{bmatrix} \end{aligned} \tag{5.9}$$

$$\begin{aligned} T.F.6_{\eta\to x} &= (sI-A)^{-1}B_1 \\ &= \frac{1}{s^2+b_1s+b_0}\begin{bmatrix} f_0(s+b_1)-b_0f_1 \\ f_0+sf_1 \end{bmatrix} \end{aligned} \tag{5.10}$$

Thus total contribution due to g at e_1 is

$$T.F.1\times T.F.5+T.F.2 = \frac{(c_0+sc_1)\left[(-b_0+b_0^k)+s(-b_1+b_1^k)\right]+(s^2+b_1s+b_0)\left[(c_0-c_0^k)+s(c_1-c_1^k)\right]}{(s^2+b_1s+b_0)(s^2+(b_1^k+L_2)s+(b_0^k+L_1))} \tag{5.11}$$

Thus the distance of the plant model from observer model reflects as coefficients of zeros of this transfer function. It must be noted that this structure is created only when the plant and observer model are different. If these models are same then this transfer function is identically zero indicating perfect cancellation of the plant input $g(t)$.
Total contribution of η at e_1 is

$$T.F.1\times T.F.6+T.F.3 = \frac{f_0+f_1s}{s^2+(b_1^k+L_2)s+(b_0^k+L_1)}\{1+\frac{(-b_0+b_0^k)+s(-b_1+b_1^k)}{s^2+b_1s+b_0}\} \tag{5.12}$$

Thus $e(t)$ has components due to $g(t)$, $\eta(t)$ and $\nu(t)$.

5.2.2 Application: Cantilever-Sample System in Tapping Mode Operation

In dynamic mode operation, when the cantilever is interacting with the sample, it can be viewed as a linear second order system with time varying parameters ([52]). These parameters change depending on the material properties. As shown in ([52]), even though the input-output characterization of cantilever yields a zero in transfer function, this zero is seen to be independent of sample properties. Thus the equivalent cantilever can be represented as

$$G(s) \quad = \quad \frac{c_1 s + c_0}{s^2 + (\omega_e/Q_e)s + \omega_e^2} \tag{5.13}$$

where c_1 and c_0 are fixed and ω_e and Q_e vary depending on sample properties. Thus $A = \begin{bmatrix} 0 & -\omega_e^2 \\ 1 & -\omega_e/Q_e \end{bmatrix}$, $B = \begin{bmatrix} c_0 \\ c_1 \end{bmatrix}$, $C = \begin{bmatrix} 0 & 1 \end{bmatrix}$ and $D = 0$ for this system. By using derivations presented in previous section, one can show that the transfer function from $g(t) \rightarrow e_1(t)$, where $g(t)$ is the cantilever excitation and $e_1(t)$ is the error signal from the observer, is given by

$$T.F._{g \rightarrow e_1} \quad = \quad \frac{(c_0 + c_1 s)(s(\frac{\omega_k}{Q_k} - \frac{\omega_e}{Q_e}) + (\omega_k^2 - \omega_e^2))}{(s^2 + (\omega_e/Q_e)s + \omega_e^2)(s^2 + s(\omega_k/Q_k + L_2) + (\omega_k^2 + L))} \tag{5.14}$$

Thus if $g(t) = A_0 \sin(\omega t)$ then we have $A_e = \left[\frac{(\omega_k^2 - \omega_e^2)^2 + \omega^2(\omega_k/Q_k - \omega_e/Q_e)^2}{(\omega_k^2 + L_1 - \omega^2)^2 + \omega^2(\omega_k/Q_k + L_2)^2}\right]^{1/2} A_1$ where $A_1 = (\frac{c_0^2 + \omega^2 c_1^2}{(\omega_e^2 - \omega^2)^2 + \omega^2\omega_e^2/Q_e^2})^{1/2} A_0$. Thus in steady state, the error signal will be $e_1(t) = A_e \sin(\omega t + \theta_e)$ where θ_e is the resultant phase between $g(t)$ and $e_1(t)$.

The signal of interest for imaging is the rms of the error signal, $e_1(t)$. Thus, assuming $g(t)$, $\eta(t)$ and $\nu(t)$ to be uncorrelated we obtain

$$RMS_{e_1} \quad = \quad E\left[e_1^2\right]^{1/2} \quad = \quad A_e/\sqrt{2} + \sqrt{\sigma_{\eta e}^2} + \sqrt{\sigma_{\nu e}^2} \tag{5.15}$$

where $\sigma_{\eta e}^2$ is the resultant variance due to thermal noise and $\sigma_{\nu e}^2$ is the resultant output variance due to measurement noise.

5.2.3 Sensitivity of Steady State RMS to changes in Equivalent Cantilever Parameters

Since we want to use the rms signal of error output from the observer for imaging, we are interested in analyzing the sensitivity of this signal with respect to changes in

the plant model. Plant model changes in terms of shifts in its resonant frequency and quality factor due to changes in material properties. We would like to maximize this sensitivity with respect to the changes in model parameters ω_e and Q_e. In this chapter, we will derive the expressions for this sensitivity and study it's behavior with respect to different choices of observer model.

Changes in error signal output variance due to input $g(t)$ can be represented as

$$dA_e^2 = \frac{\partial A_e^2}{\partial \omega_e} d\omega_e + \frac{\partial A_e^2}{\partial Q_e} dQ_e \tag{5.16}$$

where

$$\begin{aligned} A_e^2 &= P_1.P_2 \\ P_1 &= \frac{(c_0^2+\omega^2 c_1^2)A_0^2}{(\omega_k^2+L_1-\omega^2)^2+\omega^2(\omega_k/Q_k+L_2)^2} \\ P_2 &= \frac{(\omega_k^2-\omega_e^2)^2+\omega^2(\omega_k/Q_k-\omega_e/Q_e)^2}{D} \\ D &= (\omega_e^2-\omega^2)^2+\frac{\omega^2\omega_e^2}{Q_e^2} \end{aligned} \tag{5.17}$$

We can express the partial sensitivities as

$$\begin{aligned} \frac{\partial A_e^2}{\partial \omega_e} &= P_1 \frac{\partial P_2}{\partial \omega_e} \\ \frac{\partial P_2}{\partial \omega_e} &= \frac{D\{-4\omega_e(\omega_k^2-\omega_e^2)-(2\omega^2/Q_e)(\omega_k/Q_k-\omega_e/Q_e)\}-\{(\omega_k^2-\omega_e^2)^2+\omega^2(\omega_k/Q_k-\omega_e/Q_e)^2\}\{4\omega_e(\omega_e^2-\omega^2)+2\omega_e\omega^2/Q_e^2\}}{D^2} \end{aligned} \tag{5.18}$$

$$\begin{aligned} \frac{\partial A_e^2}{\partial Q_e} &= P_1 \frac{\partial P_2}{\partial Q_e} \\ \frac{\partial P_2}{\partial Q_e} &= \frac{D\{(2\omega^2\omega_e/Q_e^2)(\omega_k/Q_k-\omega_e/Q_e)\}-\{(\omega_k^2-\omega_e^2)^2+\omega^2(\omega_k/Q_k-\omega_e/Q_e)^2\}\{-2\omega^2\omega_e^2/Q_e^3\}}{D^2} \end{aligned} \tag{5.19}$$

Since Q_k and ω_k can technically belong to entire real space, we would like to define a meaningful subspace over which we will vary the observer parameters to study the behavior of equations 5.18 and 5.19 and compare the trends with experimental data. To define this subspace, we perform a force curve experiment in tapping mode operation. In this experiment, a ramp is applied at the z-piezo such that the tip-sample separation first reduces linearly and then increases linearly. This experiment is done at 1 Hz input frequency to the z-piezo. The cantilever amplitude varies from free air amplitude to a very small value close to zero. Using REEP method as reported in ([52]), we can calculate the equivalent plant parameters, ω_e and Q_e, for each point during the force curve. Thus we have $[Q_{e_1}, Q_{e_2}]$ and $[\omega_{e_1}, \omega_{e_2}]$ where Q_{e_1} is the minimum equivalent

quality factor during the force curve, Q_{e_2} is the maximum quality factor, ω_{e_1} is the minimum resonant frequency and ω_{e_2} is the maximum resonant frequency. In the current work, the simulation results presented are based on a AC-240TS cantilever from Asylum Research. This cantilever had a off-sample resonant frequency of 70692.44 and quality factor of 182.564.

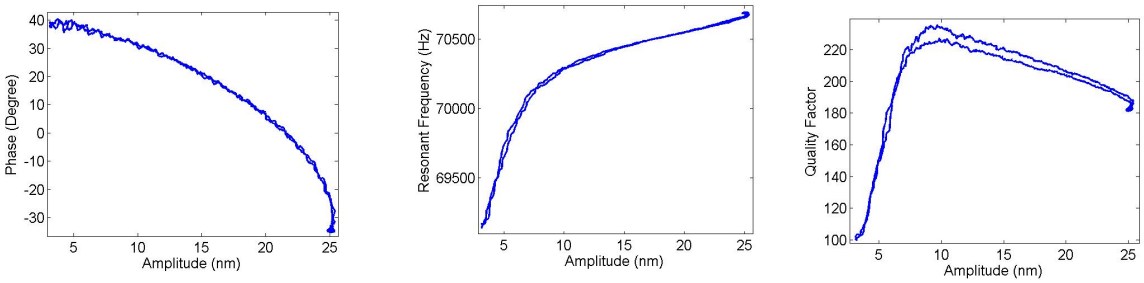

(a) (b) (c)

Figure 5.2: (a) Phase (b) Equivalent resonant frequency and (c) Equivalent quality factor force curves of the cantilever with respect to amplitude. Plots (b) and (c) provide (ω_e, Q_e) pairs for each amplitude point and thus each tip-sample separation during the force curve. This is used to define a direction of analysis in (ω, Q) space for analysis.

Figure 5.2(a),(b) and (c) show the phase, equivalent resonant frequency and equivalent quality factor force curves for this cantilever. Even though this is a 2-D space over (Q_e, ω_e), we can still define a direction along which the cantilever model changes during the force curve i.e. $(Q_{free}, \omega_{efree})$ till (Q_{low}, ω_{elow}). Here Q_{free} and ω_{efree} are the cantilever parameters in free air and Q_{low} and ω_{elow} are the cantilever parameters when the amplitude is minimum.

Figure 5.3 shows the variations in the rms of the error signal in the 2-D space when the nominal plant model is the off-sample cantilever model. Figure 5.4 and 5.5 indicate the sensitivity $\frac{\partial A_e^2}{\partial \omega_e}$ and $\frac{\partial A_e^2}{\partial Q_e}$ where the nominal cantilever parameter model is $(Q_{free}, \omega_{efree})$ and observer model is changing at each point in the matrix. It can be seen from these plots that the minima is reached when the observer model and the off-sample cantilever model coincides. As the observer model moves "farther" from the plant model these curves increase in value.

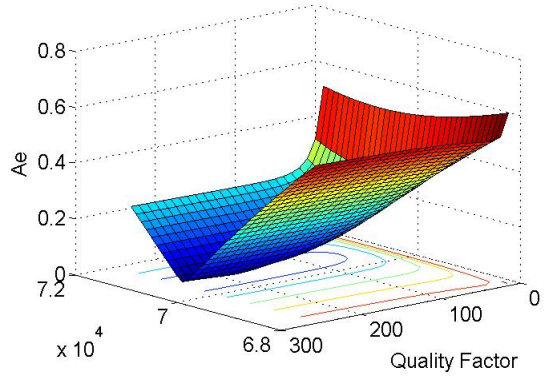

Figure 5.3: 2-D plots for RMS of the error signal. The nominal cantilever model about which these sensitivities are plotted is off-sample cantilever model. Each point in the 2-D space represents a particular combination for the observer model. It can be seen from the plots that the minima is obtained when the observer model coincides with the off-sample cantilever model.

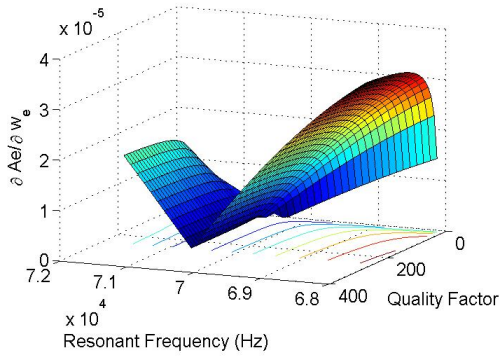

Figure 5.4: 2-D plots for sensitivity of the error rms to changes in the equivalent resonant frequency of the cantilever. The nominal cantilever model about which these sensitivities are plotted is off-sample cantilever model. Each point in the 2-D space represents a particular combination for the observer model. It can be seen from the plots that the minima is obtained when the observer model coincides with the off-sample cantilever model.

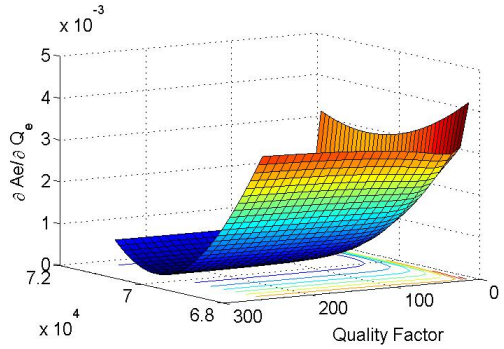

Figure 5.5: 2-D plots for sensitivity of the error rms to changes in the equivalent quality factor of the cantilever. The nominal cantilever model about which these sensitivities are plotted is off-sample cantilever model. Each point in the 2-D space represents a particular combination for the observer model. It can be seen from the plots that the minima is obtained when the observer model coincides with the off-sample cantilever model.

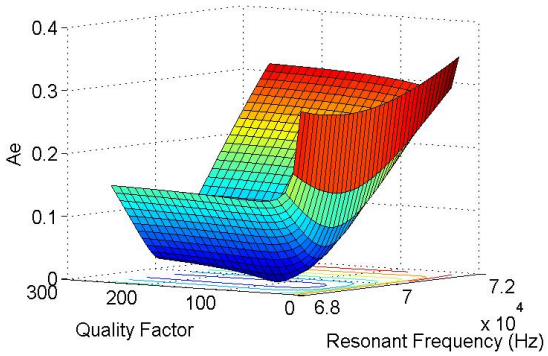

Figure 5.6: 2-D plots for RMS of the error signal. The nominal cantilever model about which these sensitivities are plotted is on-sample cantilever model corresponding to a very low setpoint amplitude. Each point in the 2-D space represents a particular combination for the observer model. It can be seen from the plots that the minima is obtained when the observer model coincides with the on-sample cantilever model.

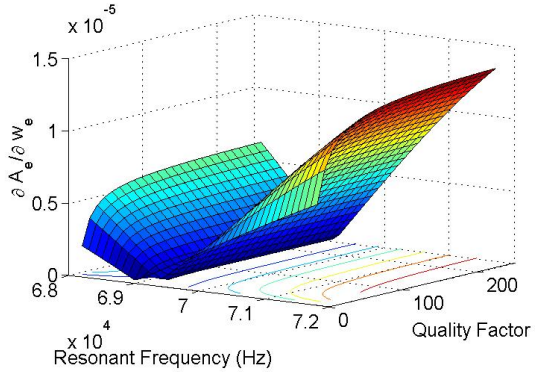

Figure 5.7: 2-D plots for sensitivity of the error rms to changes in the equivalent resonant frequency of the cantilever. The nominal cantilever model about which these sensitivities are plotted is on-sample cantilever model corresponding to a very low setpoint amplitude. Each point in the 2-D space represents a particular combination for the observer model. It can be seen from the plots that the minima is obtained when the observer model coincides with the on-sample cantilever model.

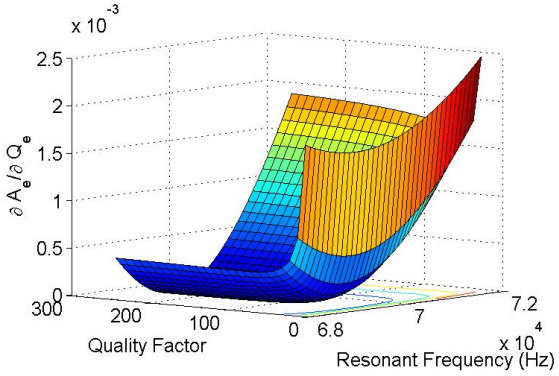

Figure 5.8: 2-D plots for sensitivity of the error rms to changes in the equivalent quality factor of the cantilever. The nominal cantilever model about which these sensitivities are plotted is on-sample cantilever model corresponding to a very low setpoint amplitude. Each point in the 2-D space represents a particular combination for the observer model. It can be seen from the plots that the minima is obtained when the observer model coincides with the on-sample cantilever model.

Figure 5.6 shows the variations in the rms of the error signal in the 2-D space when the nominal plant model is the on-sample cantilever model. Figure 5.7 and 5.8 indicate the sensitivity $\frac{\partial A_e^2}{\partial \omega_e}$ and $\frac{\partial A_e^2}{\partial Q_e}$ respectively where the plant model is (Q_{low}, ω_{elow}) and observer parameters vary at each point. From these plots it can be seen that as observer parameters move farther away from the plant parameters the A_e^2 and sensitivity of A_e^2 increases.

Figure 5.9, 5.10 and 5.11 show the projections of above 2-D plots along the direction $(Q_{free}, \omega_{efree})$ till (Q_{low}, ω_{elow}). This is the direction along which the equivalent plant model moves during the force curve. In all the three plots, the blue curve represents the response when the observer is built based on the off-sample nominal cantilever model and the observer gain is aggressive so that the error transients decay within $4 - 10$ cantilever oscillation cycles. The red curve represents the response when the observer is built based on on-sample cantilever model, $(Q_{elow}, \omega_{elow})$ and the observer gain is chosen such that the error transients decay within $4 - 10$ cantilever oscillation cycles. The green curves represent the response when the observer is built based on off-sample nominal cantilever model but the observer gain is such that the error signal decays at the time scales of nominal cantilever model. One can observe from red and blue curves that the minima in those curves occurs when the observer model coincides with the nominal cantilever model based on which it was built. Thus the minima of blue curve is at free air amplitude and the minima in the red curve is at the lowest amplitude. When we compare the blue and the green curve, then the nominal cantilever model in both cases is the off-sample cantilever dynamics. That is why the minima of both the curves is near free air amplitude. But the observer gain is much more aggressive in case of blue curve as against the green curve. It can be seen that just by varying the observer gain we can achieve a two order of increase in the magnitudes of these curves. The green plot in Figure 5.10 is divided by 100 and the green plot in Figure 5.11 is divided by 10 before plotting.

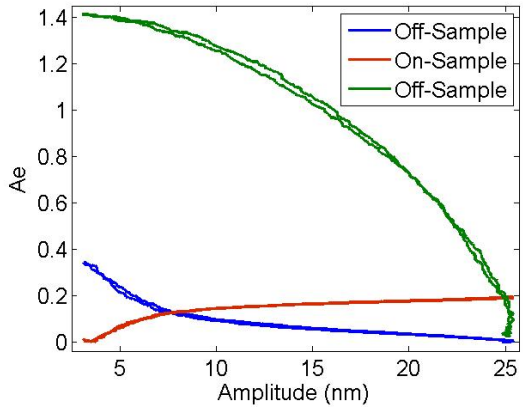

Figure 5.9: Directional plots for RMS of the error signal. The direction along which these lines are plotted corresponds to the (ω_e, Q_e) values along the force curve. The blue curve correspond to off-sample nominal cantilever model with aggressive observer gains. The red curve correspond to on-sample nominal cantilever model with aggressive controller gains. The green curve correspond to the off-sample nominal cantilever model with low observer gains. The minima in all three curves is obtained when the observer model coincides with their respective nominal cantilever model. A_e can be increased drastically by reducing the observer gains.

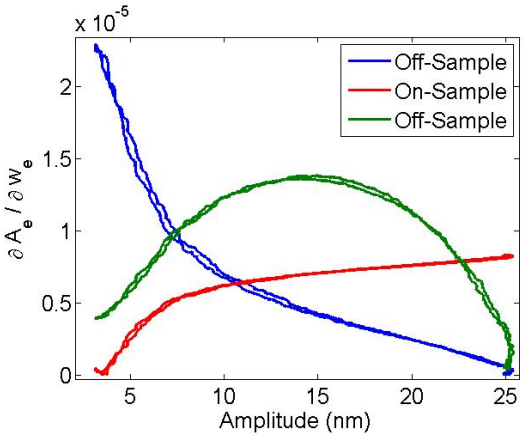

Figure 5.10: Directional plots for sensitivity of the error rms to changes in the equivalent resonant frequency of the cantilever. The direction along which these lines are plotted corresponds to the (ω_e, Q_e) values along the force curve. The blue curve correspond to off-sample nominal cantilever model with aggressive observer gains. The red curve correspond to on-sample nominal cantilever model with aggressive controller gains. The green curve correspond to the off-sample nominal cantilever model with low observer gains. The minima in all three curves is obtained when the observer model coincides with their respective nominal cantilever model. $\frac{\partial A_e}{\partial \omega_e}$ can be increased drastically by reducing the observer gains. The green curve is divided by a factor of 100 before plotting.

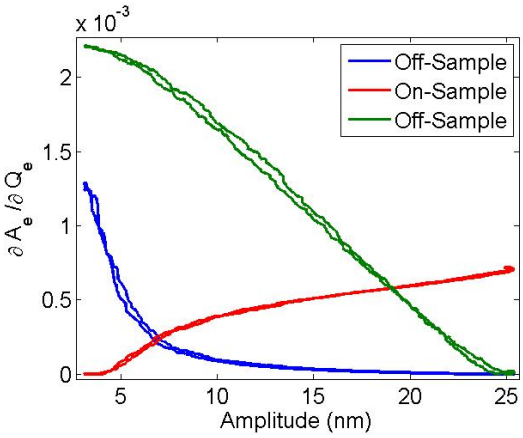

Figure 5.11: Directional plots for sensitivity of the error rms to changes in the equivalent quality factor of the cantilever. The direction along which these lines are plotted corresponds to the (ω_e, Q_e) values along the force curve. The blue curve correspond to off-sample nominal cantilever model with aggressive observer gains. The red curve correspond to on-sample nominal cantilever model with aggressive controller gains. The green curve correspond to the off-sample nominal cantilever model with low observer gains. The minima in all three curves is obtained when the observer model coincides with their respective nominal cantilever model. $\frac{\partial A_e}{\partial Q_e}$ can be increased drastically by reducing the observer gains. The green curve is divided by a factor of 10 before plotting.

5.2.4 SNR Analysis of RMS of Error Signal

In this section, we derive analytical expression for signal to noise ratio and its variations with respect to observer model parameters. Signal in this setup would include all the terms which are dependent on changes in the plant model. Thus signal at the output of the observer should constitute $S = A_e^2/2+$ part of $\sigma_{\eta e}^2$ term $= S_g + S_\eta$. Noise at the output should consist of $\sigma_{\nu e}^2+$ remaining part of $\sigma_{\eta e}^2 = N_\nu + N_\eta$. In this work, we are interested in treating only the S_g part as the signal and hence we define two different SNRs in this work. One is with respect to the input thermal noise which is defined as $S = \frac{S_g}{N_\eta + S_\eta}$ and the other is with respect to the input measurement noise which is

defined as $S = \frac{S_g}{N_\nu}$ where

$$\begin{aligned} S_g &= \frac{\left[(\omega_k^2-\omega_e^2)^2+\omega^2(\omega_k/Q_k-\omega_e/Q_e)^2\right](c_0^2+\omega^2c_1^2)A_0^2/2}{\left[(\omega_k^2+L_1-\omega^2)^2+\omega^2(\omega_k/Q_k+L_2)^2\right][(\omega_e^2-\omega^2)^2+\omega^2\omega_e^2/Q_e^2]} \\ S_\eta &= \sigma_\eta^2 \int_0^\infty \frac{\left[(\omega_k^2-\omega_e^2)^2+\omega^2(\omega_k/Q_k-\omega_e/Q_e)^2\right](c_0^2+\omega^2c_1^2)}{\left[(\omega_k^2+L_1-\omega^2)^2+\omega^2(\omega_k/Q_k+L_2)^2\right][(\omega_e^2-\omega^2)^2+\omega^2\omega_e^2/Q_e^2]}d\omega \\ N_\eta &= \sigma_\eta^2 \int_0^\infty \frac{c_0^2+c_1^2\omega^2}{(\omega_k^2+L_1-\omega^2)^2+\omega^2(\omega_k/Q_k+L_2)^2}d\omega \\ N_\nu &= \sigma_\nu^2 \int_0^\infty \frac{L_1^2+\omega^2L_2^2}{(\omega_k^2+L_1-\omega^2)^2+\omega^2(\omega_k/Q_k+L_2)^2}d\omega \end{aligned} \tag{5.20}$$

where σ_η^2 is the input noise variance due to thermal noise and σ_ν^2 is the input noise variance due to the measurement noise.

Figure 5.12(a), (b) and (c) shows the variations in S_η, N_η and N_ν in the 2-D space of (Q_k, ω_k). N_η and N_ν are not dependent on the nominal cantilever model and their magnitude increase with increasing quality factor of the observer. S_η obtains a minima when the observer model is closest to the nominal cantilever model and it grows as the "distance" of the observer from the nominal cantilever model increases. Interesting thing to note here is that in case the cantilever is not periodically excited, even then its model will change in presence of external long range perturbations. This method will give selective amplification to the thermal noise component which can then be used for sensing purposes.

Figure 5.13(a) and (b) shows the SNR plots in 2-D space. Despite an increase in S_η, the overall SNR still increases as the "distance" between the observer and the nominal plant model increases. Figures 5.14 and 5.15 show a similar trend in S_η and the SNR values respectively when the nominal cantilever model is chosen to be on-sample with $(Q_{elow}, \omega_{elow})$ parameters.

Figure 5.16(a), (b) and (c) represent the variations in S_η, N_η and N_ν along the direction in which the equivalent cantilever model changes during a force curve. The blue curves represent the values when the nominal cantilever model is off-sample and the observer gains are such that the error transients decay within $4-10$ oscillation cycles. The red curves represent the values when the nominal cantilever model is on-sample and the observer gains are such that the error transients decay within $4-10$ oscillation cycles. The green curves represent the values when the nominal cantilever model is off-sample and the observer gains are such that the error transients decay depending on the cantilever dynamics.

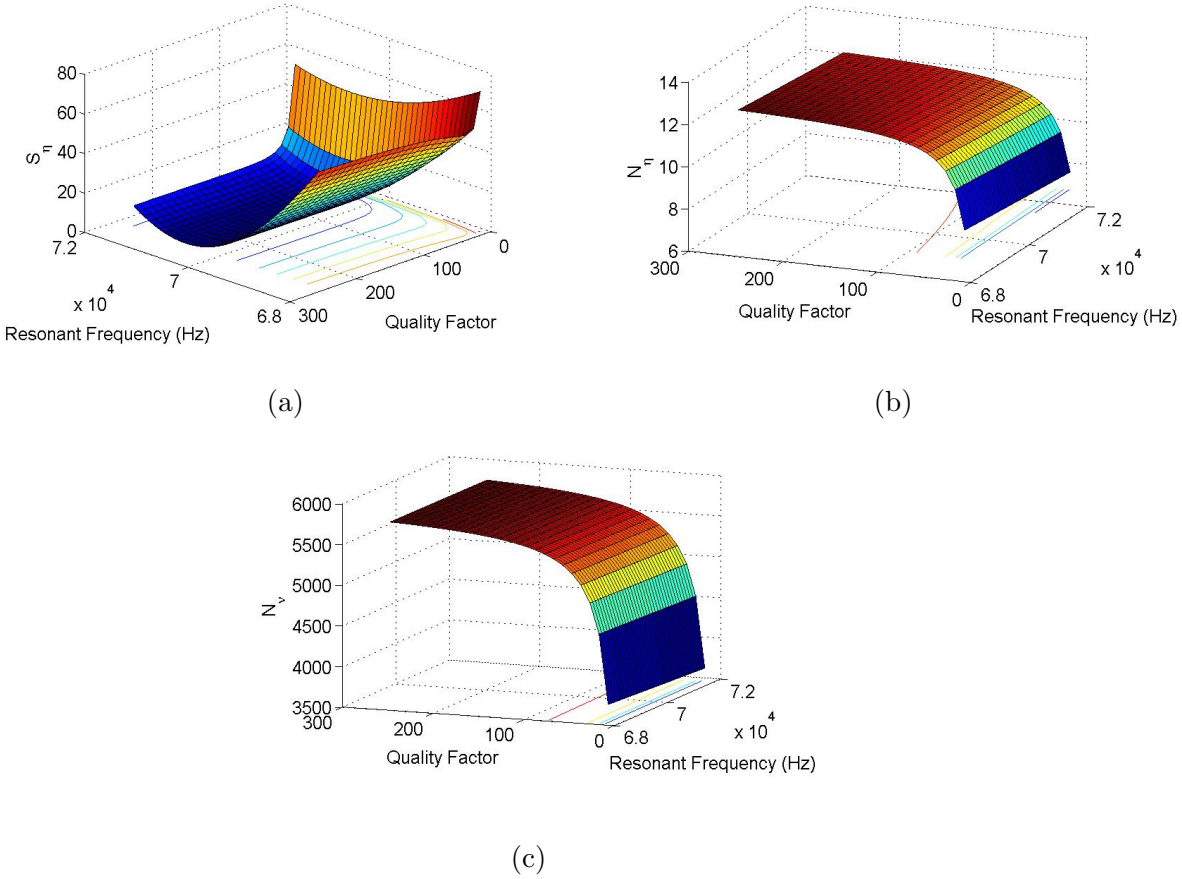

Figure 5.12: 2-D plots of (a) Signal component of the thermal noise in the error signal (b) Noise component of thermal noise in the error signal and (c) the measurement noise component in the error signal. S_η shows same trends as A_e as expected from the derived equations whereby the minima is reached when the observer model coincides with the nominal cantilever model. N_η and N_ν increase in variance as the quality factor of the observer system increases. They show negligible variation with changes in the observer resonant frequency as expected.

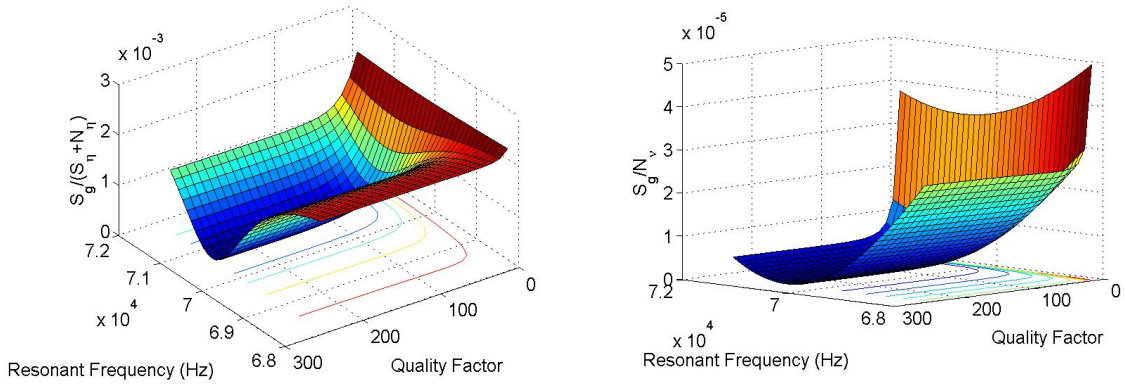

(a) (b)

Figure 5.13: 2-D plots for (a) Signal to Noise ratio ($S_g/(S_\eta + N_\eta)$) (b) Signal to noise ratio (S_g/N_ν) when the nominal cantilever model corresponds to off-sample dynamics. Signal to noise ratio increases as the "distance" of the observer from the nominal cantilever model increases.

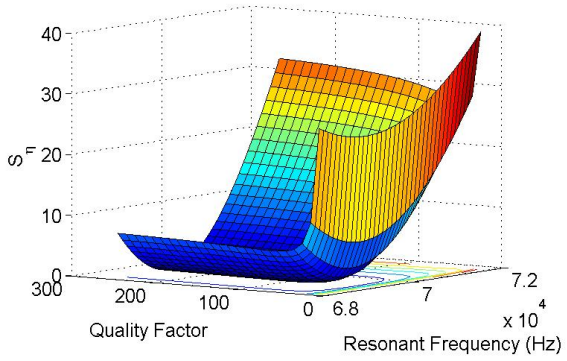

Figure 5.14: 2-D plots of signal component of the thermal noise in the error signal when the nominal cantilever model is on-sample model. S_η shows same trends as A_e as expected from the derived equations whereby the minima is reached when the observer model coincides with the nominal cantilever model. N_η and N_ν remain the same since they do not depend on the nominal cantilever dynamics.

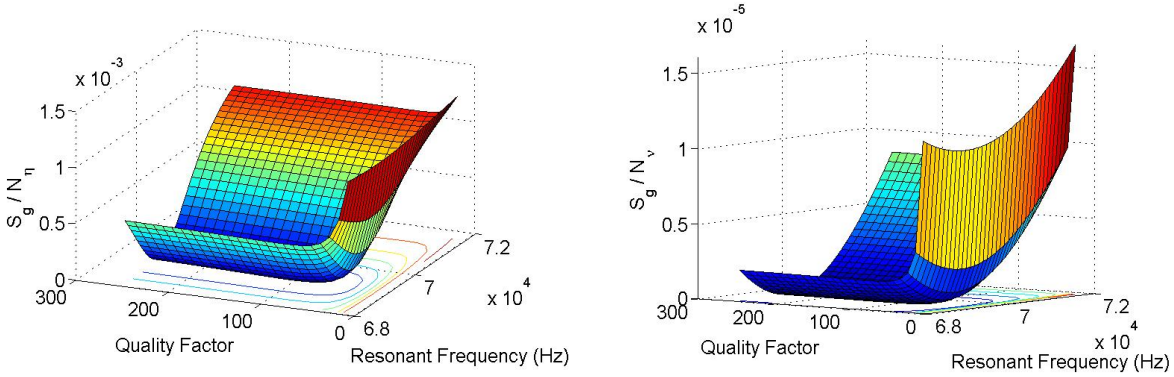

(a) (b)

Figure 5.15: 2-D plots for (a) Signal to Noise ratio ($S_g/(S_\eta + N_\eta)$) (b) Signal to noise ratio (S_g/N_ν) when the nominal cantilever model corresponds to on-sample dynamics with very low setpoint amplitude. Signal to noise ratio increases as the "distance" of the observer from the nominal cantilever model increases.

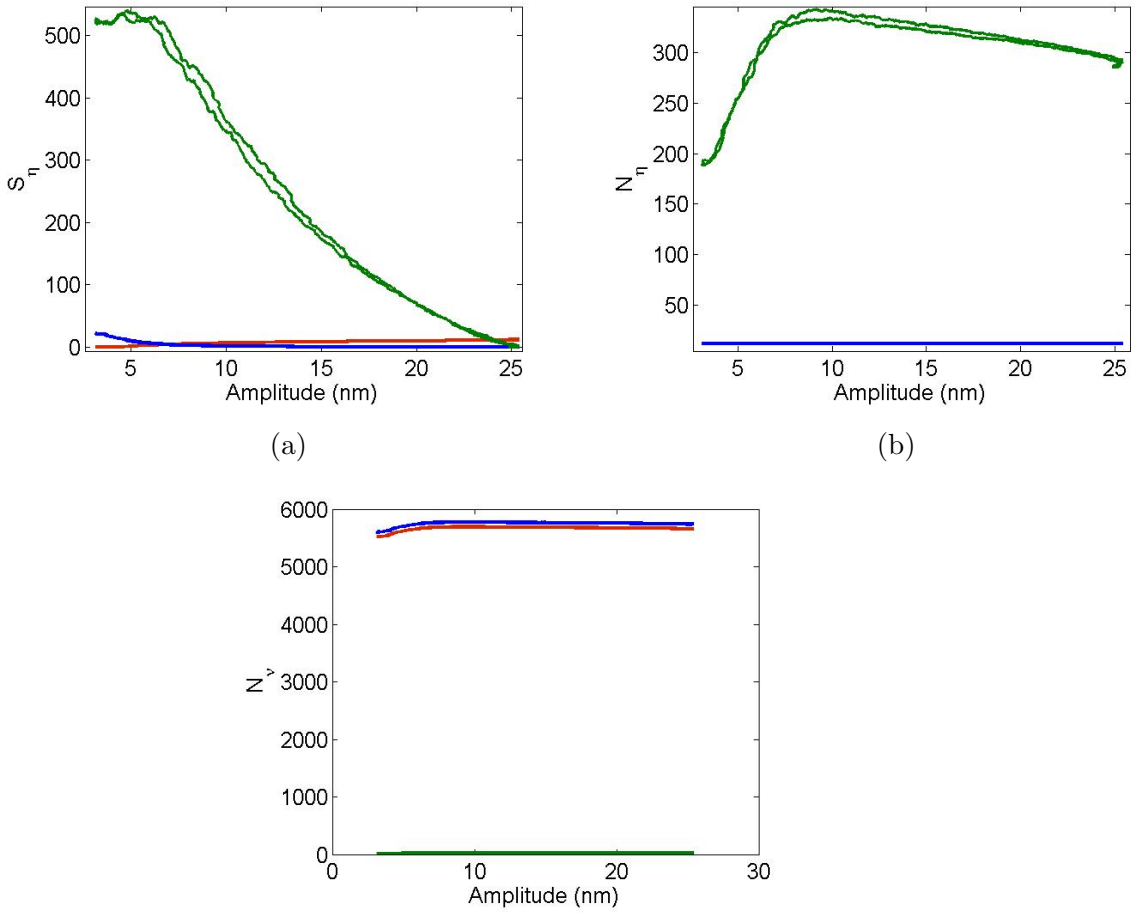

Figure 5.16: Directional plots for (a) S_η (b) N_η and (c) N_ν. The direction along which these lines are plotted corresponds to the (ω_e, Q_e) values along the force curve. The blue curve correspond to off-sample nominal cantilever model with aggressive observer gains. The red curve correspond to on-sample nominal cantilever model with aggressive controller gains. The green curve correspond to the off-sample nominal cantilever model with low observer gains. The minima in all three curves is obtained when the observer model coincides with their respective nominal cantilever model. There is a drastic increase in N_η and a drastic decrease in N_ν as the observer gains are reduced.

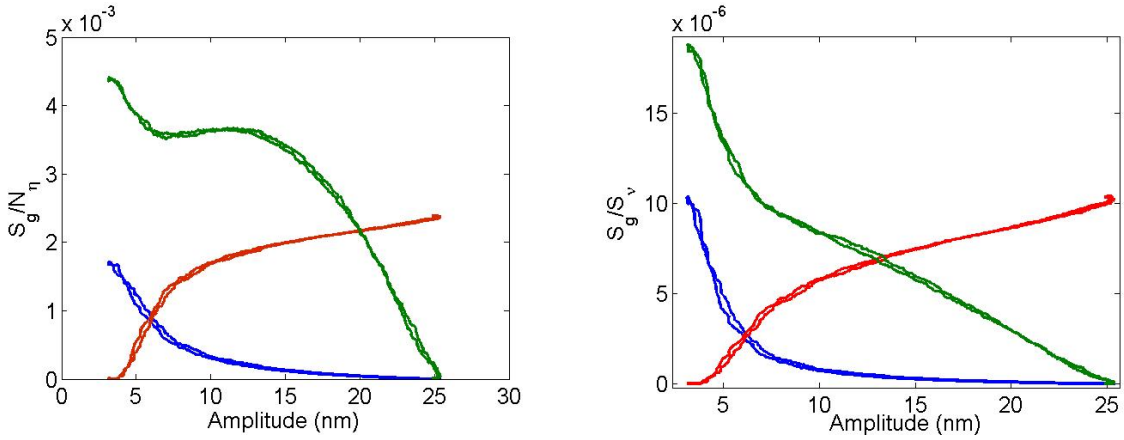

(a) (b)

Figure 5.17: Directional plots for (a) Signal to Noise ratio ($S_g/(S_\eta + N_\eta)$) (b) Signal to noise ratio (S_g/N_ν). The direction along which these lines are plotted corresponds to the (ω_e, Q_e) values along the force curve. The blue curve correspond to off-sample nominal cantilever model with aggressive observer gains. The red curve correspond to on-sample nominal cantilever model with aggressive controller gains. The green curve correspond to the off-sample nominal cantilever model with low observer gains. The minima in all three curves is obtained when the observer model coincides with their respective nominal cantilever model. The signal to noise ratio with respect to the thermal noise increases slightly with reduction in observer gains. But there is a drastic increase in the signal to noise ratio with respect to the measurement noise as the observer gains are reduced. The green curve in (b) is plotted after a division by a factor of 10000

Here we observe that N_η and N_ν are not much dependent on the observer model but they are highly sensitive on the observer gains. N_η increases while N_ν decreases when the observer gains are made sluggish. S_η does depend on the observer model but it increases in value while preserving the overall trend with respect to choice in observer models, when the observer gains are made sluggish. Figure 5.17(a) and (b) show that SNR with respect to η increases slightly when the observer gains are made sluggish and SNR with respect to ν increases by orders of magnitude by changing the observer gains. The green curve in Figure 5.17(b) is plotted after a division by a factor of 10000.
Thus we see that there is a clear benefit of choosing an observer model different from

plant model to obtain increased sensitivity and SNR while imaging using RMS of error signal from observer output. We still need a handle on bandwidth of rms signal.

5.3 Initial State Response Analysis of RMS of Error Signal

From equation (5.3) we have

$$\begin{aligned} e(t) &= e^{(A_k-LC)t}e_0 + \int_0^t e^{(A_k-LC)(t-\tau)}(A-A_k)x(\tau)d\tau \\ &\quad + \int_0^t e^{(A_k-LC)(t-\tau)}(B-B_k)g(\tau)d\tau + \int_0^t e^{(A_k-LC)(t-\tau)}\left[B_1\eta(\tau) - L\nu(t)\right]d\tau \end{aligned} \tag{5.21}$$

Thus the initial state response is given by

$$\begin{aligned} e(t) &= e^{(A_k-LC)t}e_0 + \left[\int_0^t e^{(A_k-LC)(t-\tau)}(A-A_k)e^{A\tau}d\tau\right]X_0 \\ E(s) &= \left[sI-(A_k-LC)\right]^{-1}\left[E_0(s) + (A-A_k)\left[sI-A\right]^{-1}X_0(s)\right] \end{aligned} \tag{5.22}$$

This equation indicates that if the plant model and observer model are same then by varying L one can obtain a desired decay rate of the initial state response by appropriate placement of the eigen values of the $(A_k - LC)$ matrix. But when plant and observer models are not the same then there is an additional component due to the initial state response in $x(t)$. This response is slow and it depends on the cantilever dynamics. Equation 5.22 indicates that this component gets a gain depending on how far the observer model is from the nominal cantilever model. Thus the object of interest is the peak value of the additional transient which we would need to minimize to let the error transients that results purely due to the dynamics of $(A_k - LC)$ matrix dominate. Figure 5.18(a) indicates that the peak of the additional transients also increase in $2-D$ space as the distance between the observer and the nominal cantilever model increases. Figure 5.18(b) shows these responses along the direction of force curves. The blue curve is the peak transient values when the observer is based on off-sample cantilever model and with aggressive observer gains. The red curve is the peak transient response when the observer is based on the on-sample dynamics and with aggressive observer gains. The green curve represents the peak transient values when the observer is kept sluggish. One can see from Figure 5.18(b) and Figure 5.10 that the peak transient growth is slower as compared to the increase rate of the relevant sensitivity values as the observer

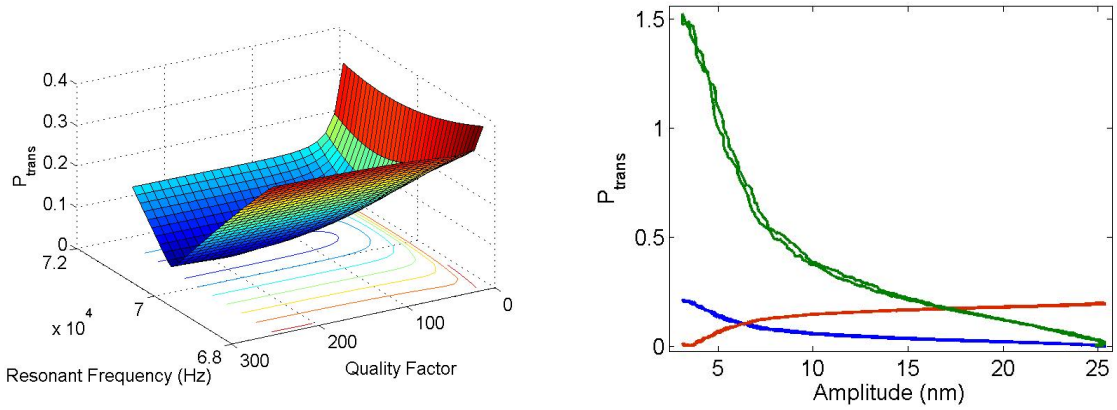

(a) (b)

Figure 5.18: (a) 2-D plot (b) directional plot along the force curves of the peak transient value due to model mismatch between the observer and the equivalent cantilever model. This extraneous contribution also increases as the distance of the observer model from the nominal cantilever model increases with the minima obtained when the two coincide. (b) shows that the rate of increase of the peak transient component increases but at a slow rate as compared to the rate at which A_e and its sensitivities increase, as the observer gains are reduced.

model starts to deviate from the plant model if we choose a sluggish observer gain. But it needs to be noted here that if the observer gains are made too sluggish then the error transients which were purely due to the dynamics of $(A_k - LC)$ matrix will also become prolonged. Thus we cannot reduce the observer gain arbitrarily. Thus one way of maintaining reasonable transients while obtaining good steady state sensitivity is by choosing an observer model that is not very far from the nominal cantilever model and by choosing reasonably low observer gains. These notions will be posed mathematically and made more rigorous as a future work.

5.4 Experimental Validation

In this section, we will experimentally verify the notions that were developed analytically and through simulations in the previous section. There were two sets of experiments performed for the verification.

5.4.1 Experimental Vs Analytical Error RMS Sensitivity Equations

Amplitude force curve was performed using an AC-240TS cantilever from Asylum Research. The cantilever excitation and deflection were captured simultaneously. REEP algorithm was used to provide the estimate of equivalent cantilever model along the force curves. This information was used to build two observers, one of which was based on the off-sample cantilever model and the other was based on the on-sample cantilever model at a very low set point amplitude. These observers had aggressive observer gains. A third observer based on the off-sample cantilever model but with a sluggish observer gain was also designed. The captured cantilever excitation and deflection were given to these observers as input and their corresponding rms signal of error output were monitored. This data was used to calculate A_e^2 and dA_e^2 plots along the force curve direction. Analytical expressions for A_e^2 and dA_e^2 were obtained using equations 5.16, 5.18 and 5.19. $\frac{\partial A_e^2}{\partial \omega_e}$ and $\frac{\partial A_e^2}{\partial Q_e}$ can be obtained a-priori once the observer and the nominal cantilever model are chosen. $d\omega_e$ and dQ_e were obtained from the equivalent resonant frequency and equivalent quality factor plots that were obtained using the REEP algorithm.

Figure 5.19(a), (b) and (c) shows the comparison of experimental and analytical plots for A_e^2 values when the nominal plant model is assumed to be the off-sample cantilever model with aggressive observer gains, the nominal plant model is assumed to be the on-sample cantilever model with aggressive observer gain and when the nominal plant model is assumed to be the off-sample cantilever model with sluggish observer gains respectively. Near quantitative match between the two plots in each figure indicate the expressions derived for A_e^2 are correct. Figure 5.20(a), (b) and (c) shows the comparison of experimental and analytical plots for dA_e^2 values when the nominal plant model is assumed to be the off-sample cantilever model with aggressive observer gains, the nominal plant model is assumed to be the on-sample cantilever model with aggressive observer gain and when the nominal plant model is assumed to be the off-sample cantilever model with sluggish observer gains respectively. Near quantitative match between the two plots in each figure indicate the expressions derived for dA_e^2 are correct. It is thus established that the rms sensitivity increases as the "distance" between the observer and the nominal plant model increases. This sensitivity increases drastically if the observer gains are made sluggish.

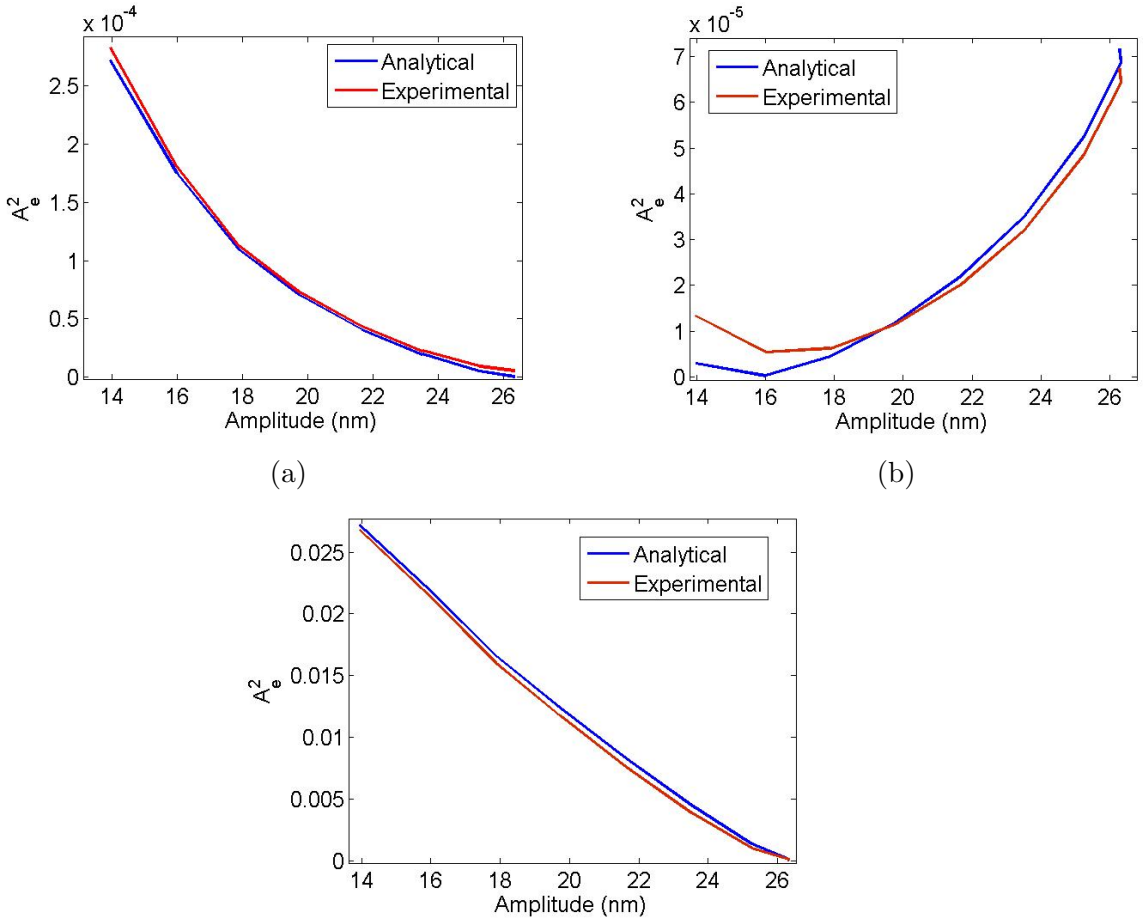

Figure 5.19: Directional plots for A_e^2 when (a) the nominal observer model is off-sample model with aggressive observer gains (b) nominal observer model is on-sample model with aggressive observer gains and (c) observer model is off-sample model with low observer gains. The blue curves are obtained analytically using equation 5.16. The red curves are obtained from the experimental data. Near quantitative match between the analytical and experimentally derived quantities indicate that the experiments follow the derived expressions closely.

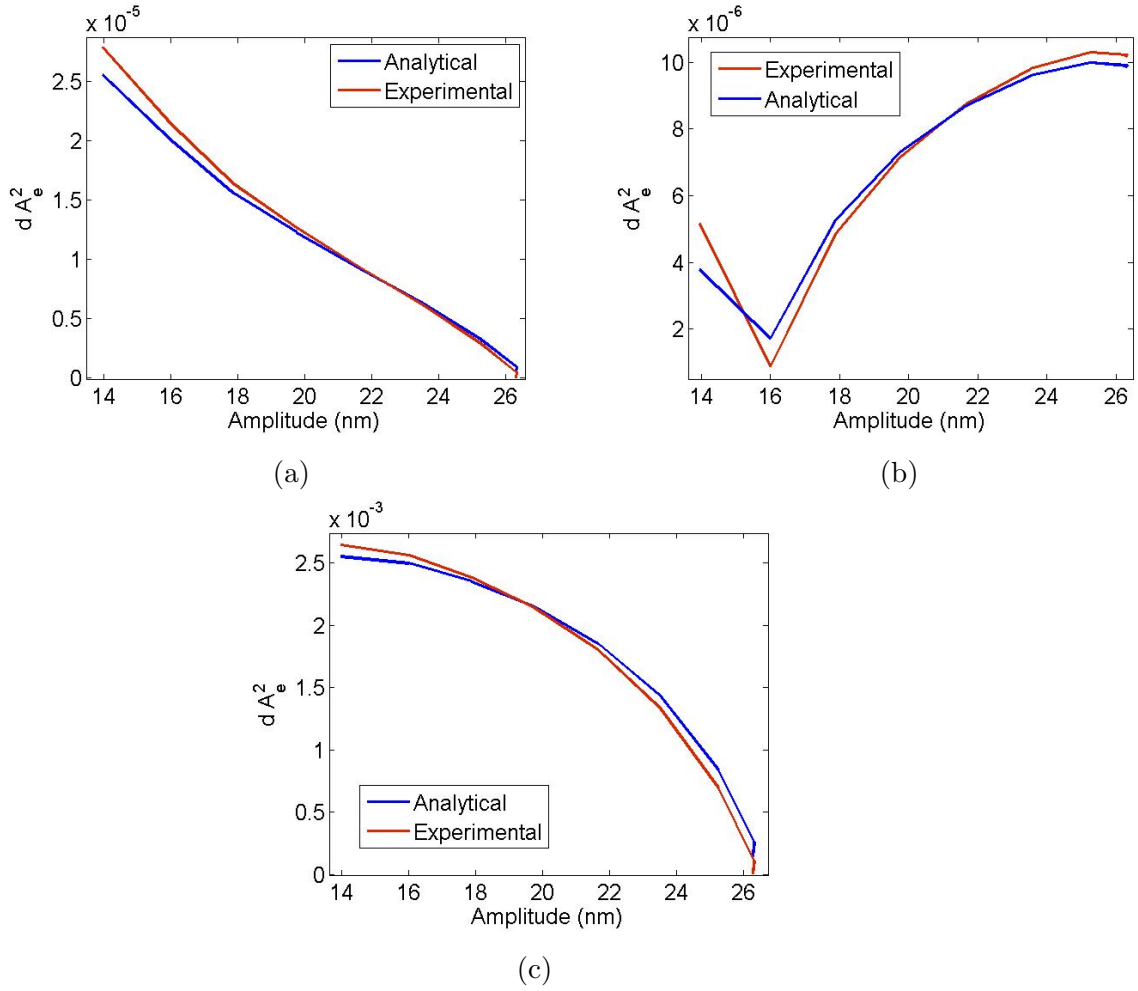

Figure 5.20: Directional plots for dA_e^2 when (a) the nominal observer model is off-sample model with aggressive observer gains (b) nominal observer model is on-sample model with aggressive observer gains and (c) observer model is off-sample model with low observer gains. The blue curves are obtained analytically using equations 5.18 and 5.19. The red curves are obtained from the experimental data. Near quantitative match between the analytical and experimentally derived quantities indicate that the experiments follow the derived expressions closely.

5.4.2 Experimental Verification of Trade off Between the Observer Model and Observer Gain for Enhanced Signal Bandwidth and Sensitivity

Another set of experiments were performed where an AC-240TS cantilever from Asylum research was used. The cantilever was engaged with the sample (mica sheet) in tapping mode. The controller gains were kept low so as to cancel the sample slope and piezo drifts only. A random three level voltage signal was applied to the z-piezo such that the cantilever interacted with three distinct levels of topography. The width of each level was 0.1 sec. Cantilever excitation and deflection signals were recorded. This data was provided to the REEP algorithm. Equivalent resonant frequency and quality factor of the cantilever along the time axis as the levels in the sample topography change were obtained. This was overlaid on the force curve data to obtain the relative position of these level changes with respect to the equivalent cantilever model change along the force curve. Thus three observers were designed corresponding to point A, B and C (see Figure 5.21). These observers were designed for aggressive observer gains, sluggish observer gains and intermediate observer gain values. Cantilever excitation and the deflection data was provided to these observer banks and the output rms of error signal was monitored. This data was also provided to an adaptive observer, so that the observer always remained at the instantaneous equivalent cantilever model. The output rms of the error signal from the adaptive observer was also monitored.

Figure 5.22(a), (b) and (c) shows the rms of error signal from the three observers (A, B and C respectively) when the observer gains are aggressive. One can see that the sensitivity of detecting levels is low in (b) and (c) since their observer models are close to the equivalent cantilever models. But since the observer gains are aggressive, we are still able to see the transient behavior due to purely $(A_k - LC)$ matrix in the rms signal. The rms sensitivity is minimum when we use the adaptive observer since it is ensured that the observer model is always in sync with the instantaneous equivalent cantilever model. This is shown in Figure 5.23. If we choose to reduce the observer gains drastically to improve the imaging sensitivity and the SNR of the rms signal, then we do see an enhanced sensitivity to the topography levels (see Figures 5.24(a), (b) and (c) but at the cost of poor signal transients. The transients due to $(A_k - LC)$ matrix are prolonged. Therefore they are not visible in the plots. By choosing an observer model

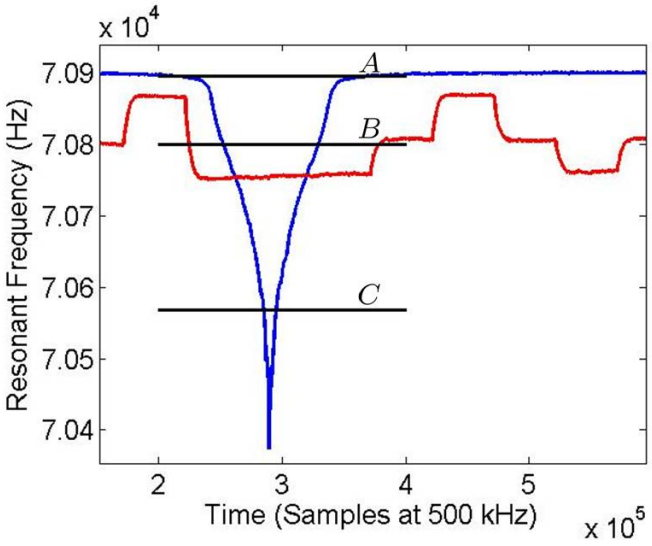

Figure 5.21: Blue curve shows the equivalent resonant frequency of the cantilever during a force curve. It reduces with decrease in the tip-sample separation. The red curve is the equivalent cantilever frequency when the sample topography consists of three different step heights. Three observers are designed based on the nominal cantilever model at points A, B and C.

which is farther from the range of equivalent cantilever models during the operation and by choosing an appropriately small observer gain, one can achieve reasonable sensing sensitivity as required by the application and the transients are preserved as well. This is shown in Figures 5.25(a), (b) and (c).

5.5 Conclusion

Thus we have established in this work that by increasing the distance between the observer model and the nominal plant model, one can obtain increased sensitivity for the steady state RMS of error signal with respect to small changes in the equivalent plant model about the chosen nominal dynamics. This happens at the cost of reduced signal bandwidth since the peak transient value due to the slow cantilever dynamics also gets amplified by such a choice. A careful choice of the observer model and the observer gains can get the good of both scenarios. Systematic ways to choose the observer model will be studied in future.

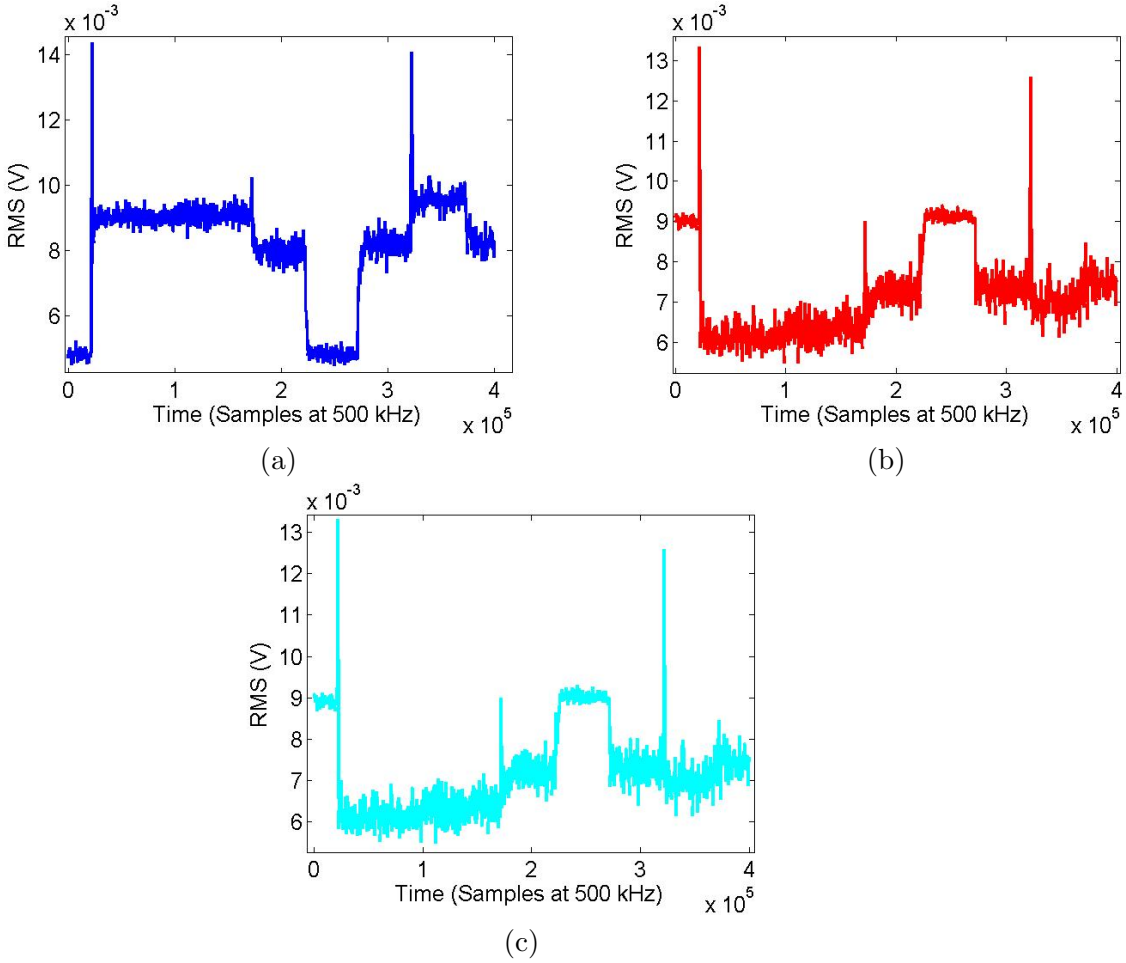

Figure 5.22: RMS of the error signal when (a) the observer is built on point A (b) the observer is built on point B and (c) the observer is built on point C with aggressive observer gains. The change in the equivalent cantilever model during the experiment is around point B. So point B is the closest to the cantilever models and then point C followed by point A. It can be seen that the transients due to sudden change in the tip-sample interaction are visible in all three plots but the sensitivity to steady state levels is very low. It is a little better in (a) because the observer model is a little farther from the nominal cantilever model.

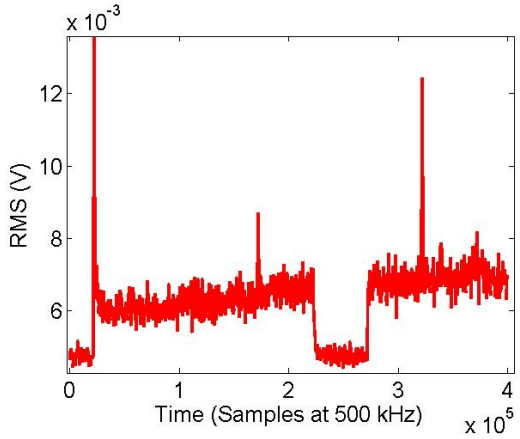

Figure 5.23: RMS of the error signal which is the output of an adaptive observer. It can be seen that the transients are visible in the signal but the sensitivity to steady state levels is even lower than figure 5.22. This is because in the case of an adaptive observer, the observer is always at the instantaneous equivalent cantilever model.

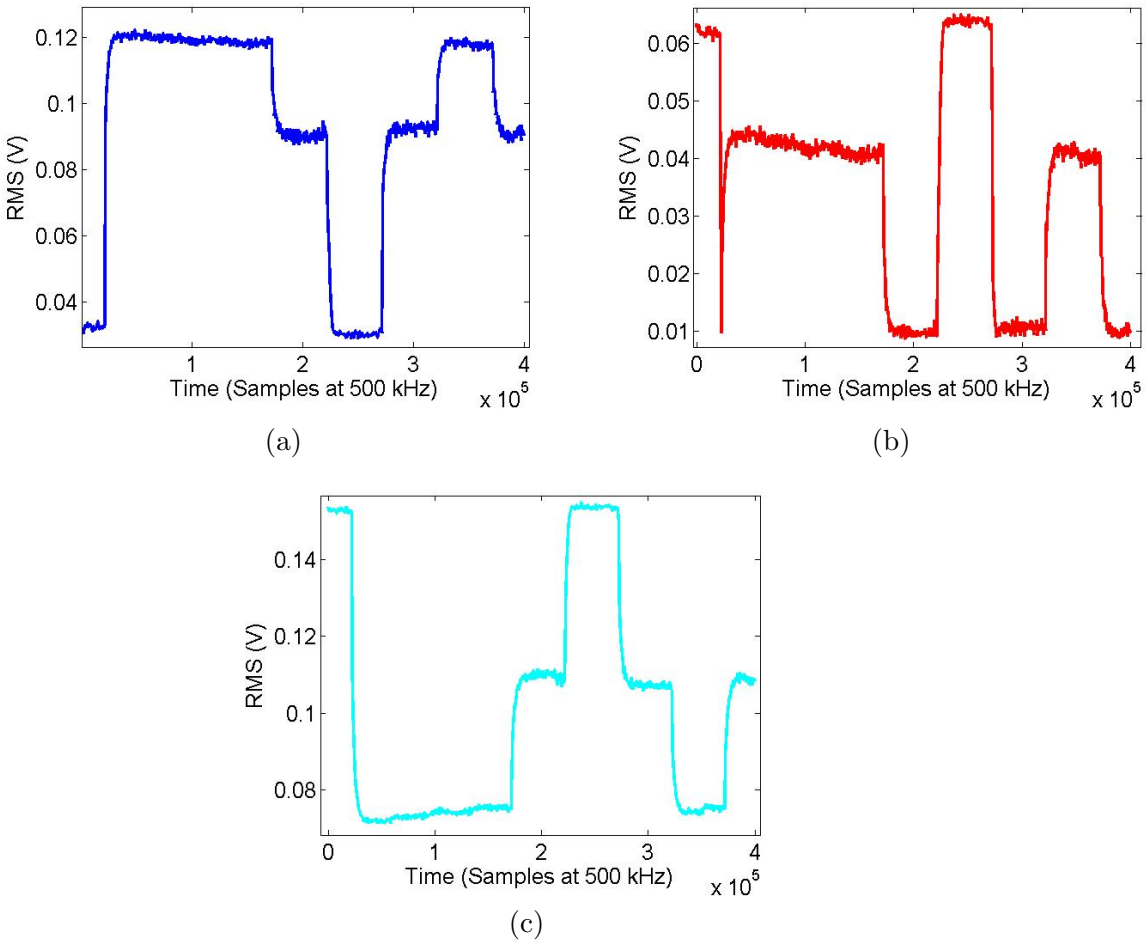

Figure 5.24: RMS of the error signal when (a) the observer is built on point A (b) the observer is built on point B and (c) the observer is built on point C with very low observer gains. The change in the equivalent cantilever model during the experiment is around point B. So point B is the closest to the cantilever models and then point C followed by point A. The sensitivity for the levels is maximum in (a) followed by (c) and then (b). It can be seen that the transients due to sudden change in the tip-sample interaction are not visible in all three plots anymore. This is because at such low observer gains the transients due to purely $(A_k - LC)$ matrix are very slow and mainly governed by the cantilever dynamics. Moreover the peak transient contribution due to model mismatch between the observer and the cantilever model is also substantial.

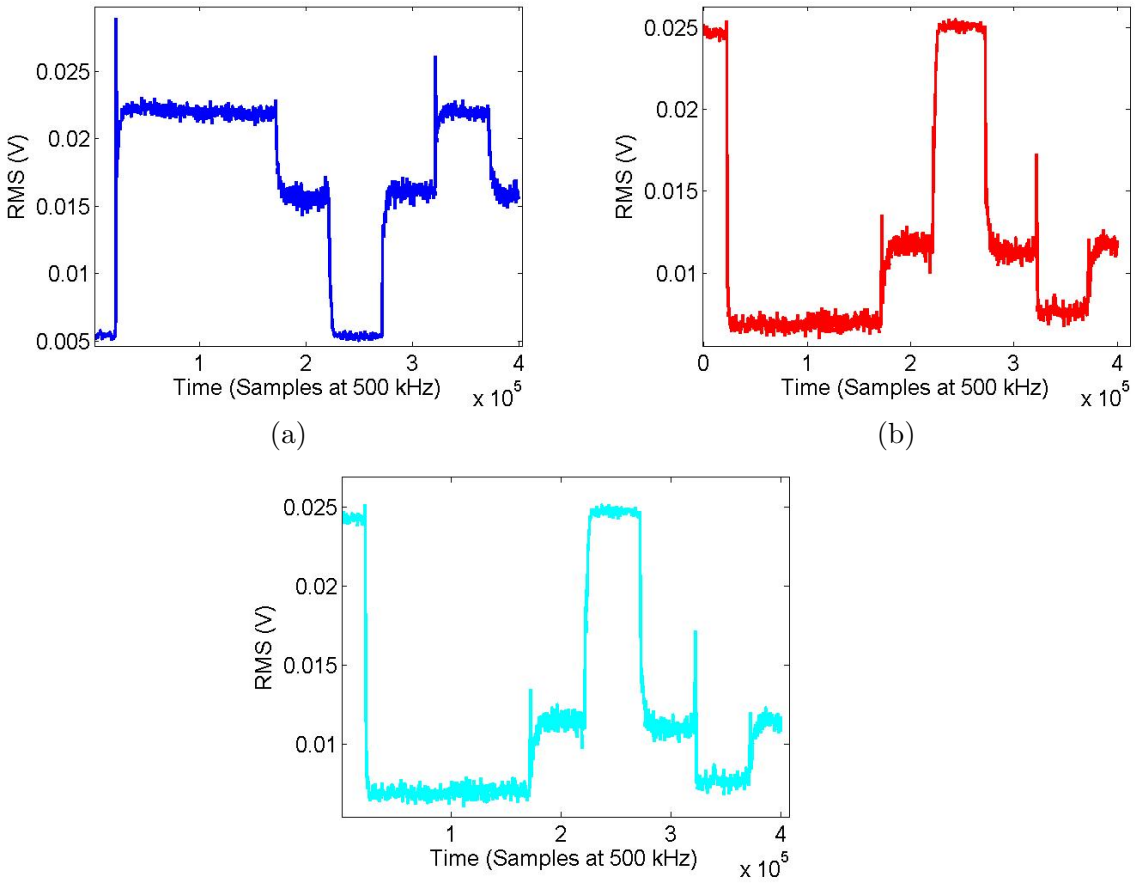

Figure 5.25: RMS of the error signal when (a) the observer is built on point A (b) the observer is built on point B and (c) the observer is built on point C with intermediate observer gains. The change in the equivalent cantilever model during the experiment is around point B. So point B is the closest to the cantilever models and then point C followed by point A. The sensitivity for the levels is maximum in (a) followed by (c) and then (b). In these plots, the sensitivity to the steady state levels is substantial and the transients due to sudden changes in the tip-sample interactions are also visible.

Chapter 6

Real Time Models of Electrostatically Actuated Cantilever Probes with Integrated Thermal Sensor for Nanoscale Interrogation

6.1 Introduction

The importance of cantilevers with integrated thermal sensors is exemplified by a variety of applications viz. calorimetry [53], thermal dip pen lithography [54], thermal metrology [55, 56], room temperature chemical vapor deposition [57], microfluidic actuation [58], thermomechanical actuation [59], local thermal property measurements [60] and high density data storage [18]. Typical thermo-mechanical cantilevers rely on dependence of the resistance of an electrical path on the temperature of the surrounding environment. For example, in probe based data storage, the separation of the media from the cantilever determines the heat transfer from the cantilever to the media, which in turn determines the resistance of the electrical path. Also, most of the resistance of

the electrical path is typically concentrated in a small region, which is achieved by differentially doping cantilever legs (see Figure 6.1). This region is termed as the *thermal sensor* in this article. As the resistance of the electrical path is primarily determined by the thermal sensor, the current through the electrical path is primarily determined by the thermal sensor. We define this current as the thermal sensor output. Various studies that research heat transfer processes which affect the thermal conduction pathway from the cantilever to the sample are reported in [61, 62, 63, 64, 65, 66, 67, 68] and [69].

In most present operation schemes, cantilevers are operated in contact mode where cantilever dynamics do not play a significant role, and the thermal sensor output is interpreted in a quasi-static sense. Operation in contact mode leads to significant tip-sample wear due to high lateral forces. It is known (see [70], [71]) that in dynamic mode operation where the cantilever is in intermittent contact mode with the sample, frictional forces between media and the cantilever are smaller, resulting in considerable reduction of tip and media wear. An attractive method of obtaining such an operation is to oscillate the cantilever by inducing a changing voltage between media surface and the cantilever, producing a changing electrostatic force on the cantilever.

In dynamic, intermittent contact operation with electrostatic actuation, cantilever trajectories result from interaction of cantilever beam mechanics with electrostatic, Van Der Waal's and adhesive forces. In addition, the current through the cantilever for certain cantilever geometries can be influenced by capacitive and magnetic affects that can make the interpretation of the thermal sensor output challenging. Thus the complexity of quantitatively predicting the cantilever motion and the associated thermal sensor output is considerable.

In this chapter, a characterization of time constants of various physical processes with the ability of quantitatively predicting thermally as well as optically measured trajectories is presented. Viewing dynamics of components as feedback interconnections [65, 38] together with system identification tools enable the modeling of complex processes by simpler components. Interconnections and simpler components provide useful insights into overall dynamics. It is shown that all parameters used in the model can be identified using thermal sensor output alone making this approach applicable where optical sensing is not available. The complex geometry of MEMS levers precludes a

tractable physical model of thermal sensor dynamics. It is shown that for practical operating amplitudes of dynamic mode operation, linearized characterizations obtainable from black box identification techniques using Fourier methods suffice. It is discovered that the thermal sensor output is affected by extraneous factors with capacitive and possibly magnetic origins that need to be considered. Experimental strategies that isolate these deleterious effects are presented. An experimental characterization of thermal sensor dynamics is achieved and compared with FEM simulations. The efficacy of the paradigm developed in this chapter is verified with comparison between simulated and experimental data. In summary, this chapter provides a comprehensive understanding of physical effects governing dynamics of an electrostatically actuated MEMS lever with integrated thermal sensing. It also provides a means of identifying time constants of various physical processes from thermal sensor measurement. Steps needed to construct the model are straightforward, enabling quantitative real time prediction of the motion of the cantilever and the thermal sensor measurement.

6.2 Device Description

The cantilevers studied in this article are made of highly doped material with a lowly doped region that forms the thermal sensor (see Figure 6.1 and [9] for a detailed description). The resistance of electrical path is primarily due to the resistance of the thermal sensor. The resistance of rest of the electrical path is negligible. Thus, the current I_R flowing through the electrical path when a voltage V_R is applied, is determined by the resistance of the thermal sensor. The proximity of the thermal sensor to the sample being imaged governs the heat lost from the cantilever, and thereby governs the temperature and resistance of the thermal sensor. As the sample is positioned laterally with respect to the cantilever, distance between the sample and the thermal sensor is changed due to the topography of the sample. This change in proximity leads to a change in resistance of the thermal sensor which, in turn, results in a change in the current. The above mechanism provides a means of inferring the topography of the substrate from the thermal sensor output.

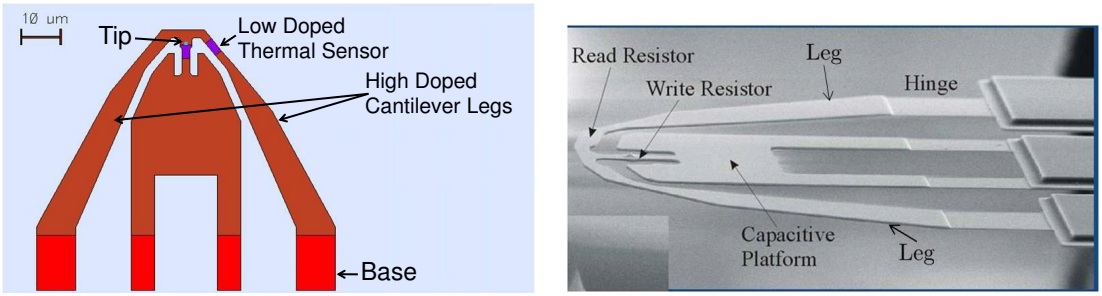

(a) (b)

Figure 6.1: (a) Schematic and (b) SEM image of the cantilever with integrated thermal sensor. The cantilever with integrated thermal sensor is made out of monolithic silicon. The legs are 65μm long and 1.5μm thick. Dimensions of thermal sensor are 4μm $\times$ 3.2μm $\times$ 0.5μm (LxWxT). Hinge is 15μm long and 0.5μm thick. Legs of the cantilever are doped higher at $1 - 2 \times 10^{20} cm^{-3}$ as compared to the thermal sensor which has a doping concentration of $4 \times 10^{17} cm^{-3}$. The mass of the cantilever is roughly 6×10^{-13} kg. There is a capacitive platform in the cantilever for electrostatic actuation. All the experiments in this study were done at room temperature with no active control of temperature, pressure or humidity.

6.3 Experimental Setup

Figure 6.3 shows a cantilever with the capability of sensing the distance of the cantilever from the media (also termed as the "sample") by monitoring the heat transfer to the media. This cantilever is made compatible with the Digital Instrument, Multimode Atomic Force Microscope (AFM) that has the following features (1) an optical means of detecting cantilever deflection p. (2) positioning capability with nanometer resolution, laterally (x, y direction) and vertically (z direction). In addition to the z positioning capabilities of the long range tube piezo (J-scanner), a small disc piezo, placed on the J scanner provides positioning in the z direction with a bandwidth close to 300 kHz (3) a means to electrostatically actuate the cantilever by applying a voltage V_{sub} to the sample.

Before providing the modeling assumptions, notation is provided with the aid of Figure 6.6. p and z_s represent the cantilever tip deflection and sample position respectively. t_h, t_s and ℓ_0 are the tip height, the tip-sample separation and the initial distance of the

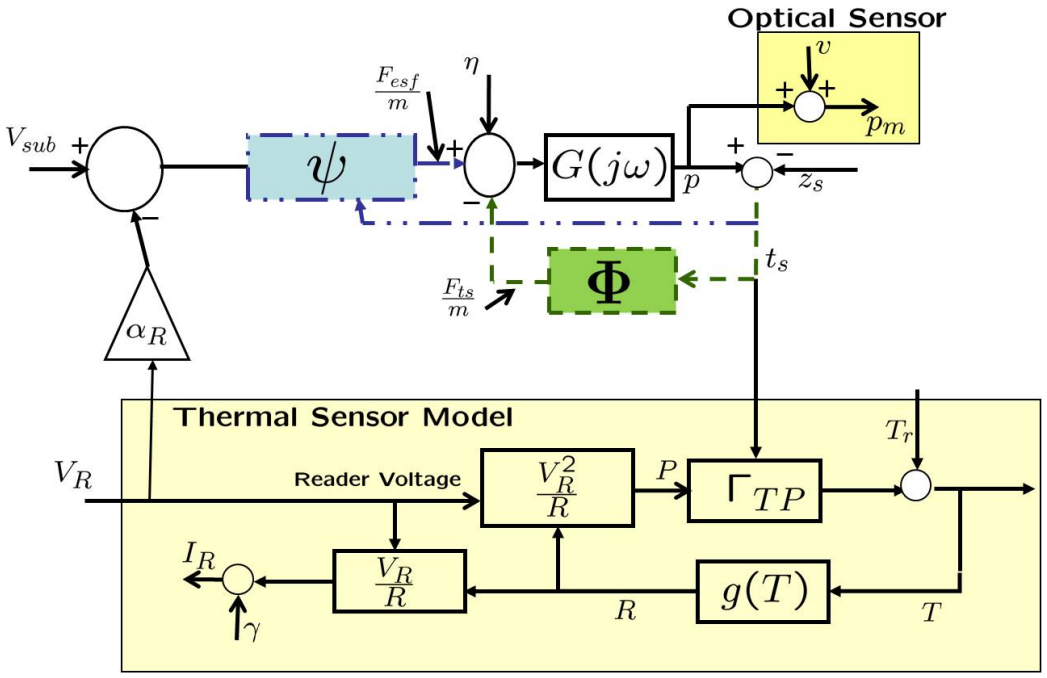

Figure 6.2: Integrated systems model with a detailed model of the thermal sensing mechanism. Cantilever beam is modeled as a second order linear time invariant system $G(j\omega)$ which takes as input the thermal noise forcing η, electrostatic force (per unit mass) F_{esf} and tip sample interaction force (per unit mass) F_{ts} and gives tip-deflection p as the output. p is measured by an optical sensor where the output is p_m and is corrupted by a measurement noise ν. Electrostatic force F_{esf} depends on the instantaneous potential difference between the cantilever and the sample which is modeled as $\alpha_R V_R - V_{sub}$. α_R accounts for the non uniform potential distribution along the cantilever legs. Tip sample separation $t_s = p - z_s$ modulo $(l_0 - t_h)$ is sensed by a thermal sensor which takes as input tip sample separation t_s and the thermal sensor voltage V_R and gives current $I_R = \frac{V_R}{R}$ as the output. Measurement of I_R is corrupted by measurement noise γ. Γ_{TP} is the dynamic map that relates instantaneous power dissipation (V_R^2/R) in the cantilever and instantaneous tip-sample separation (t_s) to the cantilever temperature (T). Resistance, R, of the thermal sensor is related to temperature (T) by a nonlinear static map, $g(T)$.

lever from the sample respectively. ℓ_0 can be interpreted as the initial reference distance between the sample and a nominal point on the lever surface. The lever-sample separation ℓ_s is the instantaneous separation between the cantilever and the sample. With the above notation it follows that $t_s = l_0 + p - t_h - z_s$ and $\ell_s = \ell_0 + p - z_s$. Note that p can be measured using the laser and the photodiode arrangement and z_s can be changed by using the piezo scanner to position the sample in the vertical direction.

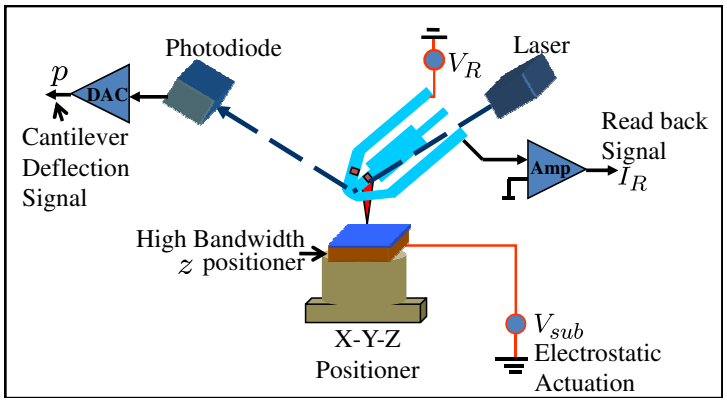

Figure 6.3: Experimental setup. V_R is the voltage applied across the cantilever. I_R is the measured cantilever current. V_{sub} is the voltage applied to the sample for actuating the cantilever electrostatically. Cantilever deflection is sensed through a laser-photodiode mechanism. Sample positioning is controlled through X-Y-Z positioner of DI microscope. Sample can also be positioned with high bandwidth in z direction using a high bandwidth z positioner.

6.4 Cantilever Beam Mechanics and Force Modeling

6.4.1 Cantilever Model

The cantilever is considered to be a flexure member and is modeled as a linear filter G (see Figure 6.2). G processes input forces on the cantilever and provides the displacement p of the cantilever as the output. Though an experimental means of identifying the cantilever dynamics is employed for the development of the model for dynamic mode operation purposes, the following second order approximation of the cantilever dynamics given by

$$\ddot{p} + \frac{\omega_0}{Q}\dot{p} + \omega_0^2 p = f \tag{6.1}$$

where f, ω_0 and Q are the total external force, first modal resonant frequency and the quality factor of the cantilever respectively, proves useful for the approach curve analysis described later.

The primary forces on the cantilever are (1) the tip-sample interaction force F_{ts} that is dominated by attractive forces at large range and at short range the forces are predominantly repulsive. This force depends on the separation between the tip and the sample, t_s (2) the electrostatic force F_{esf} that is caused by the difference in potential between the tip/cantilever surface and the sample surface and depends on the lever sample separation ℓ_s (3) the Langevin thermal noise forcing.

The tip-sample interaction forces are appreciable over a relatively shorter range when compared to electrostatic forces. Tip-sample interaction forces, which include Van de Waals, adhesive and meniscus forces, are negligible for tip-sample separation t_s greater than 20 nm, whereas the electrostatic force remains effective over the entire operating range of the cantilever motion. Electrostatic forces are realized by applying a voltage V_{sub} to the substrate.

The modeling of the various components of the dynamics follow the principle of separating the parts of the dynamics that can be precisely characterized from the components that are either not known or are not tractable for real-time applications. Such a separation is facilitated by the feedback interconnection modeling of the various forces on the cantilever that is presented next.

6.4.2 Feedback Models of Tip-Sample Interaction Forces and Electrostatic Forces

The cantilever tip deflection p depends on the tip-sample interaction force. The related model, denoted by G, that processes the input force to generate the deflection p is linear and does not vary with time. Also, the related cantilever dynamics can be characterized precisely [72, 73]. However, the tip-sample interaction force, that depends on the tip-sample separation t_s is non-linearly related to p and often only a qualitative nature of tip-sample force (Φ) is known. The entire dynamics can be considered as a feedback interaction of a linear time invariant system G that models the cantilever and a static nonlinearity, Φ, in the feedback path [38]. This feedback interaction model of a linear

and time-invariant system with a static nonlinearity $\Phi = \frac{1}{m}F_{ts}$ is shown in Figure 6.4(a). The above feedback interconnection model consolidates the known information about the system G and the unknown part Φ into two separate operators that interact with each other.

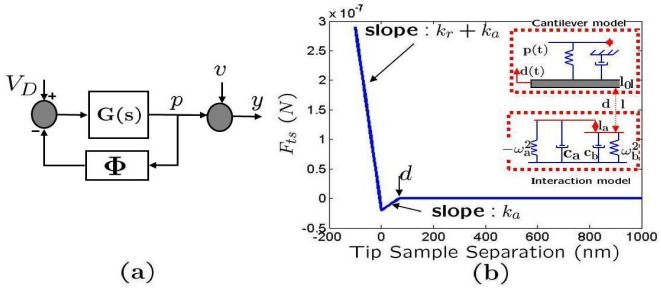

Figure 6.4: (a) The feedback interconnection model encapsulates the interdependence of the cantilever tip-deflection p and the tip-sample interaction force F_{ts}. The cantilever is modeled as a linear time invariant system $G(s)$ that takes as the input the dither V_D and the tip-sample interaction force h (per unit mass) and provides the tip deflection p as the output. The tip-sample interaction force (per unit mass) takes as the input the tip deflection p and provides the tip-sample force per unit mass h as the output. The static nonlinearity Φ typically also depends on the tip velocity $\dot{p}$. The signal y is the photo-diode output that provides a corrupted version of the tip-deflection p with v being the measurement noise. (b) Piecewise linear model of the tip-sample interaction. k_r and k_a denote the repulsive and attractive spring constants. d is the parameter that characterizes the difference in separations between the onset of attractive and repulsive forces. d is a good measure of the thickness of the adhesion layer

A piecewise linear model is assumed to approximate the tip-sample interaction force described by

$$\begin{aligned} F_{ts} &= 0 && \text{if } t_s > d \\ &= k_a(t_s - d) && \text{if } 0 \le t_s \le d \\ &= k_r t_s + k_a(t_s - d) && \text{if } t_s \le 0 \end{aligned} \tag{6.2}$$

where t_s is the tip sample separation, d is a parameter that characterizes the onset of the attractive interaction, k_a is the spring constant modeling attractive tip-sample interaction forces and k_r is the spring constant modeling repulsive forces [38]. The origin is placed at the onset of the repulsive interaction (see Figure 6.4(b)). This model

depends on the parameters $k_r,\ k_a$ and d. Effects of adhesive and meniscus forces are accounted for by suitably modifying parameters d and k_a.

The main source of inducing oscillations in the lever are electrostatic where a voltage differential is applied between the cantilever and the sample. The cantilever acts as one plate of a capacitor while the substrate forms the other plate. The cantilever feels a capacitive force denoted by F_{esf} that depends on the difference of potentials on the cantilever and on the sample. When the voltage V_R is applied across the legs of the cantilever and V_{sub} is applied to the sample, that can be assumed uniform across the substrate, the voltage difference between the cantilever and the sample varies with the spatial coordinate on the cantilever surface. This variation is caused due to variability of resistance along the cantilever. The cantilever surface and the substrate are modeled as a parallel plate capacitor with the voltage difference being

$$V_{esf} = \alpha_R V_R - V_{sub} \tag{6.3}$$

where α_R is the scaling factor that accounts for the non-uniform voltage on the cantilever surface. The capacitive (electrostatic) force on the cantilever is described by

$$\begin{aligned} F_{esf} &= -\frac{K_{esf} V_{esf}^2}{\ell_s^2} \quad \text{if } \ell_s > t_h \\ &= -\frac{K_{esf} V_{esf}^2}{t_h^2} \quad \text{if } \ell_s \leq t_h, \end{aligned} \tag{6.4}$$

where V_{esf} is given by (6.3), K_{esf} is an electrostatic force constant and $\ell_s = \ell_0 + p - z_s$ is the instantaneous lever-sample separation. The above characterization reflects the fact that if the lever-sample distance ℓ_s is smaller than the tip-height t_h then t_h governs the electrostatic force on the cantilever. The above model depends on parameters $K_{esf},\ \ell_0,\ t_h$ and α_R. Figure 6.5(b) shows the forces felt on the cantilever when the lever-sample separation ℓ_s is varied. Similar to the tip-sample interaction force, the cantilever deflection affects the electrostatic force, which in turn is affected by the electrostatic force. This scenario admits a feedback interconnection as shown in Figure 6.2 (dash-dot line). One crucial difference between the electrostatic and tip-sample forces is that electrostatic forces, though nonlinear, admit a more precise physical model. Unlike tip-sample interaction forces, (that are in a sense to be measured) electrostatic forces are introduced in a controlled manner. Figure 6.2 also shows the assumption that electrostatic and tip-sample forces appear additively on the cantilever. Measurement of

cantilever deflection p, is corrupted by white noise ν with a variance of 100 pm and the measurement of the thermal sensor output I_R, is corrupted by white noise γ with a variance of 107μA.

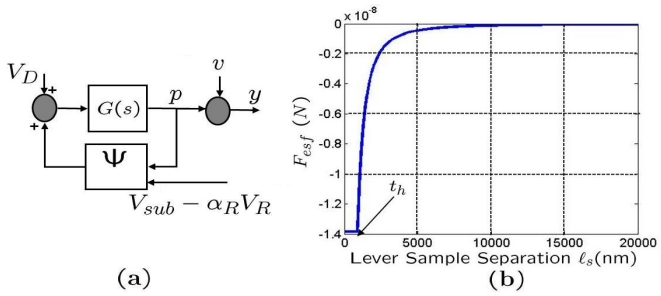

Figure 6.5: (a) The electrostatic force modeled by a feedback interconnection of a linear operator of the cantilever dynamics and the non-linear electrostatic force (b) Simulated electrostatic force felt by the cantilever when the lever-sample separation ℓ_s is varied.

6.4.3 Thermal Sensor Model

A voltage V_R generates a current $I_R = \frac{V_R}{R}$ through the cantilever depending on the instantaneous resistance R, of the cantilever. The generated heat with power $P = \frac{V_R^2}{R}$ dissipates by conduction through the cantilever as well as the sample through the surrounding medium. The operator Γ_{TP} (see Figure 6.2) maps the dissipated power to the thermal sensor temperature T. It is assumed that time constants relating the resistance and the temperature are negligibly small. It is thus assumed that a relation $R = g(T)$ holds, with g a nonlinear and memoryless map. Thermal sensor dynamics is also cast as a feedback interconnection (see Figure 6.2) wherein dissipated power leads to a temperature change of the sensor, which leads to a change in the sensor resistance, which in turn changes the power dissipated in the thermal sensor. Such a model was first developed in [65] to shape the temperature profile of the write heater for the contact mode operation. In this thesis, sensing dynamics of the read heater (thermal sensor that is used to read bits in a high density data storage application) for dynamic mode operation is addressed. As the power dissipation depends on the applied voltage V_R, and tip-sample distance t_s, it follows that $\Gamma_{TP} = \Gamma_{TP}(V_R, t_s)$. The above description requires characterization of Γ_{TP} and $R = g(T)$. Unlike models for forces

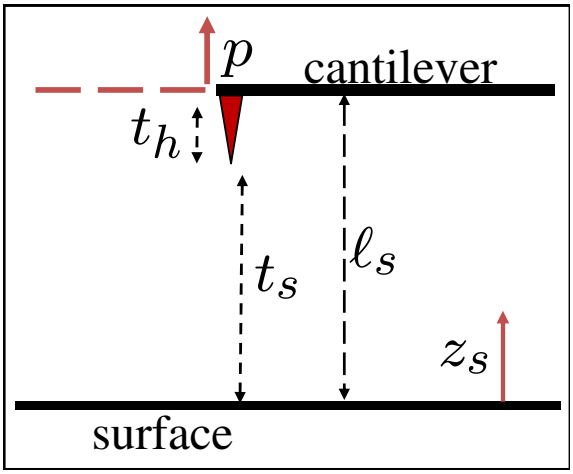

Figure 6.6: p and z_s are the tip-deflection and the sample position respectively. t_s and t_h are the tip-sample separation and the tip height respectively. ℓ_0 can be interpreted as the initial reference distance between the sample and a nominal point on the lever surface. The lever-sample separation ℓ_s is the instantaneous separation between the cantilever and the sample.

presented earlier, an exact form of the operator Γ_{TP} is not known for realistic cantilever geometries even though some intuition of the form of the Γ_{TP} operator is gained from closed form expressions derived for simplified cantilever geometries [64].

6.5 System Identification

The characterization framework provided in the previous section assumes that (1) cantilever and the substrate form a parallel plate capacitor. Even though the sample remains flat, bending of the cantilever due to forces might violate these assumptions (2) adhesive, meniscus and tip sample interaction forces appear as single piecewise linear forcing (3) cantilever mechanical response is in cascade with the thermal sensor dynamics. Typically, the temperature, $T(x,t)$, is a function of position (x) along the legs and time. Thus, the operator Γ_{TP} that maps the thermal sensor voltage, V_R, and tip-sample separation, t_s, to thermal sensor temperature, T, is also dependent on x. In this study we assume a lumped parameter model wherein T, not a function of x, is

able to predict changes in thermal sensor current, I_R. This makes the operator Γ_{TP} independent of x. As will be demonstrated later, these assumptions are realistic, and furthermore an effective means of identifying parameters from experimental data will be developed. As optical sensing is not available in many integrated applications, it will be shown that model parameters can be identified accurately using only thermal sensor measurement and electrostatic actuation. The optical deflection signal will be used to verify the accuracy of identified parameters and understand dynamics of the cantilever beam.

6.5.1 Laser-Photodiode Sensor Based Identification

Static mode approach curves with tip-sample and electrostatic forces provide the first means of characterizing model parameters. Consider the cantilever that is experiencing a force $F(p, q)$ where p is the deflection of the cantilever and q is an independent parameter that is available as an input. For example, q can be the sample position z_s that can be changed by using the piezo positioner or it can be the electrostatic potential V_{sub} applied to the sample substrate. Assuming a one mode approximation as given in (6.1), it is straightforward to show that the equilibrium position p is unstable if $\frac{\partial F(p,q)}{\partial p} > k$ where k is the stiffness of the cantilever. If this condition occurs while the tip is coming closer to the sample then the tip "snaps-in" with the sample otherwise the approach is smooth. Note that in (6.1), the resonant frequency $\omega_0^2 = \frac{k}{m}$ where k is the spring constant of the cantilever and m is the mass of the cantilever.

The electrostatic approach curve is obtained by using V_{sub} as the input q and recording both the optical measurement and the thermal measurement. V_{sub} is ramped up quasistatically in a linear manner and then ramped down linearly. During this process V_R is maintained at a set voltage. Note that for the electrostatic approach curve both the tip-sample interaction forces and the electrostatic forces affect the cantilever. Thus $F(p, V_{sub}) = F_{esf}(p, V_{sub}) + F_{ts}(p)$. At relatively large tip-sample separations (termed Region 1) the tip-sample interaction force is minimal and can be neglected. Assuming that the piecewise linear model (see (6.2)) of the tip-sample interaction force holds, if the tip-sample separation $t_s > d$ then the tip-sample interaction force is zero. In such a case, as V_{sub} is increased, the cantilever tip assumes a new equilibrium position that

satisfies

$$\begin{aligned} kp = F_{esf} &= -\frac{K_{esf}V_{esf}^2}{\ell_s^2} \\ &= -\frac{K_{esf}(-V_{sub}+\alpha_R V_R)^2}{(\ell_0+p)^2}. \end{aligned} \tag{6.5}$$

This implies that the (p, V_{sub}) pair satisfies the polynomial

$$(k)p^3 + (2\ell_0 k)p^2 + (\ell_0^2 k)p = -(K_{esf}(-V_{sub} + \alpha_R V_R)^2). \tag{6.6}$$

This polynomial dependence in the measured quantity p and the applied V_{sub} can be used to identify related model parameters $k,\ \ell_0,\ K_{esf}$ and α_R when the optical sensor is available for measuring the deflection signal p.

6.5.2 Thermal Sensor Based Identification

In this section, the aim is to estimate all physical parameters of the system, in Figure 6.2, from thermal sensor measurement alone and to compare estimates with ones obtained from the optical signal.

I-V curves and resistance as a function of temperature

In this part we provide a method to identify $g(T)$. The input V_R is first ramped up and then ramped down in a quasistatic manner at 3 Hz and the signal I_R is recorded (see Figure 6.2 and Figure 6.7(a)). Since the current and the applied voltage V_R are known, the resistance $R = \frac{V_R}{I_R}$ can be found. Similarly, once R is known, the power $\frac{V_R^2}{R}$ can be evaluated. As the power P or the current through the thermal sensor is increased, beyond a value P_k, characteristics of the sensor change abruptly due to intrinsic carrier thermal runaway [68, 69]. The temperature T_k at which this breakdown of the sensor happens depends on the doping concentration of the heater and is assumed to be known (which was 550 ^0C for the present study). The power P_k at which the breakdown happens can be read from the data by recognizing the "knee" in the $P - V_R$ relationship. Note that the temperature at the thermal sensor is T_r (the room temperature) when the power is zero. From the above identification, the pair (T_k, P_k) is known. In the above experiment where V_R is ramped up and down, the ramp input is slow. Therefore, from the linearity assumption of the power-temperature map Γ_{TP}, at a particular tip-sample separation, it follows that the slope of the line joining $(T_r, 0)$ and (T_k, P_k) identifies

K_{TP}, the DC gain of Γ_{TP}. Once this information is obtained, the temperature T can be found at various values of V_R. The resistance at corresponding values of V_R was found earlier and thus the functional dependence $g(T)$ of the resistance R on temperature T (see Figure 6.7(b)) can be found.

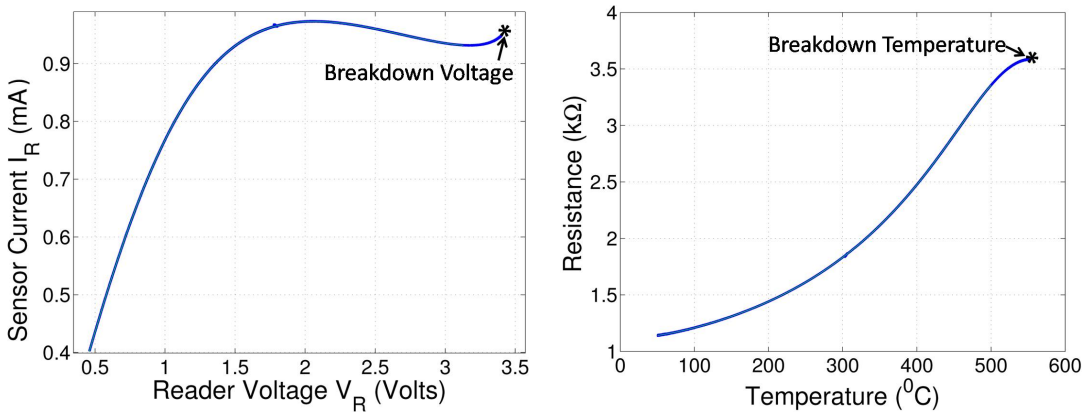

(a) (b)

Figure 6.7: (a) Experimentally obtained I-V curve. Voltage V_R is ramped up linearly from 0V till 3.5V and then ramped down linearly at 3 Hz. Thermal sensor output I_R is measured. This is done in a quasistatic manner so that at each point the thermal sensor is in equilibrium with its surroundings. Breakdown voltage is ≈ 3.4 V (b) Experimentally identified nonlinear static relationship, $g(T)$, between thermal sensor resistance (R) and temperature (T). This relationship is assumed to be same for all the operating points of V_R and t_s.

Relationship of power-temperature DC gain, K_{TP}, vs tip-sample separation, t_s

The relationship between the power-temperature DC gain K_{TP} and tip-sample separation t_s can be found by keeping V_R constant and performing a force curve with the sample position z_s as the input and I_R as the output. Such a force curve is shown in Figure 6.8(a).

Note that for a given V_R and z_s, as I_R is known, $R = \frac{V_R}{I_R}$ can be evaluated and thus $P = \frac{V_R^2}{R}$ can be found. Also, as $g(T)$ and $g^{-1}(R)$ are functions that were evaluated previously, the temperature can be found by $T = g^{-1}(R) - T_r$. Thus the ratio $K_{TP} = \frac{P}{T}$ can be found at each value of z_s. The task of converting z_s to tip-sample separation

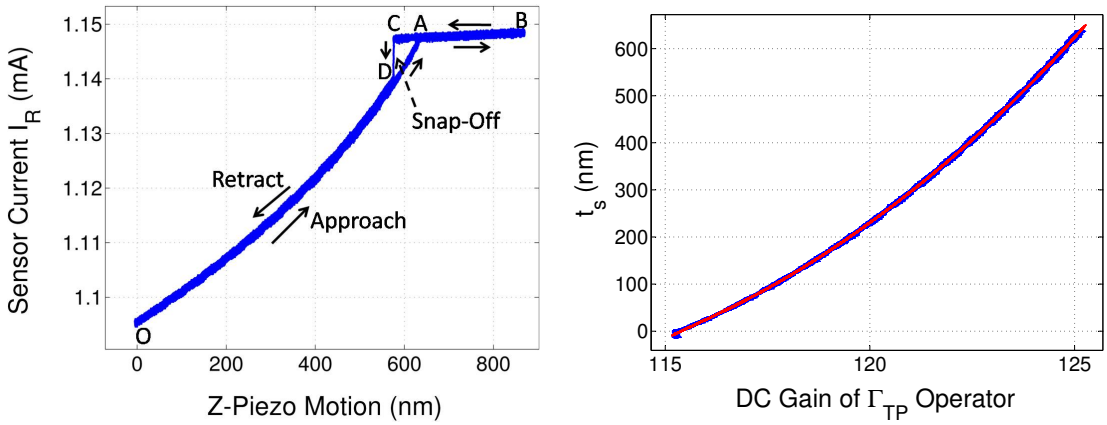

Figure 6.8: (a) The experimental z force curve with the monitored signal being I_R. z-piezo is ramped up linearly by a distance of 900nm and then ramped down at 3 Hz. Thermal sensor output I_R is recorded. Piezo is ramped up from O to A to B. At A, the tip comes into contact with the sample. The piezo is then ramped down from B to C to D to O. At C, the tip loses its contact with the sample. This is called snap-off. (b) Experimentally obtained DC gain of $\Gamma_{TP} = K_{TP}$ as a function of t_s is plotted. K_{TP} is a strong function of t_s which results in tip-sample separation sensing capability of the thermal sensor.

remains. It is assumed that the value z_{s_n} of z_s at which the tip snaps into contact with the sample in the $I_R - z_s$ force curve is where the tip-sample separation is zero. Cantilever bending is assumed to be negligible during z-force curve when the tip is not in contact with the sample. With these assumptions, the sample position z_s can be converted to t_s as $t_s = z_{s_n} - z_s$. As K_{TP} is known at each value of z_s, the plot of K_{TP} versus t_s can be obtained (see Figure 6.8(b)).

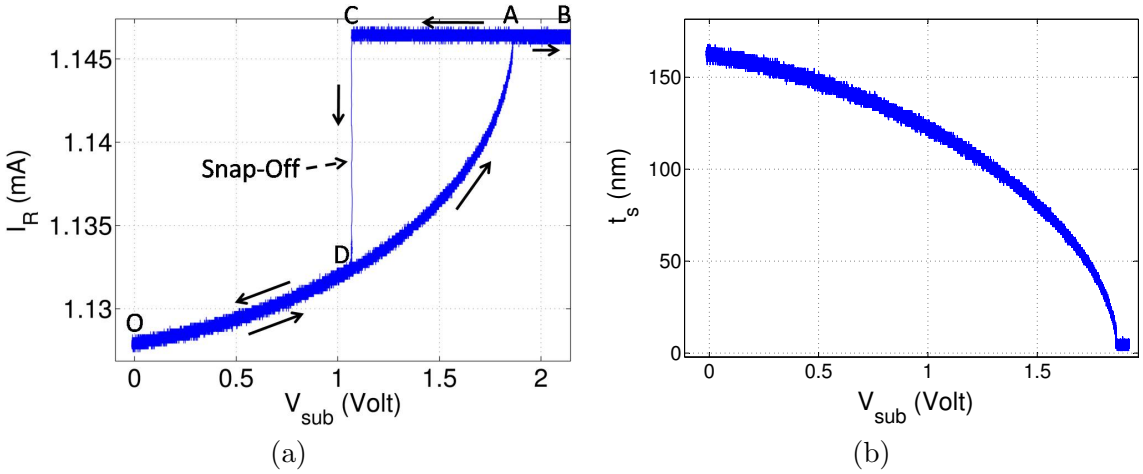

Figure 6.9: (a) Experimental electrostatic force curve with no snap-in i.e. the cantilever tip is in stable equilibrium with the forces at all the points in electrostatic force curve. V_{sub} is ramped up from O to A to B. At A, the tip comes into contact with the sample. The piezo is then ramped down from B to C to D to O. At C, the tip snaps-off the sample.(b) shows the I_R axis in (a) converted to the tip-sample separation t_s axis. This experiment is performed to check the validity of the assumptions made in converting the I_R axis to the t_s axis. The flat portion (t_s not changing with V_{sub}) should be at a value of $t_s = 0$. Small experimental value indicates that the assumptions made during conversion of z_s into t_s are reasonably valid.

The validity of assumptions to obtain K_{TP} vs t_s relationship is assessed by performing an electrostatic force curve where V_{sub} is ramped up and down at 3 Hz and I_R is recorded (see Figure 6.9(a)). V_R is chosen to prevent the tip from snapping into contact with the sample ([74]). I_R can be converted to t_s by following steps: $R = \frac{V_R}{I_R}$, $P = \frac{V_R^2}{R}$, $T = g^{-1}(R) - T_r$, $K_{TP} = \frac{P}{T}$. Once K_{TP} is known, using Figure 6.8(b), t_s can be evaluated. Thus the $I_R - V_{sub}$ plot is converted to $t_s - V_{sub}$ plot (see Figure 6.9(b)). Note that when $t_s = 0$ any further change in V_{sub} cannot change the

current I_R. Thus the value of t_s where the I_R remains constant (the part of the curve in Figure 6.9(b) that remains constant) should be zero. This value is approximately 5.8% of the entire trajectory. This discrepancy, though small, is attributed to partial violation of assumptions which were made during the conversion of z_s into t_s.

Electrostatic force curve for identification

Consider an electrostatic force curve with V_{sub} as input and I_R as the monitored variable where the tip does snap into contact with the sample (see Figure 6.10(a)). By converting I_R to t_s, the t_s versus V_{sub} plot, as shown in Figure 6.10(b), is obtained.

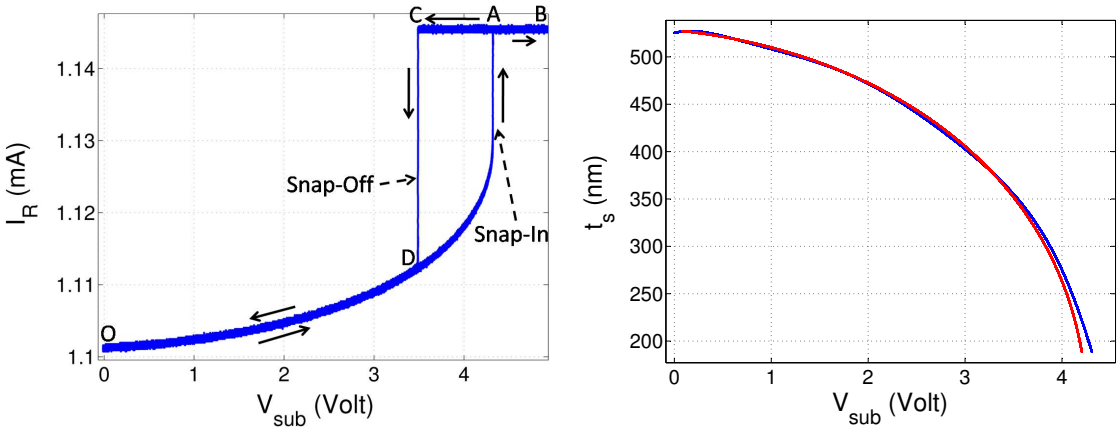

Figure 6.10: (a) Experimental electrostatic force curve with I_R vs V_{sub} plotted. V_{sub} is ramped up from O to A to B. At A, the tip comes into contact with the sample suddenly. This is called snap-in. The piezo is then ramped down from B to C to D to O. At C, the tip snaps-off the sample. The I_R axis is converted to the tip-sample separation axis; a polynomial fit is obtained to obtain a clean version of the data. The region where the tip-sample interaction forces are negligible is used to identify the model parameters. (b) shows the parameter fit (red-dashed) and experimental data (blue-solid). Estimated model compares well with the experimental data at large tip-sample separation. Slight deviation is observed at small tip-sample separation indicating that the parallel plate model for electrostatic force is not sufficient to capture the cantilever behavior in this region.

In the region of the force curve where the tip-sample interaction forces are negligible, forces on the cantilever are predominantly electrostatic and the equilibrium position

$p = t_s + t_h - \ell_0$ of the cantilever satisfies

$$k(t_s + t_h - \ell_0)(t_s + t_h)^2 \quad = \quad -K_{esf}(-V_{sub} + \alpha_R V_R)^2. \tag{6.7}$$

The above is a polynomial in data (t_s, V_{sub}) where coefficients k, t_h, ℓ_0, K_{esf} and α_R have nonlinear dependence on each other. Nonlinear least squares curve fitting algorithm [75] is used to identify the best fit to data in Figure 6.10(b). Parameters identified are $\alpha_R,\ K_{esf},\ k,\ t_h$, and ℓ_0 where k is the cantilever spring constant.

Estimation of mechanical cantilever parameters, viz. resonant frequency and quality factor of $G(j\omega)$, is done by fitting a second order transfer function around the resonance of the transfer function from V_{sub} to I_R (see Figure 6.11). Experimental data for this step is collected at a large tip-sample separation such that the electrostatic forcing does not alter the parameters of cantilever mechanical response, $G(j\omega)$ significantly. This provides an estimate of f_0 as 51.8578 kHz and quality factor, Q, as 2.37148. Estimating the relationship of the cantilever deflection p and the electrostatic forcing using only the thermal sensor measurement involves decoupling thermal sensor dynamics from mechanical dynamics of the cantilever. An optical beam-bounce method provides a direct measure of p without introducing its own dynamics and therefore provides precise characterization of the relationship between V_{sub} and p. The p-V_{sub} relationship as obtained independently from the optical beam-bounce measurement and from the thermal sensor measurement respectively is shown in Figure 6.12. Evidently with methods provided, there is a quantitative match of the thermal sensor based model response to the optical beam bounce based experimentally measured response, indicating that $G(j\omega)$ can be identified well from thermal sensor data alone.

Thus, using the above procedure, model parameters can be estimated fairly well using the thermal sensor output and actuation signal V_{sub}.

6.5.3 Virtual Position Sensor

The cantilever, the tip sample interaction and electrostatic interaction models can be identified based on the optical beam bounce measurement of the cantilever deflection p. The optical measurement does not introduce any new dynamics unlike the thermal sensor and therefore is expected to provide a more precise and easier identification of parameters. Such an identification strategy is reported in [48], which also demonstrates

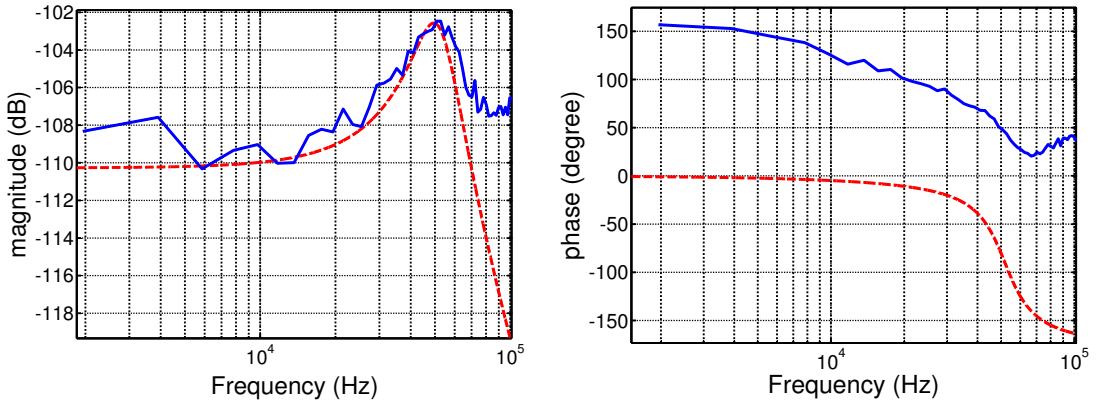

(a) (b)

Figure 6.11: Fitting a second order transfer function around the resonance in measured transfer function from V_{sub} to I_R (a) magnitude (b) phase. Blue solid line is the experimentally obtained response of $\Gamma_{\tilde{I}_R\tilde{V}_{sub}}$ and red dashed line is the second order fit around resonance. This process allows estimation of f_0 and Q of the cantilever from the thermally sensed data.

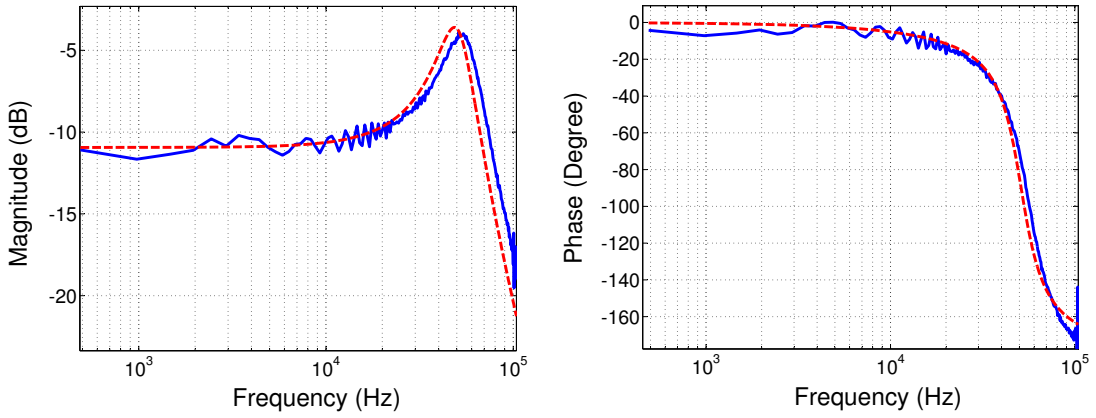

(a) (b)

Figure 6.12: Cantilever mechanical transfer function $G(j\omega)$ (a) magnitude comparison (b) Phase comparison. Blue-solid is experimental cantilever mechanical transfer function obtained using optical beam bounce method. Red-dash line is second order fit around the resonance of $\Gamma_{\tilde{I}_R\tilde{V}_{sub}}$ transfer function obtained using thermal sensor output I_R (see Figure 6.11). Good agreement between both the plots indicate that parameters for the cantilever mechanical transfer function can be estimated from the thermal sensor output alone in the absence of an optical sensor.

Parameter	Optical	Thermal
α_R	0.2504	0.2156
ℓ_0	1166 nm	1243 nm
K_{esf}	1.39744e-021	1.64991e-21
t_h	not estimated	711.75 nm
k	0.14123	0.13975
f_0	54.41 kHz	51.858 kHz
Q	2.1234	2.3715

Table 6.1: Comparison of the optical sensor and thermal sensor based identified parameter values

that optical sensor-based identified parameters quantitatively predict cantilever deflection. Table 6.1 provides a comparison of the parameters as identified by the thermal sensor using methods proposed earlier in the chapter, and the optical sensor based methods. The fact that these models are amenable to real time implementation and fast simulations facilitate better understanding of the device, and obviate the need for elaborate experiments to test various hypotheses. In an integrated environment, where optical position sensing is not available, the proposed technique enables estimation of parameters from thermal sensor measurement. One can then obtain estimates of cantilever position in real time from the implementation of this model. This can be viewed as a virtual position sensor that replaces the optical sensor.

6.6 Dynamic Characterization of Thermal Sensor

In this section, the notation $\Gamma_{\tilde{o}\tilde{i}}$ will denote the dynamic operator between the input i and output o. Thermal means of sensing topography enables an operation where an array of cantilevers can probe the sample in a parallel operation. However, the thermal sensor introduces new dynamics (unlike the optical beam-bounce method) that need to be understood for appropriate interpretation of data. Also, there are a number of applications where the thermal sensor is used to study thermal processes at the nanoscale. A dynamic characterization of the thermal sensor provides insights on how to better employ these sensors for fundamental studies of thermal transport, and also characterizes the limitations and capabilities of the sensor. In this section, the primary

aim is to understand thermal sensor dynamics and its relation to cantilever dynamics. Note that, in the previous sections, a quasistatic characterization of the thermal sensor was achieved.

Unlike the electrostatic force model where the form of forcing is known, physical models relating the power to the temperature of the thermal sensor for realistic cantilever geometries are not readily available for the operator Γ_{TP}. A characterization of the operator for quasistatic inputs is achieved in Section 6.5. Γ_{TP} operator can be linearized (see Figure 6.13) about (V_{R0}, t_{s0}) as follows:

$$\Delta T = \underbrace{\left.\frac{\partial \Gamma_{TP}}{\partial P}\right|_{P_0,t_{s0}}}_{C(j\omega)} \Delta P + \underbrace{\left.\frac{\partial \Gamma_{TP}}{\partial t_s}\right|_{P_0,t_{s0}}}_{H(j\omega)} \Delta t_s. \tag{6.8}$$

It is assumed that the temperature of the thermal sensor depends primarily on the

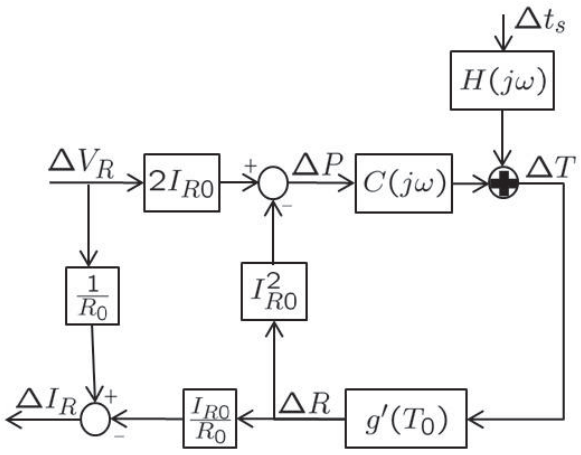

Figure 6.13: Small signal model for the thermal sensor about a nominal point (I_{R0}, R_0, T_0). Γ_{TP} has been linearized as in Equation (6.8). $C(j\omega)$ is the frequency response from ΔP to ΔT and $H(j\omega)$ is the frequency response from Δt_s to ΔT. Nonlinear operators $\frac{V^2}{R}, \frac{V}{R}, g(T)$ are also linearized to obtain the rest of the model.

power P, and the tip sample separation t_s.

As no physical model to describe the dynamics of the operator Γ_{TP} is available, the validity of the small signal model in (6.8) takes special significance. If the small

signal model is valid for practical operating conditions of dynamic mode, then one can identify the small signal model parameters in (6.8) using Fourier methods. One can thus overcome the lack of a tractable physical model of the operator Γ_{TP}. Fortunately, as is shown later in the article, a small signal model does suffice for quantitative prediction of thermal trajectories in the dynamic mode.

Nonlinear operators $\frac{V_R}{R}$, $\frac{V_R^2}{R}$ and $R = g(T)$ (see Figure 6.2) can also be linearized about the operating point $(I_0, R_0, T_0, P_0, t_{s0}, V_{R0})$ to obtain small signal model for the thermal sensor (see Figure 6.13). The dynamic relationships $\Gamma_{\tilde{I}_R \tilde{t}_s}$ (Sensing transfer function) and $\Gamma_{\tilde{I}_R \tilde{V}_R}$ (Thermal transfer function) that relate tip-sample separation to thermal sensor current and V_R to thermal sensor current respectively can be experimentally obtained by varying V_R and t_s while measuring I_R (the means of varying t_s are discussed later). Note that the sensing transfer function is of fundamental importance as it provides information on the speed with which the thermal sensor can measure the topography of the sample.

Using the small signal model shown in Figure 6.13, the following relationships can be derived:

$$\Gamma_{\tilde{I}_R \tilde{V}_R} = \frac{\Delta I_R}{\Delta V_R} = \frac{1}{R_0} \left[\frac{1 - g'(T_0) C(j\omega) I_{R0}^2}{1 + g'(T_0) C(j\omega) I_{R0}^2} \right], \tag{6.9}$$

$$\Gamma_{\tilde{I}_R \tilde{t}_s} = \frac{\Delta I_R}{\Delta t_s} = \frac{-I_{R0}}{R_0} \left[\frac{g'(T_0) H(j\omega)}{1 + g'(T_0) C(j\omega) I_{R0}^2} \right]. \tag{6.10}$$

From (6.9), it follows that

$$C(j\omega) = \frac{1}{I_{R0}^2 g'(T_0)} \left[\frac{1 - R_0 \Gamma_{\tilde{I}_R \tilde{V}_R}}{1 + R_0 \Gamma_{\tilde{I}_R \tilde{V}_R}} \right]. \tag{6.11}$$

Note that from (6.10) and (6.11) it follows that

$$H(j\omega) = \frac{-R_0}{I_{R0} g'(T_0)} \Gamma_{\tilde{I}_R \tilde{t}_s} \left[\frac{2}{1 + R_0 \Gamma_{\tilde{I}_R \tilde{V}_R}} \right]. \tag{6.12}$$

Such a relationship (6.11) provides useful information on the rate at which the thermal sensor can be heated and therefore translates into assessing, for example, the write speeds in a high density data storage application. Once $C(j\omega)$ and $H(j\omega)$ are identified, important closed loop relations (for example ΔV_R to ΔT) can be obtained, which reflect on the bandwidth with which the temperature of the thermal sensor can be changed using voltage V_R.

Electrostatic forcing of the cantilever changes the tip-sample separation t_s, allowing $\Gamma_{\tilde{I}_R\tilde{t}_s}$ to be obtained. The small signal model $\Gamma_{\tilde{t}_s\tilde{V}_{esf}}$ that relates small changes in V_{esf} to small changes in tip sample separation t_s, can be found by linearizing the nonlinear electrostatic forcing (6.4), as follows

$$\begin{aligned}
\underbrace{\ddot{p}+\frac{\omega_0}{Q_0}\dot{p}+\omega_0^2 p}_{G(j\omega)\text{ dynamics}} &= \omega_0^2\left(\frac{-K_{esf}V_{esf}^2}{(l_0+p)^2}\right) \\
\ddot{p}+\frac{\omega_0}{Q_0}\dot{p}+\omega_0^2 p &= \omega_0^2\left(\frac{-2K_{esf}V_{esf0}}{(l_0+p_0)^2}\Delta V_{esf}+\frac{2K_{esf}V_{esf0}^2}{(l_0+p_0)^3}\Delta p\right).
\end{aligned} \tag{6.13}$$

Thus the following relationships can be evaluated (see Figure 6.2) and are found to be

$$\begin{aligned}
\Gamma_{\tilde{p}\tilde{V}_{esf}} &= L\frac{\omega'^2}{s^2+\frac{\omega'}{Q'}+\omega'^2}, \\
\omega' &= \omega_0\sqrt{1-\frac{2K_{esf}V_{esf0}^2}{(l_0+p_0)^3}}, \\
Q' &= Q_0\sqrt{1-\frac{2K_{esf}V_{esf0}^2}{(l_0+p_0)^3}}, \\
L &= \frac{-2K_{esf}V_{esf0}}{(l_0+p_0)^2}\left[1-\frac{2K_{esf}V_{esf0}^2}{(l_0+p_0)^3}\right]^{-1},
\end{aligned} \tag{6.14}$$

where V_{esf0} and p_0 are nominal electrostatic voltage and cantilever deflection respectively, and it is assumed that sample height is not varying.

Remark: It is evident from (6.14) that Q' and ω' reduce as lever-sample separation (l_0+p_0) reduces. DC Gain L of frequency response $\Gamma_{\tilde{p}\tilde{V}_{esf}}$ increases as lever-sample separation decreases. Experimental results confirm these trends, as shown in Figure 6.14. As tip-sample separation increases, Q' and ω' converge to Q_0 and ω_0, latter being the cantilever model parameters without electrostatic forcing. L converges to zero indicating that the effect of electrostatic forcing reduces with increasing tip-sample separation. Cantilever parameter identification is therefore done at a tip-sample separation where Q' and ω' are close to Q_0 and ω_0, and L is sufficient to actuate the cantilever.

$\Gamma_{\tilde{t}_s\tilde{V}_{esf}}$, $\Gamma_{\tilde{I}_R\tilde{t}_s}$ and $\Gamma_{\tilde{I}_R\tilde{V}_R}$ can be represented as in Figure 6.15 where it is assumed that the cantilever sensor with V_{esf} as an input and I_R as the output can be modeled

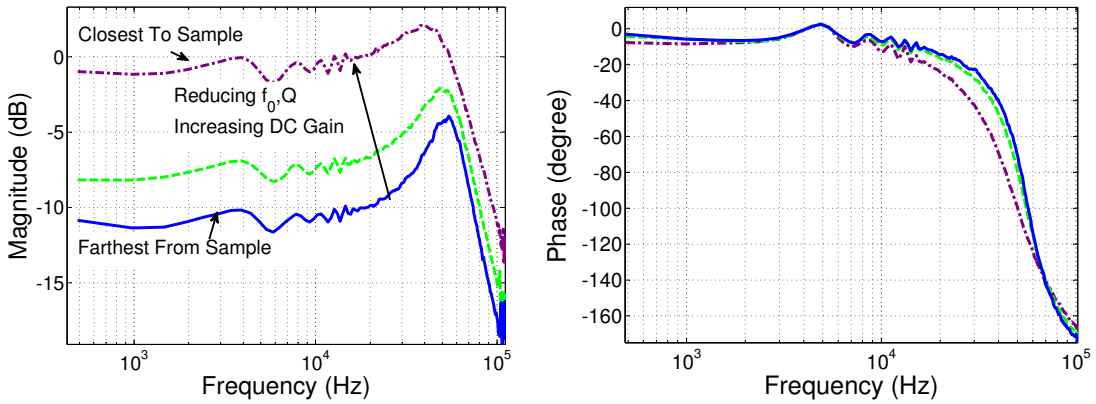

(a) (b)

Figure 6.14: Experimentally obtained magnitude and phase of cantilever mechanical transfer function (V_{sub} to p) at various tip sample separation. (a) Magnitude (b) Phase. Tip sample separation increases from top to bottom. DC gain increases with reducing tip-sample separation and f_0 and quality factor Q decrease with reducing tip-sample separation as indicated by Eqn 6.14

as a cascade in series of two maps: the mechanical transfer function that maps the substrate voltage V_{sub} to the tip deflection p, and the thermal sensing transfer function that maps the tip deflection p into the measured current I_R (Figure 6.15). Note that with the experimental setup in place, it is possible to monitor the tip deflection p as well as the thermal sensor current I_R. $t_s = l_0 + p + t_h - z$ (see Figure 6.6) and therefore we have $\Delta t_s = \Delta p$ since z, ℓ_0 and t_h are constant. Also as V_R is constant we have $\Delta V_{esf} = \Delta V_{sub}$.

6.6.1 Identification of Sensing Transfer Function ($\Gamma_{\tilde{I}_R\tilde{t}_s}$)

In this part of the chapter, experimental results and procedures for identifying the dynamic map $\Gamma_{\tilde{I}_R\tilde{t}_s}$ are presented. In related experiments, the voltage V_R is kept constant at 3 V. The sample is held fixed in the lateral direction and small-signal dynamic maps are obtained at various nominal tip-sample separations t_{s0}. The nominal tip-sample separation can be changed using a piezoelectric actuation based sample positioner.

The substrate voltage V_{sub} provided is sinusoidal (of the form $A\sin(2\pi f)$), with one volt peak to peak voltage. A sinusoidal V_{sub} with frequency at the resonant frequency,

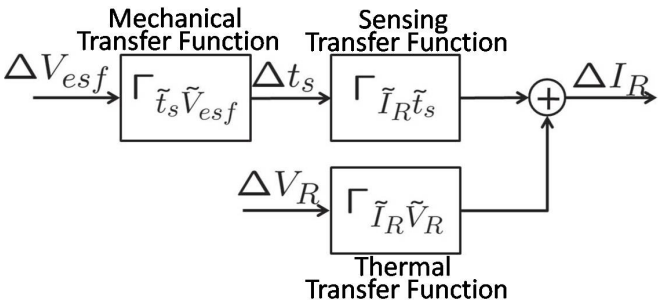

Figure 6.15: Simulation Model for an electrostatically actuated cantilever with integrated thermal sensor, about a nominal point of operation of dynamic mode operation. Tip sample separation t_s changes in response to changes in electrostatic voltage V_{esf} related by transfer function $\Gamma_{\tilde{t}_s \tilde{V}_{esf}}$. Any manifestation of sample profile z_s in the cantilever trajectory manifests itself in Δt_s. Δt_s perturbs the thermal system and results in a consequent change in the thermal sensor output I_R related by the transfer function $\Gamma_{\tilde{I}_R \tilde{t}_s}$. This map is low pass in nature with a bandwidth of approximately 12kHz (see Figure 6.19). Alternatively ΔI_R can also change through ΔV_R related by the transfer function $\Gamma_{\tilde{I}_R \tilde{V}_R}$. All these three maps are experimentally measurable.

f_0, of the electrostatically forced cantilever results in cantilever oscillations with approximately 60 nm amplitude. These amplitudes translate to practical values for dynamic mode operation. The thermal sensor current I_R and the optical deflection signal p are recorded. Effectively, data is recorded with $V_{sub} = A\sin(2\pi f)$, for various values of $f \in [0, 100 \text{ kHz}]$. At each V_{sub} actuation frequency f, the measured deflection signal p and the thermal signal I_R, are found to be nearly sinusoids with frequency f, with steady state amplitudes $|\hat{p}(j\omega)|$ and $|\hat{I}_R(j\omega)|$ respectively. The higher harmonics are negligibly small for most of the frequency range of f. The gains $|\frac{\hat{p}(j\omega)}{A}|$ and $|\frac{\hat{I}_R(j\omega)}{A}|$ and their relative phase with respect to V_{sub}, thereby identifying $\Gamma_{\tilde{t}_s \tilde{V}_{esf}}$ and $\Gamma_{\tilde{I}_R \tilde{V}_{esf}}$ (see Figure 6.15), are provided in Figure 6.14 and Figure 6.16.

Throughout the article an implicit assumption made is that the substrate voltage affects the thermal sensor current I_R only through the tip-sample separation. Thus, it is assumed that when there is a change in V_{sub}, the electrostatic force on the cantilever changes and therefore the cantilever deflection is changed, leading to a changed distance from the sample. This leads to a changed current due to the changed thermal sensor resistance. However, the cantilever is a current path that is present in an oscillating electric field and there is a possibility that the voltage V_{sub} directly affects the current I_R

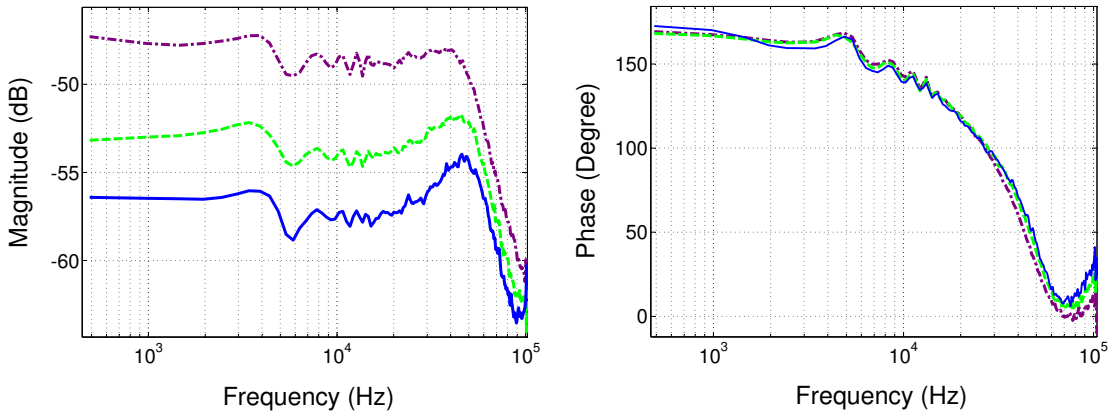

Figure 6.16: Experimentally obtained magnitude and phase of transfer function from V_{sub} to I_R at various tip sample separation. (a) Magnitude (b) Phase. Tip sample separation increases from top to bottom.

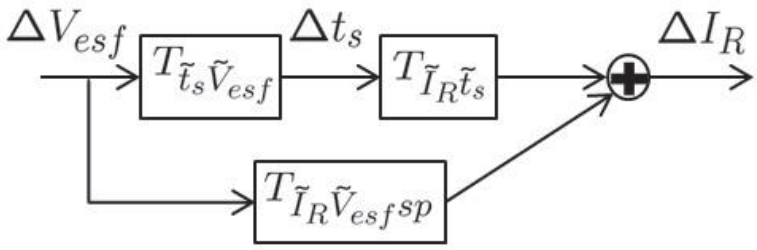

Figure 6.17: Modified Small Signal Simulation Model of the system about a nominal point of operation of dynamic mode to include a direct path from V_{esf} to I_R with no dependence on Δt_s which is called $\Gamma_{\tilde{I}_R \tilde{V}_{esf} sp}$. This needs to be included because oscillating V_{esf} voltage gives rise to oscillation on I_R even when $\Delta t_s = 0$ i.e. the tip is in contact with the sample. This can possibly be attributed to the capacitive or inductive coupling between cantilever and sample.

even when the tip-sample separation is unchanged (see Figure 6.17). In the setup, such a direct feedthrough term $\Gamma_{\tilde{I}_R\tilde{V}_{esfsp}}$, can be found by engaging the tip with the sample and then observing the current I_R while the substrate voltage V_{sub} is changed. As the tip remains in contact with the sample, Δt_s remains zero and thus the feedthrough term can be characterized. The corresponding data obtained when the tip is engaged with the sample, identifies $\Gamma_{\tilde{I}_R\tilde{V}_{esfsp}}$ and is presented in Figure 6.18.

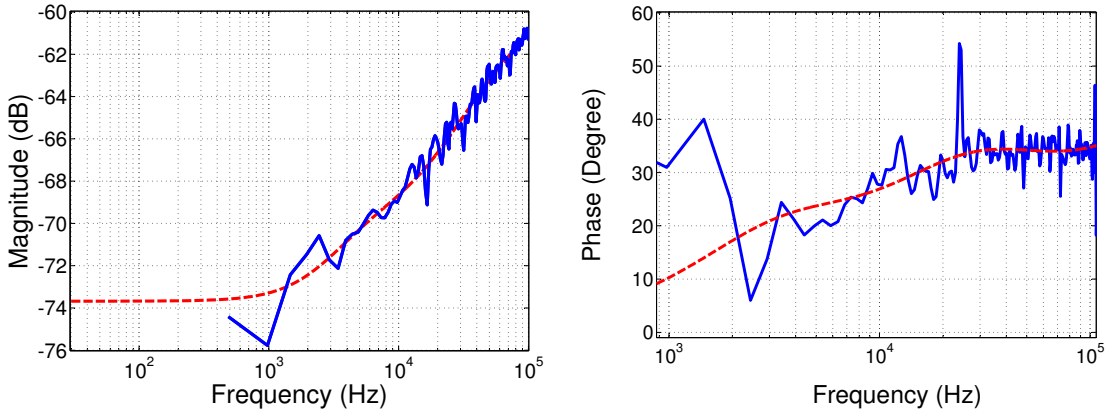

(a) (b)

Figure 6.18: Experimentally obtained magnitude and phase of $\Gamma_{\tilde{I}_R\tilde{V}_{esfsp}}$ close to the sample. (a) Magnitude (b) Phase. Blue-Solid: Experimental; Red-Dash: Transfer function fit to the data. Rise in magnitude and phase with frequency suggests of possible capacitive or inductive origins to this component of ΔI_R due to changes in V_{esf}.

The sensing transfer function is determined using the relationship

$$\Gamma_{\tilde{I}_R\tilde{t}_s} = \frac{\Gamma_{\tilde{I}_R\tilde{V}_{esf}} - \Gamma_{\tilde{I}_R\tilde{V}_{esfsp}}}{\Gamma_{\tilde{t}_s\tilde{V}_{esf}}} \tag{6.15}$$

with the tip close to the sample. Note that $\Gamma_{\tilde{I}_R\tilde{V}_{esf}}$, $\Gamma_{\tilde{I}_R\tilde{V}_{esfsp}}$ and $\Gamma_{\tilde{t}_s\tilde{V}_{esf}}$ have been experimentally identified. Figure 6.19 shows the sensing transfer function evaluated following (6.15) and presents a comparison with FEM simulations. The sensitivity of the thermal sensor output close to the sample is 102.63μA/nm and the bandwidth is nearly 12kHz. The sensing transfer function has a roll-off of 10 dB/decade as expected from theoretical calculations for the thermal sensor size under consideration [64]. Experimental identification of the sensing transfer function does not require any assumption on the form of Γ_{TP} once the overall block diagram (Figure 6.17) is fixed.

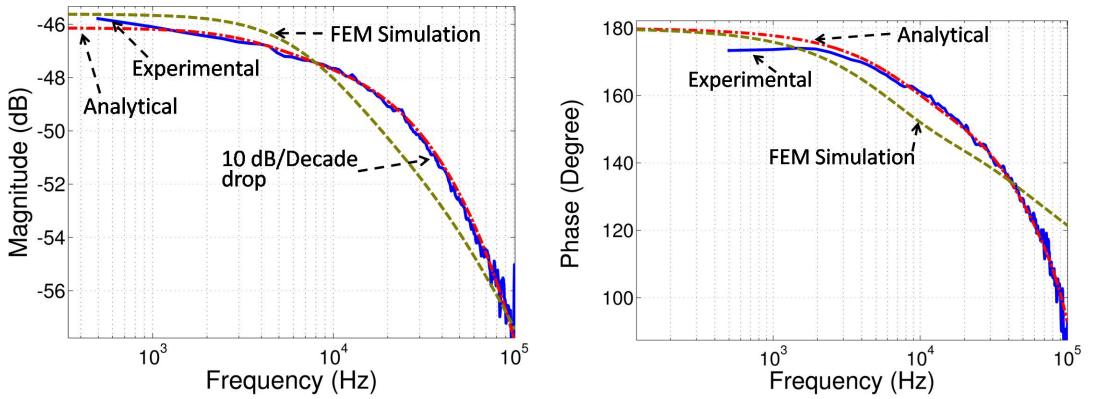

(a) (b)

Figure 6.19: Experimentally obtained magnitude and phase of sensing transfer function due to heat conduction processes. (a) Magnitude (b) Phase. Solid-Blue: Experimentally obtained without assuming any model for the thermal sensor using (6.15); Dash-Green: FEM Simulations; Red-dash/dot: obtained from (6.10) and experimentally obtained $H(j\omega)$. Experimentally obtained sensing transfer function matches with the results obtained from FEM simulations both in magnitude and phase. A 10dB/decade drop at higher frequencies and a bandwidth of approximately 12kHz is as expected from theoretical predictions.

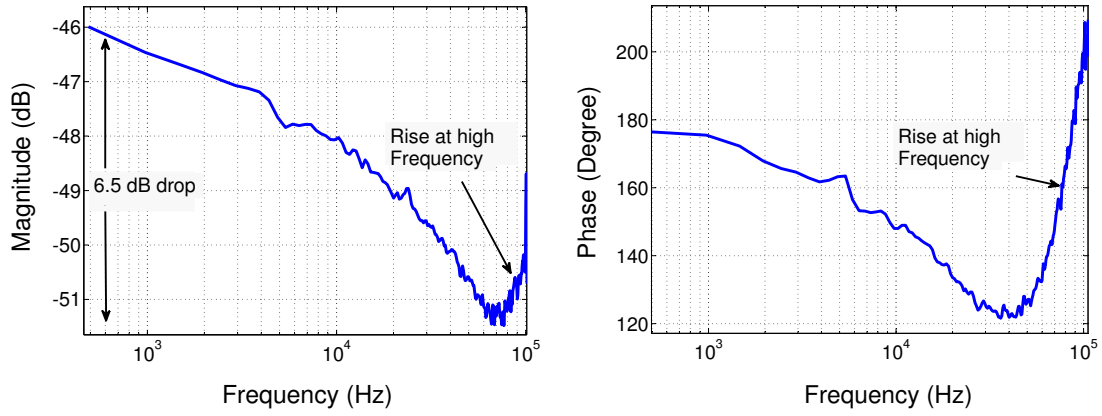

(a) (b)

Figure 6.20: Experimentally obtained magnitude and phase of transfer function from t_s to I_R at a tip sample separation close to the sample using (6.16). The total drop in magnitude plot from $0-100$kHz is around $5-6$dB and there is also a rise in magnitude and phase at high frequency. This is not in agreement with the theoretical predictions for the considered cantilever geometry.

Remark: Note that if the direct feedthrough term is neglected then the sensing transfer function can be found as

$$\Gamma_{\tilde{I}_R\tilde{t}_s} = \frac{\Gamma_{\tilde{I}_R\tilde{V}_{esf}}}{\Gamma_{\tilde{t}_s\tilde{V}_{esf}}}. \tag{6.16}$$

Such an evaluation results in $\Gamma_{\tilde{I}_R\tilde{t}_s}$ as shown in Figure 6.20. This agrees with the sensing transfer function shown in Figure 6.19 where the feedthrough term is not neglected except for the high frequency rise where Figure 6.20 shows a rise in magnitude. Such a rise is not corroborated by the existing analysis and FEM simulations. The conclusion is that the feedthrough term affects the high frequency region only and can be neglected if such a frequency region is not of interest.

6.6.2 Identification of $H(j\omega)$

We now seek to determine $H(j\omega)$, the dynamic map between t_s and temperature T, experimentally. Towards this goal, input perturbations of approximately 200mV are introduced at V_R about a nominal point of $V_{R0} = 3$V, and I_R is recorded. At this stage $g(T)$ and $g'(T)$ are known from methods described in Section 6.5.

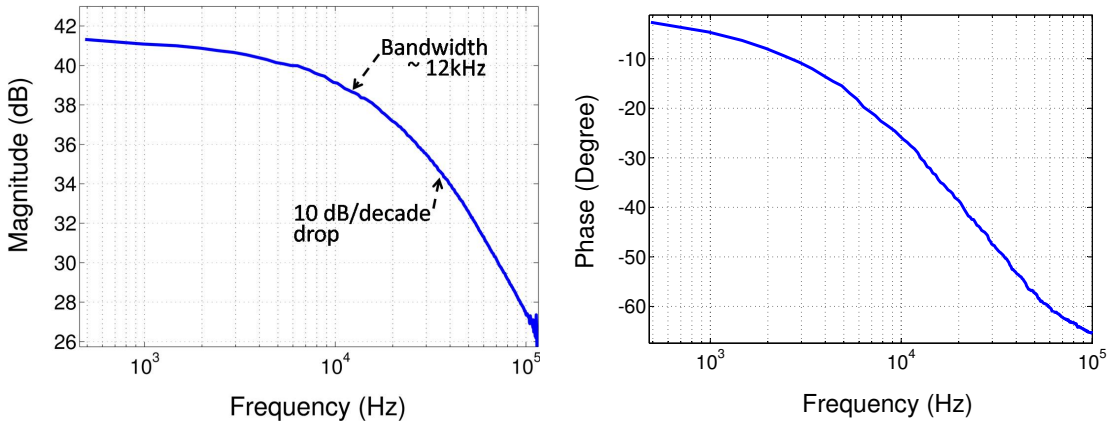

Figure 6.21: Experimentally obtained $C(j\omega)$ at a tip sample separation close to the sample (a) Magnitude (b) Phase

Figure 6.21 shows experimentally evaluated $C(j\omega)$ using methods outlined in [65] when the tip is close to the sample. It shows that $C(j\omega)$ has low pass characteristics with

roughly 10 dB/decade drop as expected for the thermal sensor size under consideration [64]. The power to temperature conversion factor when cantilever is close to the sample, represented by the DC gain of $C(j\omega)$, is 111 ^{0}C/mW and bandwidth is roughly 12kHz.

A method to evaluate $H(j\omega)$ is to use a nonlinear model (Figure 6.23) where we assume that data Δt_s (measured optically) and I_R are recorded and V_R is kept constant at a nominal value V_{R0}. At this stage, $C(j\omega)$ and $g(T)$ have been obtained experimentally. From the measurement I_R, $\Delta P = V_{R0}I_R - P_0$,$\Delta T = g^{-1}(\frac{V_{R0}}{I_R}) - g^{-1}(R_0)$ and $\Delta T_1 = \Delta T - \Gamma^{-1}(C(j\omega)) * \Delta P$ can be obtained where R_0, P_0 are the mean value of resistance and power, T_1 is the output of $H(j\omega)$ block and $\Gamma^{-1}(C(j\omega)) * \Delta P$ is the inverse Fourier transform of $C(j\omega)$ convolved with ΔP. Thus $H(j\omega)$ can be evaluated as $H(j\omega) = \frac{C_{\tilde{T}_1\tilde{t}_s}(j\omega)}{C_{\tilde{t}_s\tilde{t}_s}(j\omega)}$ where $C_{\tilde{T}_1\tilde{t}_s}(j\omega)$ denotes the cross covariance between Δt_s and ΔT_1, and $C_{\tilde{t}_s\tilde{t}_s}(j\omega)$ denote the auto covariance of Δt_s. Figure 6.22 shows experimentally obtained $H(j\omega)$ when the tip is close to the sample. DC Gain of $H(j\omega)$ is a positive value which increases with reducing tip-sample separation. Positiveness comes from the fact that a small reduction in t_s about a nominal point will further reduce the cantilever temperature. The increase in DC Gain with reducing tip-sample separation reflects increase in sensitivity with reducing tip-sample separation.

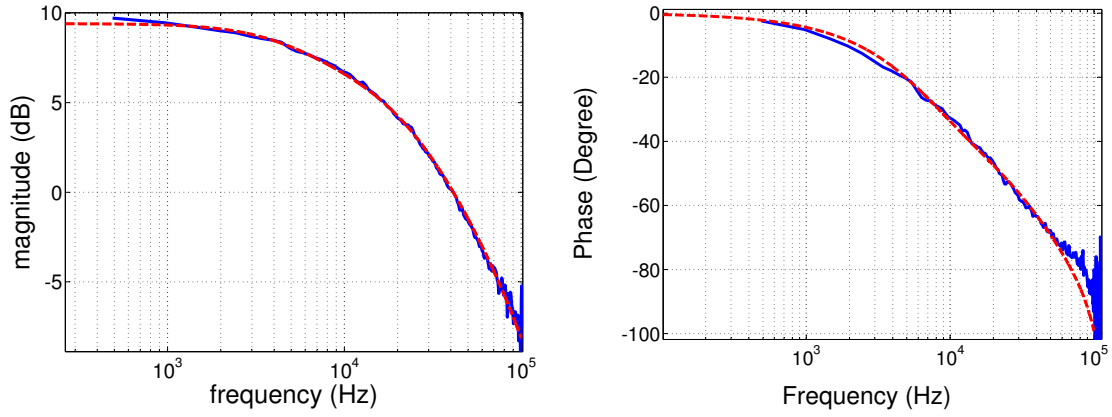

(a) (b)

Figure 6.22: Experimentally obtained $H(j\omega)$ (a) magnitude variation (b) phase variation. Deviation of $H(j\omega)$ from a simple DC gain indicates that there is dynamics in $H(j\omega)$ that needs to be considered during modeling. Blue-solid curve represents experimentally obtained data. Red-dash curve is an optimal transfer function fit to the blue curve.

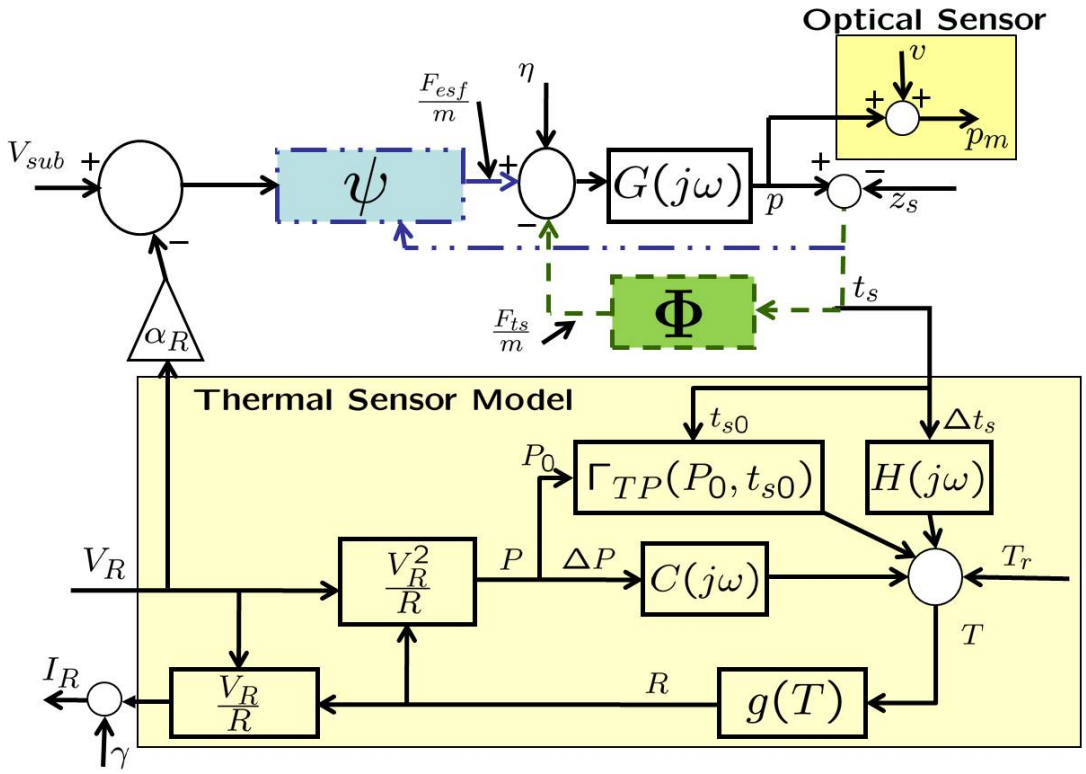

Figure 6.23: Large Signal Thermal Sensor Simulation Model with first order Taylor approximation of Γ_{TP} operator as given in (6.8). Nominal temperature T_0 is given by the relationship $\Gamma_{TP}(P_0, t_{s0})$ which is evaluated from z-force curves as explained in Section 6.5 and $C(j\omega)$ and $H(j\omega)$ are transfer function between $\Delta P - \Delta T$ and $\Delta t_s - \Delta T$ respectively.

$H(j\omega)$ evaluated in this manner can be substituted in (6.10) to obtain one estimate of sensing transfer function, $\Gamma_{\tilde{I}_R\tilde{t}_s}$. This estimate can be compared to the experimentally obtained sensing transfer function $\Gamma_{\tilde{I}_R\tilde{t}_s}$, assuming no models and using (6.16). Such a comparison is presented in Figure 6.19. The blue-solid curve is the experimentally identified sensing transfer function assuming no models, whereas the red-dash curve represents the sensing transfer function estimated using (6.10) and experimentally obtained $H(j\omega)$. There is a good agreement between the magnitude and phase response of the sensing transfer function using (6.10) and experimentally obtained $H(j\omega)$, and the sensing transfer function estimated assuming no models (see (6.15) and Figure 6.19). This indicates that linearization of Γ_{TP} operator and other nonlinear operators in the thermal sensor accurately capture system response to small input perturbations at V_{sub}.

6.7 Validation

6.7.1 Model Characterization and Validation using the Optical Based Deflection Measurement

The cantilever transfer function can be obtained by providing a chirp to V_{sub} and recording the deflection data p. A second order transfer function is fitted to obtain an input (V_{sub}) vs output (p) transfer function. The transfer function of the cantilever (see Figure 6.24) was estimated to be

$$G(s) = \frac{1.825e11}{s^2 + 1.577e5s + 2.549e11}.$$

The resonant frequency and the quality factor of the cantilever were determined to be $f_0 = 80.354$ kHz and $Q = 3.2015$, respectively. Using the piecewise linear model (6.4) to fit the experimental data, the parameters k_a, k_r and d were found to be $k_a = -0.29$ N/m, $k_r = 3.4$ N/m, and $d = 65$ nm.

Figure 6.25(b) shows the experimentally obtained electrostatic approach curve using photodiode current as the deflection sensor. As V_{sub} is increased, the deflection follows the curve from a to b. Any further increase in V_{sub} leads to the snap-in condition where the cantilever tip makes contact with the sample at c. As V_{sub} is reduced, the cantilever snaps out of contact at d and jumps to e before retracing its path from f to a. Region 1 (a to b), corresponds to the electrostatic approach curve before snap-in occurs. The

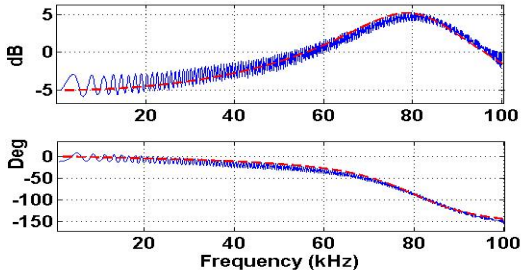

Figure 6.24: A chirp signal from DC-100 kHz is applied at V_{sub} and the photodiode voltage is recorded. The input-output transfer function is estimated using Matlab. The plot shows the comparison of the estimated (red-dash) and the experimental data (blue-solid)

vertical axis is converted to nm by using the sensitivity S (30 nm/V) obtained using the contact mode approach curve (Figure 6.25(a)). If $t_s > d$ in any region of the electrostatic approach curve, then each value of (p, V_{sub}) provides one relation (6.6) that is a polynomial in p with coefficients of the polynomial related. This aspect can be exploited to find the coefficients that best satisfy the relations imposed by (6.6). A nonlinear curve fitting algorithm based on trusted region is employed to determine a polynomial of the form (6.6) for the initial $a-b$ part of the approach curve where it can be assumed that tip-sample separation $t_s > d$ and therefore the cantilever experiences no interaction force. $V_R = 3V$ for the data presented. The parameters identified are $k = 0.16486$ N/m, $\ell_0 = 1318.25$ nm, $K_{esf} = 1.24 \times 10^{-21}$ F-m, $\alpha_R = 0.2085$.

In this part, experimental results are compared with model-based simulation results with the model parameters as identified previously. Figure 6.26(a) shows the comparison of the experimentally-obtained z approach curve (piezo positioner is moved in the z direction and the deflection signal is captured) with the one obtained from the simulation model. The figure shows that the simulation model predicts the snap-in and snap-off points relatively accurately and predicts the cantilever deflection well in the repulsive region. Figure 6.26(b) shows the comparison of the experimentally obtained electrostatic approach curve (ramp is applied at V_{sub} and optical signal is captured) with the one obtained from the simulation model.

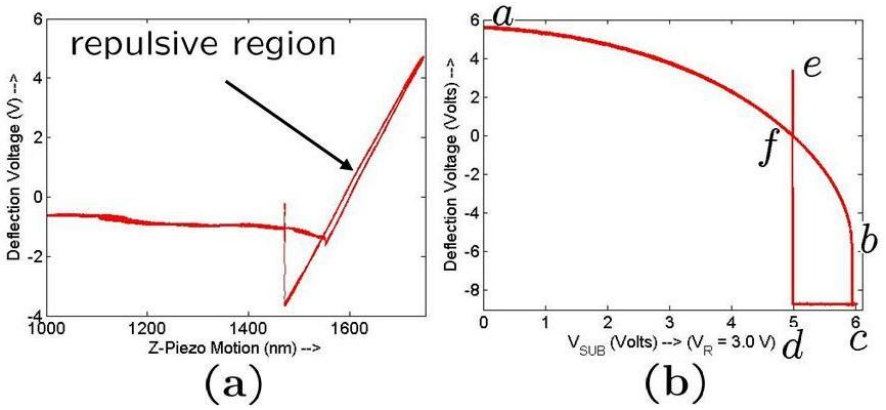

Figure 6.25: (a) Experimental optical Z-Approach curve. The slope in the repulsive region is the reciprocal of the photodiode sensitivity S. (b) Experimental optical electrostatic approach curve

Figure 6.27(a) shows the comparison between experimentally measured and simulated snap off response during Z-approach curve. Exact match of frequency reveals that the cantilever model is precise enough to capture the actual resonant frequency. Figure 6.27(b) shows the comparison between experimentally measured and simulated snap-off response during electrostatic approach curve. Exact match of frequency reveals that cantilever model also captures the reduction in resonant frequency due to electrostatic actuation.

Figure 6.28(a) shows the deflection trajectory as monitored by the optical lever when V_{sub} is a sinusoid at 1 kHz and the sample position z_s is altered in a square pattern with the square wave frequency of 3 Hz. Figure 6.28(b) shows the deflection trajectory as monitored by the optical lever when V_{sub} is a sinusoid at 50 kHz and the sample position z_s is altered in a square pattern with the square wave frequency of 3 Hz. These experiments are performed to evaluate the efficacy of the model in predicting the optical deflection trajectories when the tip encounters a sample profile. As is evident from the simulation and the experimental data a quantitative match is obtained with the simulation model capable of predicting intricate features like the snap-off conditions and the response after snap-off.

Figure 6.28(c) shows the deflection trajectory as monitored by the optical lever when

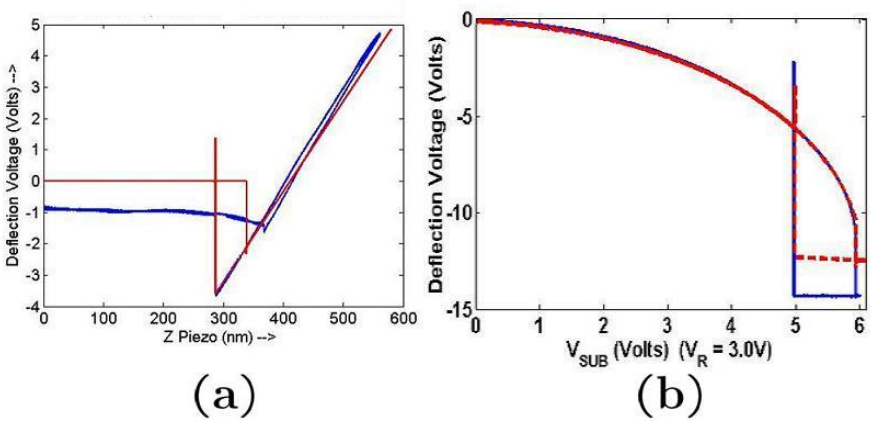

Figure 6.26: (a) The experimental (blue) and model predicted (red) z approach curves are compared. (b) The experimental (blue-solid) and model predicted (red-dash) electrostatic approach curves (V_{sub} is the input and I_R is the monitored variable) are compared

V_{sub} is a sinusoid at 1 kHz and the sample position z_s is altered in a sinusoidal pattern with the frequency of 3 Hz. Figure 6.28(d) shows the deflection trajectory as monitored by the optical lever when V_{sub} is a sinusoid at 50 kHz and the sample position z_s is altered in a sinusoidal pattern frequency of 2 kHz. The sample profile was discernible in the data indicating that topographic features can be read at 2000 bits/sec speeds.

6.7.2 Model Characterization and Validation using the Thermal Based Sensor Measurement

A characterized large signal model for the device is presented in Figure 6.23. The operator Γ_{TP} is modeled by using a small signal model with the DC part parameterized by nominal tip-sample separation and power P_0. To validate the identified model, simulation results are compared with experimentally obtained results . Thermal z-force curve is shown in Figure 6.29(a).

Identified parameters are able to reproduce the snap-in and snap-off in the z-force curve and also the slope of the curve in the repulsive regime accurately. Thus the piecewise linear model (6.2) for tip- sample interaction forces, adhesive and meniscus forces is accurate enough to capture important system behavior due to these forces. Thermal electrostatic force curve is shown in Figure 6.29(b) where a good quantitative agreement

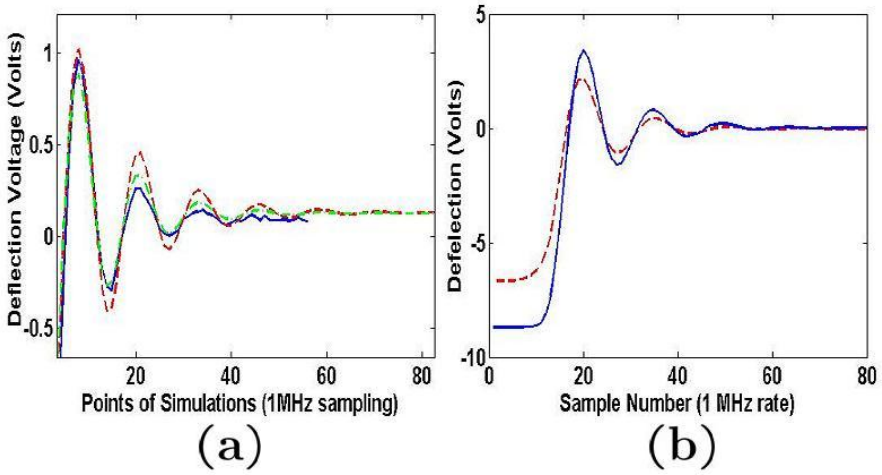

Figure 6.27: (a) The experimental (blue-solid) and model predicted (red-dash Q = 3.2, green-dash Q = 2.5) snap off response in Z-approach curves are compared. (b). The experimental (blue-solid) and model predicted (red-dash) snap off response in electrostatic approach curves (V_{sub} is the input and I_R is the monitored variable) are compared.

is obtained when the tip is away from the sample. Snap-in and snap-off instances of electrostatic force curves are not accurately captured and off-sample agreement indicates that an assumption of parallel plates for the electrostatic force model accurately predicts off-sample system behavior.

The model shown in Figure 6.23 is simulated for various V_{sub} profiles. It is seen that noninteracting optical and thermal trajectories are quantitatively predicted by simulations (see Figure 6.30 and Figure 6.31). Quantitative agreement between the simulated and experimental trajectories indicate that even though F_{esf} model (6.4) is not accurate for modeling quasistatic behavior near the sample, it is still able to quantitatively predict the overall trajectories near the sample. Periodic V_{sub} at low excitation frequencies yield I_R trajectories that are not sinusoidal, and the model is able to predict the phase and magnitude of harmonics to get a quantitative match. As the excitation frequency of V_{sub} is increased, the trajectories of I_R become sinusoidal because the cantilever mechanical response $G(j\omega)$ filters the higher harmonics of input excitation effectively. Linearized models (6.9-6.14) can thus be used at high actuation frequencies when the trajectories are near-sinusoidal while a nonlinear model is required for lower actuation frequencies for good prediction of experimental trajectories.

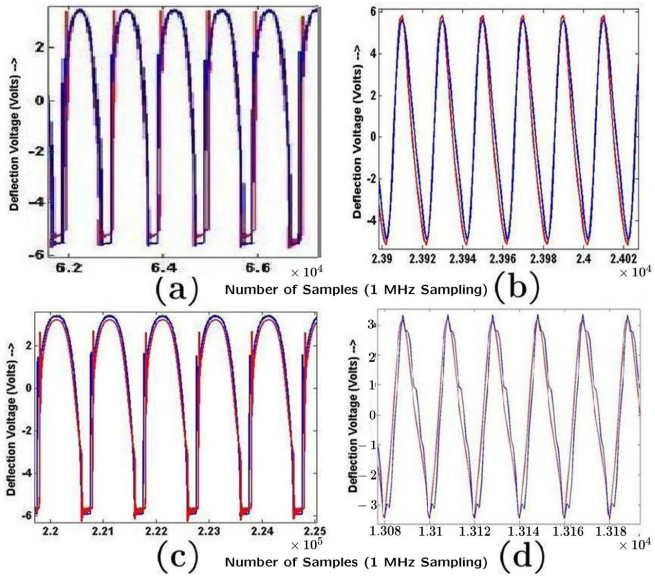

Figure 6.28: (a) and (b) show model predicted data (in red-dash) and experimental results (in blue-solid) when the sample follows a square wave profile at 3 Hz with the V_{sub} following sinusoidal pattern at 1 kHz and 50 kHz. Monitored data is the photodiode signal. (c) and (d) show model predicted data (in red-dash) and experimental results (in blue-solid) when the sample follows a sinusoidal wave profile at 3 Hz (c) and 1 kHz (d) with the V_{sub} following sinusoidal pattern at 50 kHz.

Interacting trajectories obtained by allowing the tip to interact with the sample at a single point for 1kHz and 10 kHz input excitation sinusoids are shown to agree with simulations (see Figure 6.32 and Figure 6.33).

Interacting trajectories are also periodic and non sinusoidal at low frequencies. These trajectories have more nonlinearities i.e. have more harmonics, as compared to non-interacting trajectories because they are also affected by the nonlinear tip sample interaction force. The model accurately predicts the change in harmonics with the input frequency. Interacting trajectories also become sinusoidal at higher excitation frequencies. Thus the model is accurate for on-sample and off-sample behavior of electrostatically actuated cantilever with integrated solid state thermal sensor. The model is also able to predict quasistatic large input signal behavior of the system accurately. Quantitative

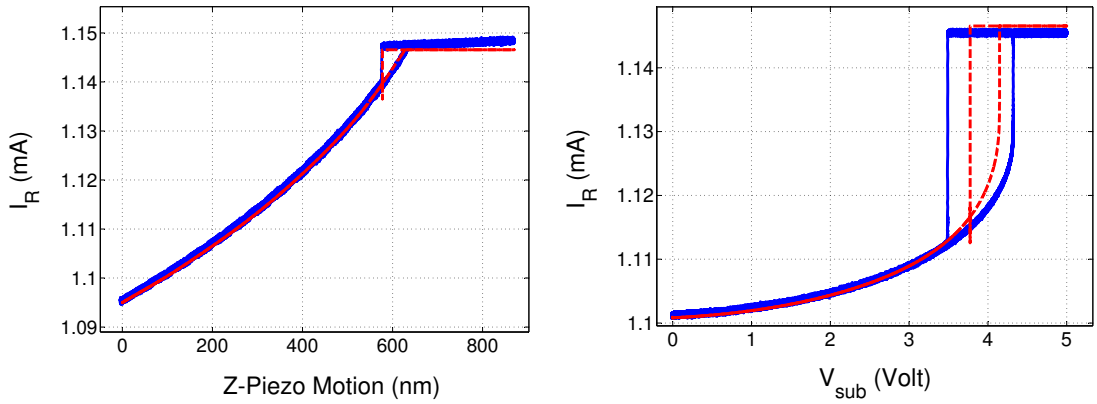

Figure 6.29: (a) z-force curve plotted between thermal sensor output I_R and z-piezo motion z_s. Experimental (solid-blue) curves agree well with the simulated curves (dash-red) curves indicating that the tip sample interaction model is able to capture snap-in, snap-off points and the slope in the repulsive region for tip interacting with the polymer sample. Quasistatic dependence of Γ_{TP} on t_s is calibrated well. (b) Electrostatic force curve plotted between the thermal sensor output I_R and substrate voltage V_{sub}. Blue solid line is experimental;Red dashed line is simulation. Electrostatic force curves agree quantitatively when the tip is far from the sample but tend to deviate slightly near sample because the parallel plate capacitor model for F_{esf} is not very accurate near the sample.

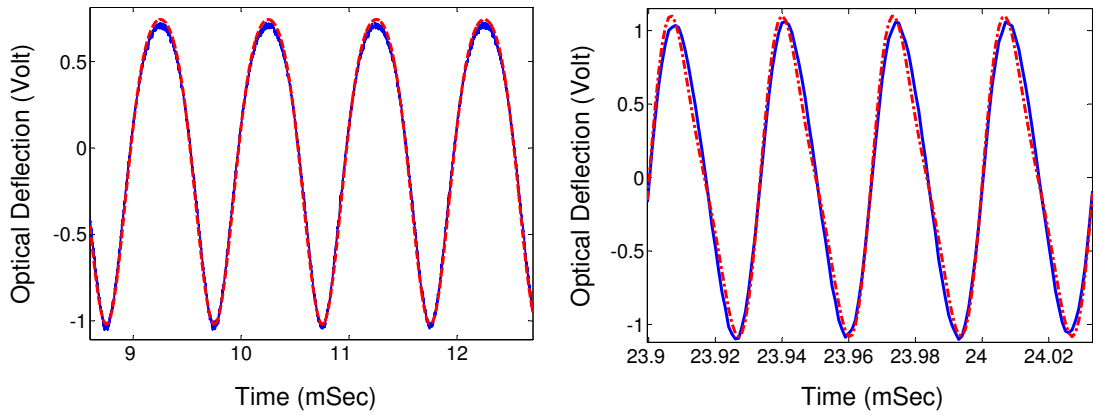

(a) (b)

Figure 6.30: Experimental (blue-solid curve) and simulated (red-dashed curve) non-interacting cantilever trajectories that are sensed optically are shown. (a) Cantilever response to 1kHz sine V_{sub} actuation measured optically (b) Cantilever response to 30kHz sine V_{sub} actuation measured optically. In these trajectories the tip is not interacting with the sample. Nominal distance of tip from the sample is approximately 70 nm. Cantilever trajectories are non-sinusoidal but periodic at low actuation frequencies. They tend to become sinusoidal at higher actuation frequencies because higher harmonics are filtered by the cantilever, $G(j\omega)$.

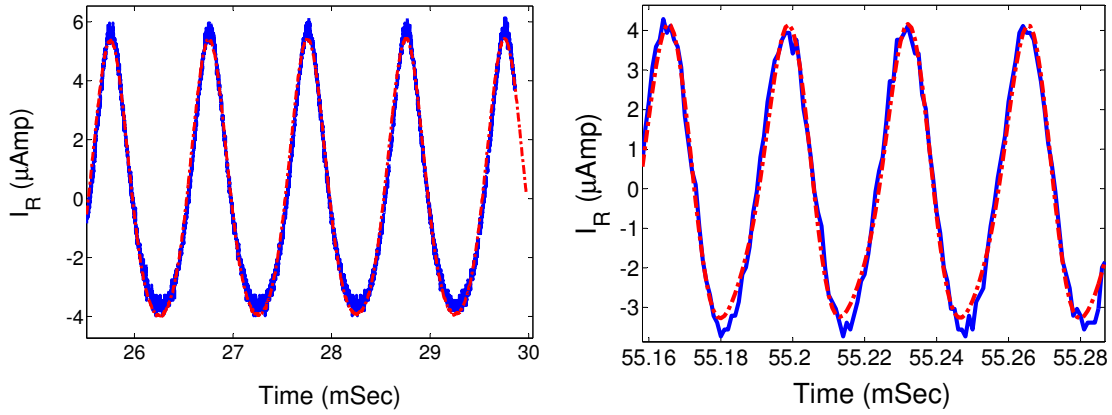

(a) (b)

Figure 6.31: Experimental (blue-solid curve) and simulated (red-dashed curve) non-interacting cantilever trajectories that are sensed thermally are shown. (a) Cantilever response to 1kHz sine V_{sub} actuation measured thermally (b) Cantilever response to 30kHz sine V_{sub} actuation measured thermally. Quantitative agreement between the simulated and the experimental trajectories at various frequencies indicate that experimental characterization of thermal sensing transfer function is accurate.

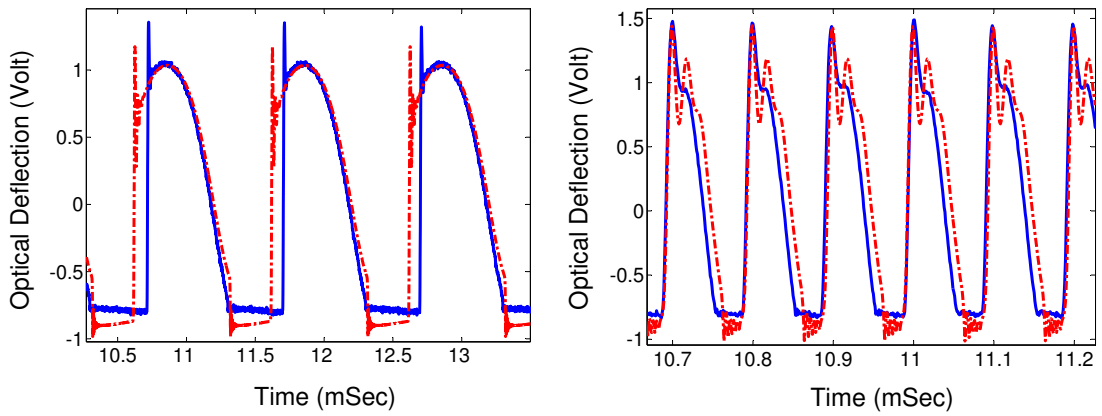

(a) (b)

Figure 6.32: Experimental (blue-solid curve) and simulated (red-dashed curve) interacting cantilever trajectories that are sensed optically is shown. (a) Cantilever response to 1kHz sine V_{sub} actuation measured optically (b) Cantilever response to 10kHz sine V_{sub} actuation measured optically.

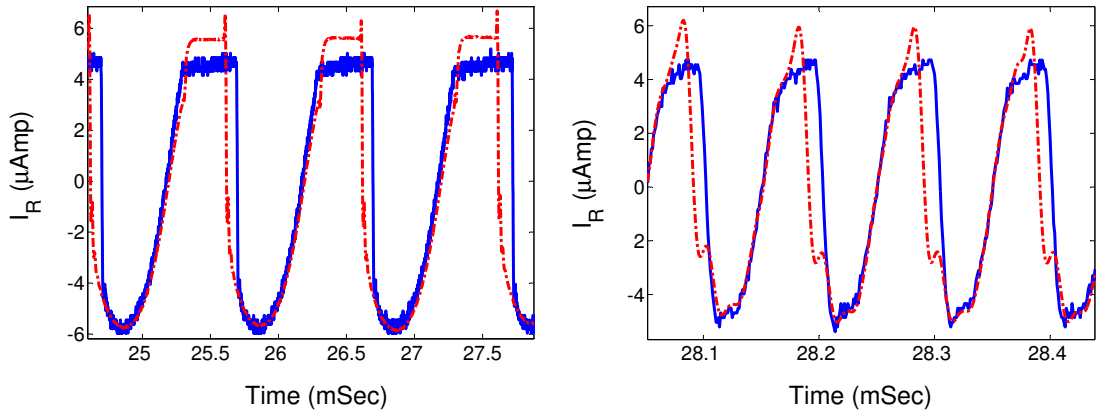

Figure 6.33: Experimental (blue-solid curve) and simulated (red-dashed curve) interacting cantilever trajectories that are sensed thermally is shown. (a) Cantilever response to 1kHz sine V_{sub} actuation measured thermally (b) Cantilever response to 10kHz sine V_{sub} actuation measured thermally. These trajectories result from tip interaction with the sample at a single point. At low actuation frequencies, snap-in and snap-off points are present in each oscillation cycle whereas their effect reduces as actuation frequency increases. Interacting trajectories also become sinusoidal at higher actuation frequencies.

agreement of the thermal sensor output for different input signals indicate that lumped parameter modeling for the thermal sensor accurately predicts its behavior.

6.8 Conclusion

This chapter presents a comprehensive modeling paradigm for a MEMS cantilever that is electrostatically actuated and has an integrated thermal sensor for topography measurement. It also provides a precise means of identifying model parameters. The proposed methodology is corroborated with experimental data to determine the reasonableness of the assumptions made in the modeling and identification procedures. It is evident that systems approach to modeling a MEMS cantilever, that interacts with the tip-sample potential and the electrostatic forces, provides an efficient means of predicting experimental data. A significant conclusion is that model parameters can be identified using thermal sensor data alone. This chapter further presents for the first time, an experimentally obtained sensing transfer function due to heat conduction processes till a bandwidth of $100kHz$ for an integrated solid state heater. A good match with FEM simulations is shown. A significant outcome of the work is a reliable simulation model that obviates the need for elaborate experimental validation.

Chapter 7

Model Mismatch Based High Bandwidth Electrostatic Force Microscopy

7.1 Introduction

Electrostatic force microscopy (EFM) and its variants like Kelvin Force Microscopy (KFM) and Scanning Capacitance Microscopy (SCM) are used extensively to probe the electrical properties of matter viz. local work functions, potential distributions, charge distributions, capacitance, polarization and piezo electric effects at nanoscale. [76, 77] summarizes the modes of operation and usage of these techniques.

To briefly summarize these modes of operation, in EFM, a voltage $(V_{DC}+V_{ac}\sin\omega t)$, is applied to the cantilever such that the local voltage difference between the lever and the sample is $(V_{DC}-V_{\phi}+V_{ac}\sin\omega t)$ where V_{ϕ} is the local potential of the sample that is closest to the tip. Force on the cantilever is modeled as

$$F_{esf} = \frac{1}{2}\frac{\partial C}{\partial z}(V_{DC}-V_{\phi}+V_{ac}\sin\omega t)^2 \tag{7.1}$$

There are a number of studies that model the effective capacitance between the cantilever and the sample ([78, 79]). There are three main contributing capacitances viz. the capacitance between the cantilever lever and the sample (C_1), capacitance between the cantilever tip cone and the sample (C_2) and the capacitance between the tip and

the sample (C_3). Total capacitance is $C = C_1 + C_2 + C_3$. The idea is to maximize C_3 and minimize C_1 and C_2 for enhanced spatial resolution. C_1 is reduced by increasing the tip height. C_3 is maximized by reducing the tip radius and operating the cantilever very close to the sample. Thus, it can be shown ([79]) that EFM sensitivity is approximately R where R is the tip radius, if the distance between the tip and the sample $\leq R$. Typically one can achieve sub 10 nm lateral resolution in EFM ([80]).

There are a number of implementations of EFM and related techniques for different applications. Initially the drive frequency 'ω' was kept way below the resonant frequency of the cantilever. Changes in cantilever deflection or resonant frequency were used to measure changes in sample properties ([76]). Then ω was chosen to be at the first mode mechanical resonance of the cantilever. This gave a boost to the sensitivity by a factor of 'Q' where Q is the quality factor of the cantilever. But there used to be considerable amount of crosstalk between the topography and the electrical properties ([76]). Thus lift-off mode was invented where in the first pass, the topography of the sample would be measured using the conventional methods. In second pass, the cantilever will be lifted by a known distance such that it is no longer interacting with the sample and the cantilever will be moved to negate the measured sample topography at each point, in an open loop operation. Sample or cantilever drifts effect this mode of operation and it is slow. Then the idea was developed to separate out mechanical oscillation frequency ω_{mech} of the cantilever with electrical oscillation frequency ω_{elec} of the cantilever such that the cantilever would be oscillated using the dither piezo at ω_{mech} which is typically the first mode resonant frequency of the cantilever and a constant interaction level will be maintained by regulating setpoint amplitude, phase or resonant frequency of ω_{mech}. Also simultaneously, the cantilever will be oscillated electrically by pulsating the voltage difference between the cantilever and the sample. There were many variations of choosing ω_{elec} but the more prevalent one is to choose ω_{elec} at second mode resonance of the cantilever. The net perturbation due to this secondary excitation is very minimal such that it does not alter mechanical interactions of the cantilever with the sample. Electrical properties are monitored by either monitoring ω, amplitude or phase of ω_{elec} or regulating them at a setpoint. Some studies show that there is still crosstalk between the topography and the electrical properties ([81]). Another variation of this technique has been developed to monitor electrical pulses in integrated circuits for fault detection

in manufacturing or for testing circuits. Since the operation of these circuits is in MHz and GHz range, the information cannot be observed by exciting the cantilever at its mechanical resonant frequency since that is approximately in the range of kHz- few MHz. So heterodyne and homodyne AC excitation techniques ([82]) were developed for these applications. In these applications, the AC voltage applied to the cantilever is in MHz or GHz and the voltage in the circuit is also assumed to be near this excitation frequency. Since voltage difference V, between the cantilever and the sample, appears as V^2 in the forcing term of F_{esf} (Equation 7.1), we get various inter modulation frequencies of these interactions which are at lower frequency and fall within the mechanical response bandwidth of the cantilever and these can then be monitored.

To understand the operation philosophy of EFM, the cantilever dynamics is modeled as

$$m\ddot{p} + c\dot{p} + kp = F_{esf}(p) + \eta(t). \tag{7.2}$$

Linearizing the dynamics about the operating point of the cantilever states we get

$$\begin{aligned} m\ddot{\tilde{p}} + c\dot{\tilde{p}} + k\tilde{p} &= \tfrac{\partial F_{esf}}{\partial p}|_{p_0}\tilde{p} + \eta(t). \\ m\ddot{\tilde{p}} + c\dot{\tilde{p}} + (k - \tfrac{\partial F_{esf}}{\partial p}|_{p_0})\tilde{p} &= \eta(t) \end{aligned} \tag{7.3}$$

Thus by monitoring the change in resonant frequency of the cantilever we can measure the force gradient due to electrostatic forces. Change in force gradient can be due to changes in various electrical properties of the sample ([76, 19]). But this does not provide quantitative measurements of these properties. KFM and SCM are used to obtain quantitative measurements. The idea is following

$$\begin{aligned} m\ddot{p} + c\dot{p} + kp &= \tfrac{1}{2}\tfrac{\partial C}{\partial p}(V_{DC} - V_\phi + V_{ac}\sin\omega t)^2 \\ &= \tfrac{1}{2}\tfrac{\partial C}{\partial p}\{\left[(V_{DC} - V_\phi)^2 + \tfrac{1}{2}V_{ac}^2\right] + 2(V_{DC} - V_\phi)V_{ac}\sin\omega t + \tfrac{1}{2}V_{ac}^2\sin 2\omega t\} \\ &= \tfrac{1}{2}\tfrac{\partial C}{\partial p}\left[(V_{DC} - V_\phi)^2 + \tfrac{1}{2}V_{ac}^2\right] + \tfrac{\partial C}{\partial p}(V_{DC} - V_\phi)V_{ac}\sin\omega t + \tfrac{1}{4}\tfrac{\partial C}{\partial p}V_{ac}^2\sin 2\omega t \end{aligned} \tag{7.4}$$

Now we can lock in on ω frequency and null it by choosing an appropriate V_{DC} such that amplitude of cantilever oscillation at ω is zero. At this point $V_{DC} = V_\phi$ and we can measure it quantitatively. This leads to KFM. To measure $\frac{\partial C}{\partial p}$ we need to lock in at 2ω. In this case ω can be so chosen such that 2ω lies at second mechanical resonant mode of the cantilever. $\frac{\partial C}{\partial p}$ can be measured by monitoring the changes in amplitude of 2ω oscillation.

Operation modes that are monitoring or regulating the changes in cantilever amplitude are slow since amplitude dynamics is dependent on cantilever dynamics. Higher quality factor cantilevers are preferred for higher operational sensitivities. This makes the amplitude dynamics slower and consequently the imaging is slower. This chapter presents model mismatch based EFM technique where the changes in the cantilever trajectory due to F_{esf} are monitored as deviations from the nominal cantilever trajectory by predicting the nominal behavior accurately.

The approach can be understood as follows. Suppose we apply a voltage $V = V_{DC} + V_{ac} \sin \omega t$ across the cantilever and the sample. The mean or nominal distance of the cantilever from the sample is ℓ_0 and the off-sample cantilever dynamics can be modeled as a second order spring mass damper system then the dynamics of the oscillating cantilever subjected to an electrostatic forcing, F_{esf}, is given by

$$m\ddot{p} + c\dot{p} + kp \quad = \quad \tfrac{1}{2} \tfrac{K_{esf} V^2}{(\ell_0 + p + z)^2} \tag{7.5}$$

The unknown parameters in this system are m, c/m, k/m, K_{esf} and ℓ_0. It must be noted here that we have modeled the capacitance between the cantilever and the sample as a parallel plate capacitor. A more detailed modeling for this capacitance can be done as presented in [78, 79] depending on the application. It must be noted that the form of nonlinear forcing is known since the cantilever is not interacting with the sample. This is critical since if the cantilever is interacting with sample then it will experience an additional Van de Waal's forces which cannot be precisely modeled a-priori. If precise characterization of this nominal behavior i.e. m, c/m, k/m, K_{esf} and ℓ_0 is possible then it should be possible for us to estimate using nonlinear observer, the nominal trajectory of this cantilever in presence of F_{esf}. When any of the parameters like K_{esf}, ℓ_0, z or V_ϕ changes due to changes in the external environment, it will induce perturbations into this trajectory which the observer can hardly track. Thus this residual nonlinear behavior which comprises of DC, f_0 and $2f_0$ residuals due to external changes can be measured with ultrahigh bandwidth since as long as we know the nominal, even slight deviation from that can be monitored assuming it is not embedded in noise.

7.2 System Identification

Precise system modeling and characterization techniques need to be developed to be able to predict the nominal trajectory of the cantilever accurately. An electrostatically actuated cantilever can be modeled as a forced Lure's model as shown in figure 6.5. The cantilever is modeled as a second order spring mass damper system with resonant frequency f_0 and quality factor Q. This transfer function is represented as G. This takes as input the nonlinear electrostatic forcing F_{esf} which is modeled as $F_{esf} = \frac{1}{2}\frac{K_{esf}V^2}{(\ell_0+p+z)^2}$. This forcing is dependent on the cantilever deflection p. This interaction can be modeled as a feedback interconnection between G and F_{esf}. Thus to be able to model the nominal system, we need to characterize the cantilever transfer function and the static parameters of the nonlinear electrostatic force.

7.2.1 Cantilever Model Identification

The cantilever transfer function from the electrostatic forcing to the cantilever deflection is represented by

$$G(j\omega) \quad = \quad \frac{\omega_0^2}{s^2+(\omega_0/Q)s+(\omega_0^2)} \tag{7.6}$$

Second order dynamics of the cantilever beam can be estimated using frequency sweep methods. In this thesis, we would assume that the cantilever deflection can be monitored using an optical beam-bounce method. Identification of the transfer function, G, can be done in two ways. In situation where the cantilever can be excited at the base using a dither piezo, then the cantilever transfer function can be measured by applying a frequency chirp at the dither piezo and simultaneously capturing cantilever deflection. Correlating cantilever deflection with applied frequency chirp provides us with the magnitude and the phase response of the cantilever. In situation where the electrostatic forcing is the only way of actuating, for instance in an integrated application viz. high density data storage ([18]), one has to be careful of choosing the initial tip-sample separation such that the electrostatic forcing is enough to move the cantilever but does not alter the cantilever resonant frequency significantly ([83]). This is explained in detail in chapter 6. Thus by applying a chirp in cantilever voltage, V, and capturing cantilever deflection and again correlating the two provides the transfer function of the cantilever response.

For present study, the cantilever transfer function was characterized by inducing an electrostatic actuation. The resonant frequency was 57185 Hz and the quality factor was 1.0148. The bode plot of the cantilever is presented in figure 7.1(a) and (b) where the blue curve is the experimentally obtained bode plot of the cantilever and the red curve is the second order transfer function fit to this response.

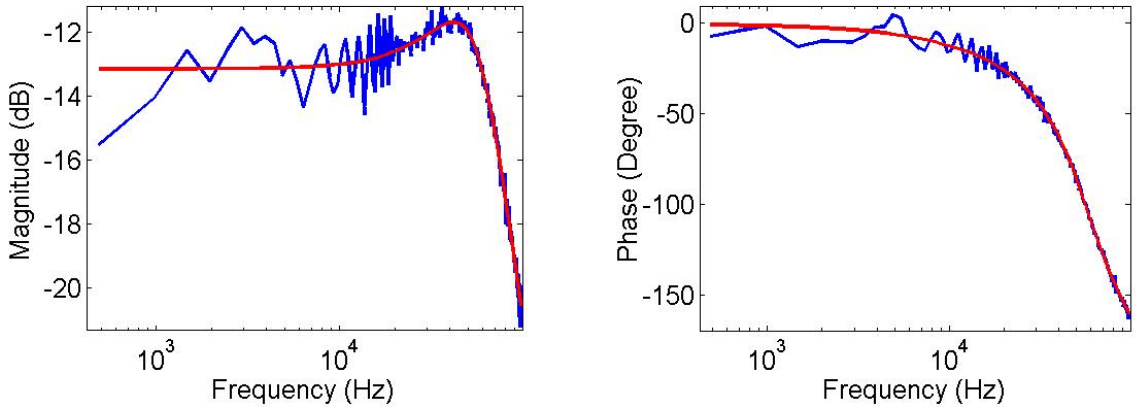

Figure 7.1: (a) Magnitude response and (b) phase response of the off-sample cantilever identified using input-output frequency sweep based method with electrostatic actuation and optical sensing. The blue curve is the experimentally obtained magnitude response of the cantilever and the red curve is a second order fit to the blue response.

7.2.2 Static Parameter Identification of Nonlinear Electrostatic Force

The static parameters of the nonlinear electrostatic forcing are identified next. Electrostatic forcing can be modeled as

$$F_{esf} = \frac{1}{2}\frac{K_{esf}(V_{sub}+\alpha_R V_R)^2}{(\ell_0+p+z_0)^2} \tag{7.7}$$

where voltage V_R is applied across the legs of the cantilever, V_{sub} is applied to the sample, α_R is the scaling factor that accounts for the non-uniform voltage on the cantilever surface and K_{esf} is an electrostatic force constant, ℓ_0 is the initial lever sample separation, z_0 is the changes in the sample topography and $\ell_0 + p + z_0$ is the instantaneous lever-sample separation. Here we are assuming that there is no variation in the system environment during the nominal characterization since we want to characterize the

nominal behavior of the cantilever. We have also assumed that the setup is similar to a parallel plate capacitor such that the electrostatic forcing is as given in eqn (7.7). This assumption is valid as long as the capacitance between the cantilever and the sample are the major contributing factor to the electrostatic forcing. In case the tip cone or the tip itself are the major contributing sources in electrostatic forcing, which will be the case in electrostatic force microscopy, then the equations of F_{esf} will need to be changed accordingly. The process and experimental demonstration in this work is based on eqn (7.7). For high resolution electrostatic force microscopy, one would need to choose a cantilever and operating conditions such that the tip capacitance is dominating. The methodology outlined in this work can still be applied with a different equation which are available in the literature.

These unknown parameters can be estimated by performing a quasi static electrostatic force curve. In this, a low frequency triangle wave is applied at substrate voltage, V_{sub}, such that the cantilever deflects till it snaps in contact with the sample and then snaps-out and comes back to its original starting deflection. Thus one can obtain an electrostatic force curve as shown in figure(7.2). Since the experiment is done such that force on the cantilever is in equilibrium at each point, we have the following relationship:

$$kp = -\tfrac{1}{2}K_{esf}\frac{(V_{sub}+\alpha_R V_R)^2}{(\ell_0+p)^2} \tag{7.8}$$

By using the fact that $-p = \ell_0 - t_s - t_h$, where t_h is the tip height and t_s is the instantaneous tip-sample separation, we get the following polynomial relationship between t_s and V_{sub}.

$$-k(t_s+t_h-\ell_0)(t_s+t_h)^2 = K_{esf}(V_{sub}+\alpha_R V_R)^2 \tag{7.9}$$

One can fit a nonlinear least squares curve fitting algorithm in eqn 7.9 to obtain an estimate of k, K_{esf}, ℓ_0, t_h and α_R. Optically sensed electrostatic force curve provides us a relationship between cantilever deflection and substrate voltage. To convert the cantilever deflection p into tip-sample separation t_s we assume the point at which the tip comes into contact with the sample as $t_s = 0$. With this assumption, we can obtain t_s from the measured cantilever deflection p. For the experiment done in this chapter,

those values were estimated to be

$$\begin{aligned} k &= 0.140431274517259 \text{ N/m} \\ K_{esf} &= 1.66457112363619e^{-21} \text{ F-m} \\ t_h &= 768.3 \text{ nm} \\ \alpha_R &= 0.254886399993193 \\ \ell_0 &= 1081.8 \text{ nm} \end{aligned} \tag{7.10}$$

It must be noted here that ℓ_0 value is experiment dependent unlike other static parameters which are system properties. These values were then fed to a simulation model and the experimental and simulated electrostatic force curves were compared (see figure 7.2). The blue curve represents the experimentally obtained electrostatic force curve and the green curve represents the simulated electrostatic force curve with identified force parameters. Slight mismatch between the two is due to inaccurate electrostatic force model assumed for this setup. It will be shown later that the proposed model based strategy is robust to such modeling errors.

7.3 Designing Extended Kalman Filter to Estimate Cantilever States in Presence of Noise

In this section, a nonlinear observer namely an Extended Kalman Filter will be designed to estimate the cantilever states in presence of process and measurement noise. The cantilever dynamics is represented as

$$\ddot{p}_1 + (\omega_0/Q)\dot{p}_1 + \omega_0^2 p_1 = \overbrace{-\frac{K_{esf}V^2}{k(\ell_0 + p_1 - d)^2}}^{f(p_1)} \tag{7.11}$$

In state space, the cantilever dynamics is represented as

$$\overbrace{\begin{aligned} \dot{x} &= Ax + B_1V^2 + B_2\eta; \quad x(0) = x_0, \\ y &= Cx + \nu, \end{aligned}}^{Plant} \tag{7.12}$$

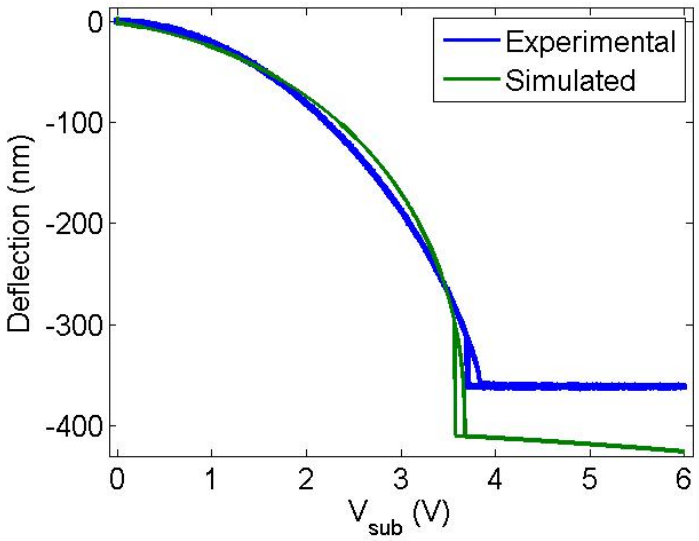

Figure 7.2: Comparison between the experimental and the simulated plot for electrostatic force curve of the cantilever. The simulations are done using the identified nonlinear forcing parameters and the cantilever transfer function. The blue curve indicates the experimentally obtained force curve and the green curve indicates the simulated force curve. Slight mismatch between the two is due to inaccurate electrostatic force model assumed for this setup. It will be shown later that the proposed model based strategy is robust to such modeling errors.

where

$$
\begin{aligned}
x &= \begin{pmatrix} p_1 \\ p_2 \end{pmatrix} \\
A &= \begin{pmatrix} 0 & 1 \\ -\omega_0^2 & -\omega_0/Q \end{pmatrix} \\
B_1 &= \begin{pmatrix} 0 \\ f(p_1) \end{pmatrix} \\
B_2 &= \begin{pmatrix} 0 \\ 1 \end{pmatrix} \\
C &= \begin{pmatrix} 1 & 0 \end{pmatrix}
\end{aligned}
\tag{7.13}
$$

Dynamics of extended Kalman filter is given by

$$\overbrace{\begin{array}{rcl}\dot{\hat{x}} &=& A\hat{x} + \hat{B}_1 V^2 + L(y - \hat{y}); \quad \hat{x}(0) = 0, \\ \hat{y} &=& C\hat{x},\end{array}}^{Observer} \tag{7.14}$$

where

$$\begin{array}{rcl}\hat{x} &=& \begin{pmatrix} \hat{x}_1 \\ \hat{x}_2 \end{pmatrix} \\ \hat{B}_1 &=& \begin{pmatrix} 0 \\ -\frac{K_{esf}}{(\ell_0+\hat{x}_1)^2} \end{pmatrix}\end{array} \tag{7.15}$$

Define error as

$$\begin{array}{rcl} e &=& x - \hat{x} \\ e_1 &=& Ce \\ \dot{e} &=& Ax + B_1 V^2 + B_2\eta - A\hat{x} - \hat{B}_1 V^2 - L(Cx + \nu - C\hat{x}) \\ \dot{e} &=& (A - LC)e + B_2\eta - L\nu + (B_1 - \hat{B}_1)V^2 \end{array} \tag{7.16}$$

where

$$\begin{array}{rcl} B_1(2,1) - \hat{B}_1(2,1) &=& -\frac{K_{esf}}{(\ell_0+x_1-d)^2} + \frac{K_{esf}}{(\ell_0+\hat{x}_1)^2} \\ &=& -\frac{K_{esf}}{\ell_0^2}(1 - \frac{2(x_1-d)}{\ell_0}) + \frac{K_{esf}}{\ell_0^2}(1 - \frac{2\hat{x}_1}{\ell_0}) \\ &=& \frac{2K_{esf}}{\ell_0^3}(x_1 - \hat{x}_1) - \frac{2K_{esf}}{\ell_0^3}d \end{array} \tag{7.17}$$

Let

$$\begin{array}{rcl} Z &=& \begin{pmatrix} 0 & 0 \\ \frac{2K_{esf}}{\ell_0^3}V^2 & 0 \end{pmatrix} \\ B_3 &=& \begin{pmatrix} 0 \\ \frac{2K_{esf}V^2}{\ell_0^3} \end{pmatrix}. \end{array} \tag{7.18}$$

then the error dynamics is given by

$$\dot{e} = (A - LC + Z)e + B_2\eta - L\nu - B_3 d. \tag{7.19}$$

This leads to distinct scenarios:

- If $d = 0$ then $\dot{e} = (A - LC + Z)e + B_2\eta - L\nu$

- if $d \neq 0$ then $\dot{e} = (A - LC + Z)e + B_2\eta - L\nu - B_3 d$

Thus one can detect the perturbations in presence and absence of the disturbance d by monitoring the error process. The plant-observer setup can be understood through figure (7.3).

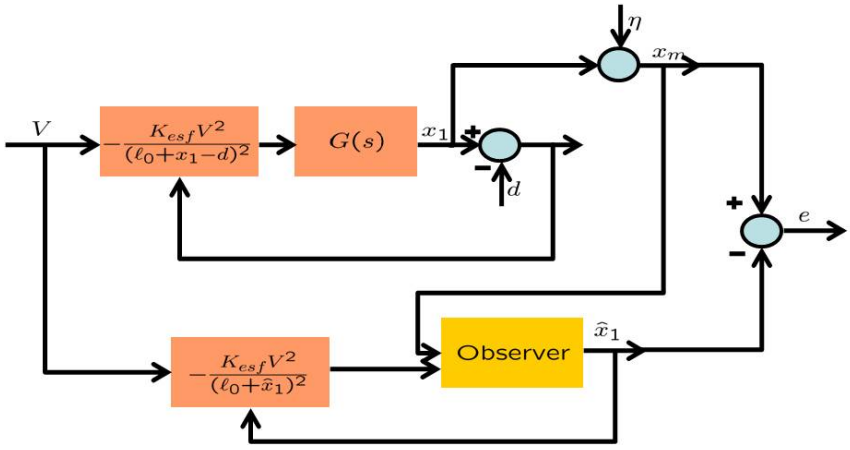

Figure 7.3: Schematic of an Extended Kalman filter (EKF) design for an electrostatically actuated and an optically sensed cantilever. The inputs to the EKF are the electrostatic voltage ($V(t)$) applied across the cantilever and the measured cantilever deflection (y). It outputs an error signal ($e_1(t)$).

7.4 Estimating ℓ_0 via Error RMS Minimization

Most of the static parameters except ℓ_0 are experiment independent once the cantilever and the nominal sample is fixed. ℓ_0 is still experiment dependent. So ℓ_0 needs to be estimated prior to the experiment. To estimate ℓ_0, we perform the experiment for some time such that there is no external perturbation and the cantilever is operated at its nominal trajectory. The input voltage and cantilever deflection is captured simultaneously. Then this data is fed to the simulation model (see Figure 7.3) and a ramp is applied to ℓ_0 in the extended Kalman filter equation. Thus the observer estimates the nominal trajectory for a range of ℓ_0 values. RMS of error signal is observed for this simulation (see figure 7.4(a)) and is plotted against the applied ℓ_0 ramp values (see figure 7.4(b)). The value of ℓ_0 at which the error rms is minimum is chosen as an estimate

of ℓ_0 of the cantilever-sample system for that particular experiment. The blue curve is the mean square error plotted against time as the ramp in ℓ_0 is applied in simulation. The red curve is the mean square error on the same data when the minimum value of ℓ_0 is chosen for simulations from the blue curve. The value of ℓ_0 chosen for the verification experiments was 1090 nm.

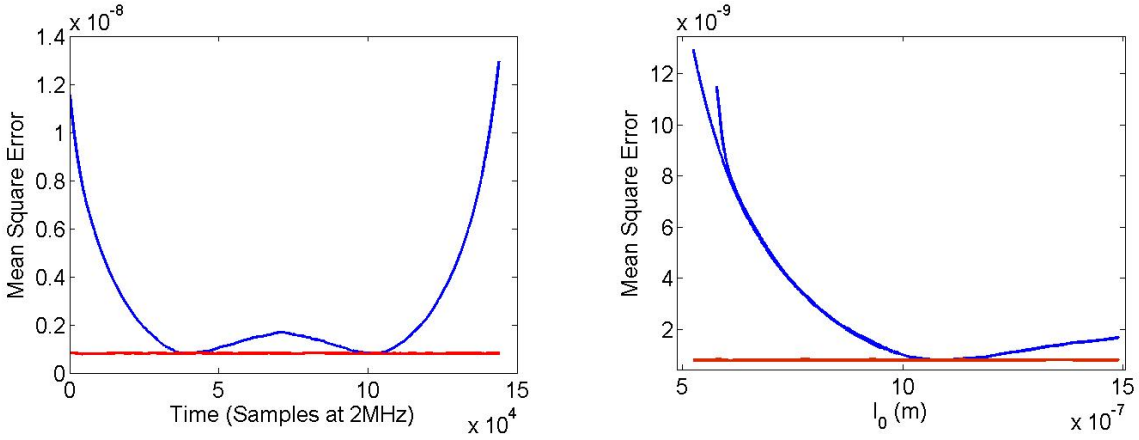

(a) (b)

Figure 7.4: (a) Mean square error at the EKF output for varying values of ℓ_0. The x-axis is time axis. (b) Mean square error vs the ℓ_0 distance. The blue curve is the mean square error when the value of ℓ_0 in the system is changing in a triangle fashion. The red curve is the mean square error when the value of ℓ_0 is fixed at the minimum value of the blue curve. There is a unique minima in plot (b) indicating that a distinct value of ℓ_0 will be able to best predict the cantilever deflection.

7.5 Verification of Nominal Experimental and Estimated Trajectories

The characterized model was verified for different input excitation frequencies. Figures 7.5(a), (b), (c) and (d) show that the proposed verification strategy result in quantitative matches between the experimentally captured and simulated dynamical trajectories. The blue curves are the experimentally obtained optical trajectories. The red curves are obtained from simulation.

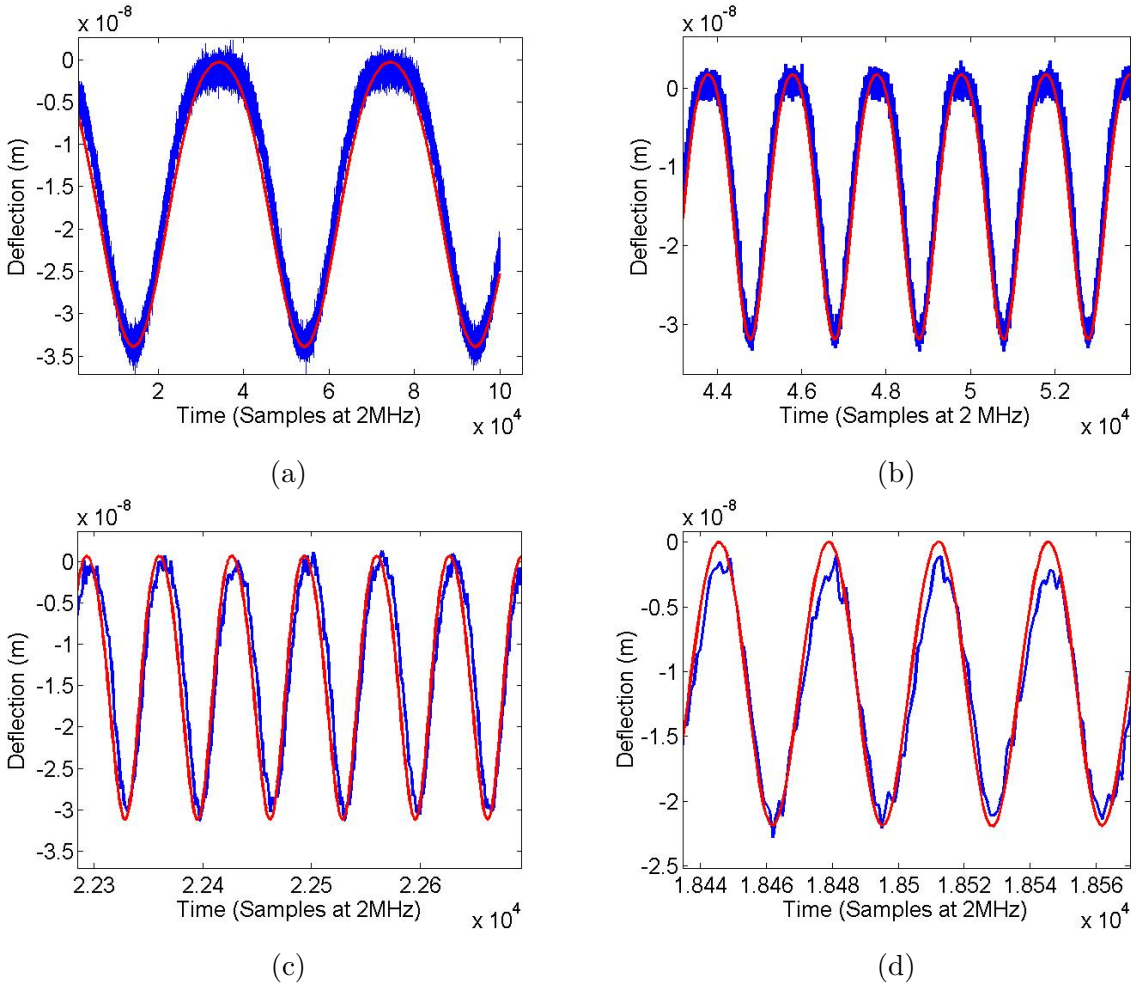

Figure 7.5: Comparison between the experimental and the simulated dynamic trajectories of a characterized electrostatically actuated cantilever for (a) 50 Hz (b) 1 kHz (c) 30 kHz and (d) 50 kHz frequency of the sinusoidal electrostatic voltage applied across the cantilever. The blue curves are the experimentally obtained cantilever deflection and the red curves are the simulated trajectories. Quantitative matches between the two indicates that the system is identified accurately.

7.6 High bandwidth sample detection using model mismatch based strategy

The proposed strategy was applied for high bandwidth sample detection. A random bit data was generated in MATLAB such that the minimum bit width corresponded to 30 kHz in one experiment and 50 kHz in the other. This bit stream was applied to a small z-piezo which moved the sample in the vertical direction according to the bit profile. The cantilever was actuated at 100 kHz which was above its resonant frequency. Bit height was less than 5 nm. Cantilever excitation voltage, deflection and applied bit profile were captured simultaneously at 2 MHz sampling frequency. This data was then processed in the simulink model. Figure 7.6(a) and Figure 7.7(a) show the bit profile and the applied bit sequence. Figure 7.6(b) and Figure 7.7(b) show the raw cantilever deflection. It can be seen that the bit profiles are not clearly visible in the raw deflection data. It must be noted that since the bit pattern was random with a minimum bit width corresponding to 30 kHz and 50 kHz, the topography data is a wide band data whose information content will be present till 30 kHz and 50 kHz respectively. Hence there was no information present in the amplitude signal when we demodulated the deflection signal at 100 kHz. Figure 7.6(c) and Figure 7.7(c) show the raw innovation error signal. It can be seen from these plots that the nominal cantilever trajectory is canceled well by the observer and the residual deviation due to the bit sequence is clearly visible in these plots. Thus it is possible to detect the bits from this data even for such a wide band data. Figure 7.8 shows the power spectral density (psd) of the raw deflection and raw error signal for the experiment in which the bit width corresponded to 50 kHz. The blue curve is psd of the raw deflection signal and the red curve is the psd of the error signal. It can be seen from this plot that the information content of the bits is present till 50 kHz. The observer is able to cancel the excitation frequencies at 100 kHz and its harmonic at 200 kHz precisely leaving the information content due to bits intact.

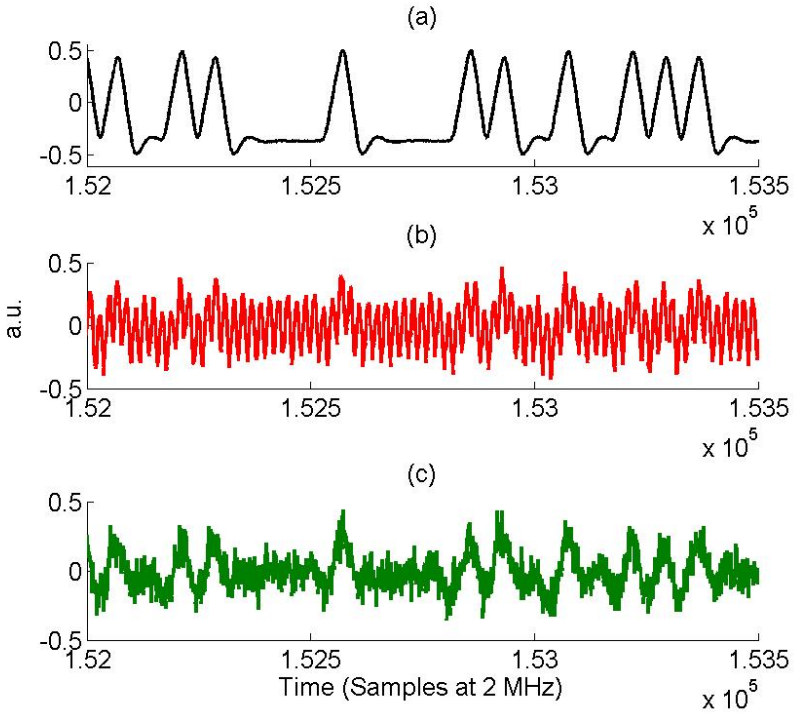

Figure 7.6: (a) Bit sequence (b) Raw cantilever deflection (c) Error signal of EKF when the cantilever is being actuated electrostatically at 100 kHz and the bit sequence is random with minimum bit width corresponding to 30 kHz. Thus each bit is sampled at least three times. The bit signature in raw deflection signal is not very clear but is very clearly visible in the error signal.

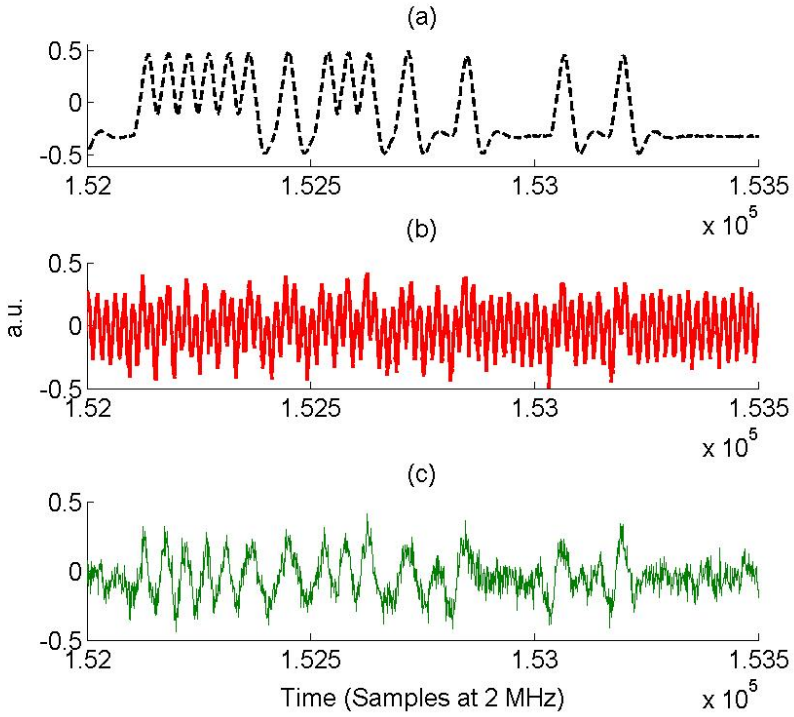

Figure 7.7: (a) Bit sequence (b) Raw cantilever deflection (c) Error signal of EKF when the cantilever is being actuated electrostatically at 100 kHz and the bit sequence is random with minimum bit width corresponding to 50 kHz. Thus each bit is sampled at most two times. The bit signature in raw deflection signal is not very clear but is very clearly visible in the error signal.

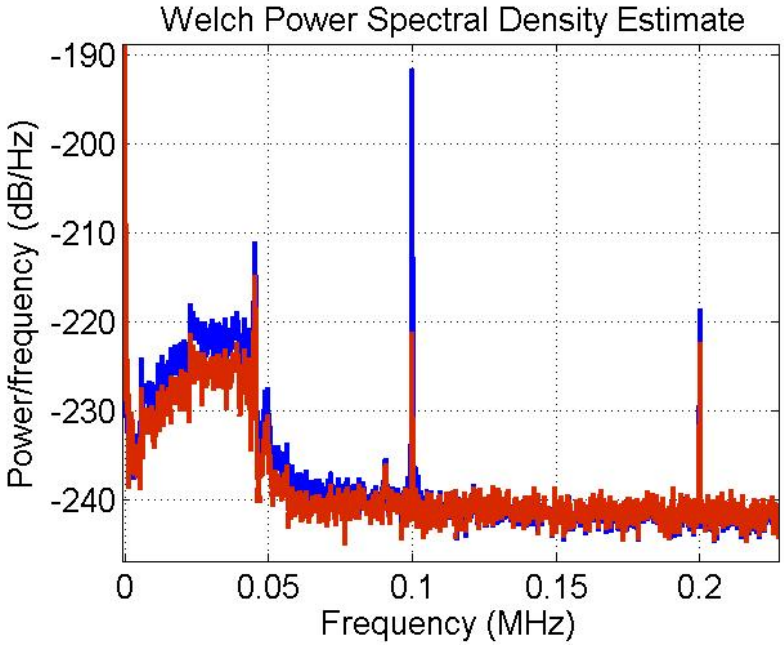

Figure 7.8: Power spectral density of raw cantilever deflection (blue curve) and the error signal of EKF (red signal) when the cantilever is being actuated electrostatically at 100 kHz and the bit sequence is random with minimum bit width corresponding to 50 kHz. This plot shows that the signal content is wideband and spans the spectrum from low frequencies till 50 kHz. EKF is instrumental in canceling the nominal behavior of the cantilever which constitutes the fundamental and the first harmonic of the excitation frequency at 100 kHz.

7.7 Analyzing the Effect of Voltage Variations of Sample in the Error Signal for Low and High Quality Factor Cantilever

Last section dealt with studying the effects of changes in topography in the error signal. This section presents the analysis of the effects in the error signal due to variations in F_{esf}, due to changes in the voltage, V_ϕ, where V_ϕ is the surface potential. Electrostatic force is a long range force that acts over the entire trajectory of the cantilever. This is in stark contrast with the Van De Waal's forces which act for only a very short period of

time of the cantilever trajectory. Thus any change in the nonlinear electrostatic forcing changes the cantilever trajectory from its nominal trajectory instantaneously depending on the cantilever dynamics.

Simulations were done for three different quality factors of the cantilever. In first case the quality factor of the cantilever was chosen to be 1.0148, in the second case it was 100.0148 and in the third case it was 1000.0148. A step of 0.1 V was given in V_ϕ during the simulation. The cantilever was actuated at 57185.01 Hz. The observer was so designed such that its error transients decayed in less than 5 oscillation cycles for $Q = 100$ and $Q = 1000$ case. The effect of the step in voltage was studied in raw deflection signal (see figure 7.9), amplitude (see figure 7.10), error signal (see figure 7.11) and the mean of the error signal (see figure 7.12). The blue curves correspond to the case where quality factor is 1.0148. The red curves correspond to the case where the quality factor is 100.0148 and the green curves correspond to the case where the quality factor is 1000.0148. The transients in the cantilever deflection and the amplitude of deflection at the oscillation frequency become slower as the quality factor increases as expected. Thus, any imaging scheme based on the amplitude of the excitation frequency will be slow. The error signal on the other hand has a high transition bandwidth due to proper equalization of the channel. Thus using mean of the error signal or raw error signal can lead to high bandwidth detection of features during electrostatic force microscopy.

7.8 Conclusion

In this work, we modeled an electrostatically actuated cantilever as a feedback interconnection system in which a linear cantilever plant is in feedback with a nonlinear electrostatic forcing. Methods to characterize these models accurately were presented. The identified model parameters were verified by comparing the experimental and simulated data. Quantitative agreement between the two indicate that the model identification is accurate. This known model of the system was used to design an extended Kalman filter to predict the cantilever trajectories in presence of noise. The error signal is shown to have a higher detection bandwidth as compared to the cantilever deflection or its amplitude. Finally it is shown experimentally that the bits (¡ 5 nm in height) which were hard to discern from the raw cantilever deflection data become prominent in the

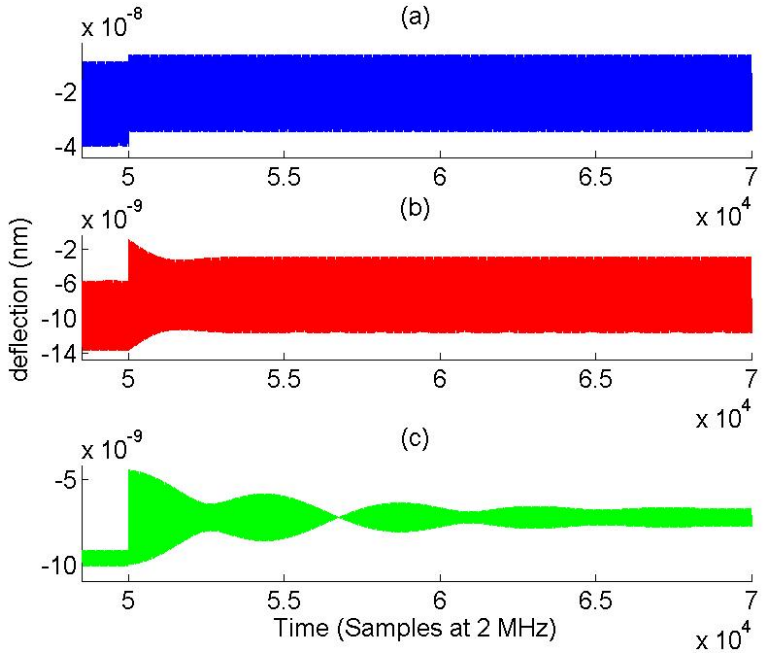

Figure 7.9: Cantilever deflection signal when the cantilever is being actuated electrostatically at 57185.01 Hz and the off-sample cantilever quality factor is (a) 1.0148 (b) 100.0148 and (c) 1000.0148. A step of height 0.1 V, is introduced in the electrostatic voltage at $5e4$ sample. It is seen that as the quality factor increases the transients take longer time to decay in the cantilever deflection signal.

error signal due to close cancellation of the nominal trajectory.

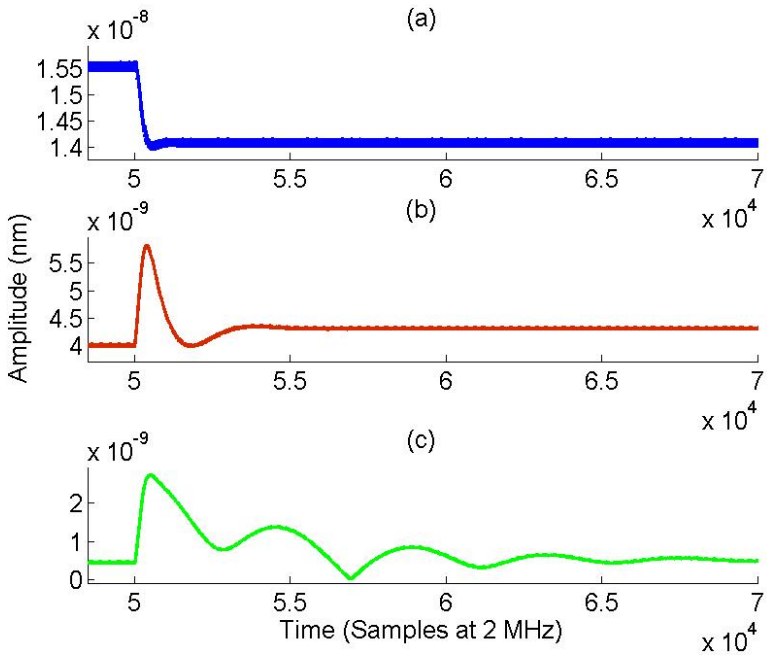

Figure 7.10: Cantilever amplitude signal when the cantilever is being actuated electrostatically at 57185.01 Hz and the off-sample cantilever quality factor is (a) 1.0148 (b) 100.0148 and (c) 1000.0148. A step of height 0.1 V, is introduced in the electrostatic voltage at 5e4 sample. It is seen that as the quality factor increases the transients in the cantilever amplitude take longer time to decay in the cantilever deflection signal.

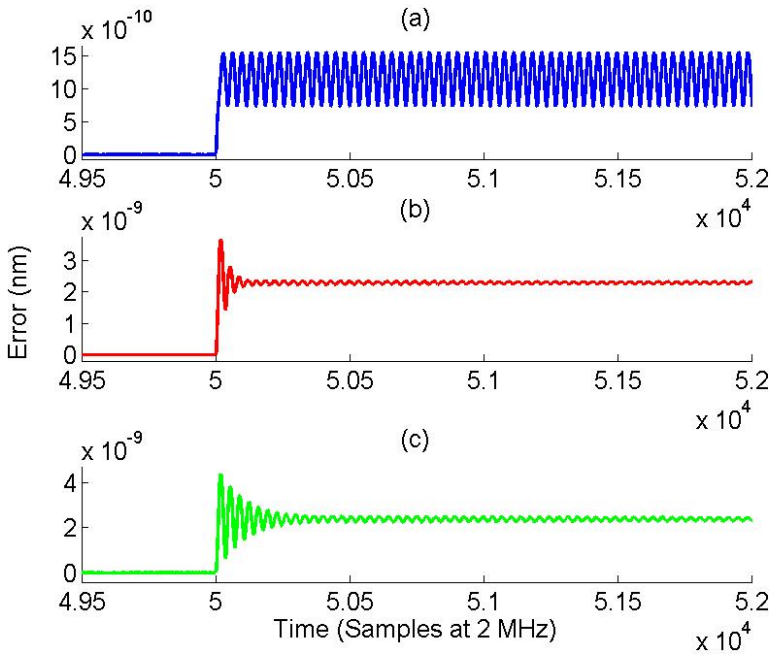

Figure 7.11: EKF error signal when the cantilever is being actuated electrostatically at 57185.01 Hz and the off-sample cantilever quality factor is (a) 1.0148 (b) 100.0148 and (c) 1000.0148. A step of height 0.1 V, is introduced in the electrostatic voltage at $5e4$ sample. It is seen that as the quality factor increases the transients decay time can be made independent of the quality factor of the cantilever. An impulse response of the disturbance to error dynamics is visible in the error signal. This can be used for detecting the presence of disturbance.

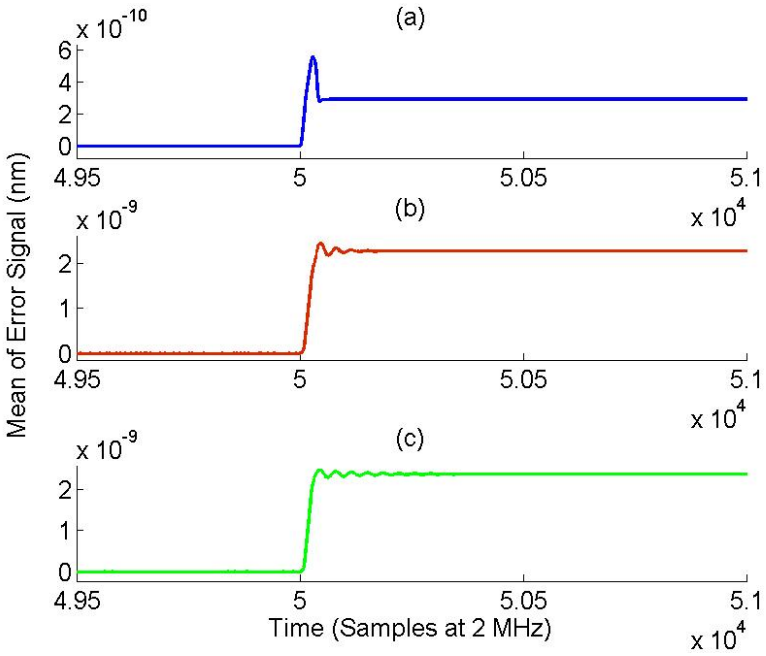

Figure 7.12: Running mean of the EKF error signal when the cantilever is being actuated electrostatically at 57185.01 Hz and the off-sample cantilever quality factor is (a) 1.0148 (b) 100.0148 and (c) 1000.0148. A step of height 0.1 V, is introduced in the electrostatic voltage at $5e4$ sample. It is seen that as the quality factor increases the transients decay time can be made independent of the quality factor of the cantilever. Thus fast detection events can be detected using this signal.

Chapter 8

CONCLUSIONS AND DISCUSSION

In this thesis, model mismatch based sensing paradigm for nanoscale imaging was developed. Open problems in high speed atomic force microscopy and quantitative material characterization using scanning probe microscopy techniques were addressed using the model mismatch and system theoretic concepts.

Application of such a paradigm can lead to enhanced sensing in terms of resolution and bandwidth at the cost of incorporating cantilever model information in the problem formulation. Thus precise and tractable system characterization techniques need to be developed. Since this approach delves into monitoring the perturbations, about a certain nominal trajectory of the system due to external environment changes, it is imperative that the nominal behavior of the sensor is quantitatively predictable. Moreover, in a sensing scenario, the nominal behavior of the sensor might change due to persistent external perturbations. Thus there is a need to adapt to this varying nominal behavior in real time.

The cantilever probe during tapping mode operation is modeled as an equivalent second order system with modified equivalent resonant frequency and modified quality factor using techniques of averaging theory. This resultant model, from cantilever excitation to the cantilever output, thus changes with changing material properties.

In absence of changes in the external environment, the nominal cantilever model corresponds to the off-sample dynamics. It was shown in the thesis that the deviations from this nominal behavior can be viewed not just in the time trajectories of the sensor output but also in the deviations of the sensor model itself. This requires real time estimation of the instantaneous sensor model.

In chapter 2 and 5, model mismatch due to external perturbations was viewed as a prediction error distance. To obtain such a measure, an observer is built on some nominal characterizable sensor dynamics. RMS of the prediction error is then used for sensing. In chapter 2, off-sample model of the cantilever is used to build the observer. RMS of the innovation error was then used to reduce probe-loss areas during high speed imaging. The problem was casted as a two state model mismatch condition wherein by thresholding of RMS of the error signal and then using it as the switching condition for a switching gain PID controller, it was experimentally demonstrated that one can obtain same imaging fidelity at an order higher scan rates. In chapter 5, sensitivity of the prediction error distance with respect to changes in the equivalent cantilever model parameter was explored. It was shown that by choosing the observer model which is not the same as the instantaneous equivalent cantilever model increases the sensitivity of rms of the error signal to changes in the equivalent plant model coefficients. Signal to Noise ratio also increases as the distance between the observer and the cantilever model increases. Although the sensing bandwidth in terms of detecting sudden changes in the external environment, in the transients of the error signal reduces as the distance between the observer and the plant model increases. Thus a trade-off between the sensitivity and bandwidth of rms of the error signal resulting from a proper choice of observer model and its gain was demonstrated through simulations. It was shown experimentally that there is a sweet spot of choosing an appropriate cantilever model and observer gain such that the high bandwidth transients are preserved in the error signal in addition to an acceptable sensing sensitivity.

Chapter 3 dealt with developing a recursive parameter estimation scheme called the REEP method to estimate the instantaneous equivalent cantilever model during tapping mode operation. It was shown that by replacing traditional single sinusoid excitation by a sum of three sinusoids excitation, one can obtain an unbiased estimate of the model parameters. Detailed on-sample and off-sample verification strategies were presented

to develop confidence in the estimates provided by the REEP algorithm. The efficacy of this technique was demonstrated experimentally for topography imaging and force spectroscopy. It was shown that the rate of convergence of this technique is two orders of magnitude better than any existing technique in the literature and is the only technique which provides these estimates during tapping mode operation.

Chapter 4 dealt with exploring the benefits of REEP algorithm for sensing applications. Model mismatch based sensing was viewed in terms of variation of plant coefficients with time. In the case of a cantilever, these coefficients are equivalent resonant frequency and equivalent quality factor/damping. It is known that the elastic and dissipative components of tip-sample separation get decoupled in equivalent resonant frequency and equivalent quality factor behavior respectively. This kind of decoupling is not present in the amplitude and the phase measurements. Hence getting these estimates in real time during tapping mode operation addresses the challenge of quantitative imaging for applications like polymer characterization where the study of the elastic and dissipative properties with variation in temperature and humidity is of interest to material scientists. In this chapter, the idea of using equivalent resonant frequency and equivalent damping estimation for topography imaging during tapping mode operation was explored. The equation for the sensitivity of these estimates with respect to the topography was derived and it was shown that contrary to the behavior of the amplitude signal whose sensitivity decreases or remains fixed at one with reduction in the quality factor of the off-sample probe, the sensitivity of the equivalent resonant frequency and equivalent damping increase with decrease in the off-sample quality factor of the cantilever. This behavior was also demonstrated through experimental force curves. This behavior is interesting because in a lot of applications viz. under fluid imaging or an application where the probe is designed for integrated sensing and actuation, the operation is intrinsically low Q. Hence there is a loss of sensitivity in using amplitude and phase measurements as topography indicators during tapping mode operation. It was suggested that the equivalent resonant frequency and the equivalent damping estimates obtained from REEP algorithm can be used for imaging during low Q operations.

Chapter 2, 3, 4 and 5 dealt with casting the model mismatch paradigm for the case where the tip experiences Van De Waal's forces. But the concepts developed are extendible to other modes of SPM operations viz. EFM, KFM, PFM and Acoustic

AFM etc..

In chapter 6 and 7, model mismatch paradigm was developed for a probe with integrated solid state thermal sensing and electrostatic actuation. This probe is being used in the high density data storage project, "Millipede", being developed at IBM Research Lab, Zurich. Initially this probe was being used in contact mode operation to read and write bits on a polymer substrate. Read channel modeling for this mode did not involve modeling of cantilever dynamics and its interaction forces since the cantilever was not being excited. However this mode led to the wear and tear of both the tip and the sample thereby reducing the life of the device. So the idea was to move towards dynamic mode operation. But since there is a drop in the sensing bandwidth when we move from contact mode operation to dynamic mode operation, it was desired to explore model mismatch based idea to achieve high bandwidth bit detection. The first crucial step in this endeavor was to develop tractable models and a characterization methodology for these devices being operated in dynamic mode. This is a particularly complicated task since the cantilever is being excited electrostatically and hence besides experiencing electrostatic and Van De Waal's forces, it also experiences capacitive and magnetic forces at the same time. These forces then effect the cantilever trajectory and one needs to dig out the perturbation due to changes in sample topography (bits) from cantilever trajectory. We made appropriate modeling assumptions wherein it was assumed that the electrostatic and Van De Waals forces effect the cantilever in an additive way and remaining forces can be clubbed into spurious effects and characterized independently. Nonlinear curve fitting algorithm and input output based frequency sweep methods were utilized to characterize the system large signal nonlinearity and small signal dynamics respectively. These parameters could also be identified by using the thermal sensor data alone which is crucial for integrated setting where the bulky optical sensor is no longer available. It was shown experimentally that a quantitative match between the experimental and simulated trajectory is obtained for non interacting dynamics and near quantitative match for the interacting trajectories. Moreover the model developed is tractable and real time implementable for control purposes unlike the exhaustive FEM simulations.

In chapter 7, this modeling was used to design an extended Kalman filter where it is assumed that optical sensor measurements are available. It was shown experimentally

that by monitoring the error signal process of this observer it is indeed possible to detect a wide band signal content reflecting the change in sample topography. Thus the extended Kalman filter uses the fact that the form on the nonlinear forcing is available along with the off-sample cantilever model and then detects changes due to unknown sample topography as perturbations to this nominal trajectory.

Thus it is effectively demonstrated in this thesis that by proper modeling and characterization of the sensor and its interaction with the environment it is possible to cast the problem wherein the known and the tractable part is well identified and the unknown part of the system dynamics is viewed as perturbation to this characterized dynamics. The model mismatch can be viewed either in time domain as a perturbation error distance by monitoring the rms of the error signal or by viewing it as a change in the equivalent sensor model itself.

References

[1] G. Binnig, C. F. Quate, and C. Gerber. Atomic force microscope. *Phys. Rev. Lett.*, 56:930, 1986.

[2] R. Garcia, R. Magerle, and R. Perez. Nanoscale compositional mapping with gentle forces. *Nature Materials*, vol. 6:405–411, June 2007.

[3] P. Girard. Electrostatic force microscopy: principles and some applications to semiconductors. *IOP Nanotechnology*, vol. 12:485–490, 2001.

[4] L. Bond, S. Allen, M. C. Davies, C. J. Roberts, A. P. Shivji, S. J. B. Tendler, P. M. Williams, and J. Zhang. Differential scanning calorimetry and scanning thermal microscopy analysis of pharmaceutical materials. *International Journal of Pharmaceutics*, vol. 243:71–82, 2002.

[5] A. Lewis, A. Radko, N. B. Ami, D. Palanker, and K. Lieberman. Near-field scanning optical microscopy in cell biology. *Trends in Cell Biology*, vol. 9, Issue 2:70–73, Feb 1999.

[6] Asylum Research Inc. asylumresearch.com.

[7] J. Xie, M. Hu, S. Ling, and H. Du. Fabrication and characterization of piezoelectric cantilever. *Sensors and Actuators A*, vol. 126:182–186, 2006.

[8] G. Neubauer, S. R. Cohen, G. M. McClelland, D. Horne, and C. M. Mate. Force microscopy with a bidirectional capacitance sensor. *Review of Scientific Instruments*, vol. 69, No. 9:2296–2308, Sept 1990.

[9] P.Vettiger, G.Cross, M.Despont, U.Drechsler, U.Dürig, B.Gotsmann, W.Häberle, M.A.Lantz, H.E.Rothuizen, R.Stutz, and G.K.Binnig. The "'millipede"'- nanotechnology entering data storage. *IEEE Transactions on Nanotechnology*, vol. 1, No. 1:39–55, March 2002.

[10] W. P. King, T. W. Kenny, and K. E. Goodson. Comparison of thermal and piezoresistive sensing approaches for atomic force microscopy topography measurements. *Applied Physics Letters*, vol. 85, No.11:2086–2088, 13 September 2004.

[11] J. N. Israelachvili. *Intermolecular and Surface Forces*. Academic Press, 1985.

[12] F. J. Giessibl. *Noncontact Atomic Force Microscopy*, chapter Principle of NC-AFM, page 11. NanoScience and Technology. Springer, Berlin, 2002.

[13] F. J. Giessibl. Advances in atomic force microscopy. *Reviews of Modern Physics*, vol. 75, Issue 3:949–983, 2003.

[14] Q. Thong, D. Inniss, K. Kjoller, and V.B. Elings. Fractured polymer/ silica fiber surface studied by tapping mode atomic force microscopy. *Surface Science Letters*, vol. 290:688–692, 1993.

[15] M. V. Salapaka, D. Chen, and J. P. Cleveland. Linearity of amplitude and phase in tapping-mode atomic force microscopy. *Phys. Rev. B.*, 2000.

[16] J. Tamayo and R. Garcia. Effects of elastic and inelastic interactions on phase contrast images in tapping-mode scanning force microscopy. *Applied Physics Letters*, vol. 71, Issue 16:2394–2396, Oct 1997.

[17] N. F. Martinez and R. Garcia. Measuring phase shifts and energy dissipation with amplitude modulation atomic force microscopy. *IOP Nanotechnology*, vol. 17:S167–S172, March 2006.

[18] E. Eleftheriou, T. Antonakopoulos, G. K. Binnig, G. Cherubini, M. Despont, A. Dholakia, U. Dürig, M. A. Lantz, H. Pozidis, H. E. Rothuizen, and P. Vettiger. Millipedea mems-based scanning-probe data-storage system. *IEEE Transactions on Magnetics*, vol. 39, No. 2:938–945, March 2003.

[19] D. C. Coffey and D. S. Ginger. Time-resolved electrostatic force microscopy of polymer solar cells. *Nature Materials*, vol. 5:735–740, Sept 2006.

[20] T. Ando, N. Kodera, Y. Naito, T. Kinoshita, K. Furuta, and Y. Y. Toyoshima. A high-speed atomic force microscope for studying biological macromolecules in action. *ChemPhysChem*, vol. 4:1196–1202, 2003.

[21] A.D.L. Humpris, M.J. Miles, and J. K. Hobbs. A mechanical microscope: High-speed atomic force microscopy. *Applied Physics Letters*, 86:12468–12472, 2005.

[22] J. R. Lozano and R. Garcia. Theory of phase spectroscopy in bimodal atomic force microscopy. *Physical Review B*, vol. 79:014110–1–9, 2009.

[23] S. Jesse, S. V. Kalinin, R. Proksch, A. P. Baddorf, and B. J. Rodriguez. The band excitation method in scanning probe microscopy for rapid mapping of energy dissipation on the nanoscale. *IOP-Nanotechnology*, vol. 18:435503, July 2007.

[24] D. Vallett. Failure analysis requirements for nanoelectronics. *IEEE Transactions on Nanotechnology*, vol.1 no. 3:117–121, 2002.

[25] R. Szoszkiewicz, T. Okada, S. C. Jones, T. Li, W. P. King, S. R. Marder, and E. Riedo. High-speed, sub-15 nm feature size thermochemical nanolithography. *Nanoletters*, vol. 7 no. 4:1064–1069, 2007.

[26] C. F. Quate T. Sulchek, G. G. Yaralioglu and S. C. Minne. Characterization and optimization of scan speed for tapping-mode atomic force microscopy. *Review of Scientific Instruments*, vol. 73 no. 8:2928–2936, 2002.

[27] T. Ando. Control techniques in high-speed atomic force microscopy. *Proceedings of the American Control Conference*, pages 3194–3200, 2008.

[28] T. De, P. Agarwal, D. R. Sahoo, and M. V. Salapaka. Real-time detection of probe loss in atomic force microscopy. *Applied Physics Letters*, vol. 89:133119, 2006.

[29] M. Sakashita N. Kodera and T. Ando. Dynamic proportional-integral-differential controller for high-speed atomic force microscopy. *Review of Scientific Instruments*, vol. 77:083704, 2006.

[30] A. Sebastian, M. V. Salapaka, D. J. Chen, and J. P. Cleveland. Harmonic analysis based modeling of tapping-mode afm. *Proceedings of the American Control Conference*, pages 232–236, June 1999.

[31] M. V. Salapaka, H. S. Bergh, J. Lai, A. Majumdar, and E. McFarland. Multi-mode noise analysis of cantilevers for scanning probe microscopy. *Journal of Applied Physics*, vol. 81(6):2480–2487, March 1997.

[32] A. Sebastian, A. Gannepalli, and M. V. Salapaka. The amplitude phase dynamics and fixed points in tapping-mode atomic force microscopy. *Proceedings of the American Control Conference*, pages 2499–2504, July 2004.

[33] A. B. Kos and D. C. Hurley. Nanomechanical mapping with resonance tracking scanned probe microscope. *IOP-Nanotechnology*, vol. 19:015504, 2008.

[34] A. S. Paulo and R. Garcia. Unifying theory of tapping-mode atomic-force microscopy. *Physical Review B*, vol. 66:041406(R), 2002.

[35] H. Stark and J. W. Woods. *Probability, Random Processes and Estimation Theory for Engineers*. Prentice Hall, Englewood NJ, 1994.

[36] K. J. Astrom and B. Wittenmark. *Adaptive Control*. Addison Wesley, USA, Pages 63-67, 1995.

[37] F. Ding, T. Chen, and L. Qiu. Bias compensation based recursive least-squares identification algorithm for miso systems. *IEEE Transactions on Circuits and SystemsII: Express Briefs*, vol. 53, No. 5:349–353, May 2006.

[38] A. Sebastian, M. V. Salapaka, D. Chen, and J. P. Cleveland. Harmonic and power balance tools for tapping-mode atomic force microscope. *Journal of Applied Physics*, 89 (11):6473–6480, June 2001.

[39] J. A. Sanders and F. Verhulst. *Averaging Methods in Nonlinear Dynamics Systems*. Springer-Verlag, 1985.

[40] H. Holscher and U. D. Schwarz. Q-controlled amplitude modulation atomic force microscopy in liquids: An analysis. *Applied Physics Letters*, vol. 89:073117, 2006.

[41] H. Holscher and D. Ebeling. Theory of q-controlled dynamic force microscopy in air. *Journal of Applied Physics*, vol. 99:084311, 2006.

[42] R. D. Jaggi, A. F. Obregon, P. Studerus, and K. Ensslin. Detailed analysis of forces influencing lateral resolution for q-control and tapping mode. *Applied Physics Letters*, vol. 79, No. 1:135–137, 2001.

[43] L. Chen, X. Yu, and D. Wang. Cantilever dynamics and quality factor control in ac mode afm height measurements. *Ultramicroscopy*, vol. 107:275–280, 2007.

[44] D. Ebeling, H. Holscher, H. Fuchs, B. Anczykowski, and U. D. Schwarz. Imaging of biomaterials in liquids: a comparison between conventional and q-controlled amplitude modulation ('tapping mode') atomic force microscopy. *IPP Nanotechnology*, vol. 17:S221–S226, 2006.

[45] L. Nony, R. Boisgard, and J. P. Aime. Nonlinear dynamical properties of an oscillating tip-cantilever system in the tapping mode. *Journal of Chemical Physics*, vol. 11, No. 4:1615–1627, July 1999.

[46] J. Kokavecz, Z. L. Horvath, and A. Mechler. Dynamical properties of the q-controlled atomic force microscope. *Applied Physics Letters*, vol. 85, No. 15:3232–3234, 2004.

[47] F. Dubourg, J. P. Aime, G. Couturier, and J. Salardenne. Apparent hardening of soft samples through q factor change in afm. *Europhysics Letters*, vol. 65, No. 5:671–676, 2003.

[48] P.Agarwal, D.R.Sahoo, A. Sebastian, H. Pozidis, and M.Salapaka. Modeling and identification of the dynamics of electrostatically actuated microcantilever with integrated thermal sensor. *Proceedings of the Conference on Decision and Control*, Dec 2008.

[49] D. R. Sahoo, P. Agarwal, and M. V. Salapaka. Transient force atomic force microscopy: A new nano-interrogation method. *Proceedings of American Control Conference*, pages 2135–2140, 2007.

[50] T. De, P. Agarwal, D.R. Sahoo, and M. V. Salapaka. Real-time detection of probe loss in atomic force microscopy. *Applied Physics Letters*, 89:133119, 2006.

[51] P. Agarwal, T. De, and M. V. Salapaka. Real time reduction of probe-loss using switching gain controller for high speed atomic force microscopy. *Review of Scientific Instruments*, Vol. 80, Issue 10:103701, Oct 2009.

[52] P. Agarwal and M. V. Salapaka. Real time estimation of equivalent cantilever parameters in tapping mode atomic force microscopy. *Applied Physics Letters*, Vol. 95, Issue 8:083113, August 2009.

[53] William P. King, Shubham Saxena, and Brent A. Nelson. Nanoscale thermal analysis of an energetic material. *Nano Letters*, Vol. 6, No. 9:2145–2149, 2006.

[54] B.A.Nelson, W. P. King, A. R. Laracuente, P. E. Sheehan, and L. J. Whitman. Direct deposition of continuous metal nanostructures by thermal dip-pen nanolithography. *Applied Physics Letters*, 88:033104, 2006.

[55] K. Park, J. Lee, Z. M. Zhang, and W. P. King. Topography imaging with a heated atomic force microscope cantilever in tapping mode. *Review of Scientific Instruments*, vol. 78:043709, 2007.

[56] K.J.Kim, K.Park, J.Lee, Z.M.Zhang, and W.P.King. Nanotopographical imaging using a heated atomic force microscope cantilever probe. *Sensors and Actuators A, Elsevier*, vol. 136:95–103, 2007.

[57] E. O. Sunden, T. L. Wright, J. Lee, W. P. King, and S. Graham. Room-temperature chemical vapor deposition and mass detection on a heated atomic force microscope cantilever. *Applied Physics Letters*, vol. 88:033107, 2006.

[58] A. S. Basu and Y. B. Gianchandani. Shaping high-speed marangoni flow in liquid films by microscale perturbations in surface temperature. *Applied Physics Letters*, Vol. 90, Issue 3:034102, 2007.

[59] D. Lange, T. Akiyama, C. Hagleitner, A. Tonin, H. R. Hidber, P. Niedermann, U. Staufer, N. F. De Rooij, O. Brand, and H. Baltes. Parallel scanning afm with

on-chip circuitry in cmos technology. *Micro Electro Mechanical Systems,MEMS '99. Twelfth IEEE International Conference on*, pages 447–452, 1999.

[60] A. Majumdar. Scanning thermal microscopy. *Annu. Rev. Mater. Sci.*, 29:505–585, 1999.

[61] A. Passian, R. J.Warmack, T. L. Ferrell, and T. Thundat. Thermal transpiration at the microscale: A crookes cantilever. *Physical Review Letters*, vol.90, no.12, 28 March 2003.

[62] W. P. King. Design analysis of heated atomic force microscope cantilevers for nanotopography measurements. *Journal of Micromechanics and Microengineering*, vol.15:24412448, 2005.

[63] J. Lee, T. L. Wright, M. R. Abel, E. O. Sunden, A. Marchenkov, S. Graham, and W. P. King. Thermal conduction from microcantilever heaters in partial vacuum. *Journal Of Applied Physics*, vol. 101:014906, 2007.

[64] U.Dürig. Fundamentals of micromechanical thermoelectric sensors. *Journal of Applied Physics*, vol. 98:044906, 2005.

[65] A. Sebastian and D. Wiesmann. Modeling and experimental identification of silicon micro-heaters: a systems approach. *IEEE/ASME Journal of Microelectromechanical Systems*, vol. 17, no. 4:911–920, 2008.

[66] C. Dames and G. Chen. $1\omega, 2\omega$ and 3ω methods for measurements of thermal properties. *Review of Scientific Instruments*, 76:124902, 2005.

[67] P.O.Chapuis, J. J. Greffet, K. Joulain, and S. Volz. Heat transfer between a nanotip and a surface. *Microelectronic Engineering*, 67-68:2978–2981, 2003.

[68] J. Kim, S. G. Kim, J. G. Koo, T. M. Roh, H. Soopark, and D. Y. Kim. Characteristics of dynamic resistance in a heavily doped silicon semiconductor resistor. *Int. J. Electronics*, vol. 86, No. 3:269– 279, 1999.

[69] B.W.Chui, M.Asheghi, Y.S.Ju, K.E.Goodson, T.W.Kenny, and H.J.Mamin. Intrinsic-carrier thermal runaway in silicon microcantilevers. *Microscale Thermophysical Engineering*, vol. 3:217–228, 1999.

[70] D.R.Sahoo, W. Häberle, P. Bächtold, A. Sebastian, H. Pozidis, and E. Eleftheriou. On intermittant-contact read operation in a mems-based scanning probe data-storage system. *Proceedings of the American Control Conference*, June 2008.

[71] Q. Zhong, D. Inniss, K. Kjoller, and V B Elings. Fractured polymer/silica fiber surface studied by tapping mode atomic force microscopy. *Surface Science Letters*, 290:L688–L692, 1993.

[72] M. V. Salapaka, H. S. Bergh, J. Lai, A. Majumdar, and E. McFarland. Multi-mode noise analysis of cantilevers for scanning probe microscopy. *J. App. Phys.*, 81(6):2480, March 1997.

[73] D. A. Walters, J. P. Cleveland, N. H. Thmson, P. K. Hansma, M. A. Wendman, G. Gurley, and V. Elings. Short cantilevers for atomic force microscopy. *Rev. Sci. Instr.*, 67(10):3583–3590, 1996.

[74] A.F.Marques and A.M.Shkel. On electrostatic actuation beyond snapping condition. *Proceedings of the IEEE Sensors*, ISBN: 0-7803-9056-3, Oct 30 2005.

[75] K. Madsen, H.B. Nielsen, and O. Tingleff. *Methods for non-linear least squares problems*. 2004.

[76] M. Nakamura and H. Yamada. Electrostatic force microscopy. *Roadmap of Scanning Probe Microscopy: NanoScience and Technology*, pages 43–51, 2007.

[77] P. Girard. Electrostatic force microscopy: principles and some applications to semiconductors. *Insititute of Physics Publishing: Nanotechnology*, Vol. 12:485–490, 2001.

[78] S. Belaidi, P. Girard, and G. Leveque. Electrostatic forces acting on the tip in atomic force microscopy: Modelization and comparison with analytic expressions. *Journal of Applied Physics*, Vol. 81, Issue 3:1023–1030, Feb 1997.

[79] S. Hudlet, M. S. Jean, C. Guthmann, and J. Berger. Evaluation of the capacitive force between an atomic force microscopy tip and a metallic surface. *The European Physical Journal B*, Vol. 2:5–10, 1998.

[80] R. M. Nyffenegger, R. M. Penner, and R. Schierle. Electrostatic force microscopy of silver nanocrystals with nanometer-scale resolution. *Applied Physics Letters*, Vol. 71 Issue 13:1878–1880, 1997.

[81] R. W. Stark, N. Naujoks, and A. Stemmer. Multifrequency electrostatic force microscopy in the repulsive regime. *Institute of Physics Publishing: Nanotechnology*, Vol. 18:065502, 2007.

[82] A. S. Hou, F. Ho, and D. M. Bloom. Picosecond electrical sampling using a scanning force microscope. *Electronics Letters*, Vol. 28, No. 25:2302–2303, Dec 1992.

[83] P.Agarwal, D.R.Sahoo, A. Sebastian, H. Pozidis, and M.Salapaka. Real time models of electrostatically actuated cantilever probes with integrated thermal sensor for nanoscale interrogation. *Journal of Microelectromechanical Systems*, Vol. 19 Issue 1:83–98, Feb 2010.